

Particle convection in thermonuclear plasmas

Citation for published version (APA):

Karelse, F. A. (2001). *Particle convection in thermonuclear plasmas*. [Phd Thesis 1 (Research TU/e / Graduation TU/e), Applied Physics and Science Education]. Technische Universiteit Eindhoven.
<https://doi.org/10.6100/IR543298>

DOI:

[10.6100/IR543298](https://doi.org/10.6100/IR543298)

Document status and date:

Published: 01/01/2001

Document Version:

Publisher's PDF, also known as Version of Record (includes final page, issue and volume numbers)

Please check the document version of this publication:

- A submitted manuscript is the version of the article upon submission and before peer-review. There can be important differences between the submitted version and the official published version of record. People interested in the research are advised to contact the author for the final version of the publication, or visit the DOI to the publisher's website.
- The final author version and the galley proof are versions of the publication after peer review.
- The final published version features the final layout of the paper including the volume, issue and page numbers.

[Link to publication](#)

General rights

Copyright and moral rights for the publications made accessible in the public portal are retained by the authors and/or other copyright owners and it is a condition of accessing publications that users recognise and abide by the legal requirements associated with these rights.

- Users may download and print one copy of any publication from the public portal for the purpose of private study or research.
- You may not further distribute the material or use it for any profit-making activity or commercial gain
- You may freely distribute the URL identifying the publication in the public portal.

If the publication is distributed under the terms of Article 25fa of the Dutch Copyright Act, indicated by the "Taverne" license above, please follow below link for the End User Agreement:

www.tue.nl/taverne

Take down policy

If you believe that this document breaches copyright please contact us at:

openaccess@tue.nl

providing details and we will investigate your claim.

PARTICLE CONVECTION IN
THERMONUCLEAR PLASMAS

Particle Convection in Thermonuclear Plasmas

PROEFSCHRIFT

ter verkrijging van de graad van doctor aan de
Technische Universiteit Eindhoven, op gezag van de
Rector Magnificus, prof.dr. M. Rem, voor een commissie
aangewezen door het College voor Promoties in het
openbaar te verdedigen op woensdag 14 maart 2001 om
16.00 uur

door

FRANK ARNOUD KARELSE

geboren te 's-Gravenhage

Dit proefschrift is goedgekeurd door de promotoren:

prof. dr. N. J. Lopes Cardozo

en

prof. dr. F. C. Schüller

Copromotor: dr. G. M. D. Hogewij



ISBN 90-9014543-5

Omslag: Linny van der Weyden

Druk: Print Partners Ipskamp, Enschede

The work described in this dissertation is a part of a research program of the 'Stichting voor Fundamenteel Onderzoek der Materie' (FOM) with financial support from the 'Nederlandse organisatie voor Wetenschappelijk Onderzoek' (NWO) and EURATOM.

The work was carried out at the 'FOM-instituut voor Plasmafysica' in Nieuwegein, the Netherlands.

'The truth is rarely pure and never simple'

Oscar Wilde (1854-1900)

Aan Dinda

CONTENTS

Samenvatting	xi
Summary	xiii
1 Introduction	1
1.1 Fusion	1
1.2 The Tokamak	2
1.3 Outstanding Issues	4
1.4 Transport	5
1.5 This Thesis	6
1.6 Publications	7
References	9
2 Tokamak Stability and Transport	11
2.1 Magnetic equilibrium	11
2.2 Neoclassical Transport	14
2.3 Anomalous transport	17
References	18
3 The RTP Tokamak and its Diagnostics	21
3.1 The RTP Tokamak	21
3.1.1 ECH	22
3.1.2 Pellet Injection	22
3.2 The RTP Diagnostics	22
References	24

4	Polarimetry	25
4.1	Interferometry and Polarimetry	25
4.2	Measurement Method and Set-up	28
4.2.1	Interferometry	29
4.2.2	Polarimetry	30
4.2.3	Experimental Set-up	32
4.3	Data Acquisition	34
4.4	Data Analysis	36
4.4.1	Refraction	36
4.4.2	Abel Inversion	38
4.4.3	Parametrisation of q	39
4.5	Experimental results	41
4.5.1	Results obtained with pellet injection	42
4.5.2	Results on current ramps down	48
4.5.3	Results in discharges with hollow T_e	49
4.6	Accuracy Analysis	50
4.6.1	Interference loops	54
4.6.2	Diffraction	56
4.7	Discussion and conclusion	59
	References	60
5	Tangential Thomson Scattering	63
5.1	Preface	63
5.1.1	Theory	64
5.2	Introduction	69
5.3	Set-up and calibration	71
5.3.1	Set-up	71
5.3.2	Comparison Radial and Tangential TS set-up	73
5.3.3	Calibration	74
5.4	Data analysis	75
5.4.1	Fit method and moment method	76
5.4.2	Simulation results	77
5.4.3	Analysis procedure	80
5.5	Experimental results	82
5.5.1	Results on Ohmic discharges	83
5.5.2	Comparison fit method and moment method	85
5.5.3	Estimate of the ion drift velocity	86
5.5.4	Steady state on- and off-axis ECH experiments	87
5.5.5	Relaxation after off-axis ECH	90
5.5.6	Electron drift velocity fluctuations	93
5.6	Summary and discussion	96
	References	98

6	Particle transport in the RTP tokamak	101
6.1	Introduction	101
6.2	Theoretical background	103
6.2.1	Ware pinch	104
6.2.2	Thermo-diffusion	105
6.2.3	Electrostatic Turbulence	106
6.2.4	Scaling with neutral density	107
6.2.5	Other pinch mechanisms	107
6.3	Particle source and Neutral density	107
6.3.1	Analytic solution of the Neutral Diffusion Equation	109
6.3.2	A Numerical Model of Neutral Penetration and the Benchmarking Against the EIRENE Code	110
6.4	RTP observations	115
6.4.1	Steady state Ohmic and ECH discharges	115
6.4.2	Density profiles during ECCD	117
6.4.3	Changes of the density profile upon switch-on of ECH	118
6.4.4	Spontaneous transitions during ECH	119
6.4.5	Bifurcation after switch-off off-axis ECH	120
6.4.6	Summary of the RTP Observations	121
6.4.7	Profile consistency	122
6.5	Determination of Particle Transport Coefficients; the ASTRA transport code	126
6.5.1	Previous RTP particle transport analysis	126
6.5.2	Introduction to ASTRA	127
6.5.3	Simulation of steady state Ohmic and EC Heated discharges	129
6.6	Test of Transport Models	131
6.6.1	Transition from Ohmic to Centrally EC Heated State	132
6.6.2	Transition from Ohmic to Off-axis EC Heated state - case I	139
6.6.3	Transition from Ohmic to Off-axis EC Heated state - case II	144
6.6.4	Relaxation to Bifurcated Ohmic State	151
6.7	Summary	157
6.8	Discussion and Conclusion	159
	Appendix	160
	References	164
7	Evaluation and Discussion	167
7.1	Current Density Diagnosis	167
7.1.1	Review of polarimetry	167
7.1.2	Review of Tangential Thomson Scattering	169
7.2	Particle Transport in RTP	169
7.3	Future Research	171
	Dankwoord	173
	Curriculum Vitae	175

SAMENVATTING

Met kernfusie kan op een veilige en schone manier energie uit water worden gewonnen. Energiewinning op deze wijze kan helpen het dreigende, toekomstige energietekort het hoofd te bieden. Daarom wordt onderzoek gedaan om tot een fusie-reactor te komen. De machine die het verst ontwikkeld is, heet 'tokamak' en sluit de brandstof, heet waterstof-plasma, met behulp van magneetvelden op in de vorm van een torus.

In de tokamak vormt het magneetveld, in het ideale geval, in elkaar liggende torus-vormige schillen. De deeltjes zijn dan in een schil opgesloten: in het oppervlak van de schil bewegen de deeltjes ongehinderd, loodrecht erop juist moeilijk. De stroming van deeltjes en warmte loodrecht op de schillen wordt hier kortweg het transport genoemd. Het transport is bepalend voor het verlies van warmte uit de reactor en daarmee voor de efficiëntie van de energieopwekking.

Een van de grote problemen in de fysica van de tokamak is, dat het transport veel groter is dan voorspeld door de theorie, neoklassieke theorie genaamd. Deze afwijking wordt anomaal transport genoemd. Het warmtetransport door de ionen en het transport van deeltjes is een orde groter dan voorspeld, het warmtetransport door elektronen is twee orden groter.

Het anormale transport is te wijten aan het optreden van turbulentie. Het blijkt uit experimenten dat het ionen-warmtetransport verhoogd wordt door elektrostatische fluctuaties. Deze fluctuaties leiden tot verhoogde stroming loodrecht op de schillen. Het warmtetransport door de elektronen wordt verhoogd door fluctuaties in het magneetveld, die leiden tot menging van de schillen.

Deze dissertatie concentreert zich op het anormale transport in tokamakplasma's en dan met name op het deeltjestransport. In experimenten met Elektron Cyclotron verHitting (ECH) in het Rijnhuizen Tokamak Project (RTP) varieert het profiel van de dichtheid (n_e) op uitgesproken wijze. Als het profiel van de elektronentemperatuur (T_e) oppiekt, wordt het n_e -profiel vlak en vice versa. Als de ECH aangaat,

neemt de gepiektheid van het dichtheidsprofiel af en kan het profiel zelfs hol worden. Uit het tijdsverloop in experimenten met niet-centrale ECH blijkt, dat de reactie van de dichtheid twee tijdconstanten kent.

Het deeltjestransport in RTP is onderzocht door de relatie tussen de dichtheid en de diverse thermodynamische krachten te onderzoeken. RTP is hiervoor uitstekend toegerust, omdat de profielen van de plasma-parameters sterk gevarieerd kunnen worden. De gradiënten van n_e , T_e en de stroomdichtheid (j) reageren op verschillende tijdschalen en zijn daarom als het ware ontkoppeld.

Om deze ontkoppeling te bereiken speelt de sterk gelokaliseerde, hoogvermogen-EC verhitting een belangrijke rol. Hiermee kan de vorm van de T_e - en j -profielen gevarieerd worden tussen gepiekt en hol. Dit biedt uitgelezen mogelijkheden om T_e , n_e en j en hun gradiënten te variëren en de transportrelaties te bepalen.

Voor dit onderzoek dienen T_e , n_e en j met voldoende nauwkeurigheid bekend te zijn. RTP heeft diverse meetinstrumenten om de elektronentemperatuur T_e en de elektronendichtheid n_e te bepalen met hoge plaats- en/of tijdsresolutie.

Er was geen standaardmeting van j voorhanden en daarom is een aanzienlijk deel van deze dissertatie gewijd aan de inspanningen om deze meting te ontwikkelen. De testen en fouten-analyses van twee diagnostische systemen worden gegeven: gecombineerde polarimetrie/interferometrie met infrarode straling en tangentiële Thomson-verstrooiing. Alhoewel de uiteindelijke metingen van j niet voldoende nauwkeurig zijn voor deze studie, kon wel aangetoond worden dat de stroom zich volgens de neoklassieke theorie verdeelt.

Dit gegeven en de metingen van T_e en n_e zijn gebruikt als invoer van transportsimulaties om het tijdsafhankelijke gedrag van het n_e -profiel te relateren aan de kruistermen in de deeltjesflux en te vergelijken met de voorspellingen volgend uit uitdrukkingen uit diverse theoretische modellen en schaalwetten. Vier verschillende, door ECH geïnduceerde overgangssituaties zijn gesimuleerd en vergeleken met de observaties.

De simulaties wijzen uit dat het dominante fysische mechanisme in geen van de toegepaste uitdrukkingen besloten ligt. De dichtheid lijkt meer indirect dan direct afhankelijk van de toestand van het plasma. Het optreden van kleine, in plaats en tijd beperkte, reproduceerbare verschijnselen tijdens de relaxatie van het dichtheidsprofiel duidt op soortgelijke variaties van de transportcoëfficiënten. Zulke variaties volgen uit geen van de uitdrukkingen uit de theorie.

Het deeltjestransport is een subtiel samenspel van meerdere fysische effecten en verder onderzoek zal dit samenspel beter moeten belichten. Aan theoretici de schone taak de waarnemingen te beschrijven.

SUMMARY

With nuclear fusion energy can be obtained from water in a safe and clean way. Energy production with fusion can help to cope with the predicted future energy shortage. Therefore, international research efforts aim at the development of a fusion reactor. The device that is most developed towards a reactor is called tokamak. It confines the fuel, hot hydrogen plasma, with magnetic fields in the shape of a torus.

In the ideal case, the magnetic field in the tokamak consists of nested, torus shaped surfaces, and the particles are confined on these surfaces. The particles move freely along the surfaces, but not perpendicular to the surfaces. The particle energy heat fluxes perpendicular to the surfaces are shortly called transport in this summary. The transport is dominant for the heat loss from the reactor. Hence, it determines the efficiency of the energy production.

One of the most important physical issues of the tokamak is the transport exceeding the predictions of the theory, the neoclassical theory, appreciably. This deviating transport is called anomalous transport. The ion thermal transport and the particle transport are one order of magnitude higher than predicted, the electron thermal transport is two orders of magnitude higher.

The anomalous transport is usually due to the turbulent phenomena. In experiments it has been shown that the ion thermal transport is enhanced by electrostatic fluctuations. These fluctuations induce enlarged drifts perpendicular to the magnetic surfaces. The enhancement of the electron heat transport seems to be due to magnetic fluctuations. These cause the surfaces to mix with each other, deteriorating the confinement.

This thesis concentrates on the anomalous transport in tokamak plasmas, especially focusing on the particle transport. In experiments with Electron Cyclotron Heating (ECH) in the Rijnhuizen Tokamak Project (RTP) the density profile (n_e) shows a rich phenomenology. The n_e profile peaks up, when the T_e profile flattens,

and vice versa. When the ECH is switched on, the peaking of the density profile decreases. The profile can even become hollow. From experiments with off-axis ECH, it appears the n_e profile relaxation has two time constants.

The particle transport in the RTP tokamak is studied by investigation of the relation between the density and various thermodynamic forces. RTP is well equipped for this study, because the profiles of the plasma parameters can be strongly varied. The gradients of n_e , T_e and the current density (j) are effectively decoupled, because they have different characteristic time scales.

For the establishment of this decoupling the high power EC heating is essential. The shape of the T_e and j profiles can be varied between peaked and hollow with this system. This offers a unique opportunity to vary T_e , n_e and j and their gradients and to determine the transport relations.

For this study, good diagnostisation of the T_e , n_e and j profiles is essential. At RTP several diagnostics are available to measure T_e and n_e with good temporal and spatial resolution.

No routine measurement of j was available, so for this thesis considerable effort has been put in the development of setups to measure j . The testing and error analysis of two diagnostic systems are given: combined polarimetry/interferometry with far infrared radiation and tangential Thomson scattering. Although the accuracy of the eventual j measurements is not sufficient, it was possible to confirm that the current density behaves according to neoclassical theory.

Together with measurements of mainly T_e and n_e , this is used as input for transport simulations with which the behaviour of the n_e profile is related to the cross-terms in the particle flux. This behaviour is compared to the predictions of expressions from several theoretical models and scaling laws. Four different transient plasma states induced by ECH are simulated and compared to the observations.

The simulations show that the dominant, physical mechanism is contained in none of the tested expressions. The density seems to depend indirectly rather than directly on the plasma state. The occurrence of minor, localised and reproducible events in the density during relaxation indicates similar variations of the transport coefficients. None of the models predicts such variations.

The particle transport is a subtle interplay of multiple, physical effects. Further investigation is needed to illuminate the dominant mechanisms.

1

INTRODUCTION

1.1 Fusion

Long before the last barrel of oil will be used, new ways of energy production must have been established. Nuclear fusion is one of the candidates for future large scale energy production [1]. It is favourable over fossil resources because of its zero emission of Carbon dioxide. The advantages over nuclear fission are that the ashes are harmless and that a chain reaction in the reactor is impossible, because the involved quantity of fuel is very small. Furthermore, the supplies of the fusion fuel are almost inexhaustible. At the current energy consumption rate, there is enough fusion fuel for thousands of years.

There is no need to choose between the so-called 'sustainable' energy sources like wind and solar energy, and fusion, because they must supplement each other. In fact, the sustainable energy sources require significant land use and investment in materials, if they are to be applied as major energy provider [2]. Fusion energy will be made in small-size, high power reactors.

The long-term global energy provision has so many uncertainties that it would be unwise to terminate the efforts in fusion research and development [3]. It will require approximately two generations of physicists and engineers to implement fusion as a major energy supply, provided the efforts are maintained. It is important to realise that to fulfill the energy demand in the future at all, it is crucial that the research into both fusion and the sustainable energy sources is continued firmly, in order to be ready when needed.

Why are we not using fusion energy already right now? That is because the physical circumstances under which fusion occurs are difficult to establish. Fusion does not occur spontaneously on earth. It does occur in the sun and the other stars, for which it serves as the energy source. The temperature in a fusion reactor must exceed 200 million degrees. To ignite the fusion reactor the product of the

pressure and the time energy can be stored in the reactor vessel must exceed $20 \text{ bar} \times \text{seconds}$. Between 1955 and 1995 the obtained value of this reactor product has been improved by a factor ten million [4]. At present, the gap to an ignited reactor is a factor ten. The present record values are obtained in JET (Joint European Torus), located in Culham, UK:

- Fusion power of 16.1 MW
- Fusion energy of 21 MJ, produced in quasi-steady state in 3 seconds
- Record value of the ratio between fusion power and input power:
 $P_{\text{fusion}}/P_{\text{in}} \sim 0.65$

The successor of JET is called International Thermonuclear Experimental Reactor (ITER). ITER is to be built in worldwide cooperation and the produced fusion power will exceed the input power by a factor ten.

How does one confine fuel at 200 million degrees? One of the possibilities is magnetic confinement. To understand how this works one has to realise that at 200 million degrees the fuel, which is hydrogen, is in the fourth state of matter, the so-called 'plasma' state. The hot fusion plasma is a gas of charged particles. The application of a magnetic field limits the motion of the charges to the direction along the magnetic field: magnetic confinement. In a 'tokamak' the confinement is further improved by creating the magnetic field lines in a ring, thus avoiding end losses. The hydrogen plasma is confined in a torus shape. The tokamak is a Russian invention and its acronym stands for 'Toroidal'naya Kamera i Magnitnaya Katushka', meaning 'toroidal chamber and magnetic coils'. JET and ITER are tokamaks.

1.2 The Tokamak

In figure 1.1 a schematic view of the tokamak is given. The plasma is confined inside the tokamak by the toroidal and poloidal magnetic field. The poloidal magnetic field (B_θ) is generated by the toroidal current. The plasma acts as the secondary winding of the transformer. The toroidal magnetic field (B_ϕ) is generated by the coils. The two fields together give helical field lines, which fill up a torus-shaped volume. The torus has a major radius R_0 and a minor radius a . The vertical and horizontal position of the plasma in the vessel is controlled by additional radial and vertical magnetic fields, respectively.

The heating of the plasma is primarily due to the current. The plasma has a finite resistivity, and heat is deposited according to Ohm's law. Plasmas without any further heating are called Ohmic plasmas. Since the electrons are much lighter than the ions, the current is carried exclusively by the electrons. The resistivity of the plasma (η) is proportional to $T_e^{-3/2}$, where T_e is the electron temperature. Note that there is a self-strengthening process: The hottest place in the plasma attracts the current, hence will be heated more intensively and becomes even hotter. The process saturates when T_e becomes so high that the level of the loss from this region

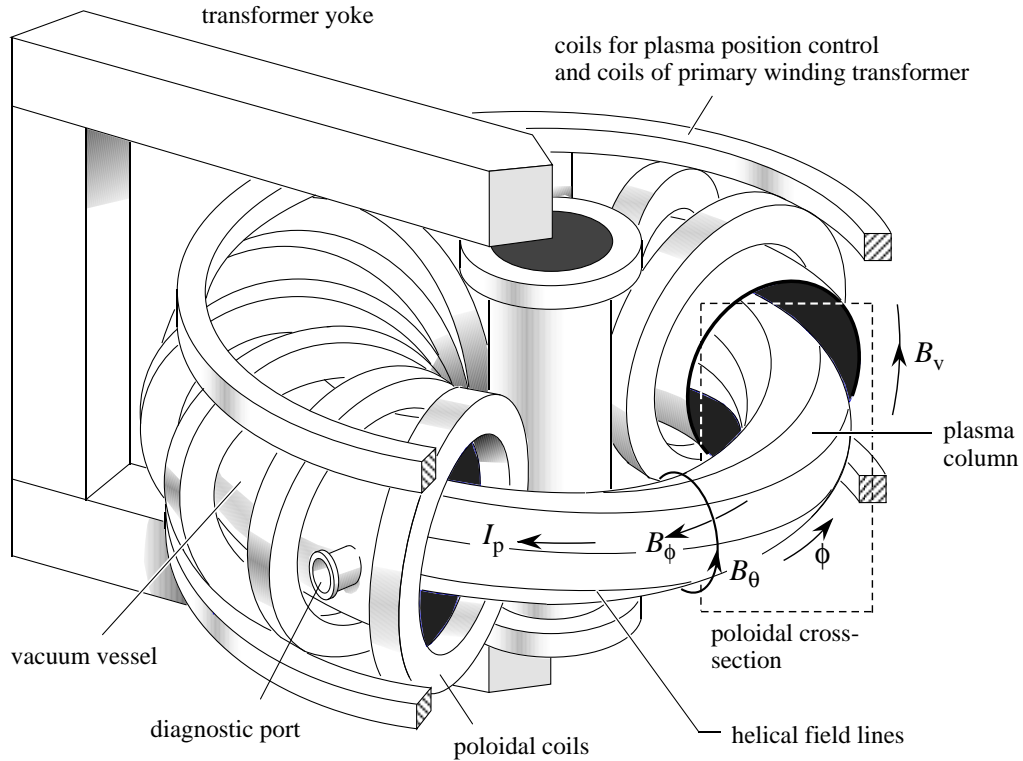


Figure 1.1: A schematic view of a tokamak

equals the Ohmic heating, or by instabilities. This is at about 10^7 K. Both the T_e profile and the profile of the current density (j) are peaked in the centre of the plasma.

The temperature of the plasma can be further increased by additional heating. In the Rijnhuizen Tokamak Project (RTP), in which the experiments described in this thesis are performed, Electron Cyclotron Heating (ECH) is used. This method uses microwaves, which are resonant with the cyclotron motion of the electrons in the magnetic field. The power is absorbed in a small region in the plasma. The total power can exceed the Ohmic power by a factor up to 7 in RTP.

The magnetic field lines can be labelled with the magnetic winding number q , the number of toroidal turns the field line experiences per full turn in poloidal direction. Thus, if the magnetic field line returns to its poloidal starting position after exactly one rotation round the torus, then $q = 1$. In the ideal case, the magnetic topology is a set of nested flux surfaces, as indicated in figure 1.2.

If q has a rational value $q = m/n$, where m and n are integers, the field lines close onto themselves after m toroidal and n poloidal turns. Especially for low values of m and n , this can give rise to resonances, which decrease the stability of

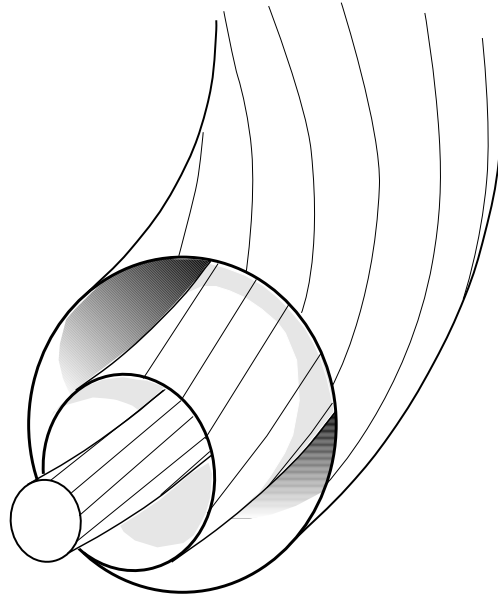


Figure 1.2: Impression of the flux surfaces in an unperturbed plasma. The lines on the surfaces are some magnetic field lines.

the plasma. For this reason, q is known as the 'safety factor'.

1.3 Outstanding Issues

The principal physics issues in the design of a tokamak reactor are the following:

1) The confinement of heat and particles.

In the plasma the transport of heat and particles perpendicular to the magnetic field is one to two orders of magnitude faster than predicted by theory. To improve the confinement of the plasma, it is necessary to understand the mechanisms of this enhanced transport.

2) The avoidance of disruptions.

There are circumstances in which the plasma can become unstable, leading to a very rapid decay of the plasma current. Since the electro-magnetic forces used for the confinement are appreciable, the disruption of the plasma is potentially harmful to the mechanical structure of the reactor. The disruptive mechanisms are still not fully understood.

3) The exhaust of the power.

The volume in which the fusion power will be produced will be relatively small compared to that of conventional power plants. As a consequence, the power must be distributed as uniformly as possible to avoid damage to the material surface. One of the methods to establish this is the so-called 'radiative mantle', a layer at

the outside of the plasma with a high neon concentration, which emits a significant fraction of the power via line radiation. A related physics area of great importance for the reactor is the interaction of the plasma with the material wall, leading to erosion of re-deposition processes.

Apart from the physical issues, there are many issues of technological nature to be addressed in the design of a reactor.

This thesis is part of the research on transport in tokamak plasmas. In the following a brief status of the transport physics is given. This creates the framework for the specific theme of this work.

1.4 Transport

One of the major issues in tokamak research is the anomalous transport of particles and heat perpendicular to the field lines. The observed transport coefficients for the electrons are one to two orders larger than the so-called neoclassical theory predicts. The neoclassical transport is the lower limit to the transport. The observed high transport is thought to be caused by turbulence in the plasma. For example, magnetic turbulence can spread the field lines around the flux surfaces in an ergodic way, thus deteriorating the magnetic confinement. Reduction of the perpendicular transport will increase the energy confinement time. It could reduce the minimal size of a fusion reactor.

Recently, the ion thermal transport has been reduced successfully down to the neoclassical limit in several tokamaks. The reduction of transport is accompanied by and linked to a strong shear of the rotation velocity as well as a strong reduction of the density fluctuation level. The electron transport, however, remains anomalous in these plasmas. Apparently, the ion and electron transport are ruled by different physical mechanisms. In the case that the ion transport is as low as the neoclassical limit, the electron transport dominates the heat loss, so it becomes even more important to reduce this.

The electron thermal transport has a strong relation with q and its derivative. It has been shown in RTP [5,6] that the electron thermal transport coefficient can be described with areas of low transport near rational q values with low m and n numbers alternating with high transport areas. The low transport areas are called transport barriers. The low net heat transport in the barriers is the result of two competing effects: an outward diffusion and an inward convection [7]. If the q gradient is low, these transport barriers become wider and therefore stronger. The areas between the transport barriers have anomalous transport.

The heat transport is largely determined by the number and strength of the transport barriers. The T_e profile is characterised by strong gradients at the locations of the barriers. Further, small, hot filaments are observed on the T_e profile. Also, the T_e profile can react non-locally to localised perturbations, layers with inward heat convection have been identified, etc. Hence, the heat transport has a variety of non-local and non-diffusive phenomena. The observed T_e profiles show strong local features such as filaments and transport barriers

The density profile, however, is usually observed to be smooth. The density usually shows only minor variations even if the plasma state is changed significantly. The density profile shape is more or less fixed, suggesting the particle transport has smooth and insensitive transport coefficients. It is a big and challenging question how particle and heat transport, though necessarily related, can display so different phenomenologies.

The nature of the particle transport is still unknown. The density profile in tokamaks is generally observed to be steeper than can be explained by particle sources alone. The presence of a strong particle flux up the density gradient is concluded from this. Neoclassical theory predicts such particle fluxes, driven by the temperature gradients and the toroidal electric field (E_{\parallel}), but these cannot account for the observed inward convection. Especially challenging is the question how the convective components of the particle and heat fluxes are related.

1.5 This Thesis

This thesis concentrates on transport phenomena in tokamak plasmas, focusing on the transport of particles. It is especially intriguing how the density profile can remain almost fixed in experiments in which the state of the plasma is changed significantly, and the heat transport undergoes strong variations. The stiffness of the density profile might be a consequence of the parametrical dependencies of the transport coefficients, which describe the transport as a function of the other plasma parameters. The local changes to these dependencies can give the net observed effect on the density profile. It is also possible that a 'meta'-mechanism fixes the global shape of the density profile. In the so-called 'profile consistency' theories, the density profile shape is derived from maximisation of the entropy, or the minimisation of the free energy. A third possibility is that discrete phenomena like filaments or convective cells are responsible for the particle transport.

A way to investigate this particle transport is to vary the different thermodynamic forces, *i.e.* the gradients of temperature, density and the toroidal electric field, in time in such a way that they are effectively decoupled and thus reach combinations of values that are not normally accessible in tokamaks. At RTP, such experiments can be done with the high-power local ECH system. Experimentally, the strategy will be to use ECH to modify the T_e and j profiles and follow the evolution of the n_e profile as function of time, so as to be able to distinguish the various contributions to the particle flux.

Thus, it is the aim of this thesis to understand the behaviour of the n_e profile under different transitions of the plasma, and to use this experimental information to test theoretical models for particle transport. Special emphasis is placed on the role of convection, since it is clear that the inward convection is a very important element in the particle balance. We shall investigate whether 'off-diagonal' particle fluxes, *i.e.* fluxes driven by gradients other than $\nabla_r n_e$, can account for the observed convective transport and changes therein. The generic question to be addressed can be formulated as follows:

Can the particle transport be adequately described by a transport matrix in which off-diagonal elements play a significant role?

Several theoretical or semi-empirical models for the enhancement of the particle transport have been proposed in the literature. The expressions for the transport coefficients derived from these models will be tested against the experimental data from RTP.

Apart from the ECH system needed to control the T_e and j profiles, good diagnostics of all profiles, *i.e.* T_e , n_e and j is essential. For T_e and n_e high resolution profile measurements are available at one time in a plasma discharge, owing to a state of the art Thomson scattering set up. These measurements are supplemented with time dependent profile measurements using Electron Cyclotron Emission spectroscopy, and Far Infrared interferometry, respectively. These diagnostics as well as the ECH system are briefly described in Chapter 3.

The current density is more difficult to measure. A relatively large effort went to the development of two different techniques to measure the j profile: polarimetry (Chapter 4) and tangential Thomson scattering (Chapter 5).

Finally, a set of 4 different transition experiments is defined:

1. Ohmic to centrally EC Heated plasma
2. Ohmic to slightly off-axis EC Heated plasma
3. Ohmic to far off-axis EC Heated plasma
4. Off-axis EC Heated to Ohmic plasma

Each of these transitions is extensively characterised experimentally.

A set of seven different expressions for particle transport, derived from theoretical models, are identified, and numerical modules representing those expressions have been made. These are used in the generic transport code ASTRA, to test the models against the data of the 4 standard transitions. In addition, two empirical transport models are tested against the same data.

The experiments and the tests of the models are described in Chapter 6. At the end of this thesis, we return to the question phrased above and discuss in how far an answer can be given.

1.6 Publications

Below a list of publications and a list of conference contributions related to this thesis are presented. The publication marked with ♣ is included in this thesis in Chapter 5.

Journals:

- *The multi-channel triple-laser interferometer/polarimeter system at RTP*, J.H. Rommers, A.J.H. Donn e, F.A. Karelse and J. Howard, REVIEW OF SCIENTIFIC INSTRUMENTS **68**, p.1217-1226 (1997).

- *First results with the triple-laser polarimeter system at RTP,*
J.H. Rommers, J. Howard, F.A. Karelse, A.J.H. Donné and the RTP-team,
FUSION ENGINEERING AND DESIGN **34-35**, p.495-499 (1997).
- *Electron thermal transport in RTP: filaments, barriers and bifurcations,*
N.J. Lopes Cardozo *et al.*, among them F. A. Karelse,
PLASMA PHYSICS AND CONTROLLED FUSION **39**, SUPPL. 12B, B303-316
(1997).
- ✦ *Measurements of the current density profile with tangential Thomson scattering
in RTP,*
F.A. Karelse, M. de Bruijne, C.J. Barth, M.N.A. Beurskens, G.M.D. Hogeweij
and N.J. Lopes Cardozo,
SUBMITTED TO PLASMA PHYSICS AND CONTROLLED FUSION.

Conference contributions:

- *Experimental results on pellet injection and MHD from the RTP tokamak,*
A.A.M. Oomens *et al.*, among them F.A. Karelse,
18th IAEA FUSION ENERGY CONFERENCE, SORRENTO, ITALY, 4-10 OCTOBER 2000.
- *Density profile changes induced by on- and off-axis electron cyclotron heating,*
F.A. Karelse, M.R. de Baar, G.M.D. Hogeweij, N.J. Lopes Cardozo and the
RTP-team,
PROCEEDINGS 26th EPS CONFERENCE ON CONTROLLED FUSION AND PLASMA
PHYSICS, MAASTRICHT, THE NETHERLANDS, 14-18 JUNE 1999, P2.008.
- *Current density measurements with tangential Thomson scattering in plasmas
with peaked and hollow temperature profiles,*
F.A. Karelse, C.J. Barth, M.N.A. Beurskens, G.M.D. Hogeweij, N.J. Lopes
Cardozo, H.J. van der Meiden and the RTP-team,
PROCEEDINGS 1998 INTERNATIONAL CONGRESS ON PLASMA PHYSICS AND
25th EPS CONFERENCE ON CONTROLLED FUSION AND PLASMA PHYSICS,
PRAGUE 1998, B106.
- *Heat transport in the RTP tokamak,*
G.M.D. Hogeweij *et al.* among them F.A. Karelse,
PROCEEDINGS 16th INTERNATIONAL CONFERENCE ON PLASMA PHYSICS
AND CONTROLLED NUCLEAR FUSION RESEARCH, MONTRÉAL, CANADA,
7-11 OCTOBER 1996, IN PLASMA PHYSICS AND CONTROLLED NUCLEAR
FUSION RESEARCH, IAEA, VIENNA, AUSTRIA, VOL. I, p.655-662 (1997).
- *Recent results on electron cyclotron current drive and MHD activity in RTP,*
A.J.H. Donné *et al.*, among them F.A. Karelse,
PROCEEDINGS 16th INTERNATIONAL CONFERENCE ON PLASMA PHYSICS
AND CONTROLLED NUCLEAR FUSION RESEARCH, MONTRÉAL, CANADA, 7-
11 OCTOBER 1996, IN PLASMA PHYSICS AND CONTROLLED NUCLEAR FU-
SION RESEARCH, IAEA, VIENNA, AUSTRIA, VOL. III, p.365-372 (1997).

- *First current density measurements with tangential Thomson scattering at RTP,*
F.A. Karelse, C.J. Barth, M.N.A. Beurskens, M. de Bruijne, G.M.D. Hogeweyj, N.J. Lopes Cardozo, H.J. van der Meiden, F.J. Pijper and the RTP-team, PROCEEDINGS 8th INTERNATIONAL SYMPOSIUM ON LASER-AIDED PLASMA DIAGNOSTICS, DOORWERTH, THE NETHERLANDS, 1997, p.253-258.
- *Current density profile measurements with multi-position tangential Thomson scattering in the RTP tokamak,*
F.A. Karelse, M. de Bruijne, M.N.A. Beurskens, C.J. Barth, G.M.D. Hogeweyj, N.J. Lopes Cardozo, H.J. van der Meiden, F.J. Pijper and the RTP-team, PROCEEDINGS 24th EPS CONFERENCE ON CONTROLLED FUSION AND PLASMA PHYSICS, BERCHTESGADEN, GERMANY, 1997, PART II, p.621-624.
- *Current density profile evolution measured with the triple laser polarimeter at RTP,*
F.A. Karelse, J.H. Rommers, A.J.H. Donn e, G.M.D. Hogeweyj, J. Howard, Th. Oyevaar, F.C. Sch uller and the RTP-team, PROCEEDINGS 23rd EPS CONFERENCE ON CONTROLLED FUSION AND PLASMA PHYSICS, KIEV, UKRAINE (1996) PART III, p. 1156-1159.
- *ECCD Experiments in RTP,*
R.W. Polman, E. Westerhof, J. Lok, F.A. Karelse, O.G. Kruyt, A.A.M. Oomens, F.C. Sch uller and the RTP-team, PROCEEDINGS 23rd EPS CONFERENCE ON CONTROLLED FUSION AND PLASMA PHYSICS, KIEV, UKRAINE, 24-28 JUNE 1996, PART II, p. 934-937.
- *First results with the rotating polarization polarimeter at RTP,*
J.H. Rommers, J. Howard, M. Drabbe, F.A. Karelse and A.J.H. Donn e, PROCEEDINGS 22nd EPS CONFERENCE ON CONTROLLED FUSION AND PLASMA PHYSICS, BOURNEMOUTH, UK, 3-7 JULY 1995.

References

- [1] H. Bruhns, in *Trans. Fusion Technol.*, edited by G. H. Miley (American Nuclear Society, Inc, Danville, Ill., USA, 1998), Vol. 33, p. 3.
- [2] J. P. H. E. Ongena and G. V. Oost, in *Trans. Fusion Technol.*, edited by G. H. Miley (American Nuclear Society, Inc, Danville, Ill., USA, 1998), Vol. 33, p. 9.
- [3] W. D. d'Haeseleer, *Plasma Phys. Control. Fusion* **41**, B25 (1999).
- [4] J. A. Wesson, *Tokamaks*, 2nd ed. (Clarendon press, Oxford, UK, 1997).
- [5] M. R. de Baar *et al.*, *Phys. Plasmas* **6**, 4645 (1999).
- [6] N. J. Lopes Cardozo *et al.*, *Plasma Phys. Control. Fusion* **39**, B303 (1997).
- [7] P. Mantica, G. Gorini, G. M. H. Hogeweyj, N. J. Lopes Cardozo, A. M. R. Schilham, and RTP Team, *Phys. Rev. Lett.* **85**, 4534 (2000).

2.1 Magnetic equilibrium

Starting-point for the description of the macroscopic behaviour of the fully ionised plasma, is the application of conservation laws on an ensemble of charged particles in a magnetic field. After applying conservation of mass, momentum and energy and some general physical restrictions, the 'magneto hydrodynamic' equations can be formulated: The plasma can be described as a single fluid of charged particles in a magnetic field. The equations for ions and electrons are averaged.

Consider an ensemble of charged particles with a distribution function $f(\mathbf{x}, \mathbf{v}', t)$ with \mathbf{x} and \mathbf{v}' the three-dimensional particle position and velocity, respectively, and t the time. The collisional kinetic equation for this function is the Boltzmann equation [1]:

$$\frac{\partial f}{\partial t} + \mathbf{v} \cdot \frac{\partial f}{\partial \mathbf{x}} + \frac{e_j}{m_j} (\mathbf{E} + \mathbf{v} \times \mathbf{B}) \cdot \frac{\partial f}{\partial \mathbf{v}} = \left(\frac{\partial f}{\partial t} \right)_c \quad (2.1)$$

where the index j marks the particle species and e_j and m_j are the charge and mass of that particle species, respectively. The term on the right-hand side represents the collisions between particles. The first factor of the third term on the left-hand side is the acceleration ($\dot{\mathbf{v}}$) by the Lorentz force, which can be recognised readily in this expression. Note that the electric field \mathbf{E} and the magnetic field \mathbf{B} consist of the external fields, but are also partially determined by the charges in the plasma itself. \mathbf{E} and \mathbf{B} can be considered as additional unknown functions, following from the Maxwell equations.

By taking the moments of this equation multiplied by the appropriate functions the equations for conservation of mass and momentum are derived. These equations

contain the mass density ρ , the fluid velocity \mathbf{v}' and the pressure tensor \mathbf{P} , which are ensemble integrated fluid quantities. The continuity equation is:

$$\frac{d\rho}{dt} = -\rho \nabla \cdot \mathbf{v}' . \quad (2.2)$$

where d/dt is the fluid derivative $\partial/\partial t + \mathbf{v}' \cdot \nabla$. In case the distribution function is isotropic, the pressure tensor reduces to the scalar pressure p . Although the tokamak plasma can be anisotropic due to the strong magnetic field, it has proven valuable to assume isotropy and the equation of motion reads:

$$\rho \frac{d\mathbf{v}'}{dt} = \mathbf{j} \times \mathbf{B} - \nabla p , \quad (2.3)$$

where \mathbf{j} is the current density. In this equation the collision term is neglected. An equation for p is obtained if the plasma is assumed to behave adiabatically:

$$\frac{d(p\rho^{-\gamma})}{dt} = 0 , \quad (2.4)$$

where γ is the adiabatic exponent. This gives

$$\frac{dp}{dt} = -\gamma p \nabla \cdot \mathbf{v}' . \quad (2.5)$$

The relation between \mathbf{E} and the other variables is obtained by assuming the plasma is perfectly conducting:

$$\mathbf{E} + \mathbf{v}' \times \mathbf{B} = 0 , \quad (2.6)$$

This equation is used in the ideal case, if the collisions between the particles are neglected. A finite resistivity, which is induced by the collisions, can simply be introduced by replacing Eq. 2.6 with Ohms law:

$$\mathbf{E} + \mathbf{v}' \times \mathbf{B} = \eta \mathbf{j} , \quad (2.7)$$

The set of equations is closed using the Maxwell's equations:

$$\mu_0 \mathbf{j} = \nabla \times \mathbf{B} , \quad (2.8)$$

$$\frac{\partial \mathbf{B}}{\partial t} = -\nabla \times \mathbf{E} . \quad (2.9)$$

In Eq. 2.8 the displacement current is neglected by assuming quasi-neutrality of the plasma. This set of equations (2.2-2.9), completed with $\nabla \cdot \mathbf{B} = 0$, is called magneto hydrodynamics (MHD). Ideal MHD is the case in which the collisions are neglected, resistive MHD has finite η . The MHD equations describe well the magnetic equilibrium and stability of the tokamak plasma.

In the case of steady state equilibrium, Eq. 2.3 reduces to:

$$\mathbf{j} \times \mathbf{B} = \nabla p . \quad (2.10)$$

If the inner product of \mathbf{B} with this equation is taken, $\mathbf{B} \cdot \nabla p = 0$ is obtained. This means that there is no pressure gradient parallel to the magnetic field lines. If we recall the magnetic topology of the tokamak plasma as introduced in section 1.1, which is a set of nested flux surface, and combine this with the absence of a pressure gradient parallel to the magnetic field lines, it is clear that p is constant on the flux surfaces. If the inner product of \mathbf{j} with this equation is taken, the equation $\mathbf{j} \cdot \nabla p = 0$ follows. As a consequence, current flows along the flux surfaces as well. From the force equilibrium, Eq. 2.10, the prescription for the flux surfaces can be obtained making use of Maxwell's $\nabla \cdot \mathbf{B} = 0$. Calculations of the magnetic equilibrium, which are outside the scope of this thesis, show that the inner surfaces are displaced outwards. This displacement is called the Shafranov shift.

For a tokamak plasma with a circular cross-section like in RTP the inner flux surfaces are also circular. The flux tube with zero radius is called the magnetic axis.

The magnetic field lines are helices following the torus. The magnetic winding number q is the number of toroidal turns a field line completes associated with one poloidal circuit:

$$q = \frac{1}{2\pi} \oint \frac{1}{R} \frac{B_\phi}{B_\theta} ds , \quad (2.11)$$

where the integral is taken over one poloidal circuit around the flux surface s and B_ϕ and B_θ are the components of the magnetic field in toroidal and poloidal direction, respectively. It is clear that all magnetic field lines in a flux surface have the same q , so q is a flux function. It follows from Ampère's law (Eq. 2.8) that the poloidal field is proportional to the current contained within the flux surface:

$$B_\theta = \frac{\mu_0}{2\pi r} \int_{S(r)} j dS , \quad (2.12)$$

where $S(r)$ is the surface inside r and μ_0 is the magnetic permeability of free space. For a large aspect ratio tokamaks ($R_0/a \gg 1$) with circular cross-section like RTP, q , can be approximated by:

$$q_{\text{cyl}} = \frac{r B_\phi}{R_0 B_\theta} , \quad (2.13)$$

where r is the minor radius of the flux surface and R_0 is the major radius. From Eqs. 2.12 and 2.13 it follows that the q value at the edge of the plasma (q_a) is determined by the external parameters:

$$q_{\text{cyl},a} = \frac{2\pi a^2 B_\phi}{\mu_0 I_p R_0} \quad (2.14)$$

where I_p is the total plasma current.

The efficiency of the plasma confinement is often expressed as the ratio of the kinetic pressure and the magnetic pressure:

$$\beta = \frac{\langle p \rangle}{B^2/2\mu_0}, \quad (2.15)$$

where $\langle p \rangle$ is the volume (V) averaged pressure, $\int p dV / \int dV$. Similarly, the poloidal β (β_p) is defined as:

$$\beta_p = \frac{\langle p \rangle}{B_\theta^2(a)/2\mu_0}, \quad (2.16)$$

where a is the radius of the last closed flux surface, also referred to as the plasma edge. $B_p(a)$ is the edge value of the magnetic field in the poloidal plane.

The normalised internal inductance of the plasma (l_i) is defined as:

$$l_i = \frac{\int_0^a (B_\theta^2/2\mu_0) 2\pi r dr}{(B_\theta^2(a)/2\mu_0) \pi a^2}. \quad (2.17)$$

The value of l_i increases if the j profile is more peaked. The combination $\Lambda = \beta_p + l_i/2 - 1$ is an important factor in the horizontal positioning of the tokamak plasma.

2.2 Neoclassical Transport

A single particle is in principle perfectly confined by the magnetic field in the tokamak configuration. The occurrence of collisions in case of many particles gives rise to transport perpendicular to the magnetic field. As a consequence of the collisions the plasma particles undergo a random walk. If we approximate the tokamak configuration with a cylinder, the time step of the random walk is the characteristic time between two collisions (τ_c) and the radial step length is the Larmor radius (ρ_L). This gives a diffusion coefficient across the field $D \sim \rho_L^2/\tau_c$. Using the RTP parameters for the electrons, $D \approx 1.3 \cdot 10^{-4} \text{ m}^2/\text{s}$. This radial transport induced by collisions in a cylinder is called classical transport.

Collisional transport in a torus is considerably larger than in a cylinder and the theory taking this into account is called the neoclassical theory [2]. Neoclassical

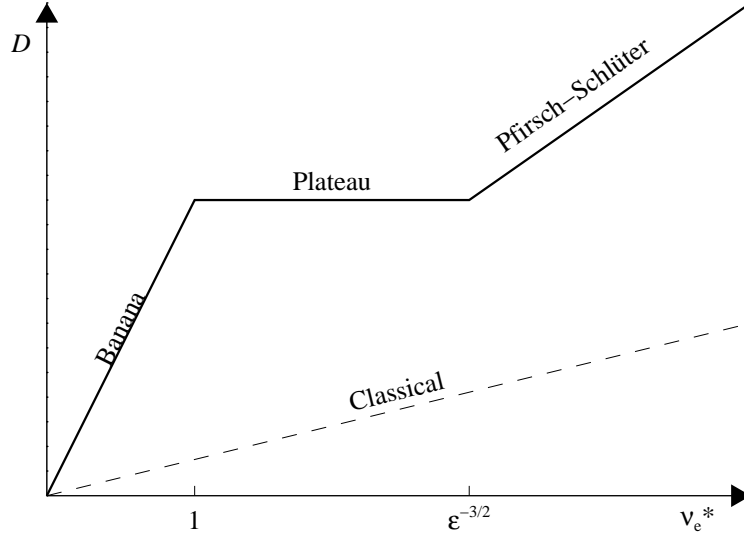


Figure 2.1: Variation of diffusion coefficient with collision frequency

theory predicts that a number of particles is trapped in so-called 'banana orbits'. The name of these banana particles is derived from the poloidal projection of their motion, which has the shape of a banana. The radial transport is increased in the case of banana orbits, because the banana orbit width becomes the radial step length in the random walk estimate and this is much larger than the Larmor radius.

Three regimes are distinguished in neoclassical transport, characterised by the level of electron collisionality ν_e^* . This is proportional to the ratio of the electron-ion collision frequency (ν_{ei}) and the circulation frequency in the banana orbit (ν_B):

$$\nu_e^* = \frac{1}{\varepsilon} \frac{\nu_{ei}}{\nu_B} = \frac{\nu_{ei} q R_0}{\varepsilon^{3/2} v_{e,th}} \propto \frac{1}{v_{e,th}^4}, \quad (2.18)$$

where $v_{e,th}$ is the electron thermal velocity and ε is the inverse aspect ratio $\varepsilon = r/R$. Note that ν_e^* decreases strongly with increasing $v_{e,th}$. In the banana regime the transport is dominated by the trapped particles. For $\nu_e^* > \nu_{ei} q R_0 / v_{e,th} \sim \varepsilon^{-3/2}$, the Pfirsch-Schlüter current dominates the transport. This is called the Pfirsch-Schlüter regime. The intermediate regime is called the plateau regime, $1 < \nu_e^* < \varepsilon^{-3/2}$. The variation of the neoclassical diffusion coefficient D as a function of ν_e^* is illustrated in Fig. 2.1. In the plateau regime D is independent of ν_e^* .

The neoclassical theory is one-dimensional with the poloidal flux as the single coordinate. It gives the general relation between the fluxes and the corresponding thermodynamic gradient forces [2]. This relation can be written in matrix notation:

$$\begin{pmatrix} \Gamma \\ q_e \\ q_i \\ j \end{pmatrix} = - \begin{pmatrix} D & c_{12} & c_{13} & W \\ c_{21} & \chi_e & c_{23} & c_{24} \\ c_{31} & c_{32} & \chi_i & c_{34} \\ D_{bs} & c_{42} & c_{43} & \sigma_{\parallel} \end{pmatrix} \cdot \begin{pmatrix} \nabla n \\ n \nabla T_e \\ n \nabla T_i \\ E_{\parallel} \end{pmatrix}. \quad (2.19)$$

In this equation Γ is the particle flux, q_e and q_i are the electron and ion heat fluxes, respectively, and j is the toroidal current density. In the vector on the right-hand side n denotes the density, T_e and T_i are the electron and ion temperatures, respectively, and E_{\parallel} denotes the electric field in toroidal direction. D is the particle diffusion coefficient, χ_e and χ_i are the electron and ion thermal diffusivities, respectively, and the $\sigma_{\parallel} \equiv 1/\eta$ is the parallel electrical conductivity. The off-diagonal coefficients have no separate label, except for W , which is the Ware pinch coefficient, and D_{bs} , which is the bootstrap current coefficient.

There is only one particle flux present in this equation. This simplification is allowed because the ion and electron densities are bound strongly to each other because the force caused by charge separation is very strong. The nearly zero net charge in the plasma is called quasi-neutrality.

The transport along the field lines is neoclassical transport. The neoclassical parallel transport coefficients are very high and as a consequence, n , T_e and T_i are in good approximation constant on the flux surfaces. Their gradients are in radial direction. The 'charge flux' j lies in the magnetic surface and is in first approximation toroidally oriented. Three of the four components are thus in radial direction and the fourth is in toroidal direction.

If the elements c_{ij} in Eq. 2.19 are constant the transport is purely diffusive. The diagonal elements are the usual diffusion coefficients. The off-diagonal terms represent the so-called cross-terms. For example, c_{42} quantifies the toroidal current density driven by the ∇T_e term. However, in general the conservation equations contain also terms due to convection, damping and sources and sinks.

Neoclassical theory gives non-zero expressions for all elements c_{ij} of the transport matrix. Most of the fluxes corresponding to the off-diagonal terms have already been observed in non-equilibrium thermodynamics applied to metals. For example, the toroidal electric current produced by a radial temperature gradient (c_{42} and c_{43}) is called the Ettinghausen effect. The radial heat flux caused by the electric field (c_{24} and c_{34}) is called the Nernst effect. Non-zero c_{12} marks the occurrence of thermo-diffusion or the Soret effect. The reciprocal effect is the electronic Dufour effect: a radial pressure gradient produces a radial electron heat flux (c_{21}). The reciprocal off-diagonal terms are related to each other by the Onsager symmetry relations, i.e. $\tilde{c}_{ij}(B) = \tilde{c}_{ji}(-B)$, where the tilde indicates the dimensionless coefficients.

In the experimental situation it is not so easy to gain data on all the coefficients. The coefficients that appear regularly in the literature on tokamak transport physics are the ones labelled explicitly in Eq. 2.19, i.e. D , $\chi_{i,e}$, σ_{\parallel} , W and D_{bs} .

The Ware pinch [3] is directed inwards and is a consequence of the interaction between the trapped particles and the electric field. It causes the plasma density

profile to peak in the centre. The bootstrap current [4] follows from the interaction of the trapped particles with the density gradient and is directed in the same direction as the inductively driven current.

2.3 Anomalous transport

Experimentally, it appears that the radial transport coefficients are much larger than given by neoclassical theory [5,6]. The ion heat diffusivity and the particle diffusion coefficient exceed the neoclassical estimates by up to one order of magnitude, the electron heat diffusivity exceeds the neoclassical value by up to two orders. This additional transport (it comes on top of the irreducible background transport given by neoclassical theory) is called anomalous, because there is no detailed understanding of it.

Since the collisional effects are contained in the neoclassical theory, it is clear that the anomalous transport is caused by a different effect. Generally, turbulence is considered to be responsible. The turbulence come in two flavours: electrostatic and magnetic fluctuations.

The fluctuations of the electrostatic potential ($\delta\phi_k$, where k indicates the wave number of a particular fluctuation) lead directly to $E \times B$ drifts (δv_k) of the particles, where for E the sum of all fluctuation modes must be inserted. The time step of the transport correlated with these drifts depends on the time the motion of the particle is correlated with the fluctuation modes, the correlation time τ_k . The spatial step associated with the drifts is $\delta r_k = \delta v_k \tau_k$. The resulting transport coefficient depends linearly on τ_k :

$$D = \sum_k (\delta v_k)^2 \tau_k \quad (2.20)$$

Several de-correlation processes can limit τ_k . If the fluctuation level becomes high, the fastest limiting process may become the fluctuation frequency itself. In that case, $\tau_k \propto (\delta v_k)^{-1}$ and D becomes linear in δv_k .

In the case of magnetic turbulence the set of nested toroidal flux surfaces are destroyed. The flux surfaces are replaced by chains of magnetic islands and X-points [7]. Around the X-points the magnetic field lines are ergodic. The higher the perturbing magnetic field, the more flux surfaces are broken and the more ergodic field lines exist. The motion of the particles along the field lines gives a loss of particles and heat.

In the collision-dominated case, the ratio of the radial displacement and the toroidal displacement of a particle between two collisions is $\delta B_r/B$, where δB_r is radial component of the fluctuating magnetic field. The associated radial diffusion is:

$$D \sim D_{\parallel} \left(\frac{\delta B_r}{B} \right)^2. \quad (2.21)$$

In the collisionless case the transport can be enhanced even more, because the radial step width can be as large as the island width, which can be significantly larger than the banana width [8]

In specific regions of the plasma the turbulence can be quenched, leading to a localised improvement of the transport coefficients. These regions are referred to as transport barriers. In Refs. 9 and 10 plasmas have been presented in which, transiently, χ_i decreased to neoclassical predictions over most of the minor radius. In this phase the n_e fluctuations, associated with electrostatic turbulence, decreased below the detection limit. The electrons remained anomalous and showed only a modest decrease of χ_e . Apparently, the anomalous electron thermal transport is not dominated by electrostatic turbulence but by magnetic turbulence.

In RTP the heat conduction via the electrons has been studied extensively. From experiments with ECH it is found that the electron thermal transport can be described by a series of transport barriers [11–13]. Inside those barriers, an up-gradient heat pinch is found. The resulting effective transport is reduced by one order with respect to the ambient plasma, where transport is anomalous. The barriers are located at simple rational values of the safety factor profile. In Chapter 6 the RTP findings will be presented in more detail.

The observed particle transport is a combination of diffusion terms driven by several thermodynamic forces. The net effect of the terms which are not driven by the density gradient is usually called 'convection'. Both diffusion and convection exceed the neoclassical predictions. Observations have shown that the ratio between the coefficients for particle diffusion (D_a) and convection (v_a) is insensitive to variations of the plasma parameters B_φ , I_p or n_e [14,15]. This means that the density profile shape is rather constant. It suggests that D_a and v_a have similar dependences.

In RTP experiments with central ECH it was found that the n profile is flat where T_e is high and peaked. In discharges with low n_e and (as a consequence) extra high T_e , ∇n even reverses sign in the centre: The n_e profile is hollow. For off-axis ECH, the T_e profiles are hollow due (probably) to outward heat convection, whereas inward particle convection seems to be enhanced in the same region. These data indicate an antagonistic coupling of the particle and heat transport in EC heated discharges.

Additionally, after ECH the formation of a strong local n gradient located close to the $q = 2$ surface has been observed. This gradient, which is an indication for a particle transport barrier, is again accompanied by relatively low T_e values. This observation is a hint for the possible existence of a relation between the q and Γ .

References

- [1] J. A. Wesson, *Tokamaks*, 2nd ed. (Clarendon press, Oxford, UK, 1997).
- [2] R. Balescu, *Transport processes in plasmas, 2. Neoclassical transport theory* (Elsevier Science Publishers B.V., Amsterdam, the Netherlands, 1988).
- [3] A. A. Ware, Phys. Rev. Lett. **25**, 15 (1970).

-
- [4] R. J. Bickerton and J. B. Taylor, *Nature Physical Science* **229**, 110 (1971).
 - [5] F. Wagner and U. Stroth, *Plasma Phys. Control. Fusion* **35**, 1321 (1993).
 - [6] N. J. Lopes Cardozo, *Plasma Phys. Control. Fusion* **37**, 799 (1995).
 - [7] M. de Rover, Ph.D. thesis, Technische Universiteit Eindhoven, Eindhoven, the Netherlands, 1996.
 - [8] P. C. de Vries, Ph.D. thesis, Universiteit Utrecht, the Netherlands, 1997.
 - [9] C. M. Greenfield *et al.*, *Phys. Plasmas* **4**, 1596 (1997).
 - [10] F. M. Levinton *et al.*, *Phys. Rev. Lett.* **75**, 4417 (1995).
 - [11] N. J. Lopes Cardozo *et al.*, *Plasma Phys. Control. Fusion* **39**, B303 (1997).
 - [12] M. R. de Baar *et al.*, *Phys. Rev. Lett.* **78**, 4573 (1997).
 - [13] G. M. D. Hogewij, N. J. Lopes Cardozo, M. R. de Baar, and A. M. R. Schilham, *Nuc. Fus.* **38**, 1881 (1998).
 - [14] K. W. Gentle, B. Richards, and F. Waelbroeck, *Plasma Phys. Control. Fusion* **29**, 1077 (1987).
 - [15] P. C. Efthimion *et al.*, *Phys. Fl. B* **3**, 2315 (1991).

3

THE RTP TOKAMAK AND ITS DIAGNOSTICS

This chapter serves as an introduction to the tokamak of the Rijnhuizen Tokamak Project (RTP) and the instruments that supply the information about the physical state of the plasma, the diagnostics. The research at RTP is focused on the electron transport. Therefore high resolution T_e and n_e diagnostics are installed. The electrons can be manipulated by powerful Electron Cyclotron Heating (ECH) and by the injection of frozen hydrogen pellets.

3.1 The RTP Tokamak

The plasma in RTP is made in a stainless steel torus-shaped vacuum vessel with a major radius of 0.72 m and a minor radius of 0.235 m. The cross-section of the plasma is circular and its size is limited by two carbon limiters to a minor radius of 0.164 m. The vessel sits inside 24 magnetic field coils, which create a toroidal magnetic field of up to 2.5 T. A 6-fold transformer yoke can apply a flux swing of ~ 1 Vs. With this a plasma current between 40 and 150 kA is run for periods of ~ 0.5 s.

The plasmas described in this thesis are made in hydrogen. To guarantee a low impurity concentration the vessel is cleaned by baking and glow discharge cleaning. Boronisation of the inside vessel lets oxygen stick to the wall, prohibits the formation of water and decreases the CO and CO₂ yield from the wall. With these measures it is possible to decrease the effective ion charge in the plasma (Z_{eff}) to $Z_{\text{eff}} \lesssim 2$.

If no additional heating is applied the Ohmic heating of the plasma gives central $T_e \sim 700$ eV. With application of ECH T_e can rise to ~ 4 keV. The central density $n_e(0)$ can be chosen in the range $0.5 - 15 \cdot 10^{19} \text{ m}^{-3}$.

3.1.1 ECH

The ECH microwave power is delivered by a Gycom gyrotron, giving up to 500 kW 110 GHz radiation for < 200 ms. The resonant condition for ECH is given by the electron cyclotron frequency $\omega_{ce} = eB/m_e$, where e and m_e are the charge and the relativistic mass of the electron, respectively. The power is injected in the second harmonic X mode and is launched from the LFS. The 'cold resonance', *i.e.* the resonance for electrons with m_e equal to the electron rest mass, occurs at $B = 1.96$ T. The beam has a diameter of 1.5 cm and is deposited in a layer of ~ 1 cm in the direction of the major radius. The deposition radius is determined by the toroidal magnetic field. The height of the deposition is set by tilting the in-vessel launching mirror. This mirror can also be tilted so that the injection is partially along the plasma current. In this case the ECH drives current in a non-inductive way. This is called Electron Cyclotron Current Drive (ECCD) [1]. The total ECH power exceeds the Ohmic input power by a factor 4 to 7.

3.1.2 Pellet Injection

Injection of pellets of frozen hydrogen is considered as a possible method to fuel a future burning reactor plasma. It can also be used for transport studies, as the pellet induces a perturbation of a steady state plasma. At RTP a pellet injector is available that can shoot up to 8 pellets into the plasma from the LFS. The pellets can have two sizes: Small pellets contain $5 \cdot 10^{18}$ atoms and are injected at 800 to 1100 m/s; Large pellets contain $2 \cdot 10^{19}$ atoms and travel at 400 to 700 m/s. The number of particles in the small pellets is roughly the same as the total number of particles contained in a typical RTP plasma. The pellet size is ~ 1 mm.

By tilting the pellet injector, injection under an angle of 0 to -7 degrees with the horizontal mid-plane can be performed. If the pellet injector is tilted maximally, the impact parameter of the pellet is ~ 10 cm.

3.2 The RTP Diagnostics

RTP features a large number of diagnostics [2]. Only the ones relevant for this thesis are discussed here.

Magnetics

The radial and poloidal magnetic field components (B_r and B_θ , respectively) are measured with two sets of 12 pick-up coils positioned in a poloidal ring around the plasma just inside the vessel wall, at $r = 0.213$ m. From these coils the plasma position is determined. The plasma position is controlled by a feedback loop, using these signals as input. The B_θ coils are used for determination and feedback of the plasma current as well. The time resolution of these coils is 0.1 ms.

The voltage in the toroidal direction can be measured by a toroidal loop around the torus. In RTP two such loops were installed in the mid-plane of the tokamak, at the inside and the outside of the vessel.

The radial plasma position is controlled by the externally applied vertical magnetic field (B_v). The strength of this field is proportional to $\beta_p + l_i/2$ and can be used as a diagnostic of this quantity. β_p is the poloidal beta and l_i is the internal inductance, or current peaking factor.

Interferometry

Two interferometers are available at RTP to measure n_e . The 19-channel heterodyne interferometer [3,4], operating at a wavelength of 0.4 mm, uses a slab-like beam to cover up to 80 % of the plasma diameter. Its error is 10° at a maximum time resolution of 1 μ s. This diagnostic is treated in detail in chapter 4. A 2 mm interferometer [5] measures the line-integrated density along a single vertical chord through the vessel axis ($n_{e,l.int.}$). Its accuracy is 1/64-th fringe, corresponding to $\int n_e dl = 1.8 \cdot 10^{17} \text{ m}^{-2}$ (l is along the line of sight), at a time resolution of 10 μ s. The signal is used as feedback for the density control via the piezoelectric valves of the gas feed.

Thomson scattering

In chapter 5 the double-pulse multi-position Thomson scattering system [6,7] is introduced in detail. This diagnostic can measure vertical profiles of T_e , n_e , the electron pressure p_e and the spectral Doppler shift $\Delta\lambda_d$ at two (close) time points with a spatial resolution of ~ 2 % of the minor radius. The statistical error on n_e is 3 %, on T_e it is 5 % and on p_e it is 6 % at $T_e = 1 \text{ keV}$ and $n_e = 5 \cdot 10^{19} \text{ m}^{-3}$. This diagnostic has been designed to measure small structures of the size of a couple of ion Larmor radii on the plasma profiles, like filaments [8] and transport barriers [9]. It can also measure the spectra tangential to toroidal axis, measuring the current density with an accuracy of 10 %

A ruby laser is pulsed once ($\lesssim 25 \text{ J}$, 25 ns pulse) or twice ($\lesssim 2 \times 12.5 \text{ J}$, 40 ns pulse), separated 20 to 800 μ s. The 90° scattered light is relayed by conventional optics to the spectrometer. On the intensified CCD camera detectors, it is resolved spectrally and spatially. The relative spectral calibration is performed with a Tungsten ribbon lamp. The absolute calibration is taken from Rayleigh scattering on hydrogen. The density is cross-calibrated to $\int n_e dl$ of the 2 mm interferometer.

ECE radiometry

The time evolution of T_e can be followed by Electron Cyclotron Emission (ECE) measurements. At RTP a 20-channel double heterodyne radiometer is operational for second harmonic X-mode ECE measurements [10]. The spectral range between 86 and 146 GHz is down-converted in two steps to the interval from 0.4 to 3 GHz. The observed cyclotron frequency (ω_{ce}) is proportional to B and thus inversely proportional to R . The intensity is proportional to T_e , provided that the plasma is thermal and optically thick. This enables spatially resolved T_e measurements.

For the the ECE Intensity I holds:

$$I \propto T_e(1 - e^{-\tau}) , \quad (3.1)$$

where τ is the optical thickness. The optical thickness depends on n_e and T_e . For

RTP, τ is usually between 1 and 3 in the core. The factor between brackets is between 0.63 and 0.95. In the edge, τ is somewhat lower than in the core.

The ECE channels are separated by 3 GHz, corresponding to 4-18 mm in the plasma. They measure along the horizontal, radial axis. The exact location of the channels depends on the magnetic field. The relative calibration of the channels is performed by a sweep of the magnetic field in a steady state Ohmic plasma [11, p. 59]. The channels shift through the plasma during this sweep and pass the previous positions of one or more neighbouring channels. The absolute calibration is taken from Thomson scattering. The noise temperature is 1 eV at a temporal resolution of 2 μ s.

Soft X-ray tomography

The Soft X-Ray tomography system (SXR) consists of five cameras of 16 pinhole detectors each, together covering almost the full poloidal plane [12,13]. The 80 channels measure the emitted radiation between 1 and 10 keV. The intensity is a function of n_e^2 . For the RTP system the intensity also depends on $T_e^{0.5}$, so the SXR diagnostic is sensitive to changes in these plasma parameters. It is well suited to qualitatively study fast events.

The almost complete coverage of the plasma cross-section enables two-dimensional reconstruction of the local emissivity from the line-integrated measurements, if the plasma parameters are assumed constant on the flux surfaces. Such a tomographic reconstruction is a solution of an ill-posed problem. It is further complicated by the fact that not all cameras are cross-calibrated.

References

- [1] A. A. M. Oomens *et al.*, in *IAEA-FI-CN-69/CDP/08(R) Japan* (IAEA, Vienna, 1998).
- [2] A. J. H. Donn e and the RTP-Team, *Plasma Phys. Reports* **20**, 192 (1994).
- [3] A. C. A. P. van Lammeren, S. K. Kim, and A. J. H. Donn e, *Rev. Sci. Instrum.* **61**, 2882 (1990).
- [4] J. H. Rommers and J. Howard, *Plasma Phys. Control. Fusion* **38**, 1805 (1996).
- [5] C. A. J. Hugenholtz, Ph.D. thesis, Technische Universiteit Eindhoven, the Netherlands, 1990.
- [6] C. J. Barth *et al.*, *Rev. Sci. Instrum.* **68**, 3380 (1997).
- [7] M. N. A. Beurskens, C. J. Barth, N. J. Lopes Cardozo, and H. J. van der Meiden, *Plasma Phys. Control. Fusion* **41**, 1321 (1999).
- [8] N. J. Lopes Cardozo *et al.*, *Phys. Rev. Lett.* **73**, 256 (1994).
- [9] M. R. de Baar *et al.*, *Phys. Plasmas* **6**, 4645 (1999).
- [10] J. F. M. v. Gelder, K. C. E. Husmann, H. S. Miedema, and A. J. H. Donn e, *Rev. Sci. Instrum.* **66**, 418 (1995).
- [11] J. F. M. van Gelder, Ph.D. thesis, Rijksuniversiteit Utrecht, the Netherlands, 1996.
- [12] D. F. da Cruz Jr and A. J. H. donn e, *Rev. Sci. Instrum.* **61**, 3067 (1990).
- [13] C. P. Tanzi, Ph.D. thesis, Rijksuniversiteit Utrecht, the Netherlands, 1996.

4

POLARIMETRY

This chapter provides an introduction to interferometry and polarimetry in general, and to the diagnostic at RTP in particular. The accuracy analysis and the experimental results of this diagnostic are discussed in detail.

From polarimetry the poloidal magnetic field (B_θ) can be deduced provided the flux geometry and the electron density n_e are known. This is one of the reasons why polarimetry is often combined with interferometry in one set-up, for the density n_e can be obtained from interferometric measurements, using the flux geometry. The current density follows from B_θ via Maxwell's equations.

In section 4.1 the basic principles of polarimetric and interferometric measurements in plasmas are presented. In section 4.2 the implementations of the experimental schemes are discussed. Special attention is paid to the RTP set-up. The remaining sections are devoted to this set-up. Consecutively, the data acquisition (section 4.3), the data analysis (section 4.4), the accuracy analysis (section 4.6) and the experimental results (section 4.5) are presented.

4.1 Interferometry and Polarimetry

Consider an arbitrary electromagnetic wave propagating through a tokamak plasma. The wave can be decomposed into its two orthogonal propagation modes, also called eigenstates. Both eigenstates are subject to changes of the polarisation with respect to vacuum due to the plasma. As we will see, the average of these changes is proportional to the particle density and the difference between them is proportional to the product of the density and the magnetic field parallel to the wave.

The propagation of waves can be described by a dispersion relation. The strong magnetic field makes the plasma highly anisotropic and as a consequence the dispersion relation is a rather complex tensor relation.

The easiest way to deduce the dispersion relation is by describing the plasma as a fluid. This is a macroscopic point of view as opposed to a kinetic treatment, which incorporates the details of the particle distribution function. The fluid description is adequate in case the thermal velocity of the particles is negligible compared to the phase velocity of the waves. This is the so-called cold plasma approximation. It can be shown *a posteriori* that for the waves under consideration here the phase velocities are close to the speed of light (c). The electron thermal velocity of a 1 keV electron is only $\sim 1 \cdot 10^7$ m/s = $c/30$, so the cold plasma approximation is valid.

As a second approximation, the interaction with the ions is neglected. Because the ion mass is much higher than the electron mass, their contribution to the dispersion is negligible, provided the frequency is high enough. We shall consider here only cases where the ion motion can be ignored.

With these approximations the reaction of the plasma electrons to an arbitrary wave with frequency ω can be characterised. The dispersion relation can be written as a quadratic relation for N^2 , where N is the refractive index $N = kc/\omega$ [1, p. 87-95]:

$$N^2 = 1 - \frac{X(1-X)}{1-X - \frac{1}{2}Y^2 \sin^2 \vartheta \pm \left[\left(\frac{1}{2}Y^2 \sin^2 \vartheta \right)^2 + (1-X)^2 Y^2 \cos^2 \vartheta \right]^{1/2}}, \quad (4.1)$$

where,

$$X = \frac{e^2 n_e}{\epsilon_0 m_e \omega^2}, \quad Y = \frac{eB_0}{m_e \omega}, \quad (4.2)$$

and ϑ is the angle between \mathbf{B} and \mathbf{k} . Eq. 4.1 is called the Appleton-Hartree formula. The z -coordinate is chosen along the magnetic field \mathbf{B} and the wave vector \mathbf{k} is chosen in the yz -plane.

The anisotropy in the solutions can easily be seen by considering the two cases of propagation, perpendicular ($\vartheta = \pi/2$) and parallel ($\vartheta = 0$) to B . First, the parallel propagation is treated. In this case, the solutions are:

$$N^2 = 1 - \frac{X}{1 \pm Y}. \quad (4.3)$$

The corresponding polarisations of the wave electric field can be obtained if the solution is filled in in the equation for dispersion. Here, only the result is given:

$$\frac{E_x}{E_y} = \pm i, \quad E_z = 0, \quad (4.4)$$

which are left and right handed circularly polarised waves, respectively. For the following analysis to be valid it is necessary that the gradient lengths are much larger than the wavelength of the incident wave. We take a linearly polarised wave incident parallel to B . This wave can be decomposed into two circularly polarised counter-rotating waves of equal amplitude. Upon exit these waves recombine again into a linearly polarised wave. The total phase lag in the plasma is:

$$\varphi = \int k dl = \int N \frac{\omega}{c} dl, \quad (4.5)$$

where l is the beam path variable. Suppose the ratio $B_0/\omega \ll m_e/e$, so that $Y \ll 1$, then Eq. 4.3 reduces to:

$$N^2 = 1 - X = 1 - \frac{n_e}{n_c}, \quad n_c \equiv \epsilon_0 m_e \omega^2 / e^2. \quad (4.6)$$

The quantity n_c is called the cut-off density, because for $n_e > n_c$, N^2 becomes negative and N purely imaginary. This means the wave is evanescent. If the density is sufficiently below the cut-off density, $n_e < n_c$, then N can be expanded to:

$$N \approx 1 - \frac{1}{2} n_e / n_c \quad (4.7)$$

and the phase lag becomes:

$$\varphi = \frac{\omega}{c} \int \left(1 - \frac{n_e}{n_c}\right) dl = \frac{\omega}{c} l - \frac{\omega}{2cn_c} \int n_e dl. \quad (4.8)$$

The first term is simply the phase lag of the wave in vacuum, the second term is the phase shift by the plasma. Note that the second term is negative.

If Y is not neglected, it is found that the two circularly polarised waves are subject to different refractive indices, see Eq. 4.3. This means that the polarisation of the recombined wave on exit is rotated. This can be illustrated by assuming that Y is finite but small. A similar expansion to Eq. 4.7 can then be used:

$$N^2 \approx 1 - X \pm XY, \quad N_{\pm} \approx 1 - \frac{X}{2} \pm \frac{XY}{2}. \quad (4.9)$$

The polarisation rotation in the plasma is the difference of the phase lags the two eigenwaves experience, cf. Eq. 4.8:

$$\begin{aligned} \alpha &= \frac{1}{2} (\varphi_+ - \varphi_-) = \frac{\omega}{2c} \int \left[\left(1 - \frac{X}{2} + \frac{XY}{2}\right) - \left(1 - \frac{X}{2} - \frac{XY}{2}\right) \right] dl \\ &= \frac{\omega}{2c} \int XY dl = \frac{e}{2cm_e n_c} \int n_e B dl. \end{aligned} \quad (4.10)$$

This effect is called Faraday rotation, after the English scientist Michael Faraday who first described it.

For perpendicular propagation ($\vartheta = \pi/2$), the situation is not so clear. The solutions of the dispersion relation are:

$$N_+^2 = 1 - X \quad \text{and} \quad N_-^2 = \frac{X(1 - X)}{1 - X - Y^2}. \quad (4.11)$$

The polarisations corresponding to these solutions can be obtained if filled in in the dispersion equation. The positive sign solution is linearly polarised along B , but the negative sign solution is perpendicular to B , and its polarisation is not simple. Nevertheless, it has been shown that the phase shift and the Faraday rotation obey Eqs. 4.8 and 4.10. The following equations can be considered as generalisations of Eqs. 4.8 and 4.10 for arbitrary propagation angle [1,2]:

$$\begin{aligned} \Delta\varphi &= \frac{\omega}{2cn_c} \int n_e dl, \\ \alpha &= \frac{e}{2cm_en_c} \int n_e \mathbf{B} \cdot d\mathbf{l} \end{aligned} \quad (4.12)$$

for $n_e \ll n_c$ and $eB \sec(\vartheta)/m_e \ll 1$. The last constraint is a generalisation of the small Y condition, in which the fact that the Faraday rotation is only sensitive to the magnetic field parallel to the wave vector is included.

If the propagation is sufficiently close to perpendicular so that $eB \sec(\vartheta)/m_e \gtrsim 1$, effects other than simple rotation of the polarisation become important. It is the consequence of the eigenwaves not being circularly polarised anymore. A linearly polarised incident wave then gets some ellipticity in its polarisation. This is called the Cotton-Mouton effect.

In RTP waves are launched vertically through the plasma, perpendicular to the toroidal magnetic field. The phase shift by the plasma can be several wave periods. The Faraday rotation is created by the poloidal magnetic field and is typically only a few degrees. The Cotton-Mouton effect is negligible.

4.2 Measurement Method and Set-up

In this section the measurements of $\Delta\varphi$ and α are discussed. Measurement of $\Delta\varphi$ yields knowledge of n_e , measurement of α yields information on the product of the magnetic field along the measuring chord and n_e (see Eq. 4.12). We focus to measurements in the poloidal plane, i.e. B_θ is probed. The poloidal magnetic field is generated by the toroidal plasma current (I_p) according to Maxwell's equation $\nabla \times \mathbf{B} = \mu_0 \mathbf{j}$. For large aspect ratio $\varepsilon = R_0/a$ the torus can be approximated by a cylinder and using Stoke's theorem we find:

$$B_\theta(r) = \frac{\mu_0}{2\pi r} \int j(r') dS, \quad (4.13)$$

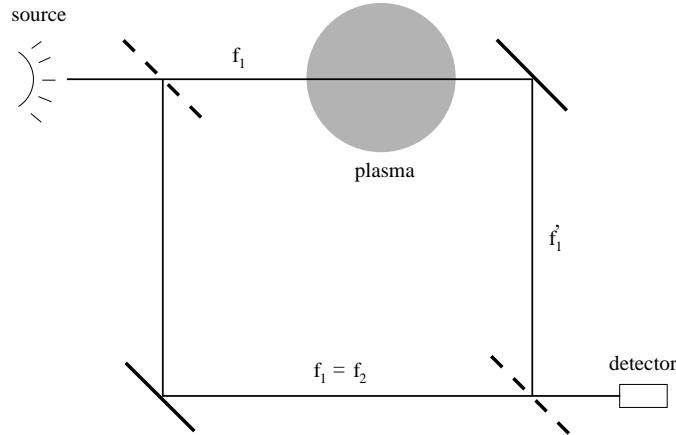


Figure 4.1: Schematic representation of a homodyne Mach-Zehnder interferometer set-up.

where r' is the minor radius and the integral is taken over the flux surface with radius r .

In section 4.2.1 the determination of $\Delta\varphi$ with interferometry is discussed, in section 4.2.2 the additional determination of α is discussed (polarimetry).

4.2.1 Interferometry

A simple way to measure the phase shift due to the plasma is to compare the phases of two waves of equal wavelength with equal path lengths of which one is influenced by the plasma. This is called a Mach-Zehnder interferometer. It can be accomplished by splitting a laser beam into two branches of equal length, one of which is passing through the plasma, and recombining them onto a single detector, see Fig. 4.1. The electric fields of the split beams can be represented by $E_1 \sin(\omega t + \Delta\varphi)$ and $E_2 \sin(\omega t)$ for the plasma and the reference branch, respectively. The amplitude of the recombined beam depends in a simple way on $\Delta\varphi$:

$$P = (E_1^2 + E_2^2) \left(1 + \frac{2E_1 E_2}{E_1^2 + E_2^2} \cos \Delta\varphi \right) \quad (4.14)$$

This method is called homodyne because of the use of a single frequency input beam. There are two disadvantages: First, variations in beam power can be mistaken for density variations. This problem can be overcome by monitoring the beam power separately. Secondly, the sign of the density variations is unclear, because of the cosine behaviour of the signal.

Both these problems can be overcome by application of a heterodyne measurement set-up, see Fig. 4.2. In this case a second beam (the local oscillator beam) with a slightly different frequency is relayed unperturbed to the detector. The effect

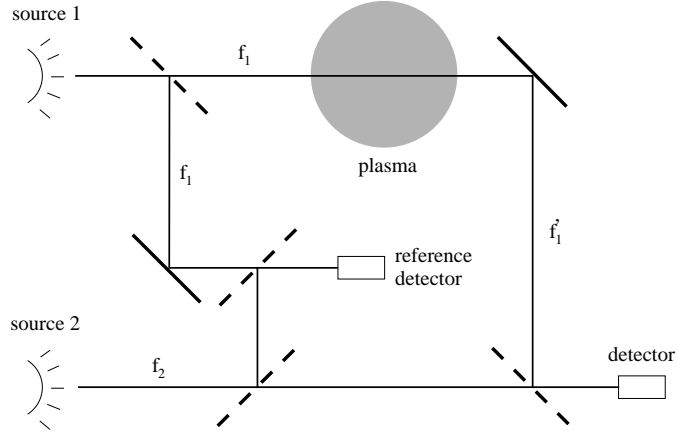


Figure 4.2: Schematic representation of a heterodyne interferometer set-up.

of this second beam is the replacement of $\Delta\varphi$ in Eq. 4.14 with $\Delta\omega t + \Delta\varphi$, where $\Delta\omega$ is the frequency difference between the two beams. The power measurement of the homodyne set-up is replaced by a phase measurement in case of heterodyne detection. A reference detector is added to monitor the phase of the unperturbed beams, not the power.

Most present-day interferometers in fusion research use heterodyne detection. The time resolution is set by $\Delta\omega$. The frequency difference between the beams is often accomplished by mechanical means, limiting the time resolution to tens of kHz. Alternatively, two identical but slightly detuned lasers are used. The time resolution is limited by the laser bandwidth and can be several MHz.

4.2.2 Polarimetry

There are two reasons to combine the measurements of the density phase shift $\Delta\varphi$ and the Faraday rotation α into one set-up: First, n_e is crucial to reconstruct B_θ from α and it is given by $\Delta\varphi$. Second, both quantities are detectable in roughly the same frequency range, the far infrared (FIR) radiation. Since measurement of α involves the polarisation of the beam, it is called polarimetry.

Probably the simplest way to extend the abovementioned interferometer with a polarimeter is to replace the beam combiner in front of the detectors with a polariser. In the polariser the wave is split into two linearly polarised waves, orthogonal and parallel to its characteristic axis, one of which is reflected and the other transmitted. By choosing the axis along the incident polarisation, the Faraday rotation is carried by one of the components and it can be measured directly. Of course, two detectors are needed instead of one to obtain both components. Further, the α determination is based entirely on the ratio of the two components, so accurate relative calibration of the detectors is crucial.

This method has been implemented successfully at the TEXTOR-94 tokamak

[3], reaching an angular accuracy of 0.15° for nine vertical channels and one horizontal. Use has been made of pyroelectric power detectors. The advantage of these detectors is that they are easy to handle so the relative calibration is well feasible. The disadvantage is their limited time resolution, which limits the time resolution of α to ~ 3 ms.

Another method to improve the time resolution, which is applied in other experiments, is to use Schottky diode detectors. The diodes are mounted in corner cube reflectors. They are polarisation sensitive and have very high time resolution. Their disadvantage is that the antenna pattern is very narrow, and the relative calibration of two detectors is too sensitive to perturbations to rely on. Together with the general fact that a double detection array considerably increases the cost and complexity of the detection system, this creates the need for a measurement scheme with a single detector per line of sight measuring both $\Delta\varphi$ and α . This can be achieved by modulation of the polarisation of the probing wave.

Kunz and Dodel [4] used a rocking polarisation vector, modulated over a few degrees. If α is small, it is proportional to the change of the modulated power level. The rocking polarisation is usually accomplished by an oscillating ferrite element, leading to very high power losses. Other disadvantages are the mechanical limit on the modulation frequency, and the fact that the α signal is contained in the DC component.

Alternatively, a rotating elliptically polarised wave [5] can be used, which has the advantage that the α is contained in the phase of the measurement. The detected signal is an amplitude modulated IF signal. The $\Delta\varphi$ signal is carried by the IF phase, α is carried by the phase of the modulation. The ellipticity guarantees the determination of $\Delta\varphi$ in the valleys of the modulation. Unfortunately, there is some crosstalk between $\Delta\varphi$ and α .

This scheme has been implemented at MTX [5]. The rotation of the elliptically polarised wave is generated using a rotating half-wave plate. The time resolution is limited by the mechanics of this rotation to a ~ 0.5 kHz.

All methods presented until now probe $\Delta\varphi$ and α directly. A perfect alternative is to probe the two refractive indices directly, see Eqs. 4.3 and 4.11. This can be done by using two counter-rotating circularly polarised waves. These are the eigenwaves for parallel propagation. Nevertheless, it can be shown that also in case of perpendicular propagation their respective phases are characterised by one of the two solutions of the dispersion relation only [2]. The left-handed and right-handed waves experience different phase shifts $\Delta\varphi_+$ and $\Delta\varphi_-$, respectively, cf. Eq. 4.10. The average of these shifts is $\Delta\varphi$, the difference between them is 2α .

A straightforward experimental implementation of the above method is to probe the plasma with two waves of slightly different wavelength instead of a single probing beam, see Fig. 4.3 [2,6]. These two probing waves are counter-rotating, circularly polarised waves. The circularly polarised waves can be obtained by passing linearly polarised waves through a quarter-wave plate at 45° . In this scheme three sources are used and the detectors obtain three IF mixing frequencies. Two of these contain the mixes of the respective probes with the local oscillator and their phases are shifted by $\Delta\varphi_+$ and $\Delta\varphi_-$, respectively. The third one is the mix of the two probing

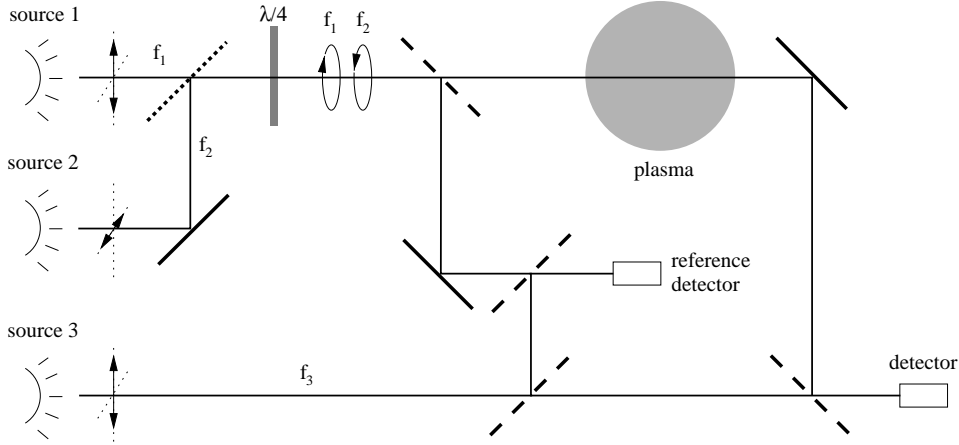


Figure 4.3: Schematic representation of a double-heterodyne combined interferometer/polarimeter set-up.

beams. The phase shift of this carrier with respect to the reference is 2α .

In this set-up, all quantities can be determined independently with phase measurements. The time resolution is set by the laser bandwidth with the remark that three sources are hosted within the bandwidth. No mechanical constraints limit operation, nor does any signal crosstalk occur. Only one detector per line of sight is needed. This scheme has been implemented on RTP and is to be implemented on NSTX in the near future [7,8].

4.2.3 Experimental Set-up

The RTP triple-laser multi-channel double heterodyne interferometer/polarimeter system, will be discussed using the three-dimensional view, given in Fig. 4.4 [2,9]. The figure is the guideline for the discussion of the set-up. Three laser cavities filled with ~ 300 mTorr formic acid (CHOOH) are optically pumped by a 150 W, $9.4\mu\text{m}$ carbon dioxide (CO_2) laser. The lasers deliver each ~ 30 mW FIR radiation with $\lambda_0 = 0.4325$ mm and are mutually slightly detuned within the bandwidth of ~ 2 MHz. Directly behind the laser exit the polarisation of one of the probing beams is rotated a quarter turn so that the polarisations of the probing beams are perpendicular. Both beams are co-aligned by combining them on a polariser. The beams are then coupled into highly oversized ($\varnothing 70$ mm) wave guides and transported to the tokamak. The part of the set-up around the tokamak is positioned on a stiff F-shaped frame, which is anchored to the building fundament. There is no mechanical connection to the tokamak.

Right after the wave guide exit a quartz quarter wave plate converts the orthogonal polarisations of the probing beams to counter-rotating circular. The next relay element is a beam splitter: It transmits a 5 % fraction towards the reference detector. This beam splitter is made of metallic mesh. Therefore the angle of in-

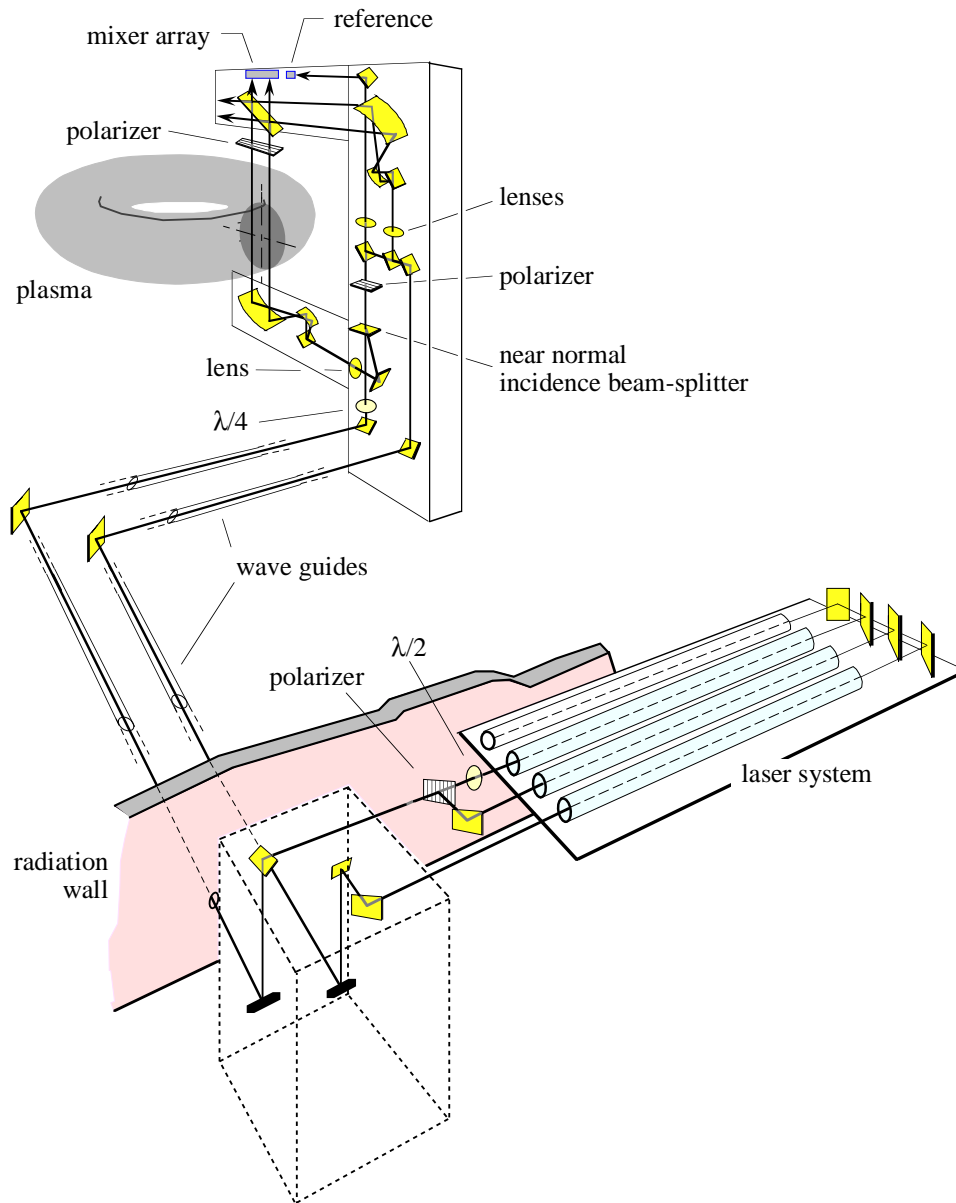


Figure 4.4: Artist view of the RTP triple laser combined interferometer/polarimeter set-up.

cence of the main beam is kept as small as possible, to conserve the polarisation properties of the beams.

A one-dimensional lens of high density polyethylene (HDPE) is used to focus the beam in the toroidal direction to the centre of the plasma. The beam is coupled onto the set of parabolic mirrors, which expand the beam a factor 7.5 in radial direction. In this way, a slab-like beam is created, which fits the available diagnostic port. In the picture, the tokamak vessel, the diagnostic ports nor the flanges containing the HDPE vacuum windows are drawn. The entrance window is positioned just above the large parabolic mirror, ~ 0.3 m from the plasma. The exit window is at a similar distance above the plasma.

After vessel exit the probes are recombined and linearised using a polariser. With exception of the quarter wave plate and the polariser, the local oscillator beam follows a similar optical path outside the vessel. The probing beams are recombined with the local oscillator on a beam splitter and relayed to the detector array. The detector array consists of up to 19 Schottky diodes mounted in corner cubes. Each detector has a parabolic mirror to focus the signal on the diode. The width of the combined mirror-corner cube elements determines the minimal spatial resolution: 14 mm. They are mounted on a rail to allow flexible positioning.

Approximately 5 % of the signal is split from both beams before expansion and relayed directly to the reference detector without interference of the plasma (see also Fig. 4.4). The reference fractions of the two probing beams are recombined on a polariser right behind the beam splitter.

Both the detector array and the reference detector are placed inside a Faraday cage to prevent the disturbance from the high power microwave heating sources of RTP. The gyrotron frequencies 60 and 110 GHz are filtered out at the entrances of the cage by a Fabry-Pérot interferometer consisting of a double nickel mesh layer.

4.3 Data Acquisition

The data obtained at the detectors is amplified and fed into the analog-digital converters. The determination of the phase is done entirely by means of software. To determine the phase of the three mixing signals, the signals have to be separated. This is done by Fourier transformation, filtering and inverse transformation. The final step is to compare the phases obtained from the detector array with those from the reference detector. The phase differences are the quantities sought for. These have to be corrected for the constant offset due to the path length difference between the detector and the reference. This offset is removed using the zero-plasma signals before and after the discharge.

In Fig. 4.5 the recorded spectrum of the reference detector is shown. The three large peaks correspond to the beat frequencies between the three carriers. The smaller peaks correspond to higher harmonics of the mixing frequencies. These are visible in the recorded signal, because they are aliased down in the analog-digital conversion. The side lobe at the right-hand side of the most right peak is also due to a higher harmonic. If the higher harmonics are too close to the primary peak they

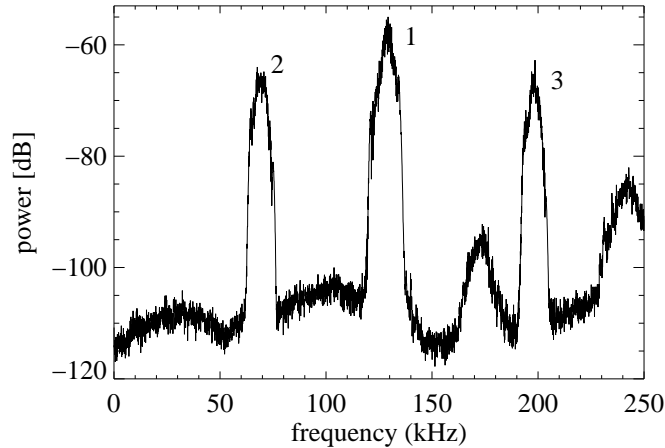


Figure 4.5: Spectrum of the reference detector signal. Peak 1 corresponds to mixing between the probes, whereas peak 2 and 3 come from mixing between the respective probes and the local oscillator. The other structures are due to higher harmonics.

can disturb the phase determination (see also section 4.6).

In the previous section we showed that the maximum measurement frequency of the set-up is basically set by the laser bandwidth. For this to hold, the sampling rate of the signal must be (much) faster than the bandwidth of the laser. For RTP, the line width of the laser is approximately 2 MHz, whereas the sampling rate of the ADCs at RTP is at maximum 500 kHz, limited by their storage capacity. In this case the sampling rate is the limiting factor for the maximum measurement frequency. The electronics involved act as a bandpass filter between 0.1 and 5 MHz and do not limit the time resolution. We will now derive the maximum measurement frequency for the RTP set-up. One should keep in mind that this is only an upper limit to the time resolution. The time resolution is further compromised with respect to this number by statistical noise.

The mutual tuning of the mixing frequencies must fulfill the following conditions for optimal data acquisition: 1) The three frequencies must be as close as possible, because of power considerations. The mixing power decreases strongly with frequency difference as the laser band width is approached. 2) The three frequencies must exceed 100 kHz, because of the electronics. 3) The stability of the laser sources demands that the mixing frequencies are chosen as high as possible. 4) The three frequencies must be well separated in the frequency domain after aliasing (which is explained below). The first three conditions have as a compromise the 0.5-1 MHz range. The fourth condition is fulfilled by careful tuning of the lasers with ~ 5 kHz accuracy. Below, first the mechanism of aliasing is explained. Then, the maximum time resolution is derived from the sampling frequency, which will illustrate the importance of the laser tuning.

In Fig. 4.6 the mechanism of aliasing is illustrated. The three laser frequencies within the laser line give three IF mixing frequencies. The mixing frequencies are recorded with 500 kHz, or, equivalently, they are folded spectrally into the Nyquist interval 0-250 kHz. The recorded frequencies df'_i can be written as:

$$df'_i = |(df_i \bmod 2 \cdot f_{\text{Nyq}}) - f_{\text{Nyq}}| , \quad (4.15)$$

where the symbols are chosen like in Fig. 4.6. Two of the three frequencies can be chosen. In the spectrum in Fig. 4.5 the mixing frequencies were tuned at 560, 625 and 1185 kHz. The corresponding aliased frequencies are 60, 125 and 185 kHz. In Fig. 4.5 the mixing frequencies are well separated from each other and from the edges of the Nyquist interval. If the frequencies were chosen to be 560 and 685 kHz, the aliased equivalent of the third would be 240 kHz, which would interfere with the edge.

In case of optimal separation each mixing frequency with sidebands has $250/3 \sim 83$ kHz. After inverse transformation, half of the data remains, so the optimal temporal resolution of the data acquisition is ~ 41 kHz. In practice, the temporal resolution can be somewhat lower, because the optimal setting is hard to obtain.

This rate is the rate with which the phase signals are obtained. The signal-to-noise ratio of the measurement determines the error on these signals. For the spectrum shown in Fig. 4.5, the thus obtained error is $\sim 1^\circ$. This error is reduced by averaging, further decreasing the time resolution.

A complicating factor in this picture is the occurrence of higher harmonics of the mixing frequencies, which are aliased down to the Nyquist band as well. Interference of higher harmonics with the mixing frequencies can give high frequency phase perturbations.

Simulated data is used to test the software for phase determination. In the simulation of the data, the observed effects polluting the spectrum are integrated, like higher harmonics aliasing and instability of the laser frequencies, are integrated. The obtained reconstruction error is in all cases below 0.1° , confirming that the phase determination is correct.

4.4 Data Analysis

4.4.1 Refraction

Before further analysis is performed, the phases have to be corrected for the consequences of refraction. These consequences are not at all negligible, mainly for the following reasons: First, the limited size of RTP means that a strong radial density gradient exists. Secondly, the distance between the plasma and the detectors is 1.5 m, and small angular deviations can lead to appreciable beam shifts at the detector rail, compared to the detector width of 14 mm. The refraction angle on exit of the plasma can be as large as 0.75° , giving ~ 2 cm radial displacement at the detector array. The data has to be corrected for this effect.

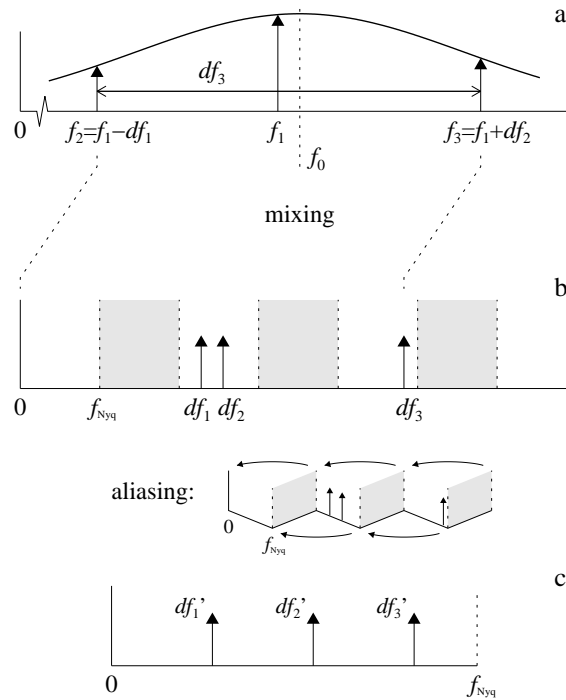


Figure 4.6: The principle of aliasing is as follows: The three lasers are positioned around the optimum line f_0 (a). The three difference frequencies are the mixing frequencies. These may not coincide with (a multiple of) the Nyquist frequency f_{Nyq} (b). In the digital recording the subsequent bands of width f_{Nyq} are 'folded' on the first interval like a harmonica (pictured schematically between b and c). The numbers in the figure c are the respective mixing frequencies after aliasing.

The effect of refraction is two-fold: First, the plasma that is probed by the detector is at a smaller horizontal distance from the magnetic axis than the detector itself. This is accounted for by correction of the effective detector position in the analysis. Secondly, the path length to the detector is increased with respect to the zero level determination without plasma. This path length change is minute relative to the path length itself but can be appreciable with respect to λ_0 . For the above example of 2 cm displacement the path length change is $\sim 270 \mu\text{m}$ or $0.6\lambda_0$. The phases are corrected directly for this effect. Note that this effect is only important for the probe-local oscillator mixes. Both the probes follow the same path so they experience the same phase change and the effective phase of the probe-probe mix, containing the α signal, is unaltered.

The correction for refraction is determined iteratively. The uncorrected n_e profile is used to determine the refracted beam path. With this beam path the mea-

sured phases and measurement positions are corrected, and the corresponding n_e profile is determined. This loop is iterated until the additional position correction is below a pre-set threshold, usually 1 mm.

Though the refraction takes place in the plasma, the lines of sight are almost perfectly straight. Hence, the channel positions are unambiguous. It is because of the large distance between plasma edge and detectors that the refraction is important.

4.4.2 Abel Inversion

The signals α and $\Delta\varphi$ contain the signals n_e and B_θ integrated over the lines of sight. The measurements can be inverted if it is assumed that the integrands are constant on the flux surfaces and that the shape and position of the flux surfaces is known. The RTP tokamak plasma has a circular cross-section. The flux surfaces can be considered as a set of nested toroids with circular cross-section, the centres of which are slightly displaced to larger major radii for smaller flux tubes as a consequence of the Shafranov shift (δ). In RTP, $\delta = 1 - 2$ cm, depending on plasma pressure and current.

The deduction of the integrand from the measurements represents an integral problem. Solution of this problem in a geometry of concentric circles is called Abel inversion, after the mathematician Abel who first studied it. The solution is calculated from the first derivative of the signal rather than the signal itself. This tends to make the result rather sensitive to any error in the measurement. Fortunately, this is partially compensated by the integration involved in the measurement.

In a tokamak the flux surfaces are usually not concentric circles. Fortunately, several numerical schemes to approximate the Abel inversion have been suggested [10–12]. The general principle which they use is the following: From the outermost measurements, the density profile up to its position is directly obtained. With this partial density profile, the contributions of this area to the other channels can be calculated, and their signals can be corrected, using the above assumptions on the two-dimensional geometry of the signals. Using the next to outermost channel another 'ring' can be added to the density profile, and the other channels can again be corrected for this. Proceeding from the edge, the whole signal profile up to the centre can be constructed in this way. Abel inversion is a standard technique for interferometer measurements. For RTP, the results of the various methods differ only for very strong asymmetries in n_e . In the data in this thesis no such extreme n_e asymmetries are met.

For the α signal, Abel inversion is not straightforward, because the inner product in the integrand is not constant on the flux surfaces (Eq. 4.12).

Due to the line integration, small structures are invisible on the interferometer and polarimeter profiles. If n_e or B_θ change locally, the change of the measured quantities is weakened by the line integration. The measured difference between two $\Delta\varphi$ profiles is always less than the difference between the corresponding n_e profiles. A similar statement holds for α profiles. As a consequence, the measured $\Delta\varphi$ and α profiles are expected to be smooth.

The RTP interferometer data has an excellent signal-to-noise ratio. The signal is in the order of 10^3 degrees. The statistical error is a few degrees at a time resolution of $\sim 50 \mu\text{s}$. The measured profiles are smooth and symmetric in r (see e.g. Fig. 4.7b). The reconstruction of the n_e profile from the data using Abel inversion is straightforward.

The signal-to-noise ratio of the polarimeter data is not so good. The typical signal level is a few degrees. To bring the noise down to an acceptable level of 0.1° degrees, low-pass filtering must be applied at 1 kHz. Apart from the statistical error, systematic errors of $\sim 0.3^\circ$ are observed. We call these errors systematic because their origin is not noise, but they are unpredictable. Therefore, the data cannot be corrected for these systematic effects. As a consequence the Faraday rotation profile is not smooth and Abel inversion is impossible. More seriously, the expected changes in Faraday rotation between j profiles in different plasmas are of the same magnitude. This makes reconstruction of B_θ rather difficult. In section 4.6 we discuss these errors in detail.

To give an impression of the measurements we first show two examples. In Fig. 4.7 two polarimeter and interferometer profiles are shown for a plasma with off-axis ECH. One profile is measured shortly before switch-on of ECH, the second one after 70 ms of off-axis heating. The T_e profile as measured by Thomson scattering (TS) has become hollow by then. The interferometer profiles nearly coincide, so the difference in α is almost entirely caused by a difference in j . The polarimeter profiles show a significant difference of the order of 0.5° . The main difference is in the profile shape.

It is clear from this figure that the α signal is much lower than the $\Delta\varphi$ signal. The relative error on α is much larger than the relative error on $\Delta\varphi$, which is too small to be seen in the figure.

The line-integrated measurement profiles are expected to be smooth, and in Fig. 4.7 polynomials are fit to the profiles. The interferometer data are well fitted by the polynomials. In the polarimeter profiles there are several points off the polynomial outside their error bar. The scatter on the α profiles is considerable and, remembering that Abel inversion is rather sensitive to errors, this excludes inversion of the α profiles. From Fig. 4.7 it seems advantageous to concentrate on the profile shape rather than the local values.

4.4.3 Parametrisation of q

In the previous section it was argued that Abel inversion is not suitable for analysis of the α profiles. However, important physical information can be obtained from the profile shape. In this section the attention is focused on an analysis method that is sensitive to the profile shape only.

The j profile can be reconstructed from the resulting n_e and the α profile using a parametrisation of the q profile. The parameters are not so sensitive to local excursions of the profile if the number of degrees of freedom is much smaller than the number of signals. The parameters are fitted to the data.

As the basis of the parametrisation for q the Natural Current Profile (NCP)

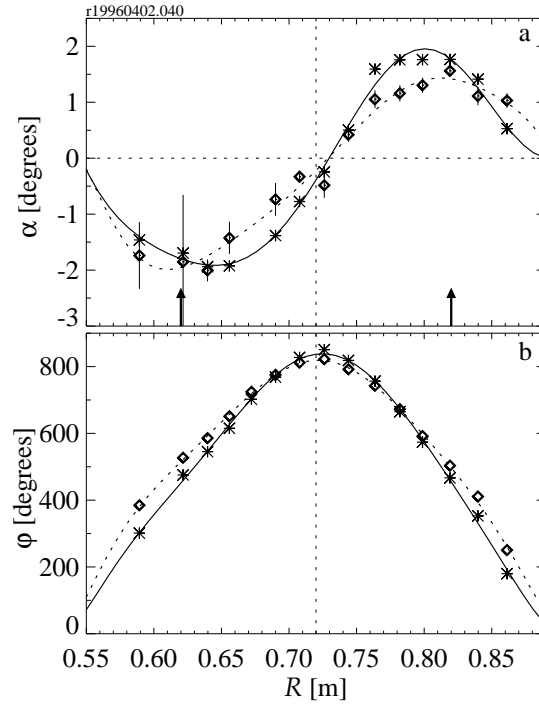


Figure 4.7: a) Faraday rotation profiles just before switch-on of off-axis ECH (asterisks) and during the hollow T_e phase, four current diffusion times after switch-on (diamonds). The lines represent polynomial fits to the data. The arrows indicate the heating position. b) The corresponding interferometer phase profiles. These are nearly identical apart from a slight increase of the edge density during ECH. $I_p = 80$ kA, $B_T = 2.24$ T, $q_a = 5.2$, $n_e(0) = 3 \cdot 10^{19} \text{ m}^{-3}$.

[13,14] is used. This profile describes the Ohmic q profile. In RTP discharges with off-axis Electron Cyclotron Heating (ECH) are performed, which have inverted j profiles and corresponding flat or hollow q profiles. To allow for such a central rise of the q profile, a Gaussian function is added to the parametrisation. This Gaussian is centred at $\rho \equiv r/a = 0$ and its amplitude is offset such that its influence is zero at the edge:

$$q_{\text{par}}(\rho) = q_{\text{NCP},0} \left[\left(\frac{q_a}{q_{\text{NCP},0}} - 1 \right) \rho^2 + 1 \right] + A \left(e^{-\left(\frac{\rho}{\sigma}\right)^2} - e^{-\left(\frac{1}{\sigma}\right)^2} \right) \quad (4.16)$$

There are three free parameters: $q_{\text{NCP},0}$, A and σ . $q_{\text{NCP},0}$ is the central value of the quadratic term, A and σ are the amplitude and the $1/e$ -width of the second term, respectively. Note that the requirement $\frac{\partial q_{\text{par}}}{\partial \rho}(0) = 0$ is fulfilled by addition of the

last term in the equation.

From this expression for q the corresponding α profile is calculated and compared to the measured α profile using the χ^2 value. The χ^2 value is calculated with the statistical errors only, not with the systematic errors. The χ^2 value is minimised using the method of Powell.

In the edge relatively little current is running. This corresponds to a derivative of q to ρ at the edge of $2q_a$. The derivative at the edge of the first term is indeed $2q_a$. The Gaussian adds less than 4 % even for relatively large $\sigma = 0.4$ and $A = 1$.

Note that q_0 is not determined by $q_{\text{NCP},0}$ only:

$$q_0 = q_{\text{NCP},0} + A(1 - e^{-(\frac{1}{\sigma})^2}). \quad (4.17)$$

For increasing A , q_{par} inside σ goes from quadratic to a shape with a local maximum at $\rho = 0$. This last shape represents negative central shear.

If the measurements are averaged to a time resolution of 1 ms, the error on $q_{\text{NCP},0}$ is typical 10 %. For A , this is also 10 % and for σ 0.10. Together, this results in a statistical error on q of 20 % on axis, decreasing to 0 towards the edge, assuming that q_a is known exactly.

4.5 Experimental results

To study the diffusion of j , both perturbative and transient experiments were performed. In these experiments the steady state plasma is perturbed or it is brought to a new state. The reaction of the plasma to the perturbation and the relaxation to the new steady state is studied via the changes of the various profiles with respect to the target plasma. This section focuses on j profile perturbations by pellet injection and j profile transitions by current ramping and off-axis ECH.

For the current ramp and the pellet injection experiments the influence of central ECH was investigated by comparing Ohmic and EC heated discharges. In case of pellet injection the ECH is started after the injection to avoid that the pellet is prematurely vaporized by the supra-thermal electrons created by ECH. The expected effect of central ECH is to increase the current diffusion time (τ_η) because of the reduced resistivity (η).

From the poloidal field pick up coils, $\Lambda = \beta_p + l_i/2 - 1$ is determined, where β_p is the poloidal β and l_i the normalised internal inductance [15]. β_p can also be determined directly from the diamagnetic loop, $\beta_{p,\text{dia}}$, but this measurement suffers from a large error bar.

In the remainder of this section q_{par} is compared to simulations of the resistively driven current diffusion, taking into account both the neo-classical correction and the bootstrap current. These simulations use as input several time-separated T_e profiles from Thomson scattering, starting from an Ohmic equilibrium T_e profile. Thomson scattering profiles of subsequent identical discharges are used, taken in dedicated measuring sessions. T_e is interpolated in time between these profiles.

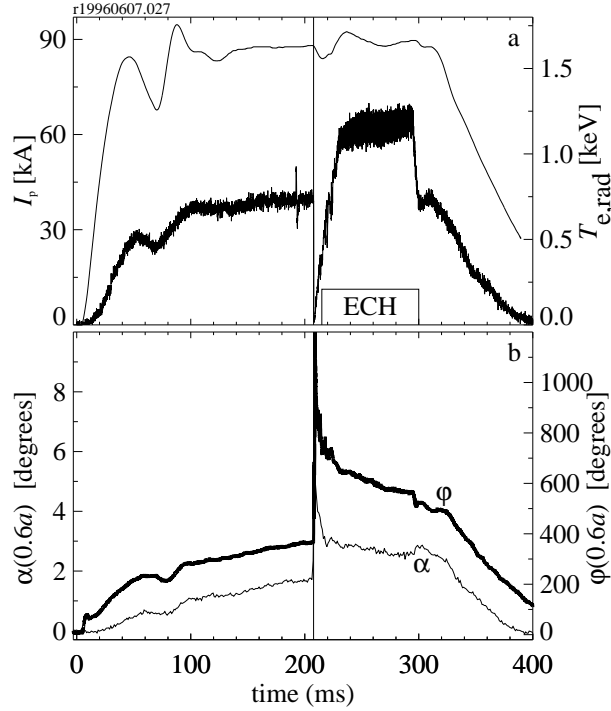


Figure 4.8: a) Time trace of the plasma current (top) and the central radiation temperature from ECE measurements (bottom) with pellet injection at $t = 207$ ms. The block indicates the presence of ECH. $B_T = 2.08$ T.
 b) Typical interferometer signal φ (top) and polarimeter signal α (bottom) at $r/a = 0.61$

4.5.1 Results obtained with pellet injection

In Fig. 4.8 time traces of a polarimeter and an interferometer signal are shown for a discharge in which a pellet is injected at $t = 207$ ms and ECH is switched on at 215 ms. In contrast to Fig. 4.7, in this case the change in the polarimeter signal after the pellet is mainly caused by the increased density due to the ablated pellet. In fact, the relative increase of the interferometer signal is larger than the relative increase of α , indicating that the current inside $r/a = 0.61$ has decreased due to the pellet ablation.

Pellets with two different sizes were injected into the plasma. Small pellets were injected in 120 kA, $B_T = 2.06$ T ($q_a = 3.2$) discharges with $n_e(0) = 4.5 \cdot 10^{19} \text{ m}^{-3}$. The total amount of injected particles ($N \approx 5 \cdot 10^{18}$) approximately equals the total amount of particles present in the plasma. Large pellets ($N \approx 2 \cdot 10^{19}$) were injected

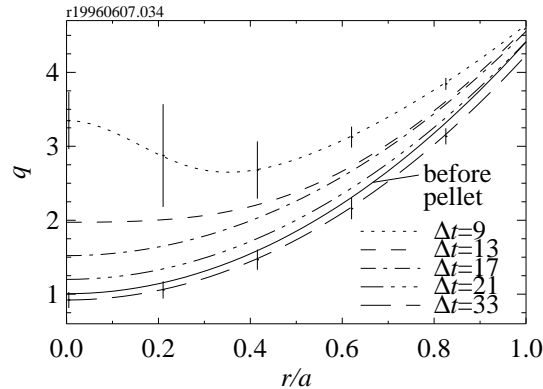


Figure 4.9: Typical q profiles for a discharge ($I_p = 80$ kA, $B_T = 2.06$ T, $q_a = 4.3$) after the injection of a large pellet. Central ECH was started 8 ms after injection of the pellet. Indicated times in milliseconds are with respect to the pellet injection.

in steady state 90 kA, $B_T = 2.06$ T ($q_a = 4.3$) discharges with $n_e(0) = 4.0 \cdot 10^{19} \text{ m}^{-3}$. In some of these discharges, central 110 GHz ECH was applied from 8 to 90 ms after pellet injection.

The small pellets penetrate only 7 cm into the plasma up to $\rho = 0.57$. No effect beyond the error bars was seen on the polarimeter data nor on Λ . l_i goes linearly with 2Λ during the pellet ablation: From TS measurements it is known that during the pellet ablation the electron pressure profile is unchanged [16], so β_p is constant.

The large pellets reach the central region. T_e decreases to 50-100 eV over the whole plasma column just after the ablation and recuperates on a time scale of 10 ms [16]. At these temperatures τ_η is reduced below 1 ms.

Examples of pellet injection followed by ECH are given in Fig. 4.9 and 4.10. In Fig. 4.9, one q profile just before injection is shown for reference. Before injection, the central q value is approximately unity. At $\Delta t = 9$ ms, the first reconstruction available after the pellet injection, the q profile is significantly changed: The central current density (j_0) is decreased by a factor of three. Subsequent profiles show a relaxation to a new steady state, which is reached at $\Delta t = 33$ ms. In this new equilibrium, the current density is more peaked than before injection. The sawtooth behaviour corroborates this development: The pre-pellet sawteeth with small inversion radius (ρ_{inv}) of $\cong 2$ cm vanish at the moment of pellet injection. The sawteeth re-appear after 35 ms and in 3 ms ρ_{inv} rapidly increases to the final value of $\cong 5$ cm.

Fig. 4.10 shows the measured time evolution of q_0 , $q(a/2)$ and q_a for the same discharge. The q_0 trace reaches 1 after ~ 35 ms, in agreement with the re-start of

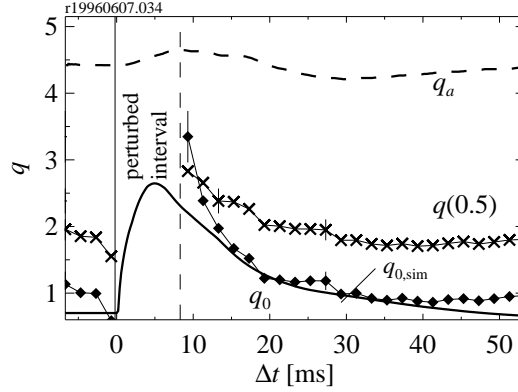


Figure 4.10: Time traces of q_0 (\blacklozenge), q_a (dashes) and q at $\rho = 0.5$ (\times) for the discharge of Fig. 4.9. The thick line results from the current diffusion simulation. In the indicated pellet perturbed interval no reliable phase measurement could be performed.

the sawtooth. Note that q_a is slightly varying in time, because I_p is slightly varying after the pellet. Unfortunately, no reliable n_e data could be obtained in the interval $\Delta t = [0, 8]$ ms due to a strong oscillation making the interferometer signal useless.

For comparison, in Fig. 4.10 the central q value, as calculated with the current diffusion simulation for a series of discharges with $I_p = 80$ kA is shown. Since the simulation does not account for sawteeth effects, the initial and final values of q_0 are well below 1. After 10 ms, the data indicate a much larger perturbation of the central j value by the pellet than the simulation, i.e. the measured $q_0 = 3.3 \pm 0.4$ and the simulated $q_0 \sim 2.4$. It should be noted that in the simulation the strength of the current perturbation is strongly influenced by the exact value of the temperature just after the pellet. At a value of 50 eV a variation of 10 eV means a variation of almost 50 % on τ_η , so a modest over-estimation of T_e during the first ten ms after pellet injection could cause an appreciable underestimation of the maximum q_0 in the simulation. Unfortunately, no reliable T_e measurement just after the pellet is available.

The measured relaxation to the final state is two times faster than simulated. In the simulation curve at least two time constants can be identified: One for the perturbation, which is about 2 ms and one for the relaxation of about 13 ms. From the measured data only the relaxation time constant can be resolved: It is about 6 ms. Partly, this difference can be due to the above-mentioned effect: If T_e just after the pellet is overestimated, τ_η is overestimated as well.

A peculiar result is obtained in case the injected large pellet does not fully ablate during the travel to the plasma centre and the remainder reaches the plasma edge, acting as an enhanced gas puff. In Fig. 4.11 the traces of the H_α emission are

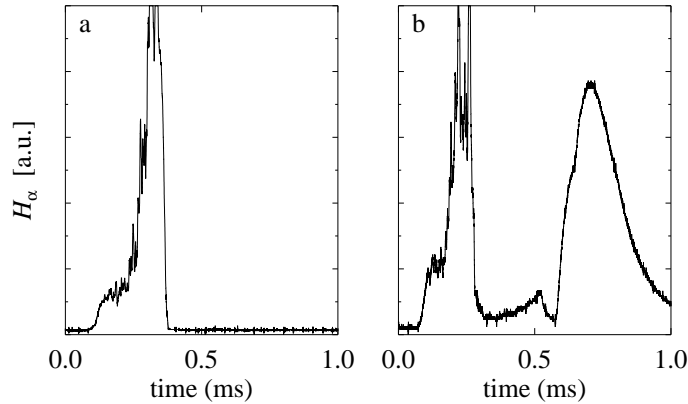


Figure 4.11: H_α radiation obtained a) in the discharge of Fig. 4.8, in which the pellet fully ablates during its travel towards the plasma centre, and b) in a discharge in which only part of the pellet ablates during the crossing of the plasma, cf. Fig. 4.12. Time is taken with respect to the pellet injection. In both cases the first peak corresponds to the ablation during the travel to the centre. After this, the plasma is very cold. This is why the signal in b) is very low during the travel from the centre to the edge, between $t = 0.3$ and 0.55 ms. The second peak in b) arises after the pellet has hit the wall and the remainders re-enter the plasma. Apparently, the signal in a) is negligible during this interval. Note the short time-scales of these figures with respect to the discharge time, cf Fig. 4.8.

shown for a discharge with regular full pellet ablation and one with partial pellet ablation. The difference between these traces is the occurrence of a second peak in the latter of a size comparable to the first peak, which originates from the plasma edge. The edge density strongly increases by the pellet remainder.

In Fig. 4.12 the effects of the partial ablation and the subsequent edge fuelling enhancement on the plasma are shown. The q_0 trace is obtained from the parametrical fit to the polarimeter data. The first obtained value after the pellet injection is high, like in the abovementioned discharge type. However, it decreases even faster than in the previous case, to values below the pre-pellet values. Note that it decreases below 1. The $\beta_p + l_i/2$ signal rises after the pellet injection relative to the β_p signal. This is in agreement with the behaviour of q_0 . The maximum of $\beta_p + l_i/2$ coincides with the minimum of q_0 . The lower part of the figure shows the radiation temperature as obtained from ECE radiometry in the centre and in the outer LFS edge. Both temperatures decrease to a fraction of their pre-pellet values. The edge channel has a sawtooth like mode immediately after the pellet injection. However, this cannot be a usual sawtooth, because the central channel misses the first couple of periods. After a few periods the central channel interferes as well. Due to this mode the plasma temperature rises very slowly. The relaxation of q_0

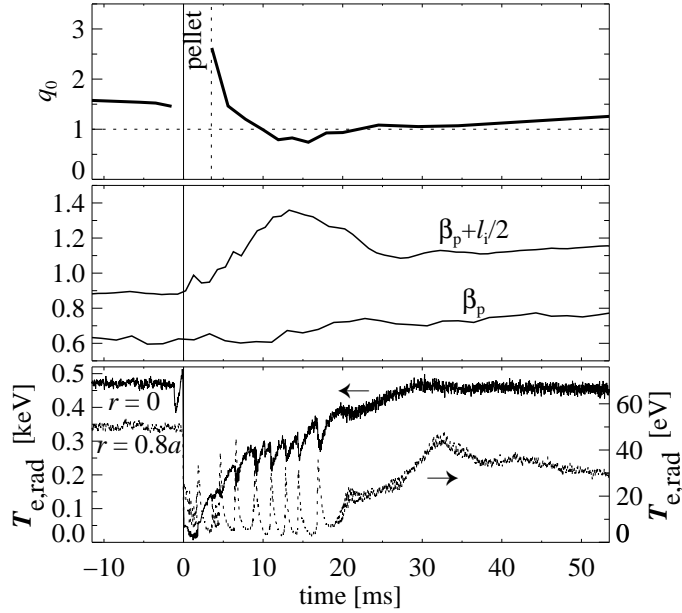


Figure 4.12: Time traces of q_0 (upper figure), $\beta_p + l_i/2$ and β_p (mid figure) and $T_{e,\text{rad}}$ at $r/a = 0$ and 0.8 (lower figure) in a discharge in which the pellet is only partially ablated in the plasma ($I_p = 80$ kA, $B_T = 2$ T). q_0 is obtained from the parametrical fit to the polarimeter data. $\beta_p + l_i/2$ and β_p are measured directly. $T_{e,\text{rad}}$ is obtained from ECE measurements. The vertical lines indicate the moment of pellet injection.

to the pre-pellet state takes much longer than in the previous case.

In Fig. 4.13 the q profiles obtained from the parametrical fit are given. The profile at $t = 201$ ms is before the pellet. It has a relatively high q_0 value of 1.5. This is partly due to the low plasma current. The first profile after pellet injection is obtained at 210 ms and its q_0 value is in good agreement with the current diffusion simulation given in Fig. 4.10. However, q decreases rapidly and reaches its minimum value at $t = 222$ ms, $q_0 = 0.7$, as we observed already in Fig. 4.12.

Apparently, the edge cooling induced by the edge ablation of the pellet has as much impact as the in-plasma ablation. We see that after the pellet, q_0 has increased like in the previous case, but this increase is quickly followed by the decrease of q_0 . The cause for this decrease is twofold: The edge is cooled down and the strong off-axis mode comes into existence, keeping the edge cool, also when the centre heats up again. Note in comparison with the Ohmic phase the T_e profile is more peaked, although the central T_e value is lower. The consequence is that j_0 becomes even higher than in the Ohmic phase. As soon as the mode stops, the temperature rises and the peak temperature reaches its pre-pellet value. It takes

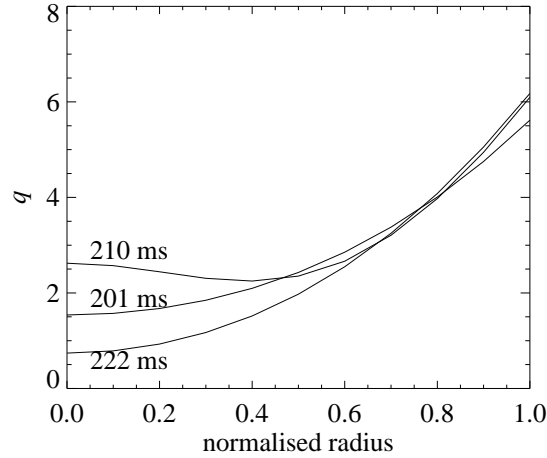


Figure 4.13: q profiles obtained from the polarimeter data, corresponding to the data in Fig. 4.12. One profile has been taken before pellet injection ($t = 201$ ms), the others are taken just after pellet injection ($t = 210$ ms) and when the minimum q_0 is reached ($t = 222$ ms).

much longer before q has relaxed and q_0 remains lower than the pre-pellet value.

The plasma perturbation by a pellet critically depends on the penetration depth and therefore on the pellet size. Thomson scattering measurements on RTP [16] have shown that only pellets which cross the sawtooth ρ_{inv} cool the whole plasma to $T_e \sim 50 - 100$ eV. A pellet not reaching the $q = 1$ surface just influences the edge, where only little current is running, and minor changes to the j profile are expected. This is indeed confirmed by the experiments with injection of small pellets. Large pellets, on the other hand, do cross the $q = 1$ surface. Indeed a strong effect on the q profiles in Fig. 4.9 is observed. Thomson scattering measurements have shown that during the first few ms after pellet injection the T_e profile is essentially flat, and since T_e is sufficiently low to allow a fast redistribution of the current, one would expect also to observe a flat current density and q profile. The parametrisation results presented in this section, however, indicate a slight hollowing of the current density profile shortly after the injection. This might be due to an enhanced bootstrap current induced by the strong n_e gradient after the pellet. The resistively driven current is expected to be flat right after the pellet. Addition of the bootstrap current would make the j profile hollow. It could also be an artifact of the parametrisation chosen in the analysis, which uses only three independent parameters. The edge measurements affect only one of the three parameters, namely $q_{\text{par},0}$. This is compensated in the central region by the other parameters resulting in a bell-shaped modification.

In case of a pellet that ablates only partially inside the plasma and cools the

edge strongly after plasma traversal, a similar q flattening is observed. This is however interrupted by a peculiar peaking of j as a consequence of a mode, that keeps the edge cool. The time-scale of this peaking is comparable to the time-scale of the flattening in this experiment, and faster than the time-scale in case of usual pellet ablation. This is due to the lower temperatures in the latter case.

4.5.2 Results on current ramps down

Current ramps were done by programming the total current to decrease from 120 to 90 kA in 30 ms ($B_T = 2.05$ T, q_a from 3.2 to 4.2). The density $n_e(0) \approx 5 \cdot 10^{19} \text{m}^{-3}$ and varies only slightly during the current ramp. For some of the discharges ECH with central resonance was applied for $\Delta t = [-60, 70]$ ms with respect to the start of the ramp.

In Fig. 4.14a, the ramped current for a discharge with ECH (indicated by the block) is shown. The actual ramp down takes about 40 ms due to an overshoot of several kA. In the same figure the signal of Λ is shown. In Fig. 4.14b the time traces of q_a and $q(\rho = 0.4)$ as determined from the polarimeter are shown. This signal is obtained using a two-parameter fit, with the same form as in Eq. 4.16 but with the width of the Gaussian fixed at 0.3. Unfortunately, the evolution of q_0 could not be resolved from the measurements due to large errors on the central channels.

On both Λ and $\beta_{p,\text{dia}}$ (not shown), two plateaux can be seen, before and after the ramp. During the transient, the increase in Λ is 0.1 larger than the increase in $\beta_{p,\text{dia}}$, indicating increased peaking of the current density. The relative rate of change of the $q(\rho = 0.4)$ is $\simeq 20$ %, i.e. half the relative change of q_a (40%), thus confirming an increased peaking of j during the current ramp down. This is further corroborated by the persisting sawtooth during the current ramp, albeit with a reduction of ρ_{inv} from $\rho = 0.21$ to 0.15 ± 0.015 , according to the soft X-ray signals. Hence q_0 increases slightly but stays below 1; if a parabolic q profile is assumed, the observed decrease of ρ_{inv} corresponds to an increase of q_0 of 10 %. The time evolution of $q(\rho = 0.4)$ follows the evolution of q_a with a time delay of ~ 10 ms, which is a good estimate of τ_η from the edge to $\rho = 0.4$. The measured values of $q(\rho = 0.4)$ before the current ramp are ~ 1 . This is in contradiction with the inversion radii determined from ECE, which are significantly smaller than 0.4. The reason for this is unknown. It is possible that the omission of the central channels and a systematic phase shift as described in section 4.6, yield this effect. Nevertheless, the relative changes can be used.

To determine the effect of ECH, in Fig. 4.15 the same signals as in Fig. 4.14b are plotted, complemented with the signals for a current ramp in a similar, Ohmically heated discharge. The q_a signals show that the ramp down is faster for the Ohmic discharge, and it has a larger overshoot. $q(\rho = 0.4)$ is slightly higher for the Ohmic discharge than for the EC heated discharge, indicating that j is somewhat less peaked in the Ohmic discharge. Although the average resistivity, as determined from the loop voltage in steady state, is $\simeq 60\%$ larger in the ohmic case, the time lag between the evolution of q_a and $q(\rho = 0.4)$ is similar for both cases. The cause for this is the localisation of ECH within the ρ_{inv} . The temperature and hence η

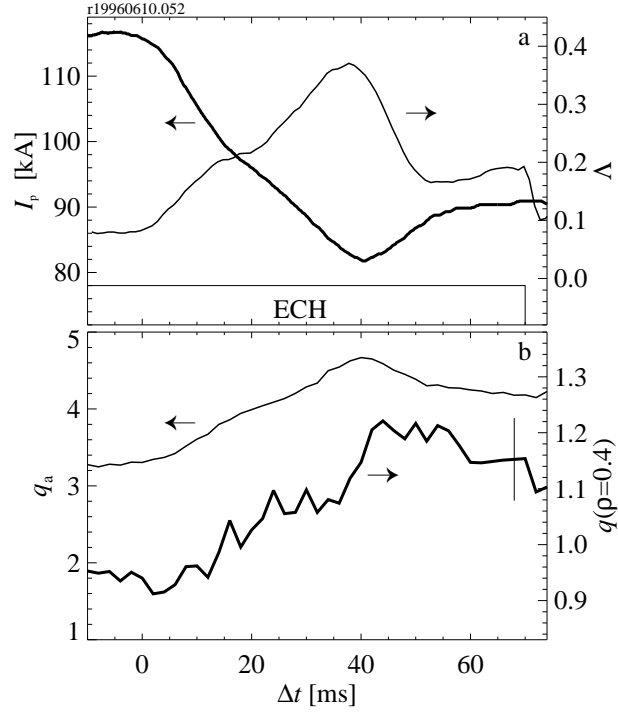


Figure 4.14: a) Time traces of the plasma current (thick) and of $\Lambda = \beta_p + l_i/2 - 1$ (thin) during a current ramp. ECH is applied from $\Delta t = -60$ to 70 ms and is indicated by the block. b) Time traces of the corresponding q_a (thin) and $q(\rho = 0.4)$ (thick). Plasma parameters: $B_T = 2.05$ T, $n_e(0) = 5.0 \cdot 10^{19} \text{ m}^{-3}$.

outside the ρ_{inv} has not changed much, and thus the current diffusion from the edge to $\rho = 0.4$ is unaltered.

4.5.3 Results in discharges with hollow T_e

The current density profile evolution was studied after switch-on of off-axis ECH with a power deposition radius (ρ_{dep}) equal to half radius in a series of discharges with $I_p = 80$ kA, $q_a = 5.5$, $n_e(0) = 5.0 \cdot 10^{19} \text{ m}^{-3}$. In such discharges a hollow T_e profile develops [17,18] (see Fig. 4.16) with local maxima at the deposition radius.

In Fig. 4.17 several reconstructed q profiles are shown for such a discharge, demonstrating the development of a low or negative shear region as a result of the change in T_e and hence η profile. In Fig. 4.18 the development of the central radi-

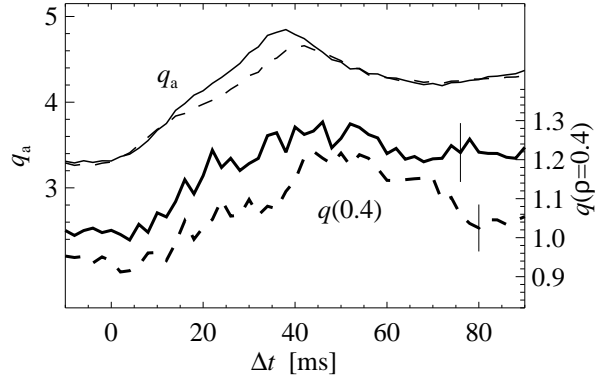


Figure 4.15: Comparison of the q_a and $q(\rho = 0.4)$ time traces with (dashes) and without (line) ECH applied during the current ramp.

ation temperature ($T_{e,\text{rad}}(0)$) is shown as well as $q_{\text{par},0}$ and q_0 from the simulation. The evolution of q_0 is lagging behind the evolution of $T_{e,\text{rad}}(0)$ by about 20 ms ($\sim \tau_\eta$) and reaches a new steady state after 45 ms. The rates of change of $q_{\text{par},0}$ and the simulated q_0 are comparable. The ultimate steady state profile agrees well with the simulation on the basis of neo-classical theory, as shown in Fig. 4.17. Both the values and the positions of q_0 and the minimum of q (q_{min}) are equal within error bars.

4.6 Accuracy Analysis

At the end of section 4.4 it is argued that the scatter on the measured α profile is too large to perform Abel inversion successfully. The scatter is at variance with the expectation that the line integration involved in the measurements results in smooth profiles. For particular discharges the scatter can be so large that it causes the minimisation procedure to fail. In this section the attention is focused on the systematic phase deviations contributing to the scatter.

Before proceeding a remark should be made concerning the possibilities to measure phase deviations. If one wants to trace disturbances of the phase of the beams which could possibly show up in the measured signals, one needs a phase-sensitive detector and a reference phase. For measurement at an arbitrary position in the set-up, this means the construction of a complete polarimeter set-up at that position. The disturbances can in principle be measured by moving the beam or the detector. Unfortunately, the phase-sensitive Schottky diodes are not stable enough to measure reproducibly while moved around or when the alignment of the entering beam is changed. This excludes them for this kind of experiments. Pyro-electric detectors are very stable, but not phase-sensitive. Both detectors are not suitable to perform the mentioned experiment. Only intensity profile measurements can be

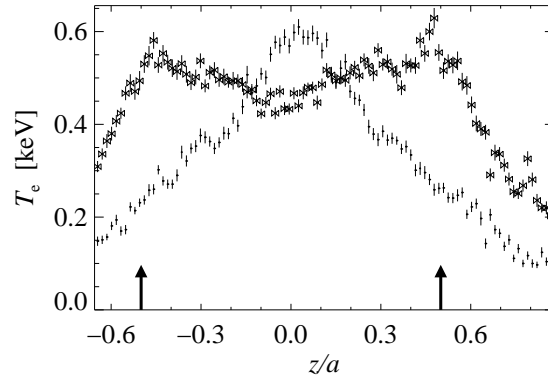


Figure 4.16: Typical T_e profiles from Thomson scattering just before off-axis ECH is started (\bullet) and 70 ms ($\tau_E \approx 3$ ms) after switch-on of the off-axis ECH (\otimes) for discharges with $I_p = 80$ kA, $B_T = 2.24$ T ($q_a = 5.5$), $n_e(0) = 4.0 \cdot 10^{19} \text{ m}^{-3}$. The arrows indicate the ECH deposition radius.

performed, with the pyro-electric detectors. These can be done at almost every location in the set-up though. For phase measurements we are limited to the set-up as used during plasma operation (see Fig. 4.4).

The systematic deviations can be diagnosed using the following considerations. Given the line-integrated nature of the measurements, no strong fluctuations within the α profile can occur. Off-central channels cannot give zero or negative signals in the presence of plasma. The signals must also be roughly proportional to both the plasma current and the density and changes must be correlated.

The systematic deviations will be illustrated with the help of some figures. In Figs. 4.19 and 4.20 α data of a discharge with pellet injection, prematurely ended by a disruption, is shown. The profiles are taken at 196 ms in the steady state Ohmic phase of the discharge and at 220 ms after the pellet has been launched. The main difference between the profiles is due to the density increase after the pellet. Three remarkable deviations appear. First, the outermost channels of the Ohmic profile give zero signal although they both measure > 2 cm inside the plasma boundaries. Secondly, the $r/a = -0.67$ is unchanged by the pellet, while n_e is strongly increased. Thirdly, the channel at $r/a = 0.49$ strongly deviates towards negative α in both profiles.

The time traces in Fig. 4.20 correspond to the channels that deviate strongest from a smooth profile in Fig. 4.19. The second channel behaves more or less as expected: The pellet ablation gives a peak and the pellet induced density increase is clearly visible in the signal. After the disruption the signal falls off to zero fast. The other traces illustrate the systematic errors. The fourth signal does not come up until the pellet is injected. At pellet injection the fourth signal has only a small peak, the third signal initially shows a decrease instead of an increase. They both cross zero at the disruption. The first signal is very large relative to its neighbouring

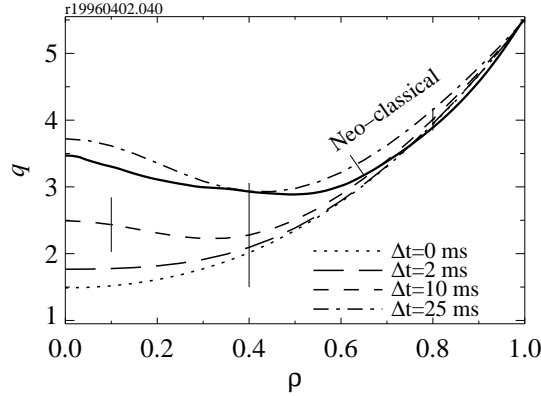


Figure 4.17: q profiles during a discharge with off-axis ECH switched on at $\Delta t = 0$ ms. After $\Delta t = 25$ ms the fully relaxed state is reached. Times are indicated with respect to switch-on of the ECH. The full line is the final equilibrium from the current diffusion simulation. $I_p = 80$ kA, $B_T = 2.24$ T.

channels during the Ohmic phase, cf. Fig. 4.19, and its signal in the post-pellet phase equals the pre-pellet signal.

In Fig. 4.21 the difference between the measured averaged profiles and the fits with Eq. 4.16 are shown for three discharges with I_p values of 140, 100 and 56 kA under further similar plasma circumstances. The maximum $|\alpha|$ values are 5.3° , 3.2° and 2.0° , respectively. Again, the deviations in the profiles are in disagreement with the line-integrated nature of the measurements. The maximum deviation is 0.3° for all three residuals as can be seen from the figure. The residuals seem independent of α . Furthermore, the fluctuations follow the same trend, regardless of the difference in α . These discharges are all taken on the same day.

The α data are determined with respect to the zero-plasma state, so the observed deviations are either related to the presence of the plasma or caused by time-varying perturbations. However, in the last case, it is unlikely that the perturbation is cancelled at the end of the discharge, like observed. This kind of perturbation should be visible as well in zero-plasma conditions. This is not the case. The deviations are thus plasma-related.

It must be noted that the deviations are seen on the mixing signal of the two probing beams. Since these beams follow exactly the same beam path, they are perturbed in exactly the same way by imperfections in the set-up and by vibrations. To verify this, a test experiment was performed in which the set-up was artificially disturbed by vibrations. Indeed, while the interferometer experienced phase changes of several fringes, the polarimeter signal remained perfectly constant. Most candidate phase disturbances have equal effect on both probing beams and

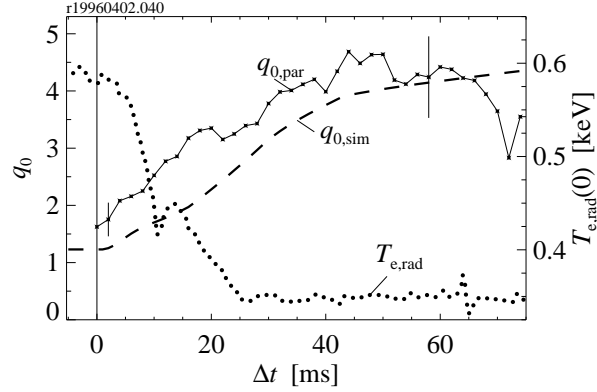


Figure 4.18: Time trace of q_0 (\times) with off-axis ECH switched on at $\Delta t = 0$ ms and $T_{e,rad}(0)$ from ECE (dotted) for the discharge of Fig. 4.17. The dashed line results from the current diffusion simulation. $I_p = 80$ kA, $B_T = 2.24$ T.

their contributions cancel in first order.

The figures 4.19 and 4.20 show that the deviations are n_e related. The presence of plasma seems to shift the zero level. The zero level after the discharges equals the starting level again. In three cases with strongly different I_p and similar n_e , the deviations are more or less fixed and independent of α , so we can conclude that the current is not involved.

To study the above effects in more detail the set of parabolic mirrors below the vessel is replaced by a single flat mirror. In this case, the probing beam is no longer expanded in radial direction, but it is more or less circular. Since the size of the beam is now only a few cm in diameter only three detectors get full signal. The purpose of this replacement is purely diagnostic, the obtained data are useless for interpretation in terms of j . The plasma is operated routinely and a density ramp up is applied around 200 ms. In Fig. 4.22 the resulting polarimeter signals are shown as well as I_p and an interferometer signal, while the small circular probing beam is located around $\rho = 0.4$. The polarimeter signals have oscillations on the phase during the density ramp up and during the density ramp down at the end of the plasma too.

Each full period of the oscillation on α corresponds exactly to a change of $\Delta\varphi$ of π radian. These oscillations and those at the start-up and end of the plasma are probably caused by interference loops, which are discussed in detail in subsection 4.6.1. In case of interference loops, the measurement is disturbed by beam power that crossed the plasma multiple times. The disturbance is phase-dependent and is periodic in a fringe of the interferometer signal divided by the number of times it traversed the plasma. The top-down amplitude of the oscillations is $\lesssim 1^\circ$,

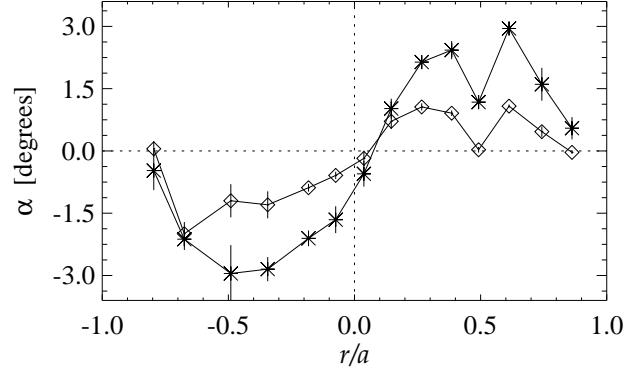


Figure 4.19: α profiles measured during the steady Ohmic state (\diamond), and after pellet injection (stars), averaged over 10 ms. The outermost channels give zero signal in the Ohmic profile, although they are located in the plasma. Note also the channels at $r/a = -0.67$, remaining unchanged, and $r/a = 0.49$, having a negative peak.

which is a significant fraction of the measured α .

This is not the only disturbance present in the signals: While $\alpha(\rho = 0.38)$ and $\alpha(\rho = 0.26)$ signals experience increases of $\sim 2^\circ$, the $\alpha(\rho = 0.50)$ signal hardly changes. Apart from the oscillations the phase experiences a phase disturbance exceeding the oscillation amplitude, $\sim 2^\circ$. A candidate explanation for this disturbance is diffraction, which causes the phase front of the beam non-flat. Diffraction can lead to erroneous measurements if the beam position on the detection array is non-constant, *e.g.* due to refraction effects.

First, the interference loops will be explained, and then the combined diffraction-refraction effect in subsection 4.6.2.

4.6.1 Interference loops

An interference loop exists when power arrives at the detector, that has been reflected back and forth in the set-up, disturbing the single pass beam. It is called a loop because the power from the reference beam can enter the probing beam and vice versa. The disturbance is like from a standing wave. Several loops are possible but the attention is focused to loops that include the plasma here, because the phase modulation is plasma dependent. Further, the loops involving the local oscillator can be neglected, because this is not contributing to the α measurement. Under this restrictions, the power is possibly reflected at the detectors, travels through the set-up backwards, is reflected at any surface perpendicular to the propagation direction, *e.g.* the quarter wave plate or the laser output coupler, and travels to the detector again, interfering with the original beam. Interference loops have never been observed in the $\Delta\varphi$ measurement, obviously because they are negligible in this case.

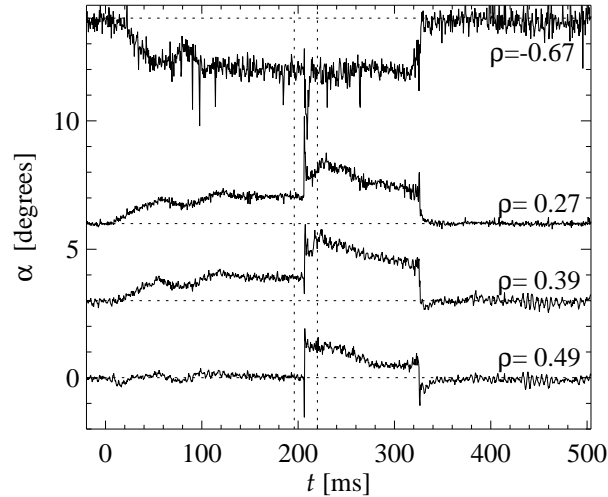


Figure 4.20: Some detector traces for the discharge of Fig. 4.19. The pellet is injected at $t = 0.207$ s. A disruption occurs at $t = 0.327$ s. The traces are offset artificially. The vertical lines indicate the time points where the profiles of Fig. 4.19 have been taken.

Since all three laser frequencies are present at the detector, the loop signal can be considered as a disturbance of the primary signal of the same frequency only, without loss of generality. The power of the loop signal is much lower than the probing beam power and its phase is different due to the additional path length and plasma phase shift. The loop signal slightly modifies the power and the phase of the probing beam. The observed loop changes twice as fast as the interferometer phase, indicating that the loop passes the plasma two additional times with respect to the primary beam.

The observed phase modulations by the interference loops are a second-order effect, because the two beams constituting the probing beam are co-aligned through the whole set-up and will suffer from interference loops simultaneously. In the mixing frequency the two respective interference loop phase modulations cancel in first order. The remaining effect is caused by misalignment of the probing beams and variations in reflected power.

The period of the interference loops is not dependent on the size of the probing beam. Nevertheless, in the expanded beam set-up similar effects have never been observed. The fact that the interference loops are so clearly visible in case of the non-expanded beam set-up, is probably due to the higher signal level in this beam and the easier alignment of this set-up.

The easiest way to prevent interference loops is by slight misalignment of all optical elements at which reflections can occur. All elements with a flat surface, like waveplates and some lenses are tilted slightly with respect to perpendicular to the beam path to exclude the interference of reflections. Misalignment of the

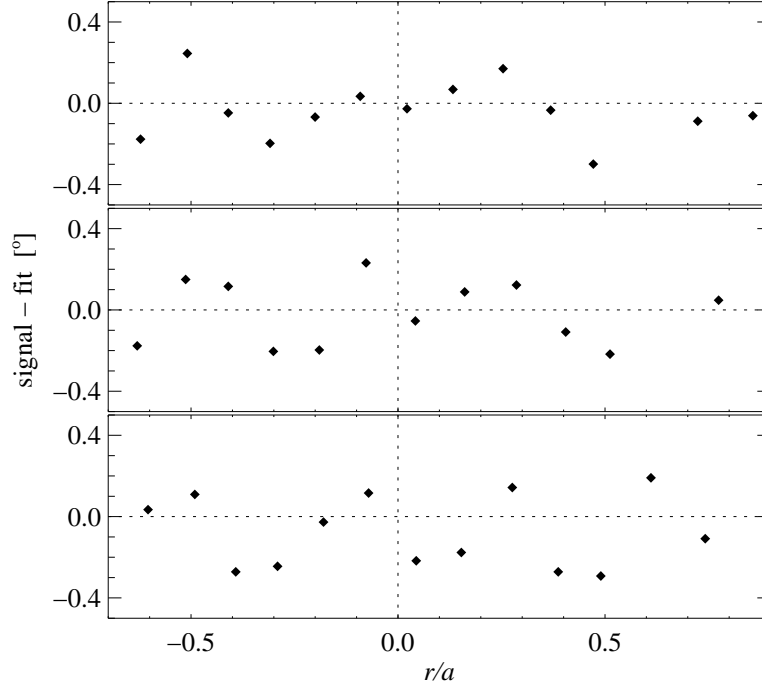


Figure 4.21: Residuals of the fit of Eq. 4.16 to data of Ohmic discharges with I_p is 140, 100 and 56 kA, respectively. $B_T \sim 2.33$ T, $\bar{n}_e \sim 4.4 \cdot 10^{19} \text{ m}^{-3}$.

laser output couplers is however not advantageous, because of the associated deterioration of the output power. Similarly, misalignment of the detectors reduces the signal amplitude, thus decreasing the signal-to-noise ratio. Further, reflections in the vessel and the flanges cannot be prevented.

In principle it is possible to filter the reflection from a single reflecting surface, because such a surface has the property to revert the polarisation direction of the wave during the reflection. With the combination of a polariser and a quarter waveplate at an angle of 45° , the reflection can be filtered. Unfortunately, if the two probing beams are combined, which is the case for the major part of the set-up, the insertion of a polariser will destroy their prepared mutual polarisation difference. Further, the power loss associated with this solution is at least a factor $\sqrt{2}$, neglecting the transmission losses in the polariser and the waveplate.

4.6.2 Diffraction

The interference loops are not the only disturbance in Fig. 4.22. The interference loop is periodic in nature, so in one period there are two situations where the net effect on the phase is negligible. This is exactly between each top and bottom of

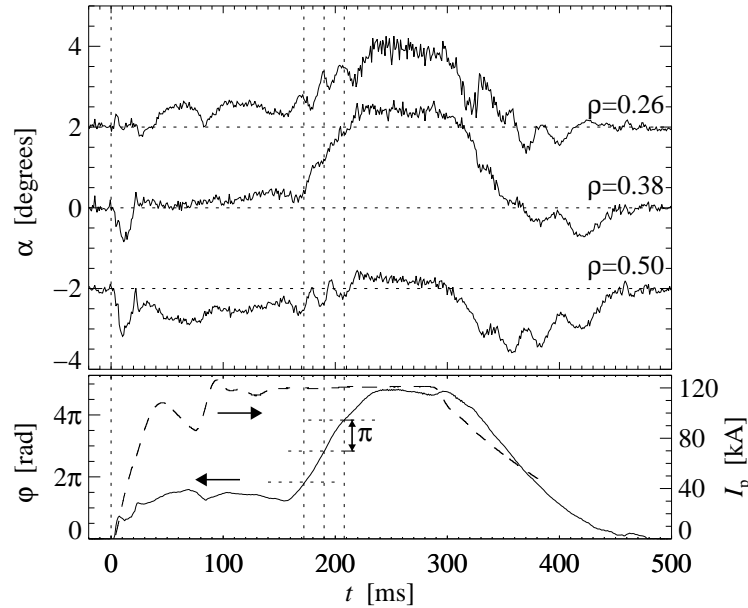


Figure 4.22: Time traces of the polarimeter in the upper part and the interferometer signal at $\rho = 0.26$ (full curve) and I_p (dashed curve) in the lower part of the figure in case of a non-expanded, circular probing beam. The polarimeter traces are artificially offset. The vertical dotted lines indicate the peaks of the oscillations in the upper polarimeter signal. The vertical dotted lines in the lower part of the figure are 180° apart.

the modulations. From Fig. 4.22 it is clear that in these situations the phase is still seriously disturbed. This disturbance seems to be larger than the top-bottom amplitude of the interference loop. The signal at $\rho = 0.38$ remains close to zero before the density ramp up, the signal at $\rho = 0.50$ remains negative for almost the entire discharge. The deviations from expected values in these cases are up to 2° degrees.

This effect could be caused by diffraction in combination with plasma refraction. As pointed out before the refraction moves the beam over the detectors. As long as the phase front of the beam is straight this induces no systematic error, but any irregularity in the phase front disturbs the measurement as soon as refraction moves it over a detector. This mechanism is in agreement with Fig. 4.22. All three polarimeter signals react strangely to the start-up of the plasma where the density and thus the refraction rapidly rise. Two signals have a very strong negative peak, the third does not react at all. Traces of this behaviour can be seen at the end of the discharge, stretched in time. In the density ramp-up the reactions are ambiguous. The signal at $\rho = 0.38$ rises strongly, whereas the signal at $\rho = 0.50$ hardly changes.

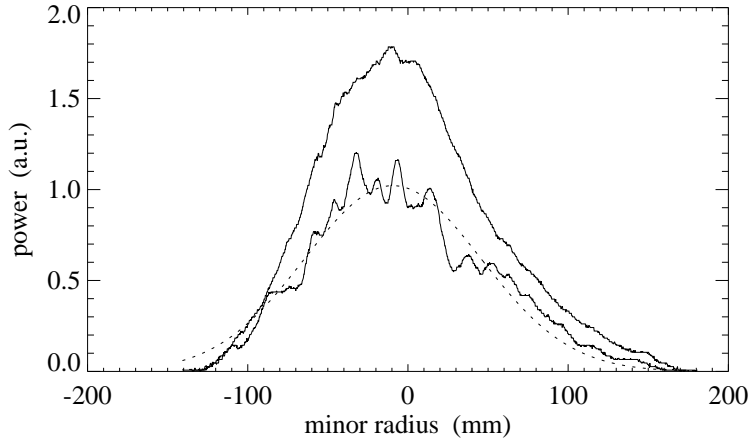


Figure 4.23: Beam intensity profiles measured 60 cm after the exit port. The top curve is without window, the bottom curve is with window. The dashed curve is a Gaussian shaped profile, drawn for comparison. The intensity difference between the curves is artificial.

The effects in Fig. 4.22 are similar to the effects observed on the signals in the expanded beam set-up, see Fig. 4.20. Hence, the disturbance is not caused by the smaller beam size, although it seems to be more pronounced in the small-beam set-up. A possible cause for this is the stronger divergence of the smaller beam¹. Also, structures on the phase profile obtained before the plasma are smaller on the non-expanded beam.

Where can the beam be diffracted? Tests have shown that the vessel ports do not disturb the beam significantly, although strictly spoken their diameter is too small compared to the beam diameter. Tests do show that the beam power profile is seriously disturbed by inhomogeneities in the windows. In Fig. 4.23 the obtained power profiles are shown with and without windows 60 cm behind the exit port. It is clear that the phase front must suffer from the structures on the power profile.

The windows are made of HDPE. This material is not very stiff. During preparation for tokamak operation, the window shrunk 1 cm in the length direction, compared to a length of 45 cm. During tokamak operation the windows suffer from the vacuum stresses. Further, the plasma itself has of course its influence on the material, although the distance to the plasma is more than 0.3 m. The inhomogeneities in the window are understandable from these considerations.

The value of the diffraction hypothesis is disputable. First, like in the case of the interference loops, the effect is cancelled in first order because both probing beams are co-aligned and experience similar diffraction and refraction. The phase front disturbance must then be $\gtrsim 20^\circ$. Regarding the structures in Fig. 4.23, this

¹The divergence of the beam is not at all negligible in this wavelength range, as ray tracing codes show.

might be the case. More importantly, one should realise that the inhomogeneities are immobile, so this means that the errors should be reproducible. On the term of days this is definitely the case as can be seen in Fig. 4.21, where all three residuals have more or less the same structure, while the corresponding density profiles are not perfectly identical. However, comparing these residuals with Fig. 4.19, the agreement is only marginal. (It must be noted here that the n_e values differ.) It is highly improbable that the inhomogeneities change on short notice, regarding the extended time they have been subject to plasma operation. The plasma parameters and the vacuum conditions most certainly do vary between the respective plasmas. It has not been possible to construct a reliable error correction, assuming fixed inhomogeneities.

To avoid any inhomogeneities in the window another material should be chosen. Only few materials have a significant transmission of FIR radiation. Polymethylpentene (PMP, registered as a trademark named TPX) has a transmission of 10%/cm. Such a transmission would seriously compromise the signal-to-noise ratio of the polarimeter. Furthermore, PMP is a plastic, like HDPE, and is likely to be as sensitive to plasma influence as HDPE is. Quartz has a reasonable transmission, though not as good as polyethylene. Unfortunately, it is very expensive, and together with the fact, that it is not clear if the window is the real error source, the result of this investment is too insecure.

Though refracted diffraction effects and interference loops could play a role in the systematic deviation of the α measurements, there might still be another, unknown effect intervening. It is clear from this section that it is very hard to identify the systematic effects, though correction for them is crucial to obtain more valuable information from the data.

4.7 Discussion and conclusion

Measurements of the Faraday rotation polarimeter in RTP have been presented. The measurements have been done in pellet-disturbed plasmas and during the transitions to a lower I_p and to hollow T_e profiles. The measurements have been analysed using a fit of a two or three parameter q profile.

The effect of pellet injection critically depends on the pellet size. After injection of a large pellet, which reaches the centre of the plasma and causes a strong cooling of the whole plasma column, a very flat j profile is observed, which then peaks again on a time scale of $\simeq 6$ ms. The observed flattening is stronger, and the subsequent peaking is faster than expected from simulations. This, however, might be caused by a modest overestimate of T_e in the first few ms after pellet injection in the simulation. A small pellet, which does not cross ρ_{inv} , does not influence the j profile outside error bars.

Strong flattening, and even shear reversal, after pellet injection into the centre of the plasma has been observed in many machines, e.g. [19,20]. However, the transient confinement improvement, the so-called PEP mode, reported in those machines, has not been observed in RTP. In pellet experiments in TEXTOR [21]

the pellets do not reach ρ_{inv} and q_0 remains well below one even after subsequent injection of 5 pellets.

In plasmas with a current ramp down, the measured current profile peaking factor increases, whereas j_0 remains almost constant as can be concluded from the sawtooth behaviour. The polarimeter measurements indicate that the current decreases in the region outside ρ_{inv} . This is in agreement with similar experiments in JT-60U [22]. The estimated τ_η of 10 ms matches the expected Ohmic τ_η within the error bars. EC heated discharges have slightly lower values of q at $\rho = 0.4$ than Ohmic discharges, both before and during the current ramp. No difference in time scale nor rate of change could be observed between Ohmic and EC heated discharges, although the average resistivity as obtained from the loop voltage is 35% lower in the ECH case. The relaxation in the centre could not be resolved.

In the last series of experiments off-axis ECH was applied with $\rho_{\text{dep}} = 0.5$, causing hollow T_e and j profiles. The T_e and j profiles reach their new steady state 25 and 45 ms after switch-on of ECH, respectively. The measured final q profile has $q_0 \simeq 4$ and $q_{\text{min}} \simeq 3$. The measured evolution of q agrees well with the simulated evolution.

Off-axis ECH was also applied in FTU [23]. In FTU hollow T_e profiles could be obtained only transiently. The main difference between FTU and RTP is the ratio P_{ECH}/P_Ω , which is $\gg 1$ in RTP and $\simeq 1$ in FTU. Apparently, dominant ECH is needed to achieve steady state hollow T_e and j profiles.

The presented results of the three experiments are in agreement with the current density distribution as expected from neo-classical theory within error bars. Therefore, the use of current diffusion simulation for the evaluation of the current density in RTP is valid.

References

- [1] I. H. Hutchinson, *Principles of Plasma Diagnostics* (Cambridge University Press, Cambridge, UK, 1987), ISBN 0-521-32622-2.
- [2] J. H. Rommers and J. Howard, *Plasma Phys. Control. Fusion* **38**, 1805 (1996).
- [3] H. Soltwisch, *Rev. Sci. Instrum.* **57**, 1939 (1986).
- [4] W. Kunz and G. Dodel, *Infrared Phys.* **18**, 769 (1978).
- [5] B. W. Rice, *Rev. Sci. Instrum.* **63**, 5002 (1992).
- [6] J. H. Rommers, Ph.D. thesis, Universiteit Utrecht, the Netherlands, 1996.
- [7] H. K. Park, C. W. Domier, W. R. Geck, and N. C. Luhmann Jr, *Rev. Sci. Instrum.* **70**, 710 (1999).
- [8] H. K. Park, S. Edwards, L. Guttadora, *et al.*, Status of Far Infrared Tangential Interferometry/Polarimetry (FIRETIP) on NSTX, PPPL, 2000, 3485, Princeton, NJ, USA.
- [9] A. C. A. P. van Lammeren, S. K. Kim, and A. J. H. Donné, *Rev. Sci. Instrum.* **61**, 2882 (1990).
- [10] N. Gottardi, *J. Appl. Phys.* **50**, 2647 (1979).
- [11] Y. Yasutomo *et al.*, in *IEEE Trans. Plasma Sc.* (Institute of Electrical and Electronics Engineers, Inc, Piscataway, N. J., US, 1981), Vol. 9, p. 18.

-
- [12] H. K. Park, *Plasma Phys. Control. Fusion* **31**, 2035 (1989).
 - [13] B. B. Kadomtsev, *Phil. Trans. R. Soc. Lond.* **A322**, 125 (1987).
 - [14] F. C. Schüller *et al.*, in *Proc. 18th EPS Conf. Control. Fusion Plasma Phys.*, (EPS, Vienna, 1991), Vol. 4, p. 185.
 - [15] J. A. Wesson, *Tokamaks*, 2nd ed. (Clarendon press, Oxford, UK, 1997).
 - [16] D. F. da Cruz *et al.*, *Phys. Rev. Lett.* **75**, 3685 (1995).
 - [17] G. M. D. Hogeweyj *et al.*, *Phys. Rev. Lett.* **76**, 632 (1996).
 - [18] N. J. Lopes Cardozo *et al.*, *Plasma Phys. Control. Fusion* **39**, B303 (1997).
 - [19] M. Hugon *et al.*, *Nuc. Fus.* **32**, 33 (1992).
 - [20] D. T. Garnier, in *Proc. Plasma Phys. Control. Fusion Res.* (IAEA, Vienna, Austria, 1997), p. 907.
 - [21] K. H. Finken *et al.*, *Plasma Phys. Control. Fusion* **39**, A351 (1997).
 - [22] T. Fujita *et al.*, *Fus. Eng. Design* **34-35**, 143 (1997).
 - [23] S. Cirant *et al.*, in *Proc. 25th Conf. Control. Fusion Plasma Phys., Prague, Czech* (The European Physical Society, Geneva, Switzerland, 1998), p. 850.

5

TANGENTIAL THOMSON SCATTERING

5.1 Preface

In this chapter the set-up and experimental results of the tangential Thomson scattering (TS) system at RTP are discussed. The tangential set-up of the TS provides a mean to measure the local electron drift velocity, which represents the major fraction of the current density. The experimental set-up and the results of this diagnostic have been reported in a paper: sections 5.2 and further contain this article. The first section contains a more general introduction to Thomson scattering. First, the general strengths and weaknesses of the method are given and several examples of application of TS are discussed. The basic principle is explained and the basics of the derivation of the scattered spectrum is given.

In sections 5.2 and further the specific set-up for TS at RTP is discussed. The data acquisition and analysis is presented and it is shown that accurate calibration and correction for background and plasma light signal is crucial to perform the fragile measurement of the drift velocity. Measurements are performed in discharges with and without Electron Cyclotron Heating (ECH) The results are presented in section 5.5.

The main strength of Thomson scattering is the possibility to determine the electron temperature (T_e) and the electron density (n_e) locally and with high spatial resolution as independent measurements. The disadvantage is that the Thomson scattering cross-section is very small. Therefore TS became only available as a diagnostic after the invention of the ruby laser in 1964, which gives high power pulses. Unfortunately, the repetition rate of this laser is low.

The process of TS is the scattering of photons at free electrons. The occurrence of free electrons in appreciable quantities is limited to plasmas. Hence, the

application of TS as a diagnostic is limited to plasmas. The technique has become well-established in high and low temperature plasma physics and is routinely available in most nowadays tokamaks.

5.1.1 Theory

The electromagnetic field of radiation interacts with charges. Suppose we have radiation of wavelength λ_0 incident on a cloud of free charge carriers. If the energy of the incident radiation is comparable or larger than the rest mass of the charged particles, then the interaction is dominated by the momentum transfer. This is called Compton scattering. Let us assume this is not the case: The momentum transfer is negligible. This is called Thomson scattering. The way the charged particles react to the photon is dependent on how strong the interaction with their neighbour particles is. The charged particles form spheres in which they shield all fields for each other. The radius of these so-called Debye spheres depends on the density. If λ_0 is comparable or larger than the shielding length, which is called Debye length, than the wave interacts with a collection of particles. This is called coherent or collective Thomson scattering. If λ_0 is much smaller than the Debye length, the particles interact as if they were isolated from their environment. This last case is called incoherent Thomson scattering. If we speak about Thomson Scattering in this thesis, we mean incoherent Thomson scattering on free electrons, unless stated otherwise.

With 'scattering' the process of absorption and re-radiation of the photon by the electron is meant. In this process the photon is Doppler shifted by the electron velocity. The scattered radiation thus contains information on the temperature of the electron population. The intensity of the scattered radiation is proportional to the electron density. If the velocity of the electron is much smaller than the speed of light and their distribution is Maxwellian, the spectrum is Gaussian. Unfortunately, relativistic effects have to be taken into account in tokamaks. If the electrons have an average velocity not parallel to the incident wave, the Doppler shifts as a consequence of this drift would give a deformed spectrum. An average drift of the electrons is a current. Since the drift velocity in tokamak plasmas is much lower than the thermal velocity of the electrons, the only effect of the drift velocity is to shift the spectrum as a whole.

Let us assume that the electron velocity distribution is isotropic. Although the movement of the electrons in a magnetic field is non-isotropic, it is shown that this assumption holds for incoherent TS [2,3]. Here, the derivation of Mattioli [1] is followed to obtain an analytical expression for the scattered spectrum for T_e below 25 keV in a scattering geometry as given by Fig. 5.1.

In the derivation the reaction of a single electron to an incident electromagnetic wave is calculated. In this reaction part of the energy is emitted as an electromagnetic field again (the scattered wave). Mattioli first calculates the spatial and spectral distribution of the scattered power by the single electron.

For the application to high temperatures, the expression must be corrected for the fact that the electrons move through the laser volume in a time much

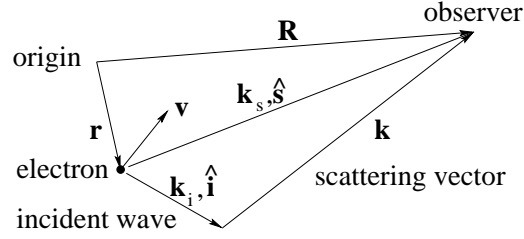


Figure 5.1: Geometry used in the derivation of the Thomson scattering spectrum according to Mattioli [1].

shorter than the 15 ns laser pulse. This correction is called the 'finite transit time' correction.

The expression for the scattering cross-section of a single electron can now be integrated for a relativistic Maxwellian electron distribution function. The merit of Mattioli's method is that the cross-section is split into two parts one of which can be integrated analytically. The other part can be shown to be negligible for electron temperatures below 25 keV.

Start of the calculation is the electric field \mathbf{E}_s at a fixed (observer) position \mathbf{R} and time t , scattered (subscript s) by an electron at position \mathbf{r} and time t' , accelerated by an electromagnetic wave. The used geometry is illustrated in Fig. 5.1. \mathbf{E}_s is given by the Lienard-Wichert potentials in the far-field region:

$$\mathbf{E}_s(\mathbf{R}, t) = \frac{e}{cR} \left[\frac{\hat{\mathbf{s}} \times \left((\hat{\mathbf{s}} - \boldsymbol{\beta}) \times \dot{\boldsymbol{\beta}} \right)}{(1 - \hat{\mathbf{s}} \cdot \boldsymbol{\beta})^3} \right]_{t'=t - \frac{|\mathbf{R}-\mathbf{r}(t')|}{c}}, \quad (5.1)$$

where $\hat{\mathbf{s}}$ is the unit vector in the scattering direction, $\boldsymbol{\beta} = \mathbf{v}/c$ (\mathbf{v} being the electron velocity and c the speed of light). The label indicates that the expression between brackets has to be evaluated at the time t' .

The electric field of the incident (i) wave is:

$$\mathbf{E}_i(\mathbf{r}, t') = \frac{\mathbf{E}_{0,i}}{2} \exp [j(\mathbf{k}_i \cdot \mathbf{r} - \omega_i t')] , \quad (5.2)$$

where j is the imaginary number. The acceleration $\dot{\boldsymbol{\beta}}$ of the electron can be expressed in this field and used in Eq. 5.1. It is assumed that the induced velocity is lower than the thermal velocity of the electron, so that its trajectory can be described by straight line.

The scattered power (P_{sv}) at position \mathbf{R} is expressed as a function of frequency, expanding it into a Fourier series. The final result for a solid angle $\Delta\Omega$ is:

$$P_{sv}(\omega_s) = \frac{c\epsilon_0 r_0^2 \Delta\Omega}{2\gamma^2} \frac{\left[\hat{\mathbf{s}} \times \left\{ (\hat{\mathbf{s}} - \boldsymbol{\beta}) \times \left(\mathbf{E}_{0,i} + \boldsymbol{\beta} \times (\hat{\mathbf{i}} \times \mathbf{E}_{0,i}) - \boldsymbol{\beta}(\boldsymbol{\beta} \cdot \mathbf{E}_{0,i}) \right) \right\} \right]^2}{[1 - \hat{\mathbf{s}} \cdot \boldsymbol{\beta}]^5} \cdot \delta(\omega_s - \omega_i + c(\mathbf{k}_i - \mathbf{k}_s) \cdot \boldsymbol{\beta}) \quad (5.3)$$

with δ the delta function, $\hat{\mathbf{i}}$ the unity vector along the incident direction and

$$r_0 = \frac{e^2}{4\pi\epsilon_0 m_e c^2} \quad (5.4)$$

the classical electron radius (m_e being the electron mass) and $\gamma = (1 - \beta^2)^{-1/2}$ the relativistic factor.

This rather complex expression can be simplified if the incident wave is polarised perpendicular to the scattering plane:

$$P_{sv}(\omega_s) = \frac{c\epsilon_0 r_0^2 \Delta\Omega}{2\gamma^2} \mathbf{E}_{0,i}^2 \frac{(1 - \beta_i)^2}{(1 - \beta_s)^3} \left[1 - \frac{\beta_E^2 (1 - \cos\vartheta)}{(1 - \beta_i)(1 - \beta_s)} \right]^2 \delta(\omega_s - \omega_i + c(\mathbf{k}_i - \mathbf{k}_s) \cdot \boldsymbol{\beta}) \quad (5.5)$$

with ϑ the angle between $\hat{\mathbf{i}}$ and $\hat{\mathbf{s}}$, also called the scattering angle, and $\beta_i = \boldsymbol{\beta} \cdot \hat{\mathbf{i}}$, $\beta_s = \boldsymbol{\beta} \cdot \hat{\mathbf{s}}$ and $\beta_E = \boldsymbol{\beta} \cdot \hat{\mathbf{E}}_i$ ($\hat{\mathbf{E}}_i$ being the unit vector along the incident electric field).

This expression for the scattered power from a single electron perpendicular to the incident polarised wave can be integrated over the electron distribution function to yield the power scattered from a volume V with an electron temperature T_e and density n_e :

$$P_s(\omega_s) = n_e V \int d\boldsymbol{\beta} \int_{\Delta\Omega} d\Omega P_{sv}(\omega_s) f(\boldsymbol{\beta}) \beta^2 \quad (5.6)$$

where $f(\boldsymbol{\beta})$ is the normalised, relativistic, isotropic electron distribution function, which is a Gaussian. Since the distribution function is assumed isotropic, the integral consists of an integration over the solid angle in velocity space, which can be performed, and an integration over β . The integral over β can be performed for the first part in brackets in Eq. 5.5. The result of the integration is given in terms of the scattering wavelength (λ_s) rather than the ω_s :

$$P_s(\lambda_s, \vartheta) = n_e V \sigma_0 Y(\Lambda) \exp \left[-\frac{Z(\Lambda)}{\beta_{th}^2} \right] \quad (5.7)$$

with

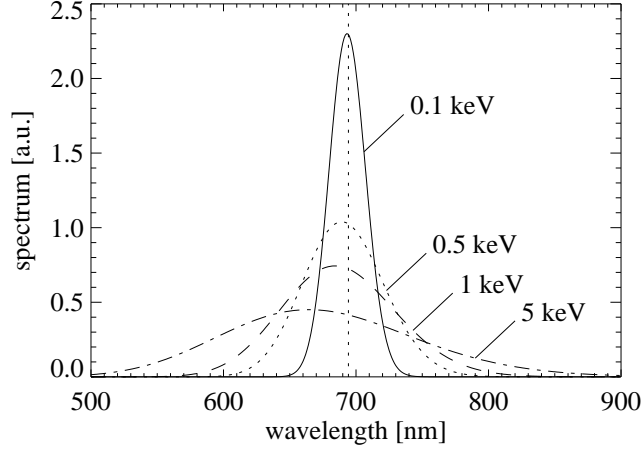


Figure 5.2: Example spectral distributions in case of ruby laser injection ($\lambda_i = 694.3$ nm) and perpendicular observation ($\vartheta = 90^\circ$).

$$\sigma_0 = \frac{r_0^2}{2\sqrt{\pi}\lambda_i \sin(\vartheta/2)} \frac{1}{\beta_{th} X(\beta_{th})} \quad (5.8)$$

the scattering cross-section at the incident wavelength λ_i and $\Lambda = \lambda_i/\lambda_s$, $\beta_{th} = v_{th}/c$,

$$\begin{aligned} X(\beta_{th}) &\approx 1 + \frac{15}{16}\beta_{th}^2 + \frac{105}{512}\beta_{th}^4, \\ Y(\Lambda) &= \frac{2\Lambda^4 \sin(\vartheta/2)}{\sqrt{1 - 2\Lambda \cos \vartheta + \Lambda^2}}, \\ Z(\Lambda) &= \frac{\sqrt{1/\Lambda - 2 \cos \vartheta + \Lambda}}{\sin(\vartheta/2)} - 2. \end{aligned}$$

In Fig. 5.2 examples of the theoretical spectra are drawn for various electron temperatures. The main consequence of the relativistic effects is that the spectrum is 'tilted' to the low wavelength side of the spectrum. The expression obtained by Mattioli can be used to fit to the data or to correct the data for relativistic effects. T_e is proportional to the square of the width, n_e is proportional to the total scattering yield, thus to the surface of the spectrum.

If a current is carried by the electrons in a direction not perpendicular to the scattering vector, then the electron velocity distribution is a shifted Maxwellian and the spectrum is not Gaussian anymore. However, if the average velocity of the electrons induced by the current (the drift velocity ($v_{d,e}$)) is small with respect to the thermal velocity, then the deformation of the distribution function is small.

In this case, the observed spectra are still like Mattioli spectra, but shifted with respect to the injected wavelength by an amount proportional to $v_{d,e}$. The spectra are 'Doppler' shifted. For this approximation of the observed spectra it must be assumed that all electrons in the distribution are shifted by the same velocity. Therefore it breaks down in case a substantial part of the current is carried by a small part of the distribution.

The value of $v_{d,e}$ in a tokamak can be measured using this principle if the scattering vector is partially along the toroidal direction. This was first proposed by Hutchinson [4]. The proof of principle was given by Alladio and Martone [5] with a single point measurement in a very small tokamak. They reached an accuracy of 40 % averaging five discharges with a temperature of 70 eV. In 1989 another single point measurement with tangential viewing was performed at TORTUR at Rijnhuizen [6]. In this experiment 8 % error could be reached thanks to the modest T_e ($T_e \sim 400$ eV) and very high current density ($j \sim 10^7 \text{MAm}^{-2}$). The accuracy of the results presented here is comparable to that of the TORTUR results, However, the presented results constitute profile measurements under reactor-relevant conditions, *i.e.* higher T_e and lower j . Typical values are $T_e \sim 1$ keV and $j = 1 - 5 \text{MAm}^{-2}$.

The rest of the chapter is a reprint of a paper submitted to the journal Plasma Physics and Controlled Fusion. The title of the paper is 'Measurements of the current density profile with tangential Thomson scattering in RTP'. The authors are: F. A. Karelse, M. de Bruijne¹, C. J. Barth, M. N. A. Beurskens², G. M. D. Hogewij, N. J. Lopes Cardozo

¹Present address: Faculteit Wiskunde en Informatica, Utrecht University, The Netherlands

²Present address: JET Joint Undertaking, Culham, UK

5.2 Introduction

The past research on tokamaks has shown that global knowledge of the plasma is not sufficient to optimise a tokamak reactor. Detailed knowledge of a number of key parameters like electric field and the magnetic field is essential to obtain high performance operation.

The current density j is one of the important parameters. The confinement of the tokamak plasma in a set of nested torus-shaped magnetic flux surfaces is determined by j and the externally applied magnetic fields. The safety factor q , which is a measure of the pitch of the field lines, is inversely proportional to the integral of j . As a consequence, the magneto-hydrodynamic (MHD) stability is determined by the j profile as well. For heat transport studies it is important to know the j profile, because the j and resistivity (η) profiles determine the Ohmic power deposition profile.

Recently, improved confinement regimes have been reached by manipulation of the j profile. In these regimes, the j profile is flat or hollow in a large central region of the plasma. The improvement of the confinement is caused by an internal transport barrier. For JET, this barrier occurs at $q = 2$ [7,8]. In RTP the observations on heat transport can be described by an electron heat transport model which is based on a set of transport barriers at rational q values [9].

Despite its importance the measurement of the j or q profile is an extremely difficult task. Several methods to measure these profiles have been developed, each with its own strengths and weaknesses. Faraday rotation polarimetry [10] measures the poloidal magnetic field (B_θ) profile. A disadvantage of this method is the line-integrated nature of the B_θ measurement, which necessitates inversion of the measured profile. For this inversion the electron density (n_e) profile is required, which is why Faraday rotation polarimeters are often combined with interferometers.

Another measurement of B is spectroscopy of the Zeeman splitting of spectral lines of impurities. This can be applied to either intrinsic [11,12] or injected [13] impurities. The observation of the intrinsic lines suffers from the limited availability of sufficiently strong lines throughout the plasma. Like polarimetry, this method gives line-integrated measurements, which necessitates an inversion procedure.

Spectroscopy of injected impurities provides a local measurement of B_θ , but it can be disturbed by collision induced fluorescence. Furthermore, the injected beam is attenuated by ionization and charge exchange. This means that the beam penetration decreases with density, limiting the applicability of the method.

Motional Stark effect polarimetry [14] measures the splitting of the spectral lines of neutrals depending on the pitch angle of the magnetic field. The localisation of this method depends on the width of the neutral beam it utilises.

Another possible measurement of the current distribution makes use of Thomson scattering. Here, a laser beam is directed through the plasma and the light scattered by the free electrons is analysed spectrally. In the normal application of this method n_e and the electron temperature (T_e) can be determined locally.

There are two basic ways to determine j from Thomson scattering; First, if the

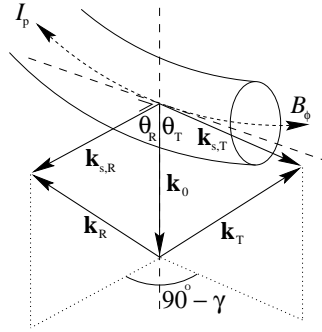


Figure 5.3: Scattering geometry of the Thomson scattering set-up at RTP. k_0 is the incident laser beam, $k_{s,\alpha}$ are the observation directions for tangential ($\alpha = T$) and radial ($\alpha = R$) detection, respectively. k_α , $\alpha = T, R$ are the corresponding scattering vectors. The angle of $k_{s,T}$ with the toroidal axis is γ .

scattering vector is taken close to perpendicular to the magnetic field, the spectrum consists of a series of peaks at multiples of the electron cyclotron frequency (ω_{ce}). From the observation of these peaks the pitch angle of the magnetic field can be determined [15–17]. To observe the separation of the peaks, the scattering vector must be within $\sim 1^\circ$ to perpendicular for plasma temperatures of a few hundred eV. The obvious problem is that the pitch angle of the magnetic field is not a constant.

The present paper is concerned with the determination of j from Thomson Scattering (TS) spectra taken in the direction tangential to the field, as suggested by [4]. The drift velocity of the electrons ($v_{d,e}$) causes a spectral shift

$$\Delta\lambda_d = -\frac{2}{c}\lambda_0 v_{d,e} \sin\frac{\vartheta}{2} \sin\left(\varphi - \frac{\vartheta}{2}\right) \cos\gamma, \quad (5.9)$$

where c is the speed of light and λ_0 is the wavelength of the incident beam. The geometrical factor contains the scattering angle ϑ , the angle γ between the scattering plane and $v_{d,e}$ and the angle φ between k_0 and the projection of $v_{d,e}$ onto the scattering plane (See Fig. 5.3.) The current density j depends linearly on $v_{d,e}$, $j = -en_e(v_{d,e} - v_{d,i})$, where e is the elementary charge. The ion drift velocity ($v_{d,i}$) has to be determined independently. In section 5.5.3, $v_{d,i}$ is estimated and it is shown that it usually is an insignificant term for the measurements presented here.

In this set-up the scattering volume is determined by the intersection of the laser beam and the sight line, both of which can be focused to ~ 1 mm. Hence, excellent spatial resolution can be achieved and no inversion is required. The intrinsic difficulty is that the scattering cross-section is very small, so that photon statistics often limits the achievable accuracy.

This measurement of j is local and does not perturb the plasma. Hutchinson [4] estimated that six to eight spectral points could give the spectral shift $\Delta\lambda_d$ with

less than 10% systematic error. This error is due to the finite width of the channels and the fact that only the first order relativistic correction was taken into account.

The challenge of the method lies in the fact that $\Delta\lambda_d$ is much smaller than the thermal line width $\Delta\lambda_e$ and the relativistic shift ($\Delta\lambda_r$) of the TTS spectrum:

$$\Delta\lambda_e = \frac{2}{c}\lambda_0 v_{\text{th},e} \sin \frac{\vartheta}{2}, \quad (5.10)$$

where the electron thermal velocity $v_{\text{th},e}$ follows from $T_e = m_e v_{\text{th},e}^2 / 2e$. A crude estimate of $\Delta\lambda_r$ in nm is obtained from $\Delta\lambda_r \approx 0.01 T_e$, with T_e in eV.

The single-point proof of principle measurement [5] was obtained in a relatively cold plasma ($T_e = 73$ eV, $n_e = 5.1 \cdot 10^{19} \text{m}^{-3}$). A statistical error of 40% on the j measurement was reported after averaging of five discharges, at a spatial resolution of 25% of the minor radius (a). The streaming parameter $\xi \equiv \Delta\lambda_d / \Delta\lambda_e \approx 0.1$. Other single-point measurements reported an error of 30% with comparable spatial resolution and $\xi \approx 0.05$, obtained from single laser pulses [6,18].

In this paper we report profile measurements with a spatial resolution of 5% of a , in plasmas with $n_e = 5 \cdot 10^{19} \text{m}^{-3}$ and $T_e = 1.5$ keV, with $\xi \approx 0.02$. A statistical error of 7% on j could be reached after averaging 7 up to 34 discharges. Normalised to the same relative resolution and streaming parameter, this constitutes an improvement of almost two orders of magnitude in the accuracy of the measurement compared to [5], while at the same time a radial profile is resolved. These improvements, which make this diagnostic viable for present day tokamaks, are mainly a consequence of high laser energy, high collection and relay efficiency and modern high efficiency detection, image intensification, and sophisticated plasma light suppression techniques.

At RTP a tangential TS (TTS) diagnostic is available based on the multi-position double-pulse TS system [19], which can also be switched to radial observation (RTS). In this paper the feasibility of the TTS diagnostic is discussed using several experimental examples. Section 5.3 gives the setup and calibration procedure of the system. In section 5.4 the data analysis is described and tests of the method based on numerical simulations are presented. Section 5.5 presents the results of experiments with Ohmic discharges and discharges with on- and off-axis Electron Cyclotron Heating (ECH), as well as a fluctuation analysis of the data.

5.3 Set-up and calibration

5.3.1 Set-up

RTP is a limiter tokamak ($I_p \leq 150$ kA, $B_T \leq 2.4$ T, $a = 0.164$ m, $R_0 = 0.72$ m) with circular cross-section. The experiments focus on electron heat transport. With a typical energy confinement time $\tau_E \simeq 3$ ms, and electron-ion energy exchange time $\tau_{ei} \simeq 20$ ms, the electrons can be considered fully decoupled from the ions. A 110 GHz 350 kW gyrotron for ECH allows the establishment of a varied set of T_e profiles, including steady state hollow and very peaked profiles.

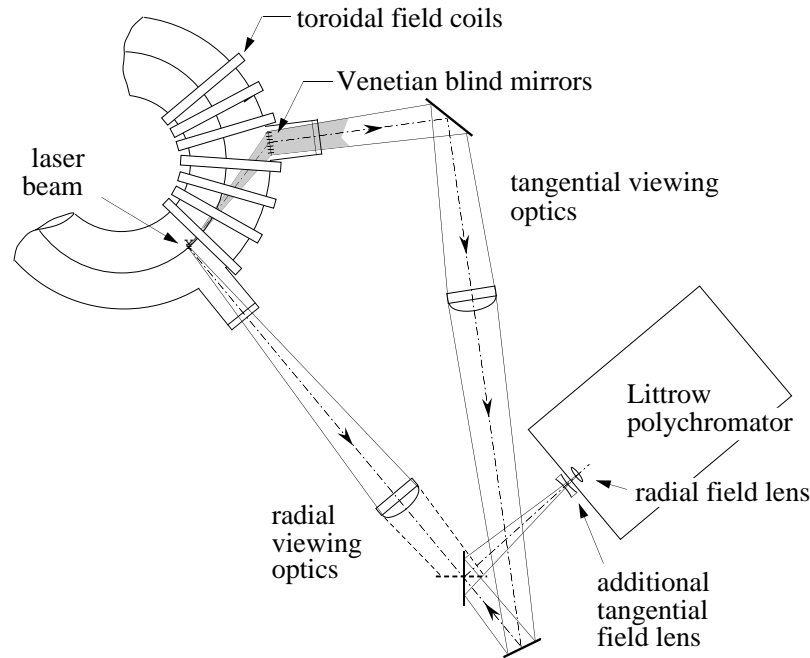


Figure 5.4: Top view of the Thomson scattering diagnostic at RTP. The shaded area marks the tangential viewing line. It originates from the vertically injected laser beam. The switch between the two viewing lines is done with the switchable mirror below.

In Fig. 5.4 a top view of the tokamak and the Thomson scattering diagnostic is shown. A detailed description of the TS diagnostic is given in [19]. Here, only the main characteristics are discussed.

A ruby laser ($\lambda_0 = 694.3 \text{ nm}$, up to 25 J in 15 ns) is injected vertically through the geometrical axis of the vessel. The scattered laser light can be collected in two directions perpendicular to the injected beam ($\vartheta \approx 90^\circ$), one along the toroidal axis of the tokamak, referred to as the radial set-up (RTS), the other almost tangential to the toroidal axis of the tokamak (TTS). Both set-ups share the laser beam line and the spectrometer.

The fact that the laser passes through the geometrical centre of the vessel implies that it misses the plasma magnetic axis by a distance equal to the Shafranov shift. The TS profiles lack measurements around $\rho = 0$, where ρ is the normalised flux coordinate $\rho = r/a$. In this paper, measurements in the upper (lower) half of the laser chord are represented by positive (negative) values of ρ . This is illustrated by Fig. 5.5 in which T_e is plotted vs. ρ .

The ruby laser is focused at the geometrical centre of the vessel to a waist of $\sim 1.5 \text{ mm}$. At the plasma edge the waist is still smaller than 2.5 mm. The tangential observation vector $k_{s,T}$ is under an angle $\gamma = 17^\circ$ with the toroidal axis (see Fig.

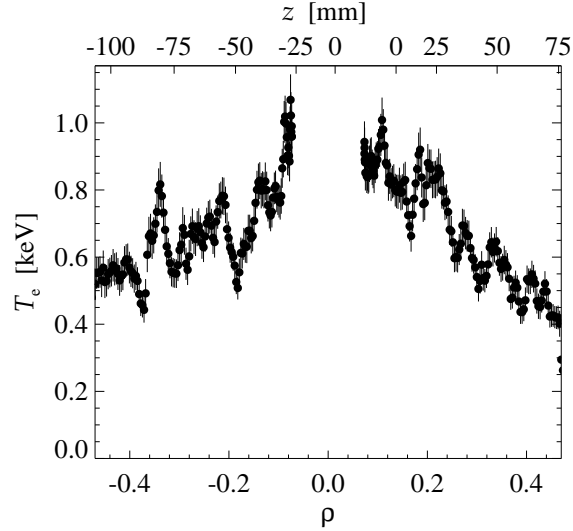


Figure 5.5: Typical T_e profile from TTS of an Ohmic discharge plotted versus the normalised flux coordinate ρ . The central gap comes from the fact that the laser misses the magnetic axis.

5.3.) Using a half wave plate, the laser polarisation is set perpendicular to $k_{s,T}$. The scattered light is gathered using an in-vessel Venetian blind mirror (VBM) system [20]. It consists of 2 arrays of six vertical mirrors, aligned in such way that they focus on the laser chord. The signal is relayed to and focused onto the entrance slit of the spectrometer using three mirrors and a 260 mm diameter, $f = 1700$ mm doublet lens. The last mirror can be switched to select between RTS and TTS.

The detector is a 2D CCD array. In one direction the image is spatially resolved, in the other direction spectrally resolved in the range between 530 and 860 nm with 0.9 nm per pixel. The spatial resolution is determined by the resolving power of the optical elements and the detector and is typically $\lesssim 4$ pixels.

5.3.2 Comparison Radial and Tangential TS set-up

The image-slit distance is 6.8 m compared to 4.0 m for RTS. Since the distance between the viewing doublet and the slit is also larger for TTS, a different field lens is needed at the position of the slit. The switch to TTS is established by insertion of a correction lens. The system parameters are summarised in Table 5.1, both of RTS and TTS.

The magnification for TTS is 1:1 (RTS: 3:2). This means that the length of the laser beam seen by 1 CCD pixel is 0.55 mm for TTS and 0.82 mm for RTS. The central 20 cm of the plasma can be viewed by TTS, whereas RTS observes the plasma from $z = -12$ to $+17$ cm. The slit width is increased with respect to the RTS setting from 2 to 2.3 mm. The solid angle of collection for TTS is $4.5 \cdot 10^{-3}$ sr,

Table 5.1: Summary of wavelength independent system parameters of the tangential and radial TS set-up.

Symbol	Description	TTS	RTS	Unit
E_{laser}	Laser energy at the scattering volume	10	10	J
$h\nu_0$	Single photon energy at 694.3 nm	2.86×10^{-19}		J
ΔL	Length of scattering volume (seen by 1 pixel)	0.55	0.82	mm
L	Length of observed laser chord	0.2	0.3	m
Ω	Solid angle of collection	4.5	2.1	m sr
σ_{Thomson}	Classical TS cross-section	7.94×10^{-30}		m^2/sr
τ_{overall}	Overall system transmission (incl. polarizer)	5.1	17	%
η_1	Efficiency of intensifier 10	18		%
G_1	Photon gain of the first intensifier	2.5×10^3		
T_1	Efficiency of the lens coupling system	6		%
η_2	Efficiency of the ICCD intensifier	3		%
κ	Collection fraction second image intensifier	30		%
K_{CCD}	ICCD detection efficiency: counts/photon	5×10^{-2}		cnt/ph
ζ_{CCD}	CCD conversion factor: photoelectrons/count	10		pe/count

limited by the doublet lens. For RTS the solid angle is only $2.1 \cdot 10^{-3}$ sr, limited by the spectrometer.

The overall system transmission is 5.1% for TTS and 17% for RTS. The difference is mainly due to the reduced reflection of the VBM system, which faces the plasma. The transmission of TTS was determined from the absolute calibrations of TTS. It remained almost constant in a year of plasma operation. Following the error analysis of [21] we obtain an error on n_e of 3.5% at typical densities of $5 \cdot 10^{19} \text{ m}^{-3}$ cf. 2% for RTS. This corresponds well to results from simulations [21] of TTS spectra, as shown in section 5.4.2.

5.3.3 Calibration

A detailed discussion of the calibration of the RTS set-up is given in [22]. Here, the differences with the calibration of the TTS set-up will be summarised.

Since the in-vessel VBM system dominates the transmission, the relative sensitivity in wavelength direction is calibrated *in situ*. A Tungsten band lamp of known temperature is scanned along the laser chord position. In Fig. 5.6a the relative spectral sensitivities of TTS and RTS are compared. The TTS sensitivity decreases stronger than the RTS one towards shorter wavelength. Part of the red wing of the spectrum is also lower.

The scan of the band lamp gives the position calibration as well. The calibration of the wavelength is done using the lines of He, Ar and Hg lamps. This is assumed to be identical for both set-ups since they share the spectrometer.

In Fig. 5.6b the signal in wavelength direction is shown in case of Rayleigh

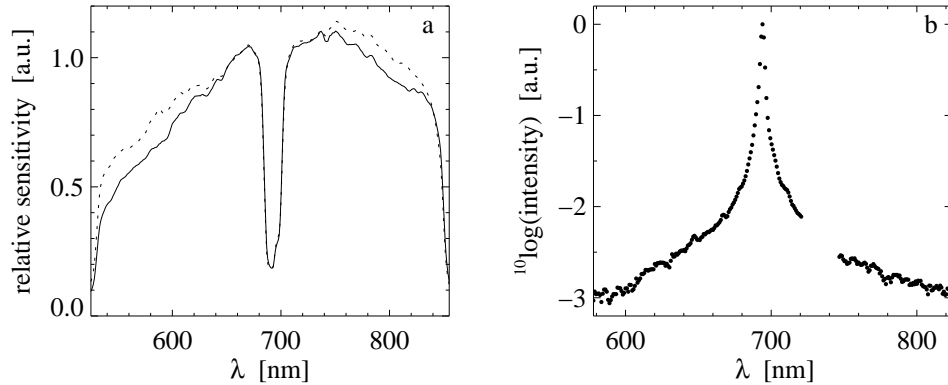


Figure 5.6: a) Central relative spectral sensitivities of TTS set-up (full line) and RTS set-up (dotted line). The gap around 700 nm is the instrumental gap. The reductions at the edges of the curve are at the edges of the spectral image. b) Signal in wavelength direction in response to a line source in z -direction as obtained from Rayleigh scattering on H_2 . The empty region represents the instrumental gap, which is shifted towards higher wavelength for this calibration. It falls around the laser frequency in case of scattering in the TS set-up.

scattering on low pressure H_2 . The scattered light acts as a line source and if the instrument function of the set-up would have been ideal, a single peak on the noise had been detected. The real instrument function is characterised by a sharp central peak and long tails. The central peak has a width of 3.5 nm and redistributes the light over a few pixels. This redistribution smoothes the signal, hence reduces the noise. The long tail is caused by the halo of the phosphor of the image intensifier rather than by the stray light. The stray light ratio $\lesssim 5 \cdot 10^{-4}$. The phosphor tail is lower than in the figure, because the figure is obtained with a line source.

Measurements with a pinhole source in front of the entrance slit of the detector have shown that the spectral resolution of the spectrometer is 2.4 nm [21].

5.4 Data analysis

In this section the data analysis of the TTS data is discussed. First, two methods to obtain the shift from the data are introduced in section 5.4.1. These two methods are tested on simulated data and their results are compared in section 5.4.2. The way the data are simulated is presented in section 5.4.2. From the knowledge obtained from the simulations, the data analysis procedure is established, section 5.4.3.

5.4.1 Fit method and moment method

The electron temperature T_e and density n_e are routinely obtained by fitting a thermal distribution function to the spectrum [22]. Since $\beta = v_{\text{th},e}/c$ is not negligible in a tokamak plasma, the spectrum is deformed by relativistic effects. We use the approximate analytical expression proposed by Mattioli [23] to take this into account.

The width of the spectrum is proportional to $T_e^{1/2}$, the integral of the spectrum is proportional to n_e . The fit function normally has 2 parameters but can readily be modified with a spectral shift, of magnitude $\Delta\lambda_d$, as a third parameter. It is assumed that $\Delta\lambda_d$ is so small that it is unnecessary to modify the shape of the fitting function. The simulations show that this assumption is justified and that indeed the addition of the third parameter does not influence the determination of T_e or n_e .

The scattering process is governed by Poisson statistics. The detection noise includes the photon noise at the two image intensifiers, the photon noise at the CCD-chip and the read-out noise of the CCD-chip. The detection error σ_{ij} can be written for each pixel (i, j) as follows:

$$\sigma_{ij}^2 = C_{\text{photon}} \cdot S_{ij} + \sigma_{\text{read-out}}^2 \quad (5.11)$$

where C_{photon} contains the three above-mentioned sources of photon noise and S_{ij} is the TS signal at pixel (i, j) . Both S_{ij} and σ_{ij} are number of counts. The CCD read-out noise $\sigma_{\text{read-out}}$ is a constant: 2 counts for each pixel. The photon noise dominates σ_{ij} , because C_{photon} is ~ 5 . Gaussian weighting of the error gives the weight function for the fit. The errors on the fit parameters follow from the variance matrix.

A drawback of the fit method is that an approximated analytical expression has to be used as a fit function. If the distribution function is non-thermal, this method may have a systematic error. This is the case, for example, when a supra-thermal electron population carries a substantial part of the current.

A method which is not dependent on any analytical expression is the so-called moment method. This method tests the symmetry of the spectrum by calculation of the first moment. The current density j depends on the first moment only (which is an additional advantage of this method), $\Delta\lambda_d$ follows after normalisation with the zeroth moment:

$$j = -\frac{ecC_R}{\lambda_0} \int y \cdot (\lambda_0 - \lambda) d\lambda, \quad (5.12)$$

$$\Delta\lambda_d = \int y \cdot (\lambda_0 - \lambda) d\lambda / \int y d\lambda, \quad (5.13)$$

where y is the spectrum and C_R is a constant from the Rayleigh calibration.

The fit and moment methods are compared in section 5.5.2.

To obtain the moments of the spectrum caused by $v_{d,e}$ only, the spectrum has to be corrected for relativistic effects. This is done by application of the same expression of Mattioli [23], that is used as the fit function. Further, this expression contains T_e , which has to be taken from the fit result. Nevertheless, the moment method is intrinsically less sensitive to spectral disturbances [18].

The errors on the moments follow from the integrals of the estimated Poisson errors. The errors on j and $\Delta\lambda_d$ from the moment method are almost equal, because the relative error on the zeroth moment is much smaller than that on the first moment.

5.4.2 Simulation results

To test the analysis for errors on the determination of T_e , n_e and $\Delta\lambda_d$ the measured spectra are simulated. The starting point of the simulation is the expression of Mattioli [23] for spectra scattered from relativistic electrons. To obtain spectra which are similar to the measured ones, the various noise sources are applied to the simulated signal in the order they would be met in the set-up by a real signal. An additional advantage of this method is that by simulating the data in the format of the measurements, the calibration and analysis software can be tested. First, the actual simulation of the CCD images will be discussed and after that the results of the analysis methods applied to these images are discussed.

Simulation of spectra.

The noise sources and the way they should be treated in the simulation are extensively discussed in [21]. Here, the same procedure will be used using the TTS system parameters listed in Table 5.1.

The starting point of the simulation is the number of photons scattered at the laser chord. Their spectral distribution is given by the Mattioli function. The number of photons on entrance of the first image intensifier is reduced by the overall transmission factor. At this stage we also correct the simulated data for the measured spectral sensitivity¹. Furthermore, the spectral points in the laser gap are cut out.

The following operations are performed subsequently:

1. Addition Poisson noise of the first image intensifier;
2. Convolution with a two-dimensional instrument profile;
3. Addition Poisson noise of the ICCD cathode;
4. Addition Poisson noise of the CCD chip;
5. Addition read-out noise of the CCD.

¹Note that the measured spectral sensitivity is the convolution of the sensitivities of the individual elements. However, the individual sensitivities are unknown.

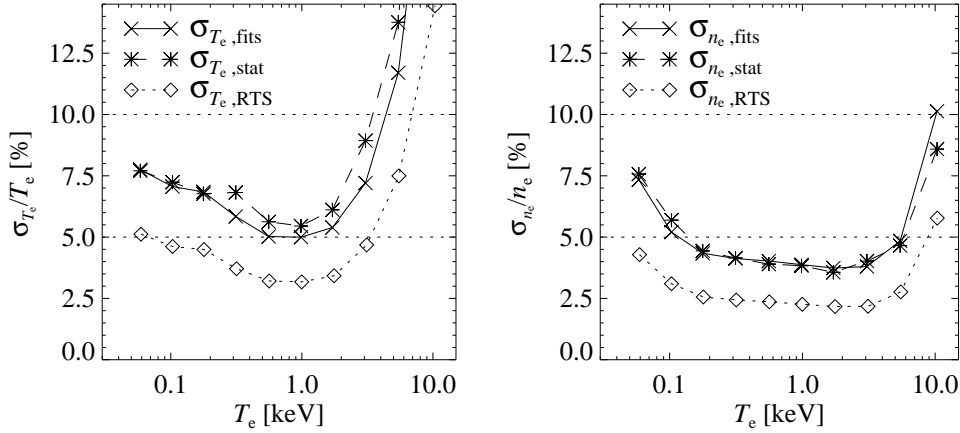


Figure 5.7: Relative error on T_e (left) and n_e (right), respectively, as a function of the logarithm of T_e . The full line with the crosses represents the errors resulting from the fit, the dashed line with stars gives the standard deviations of the simulation results. For comparison, the relative errors of RTS are given as well (dotted line with diamonds). $n_e = 5 \cdot 10^{19} \text{m}^{-3}$, $\Delta\lambda_d = 0 \text{nm}$, $E_{\text{laser}} = 10 \text{J}$.

The subsequent steps indicate the conversion steps the signal undergoes during the transformation to the digital CCD image. For the two-dimensional instrument function the pinhole measurement referred to in section 5.3.3 is taken. This function is a nearly triangular function with a FWHM of 2.8 pixels in both directions. This instrument function has no tails. Note, that this function represents the over-all function of the detector and no information is available on the characteristics of the individual elements.

The main source of noise is the cathode of the first image intensifier. Other noise sources are relatively low, because of the high image intensifier gain (2500 to 8750).

In the end the CCD background and read-out noise are added. The spectra can now be calibrated and analysed like measured spectra.

Analysis of simulated spectra.

The operational area of the CCD camera consists of 350 pixel rows, so 350 similar spectra are simulated per CCD image. In addition to T_e and n_e , the output contains two estimates of the shift, $\Delta\lambda_{d,\text{fm}}$ and $\Delta\lambda_{d,\text{mm}}$, resulting from the fit method and the moment method, respectively. The averaged outputs are compared with the input to keep track of systematic deviations. The standard deviations of the output are compared with the errors resulting from the analysis methods.

In Fig. 5.7 the relative errors on T_e ($\sigma_{T_e}/T_e \equiv \epsilon_{T_e}$) and n_e ($\sigma_{n_e}/n_e \equiv \epsilon_{n_e}$) as resulting from the fit, and their standard deviations are plotted against T_e . For comparison the result for RTS is given as well. As can be seen from the figure the

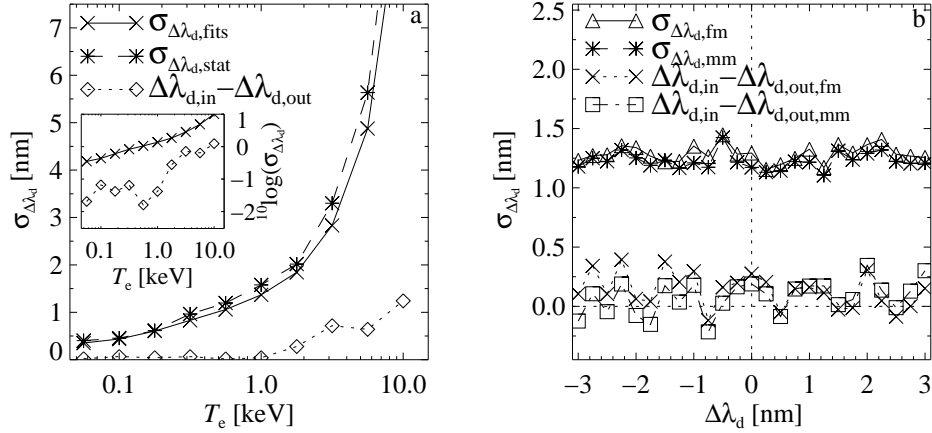


Figure 5.8: Absolute errors on $\Delta\lambda_d$ as a function of the logarithm of T_e (a) and $\Delta\lambda_d$ (b), respectively. In a the subscript fits stands for the errors resulting from the fit, the subscript stat. indicates the standard deviation of the simulation result. The third curve gives the deviation between input and output of the simulation ($n_e = 5 \cdot 10^{19} \text{m}^{-3}$, $\Delta\lambda_d = 0 \text{ nm}$, $E_{\text{laser}} = 10 \text{ J}$). The insertion contains the same figure with logarithmic $\Delta\lambda_d$ scale. In figure b the errors and deviations of the fit method (fm) and the moment method (mm) are compared. $T_e = 1 \text{ keV}$, $n_e = 5 \cdot 10^{19} \text{m}^{-3}$, $E_{\text{laser}} = 10 \text{ J}$.

results from the fit and the statistics are very similar. The fit error ϵ_{T_e} decreases slowly to its minimum at $\sim 1 \text{ keV}$ after which it increases rapidly. The fit error ϵ_{n_e} basically has the same behaviour except that the curve is much flatter and the increase starts at higher T_e . Towards low T_e , ϵ_{T_e} and ϵ_{n_e} slightly increase. In this case, a relatively large part of the spectrum is cut due to the laser gap and the H_α window. For high T_e the spectra becomes broader than the spectral range of the detector, causing a rise of both ϵ_{T_e} and ϵ_{n_e} .

The RTS set-up gives very similar curves, but the errors are lower. The rise for high T_e is less pronounced. The reason is that the transmission yield of the RTS branch is a factor 2.3 higher than that of the TTS branch (see section 5.3.2.)

The systematic deviations of the T_e and n_e outputs with respect to their input values are much lower than the errors. For the region from 0.1 to 1 keV the deviation is $< \pm 2\%$ for T_e and within $+1\%$ for n_e .

In Fig. 5.8a the fit error, the standard deviation and the systematic deviation of the obtained shift are plotted against the logarithm of T_e for $n_e = 5 \cdot 10^{19} \text{m}^{-3}$ and $\Delta\lambda_d = 0 \text{ nm}$. The error and the standard deviation are similar and the systematic deviation stays below those two. The error strongly increases for $T_e > 2 \text{ keV}$. This is a consequence of two effects: 1) The increase of the spectral width with T_e ; 2) The finiteness of the observed spectral range, cf. the above-mentioned increase of

ϵ_{T_e} and ϵ_{n_e} for high T_e . The systematic deviation increases for $T_e > 1$ keV, though it remains a small fraction of the error. For $T_e \leq 1$ keV the systematic deviation is small compared to the error.

In Fig. 5.8b the standard deviations and systematic deviations of the fit method and moment method are compared for $T_e = 1$ keV and $n_e = 5 \cdot 10^{19} \text{m}^{-3}$ as a function of $\Delta\lambda_d$. The point-to-point scatter is caused by the finite length of the simulated array. The agreement of both standard deviations is good. Both systematic deviations deviate from zero. The systematic deviation of the fit method is constant over the whole $\Delta\lambda_d$ range at ~ 0.2 nm. The systematic deviation of the moment method lies around zero but it has a small positive slope of ~ 0.06 . This means that the moment method gives a 6 % overestimate of relative $\Delta\lambda_d$ measurements.

For a typical Ohmic RTP plasma with $T_e = 1$ keV, $n_e = 5 \cdot 10^{19} \text{m}^{-3}$ and $j = 4 \text{MAm}^{-2}$, Eq. 5.9 gives a value of $\Delta\lambda_d$ of 1.1 nm. This shows that the statistical error is of the order of the shift itself. Note, that for lower n_e the error on $\Delta\lambda_d$ is higher, but the expected $\Delta\lambda_d$ is higher as well. Their ratio is independent of n_e . This 100 % error means that to obtain a 10 % error on the $\Delta\lambda_d$ results, 100 measurements have to be averaged.

The systematic deviation of the shift can be significant compared to the expected measurement of $\Delta\lambda_d \lesssim 1.1$ nm. In principle, the measured $\Delta\lambda_d$ could be corrected for the systematic shift using the simulations. However, we think it is better to compare measurements of positive current ($\Delta\lambda_d < 0$) and negative current ($\Delta\lambda_d > 0$) discharges, so that the systematic shift cancels out. In this way, any systematic shift of unknown nature is removed as well.

Both analysis methods give equal results on the simulated data. In section 5.5.2 the results of both methods applied to measured data are compared.

5.4.3 Analysis procedure

In the previous subsection we saw that averaging is needed to reduce the statistical error to acceptable values. It is favourable to do as much averaging as possible before the analysis is applied. In this way, the analysis is applied to very clear spectra. This was kept in mind when the analysis procedure was established.

The obtained raw data is corrected for the plasma light, that is measured with a second CCD detector 100 μs before the laser shot [24]. The plasma light is bilinearly interpolated from one to the other CCD grid, and corrected for the difference between the respective calibrations of the CCDs. We assume that the emission of H_α is constant between the two exposures. The resultant plasma light signal can then be normalised to the TS signal using the amplitude of the H_α line. This is necessary since the interpolation under-estimates the plasma light. Though the signal level of the plasma light varies, it is in all cases well below the TS signal level (except at the H_α and He lines). Nevertheless, the $\Delta\lambda_d$ determination is extremely sensitive to the plasma light and accurate correction is crucial.

The H_α line and the laser gap are cut from the spectrum by the analysis software. The much weaker He lines are well compensated by the plasma light correction.

Both the TS signal and the plasma light signal are carefully corrected for the

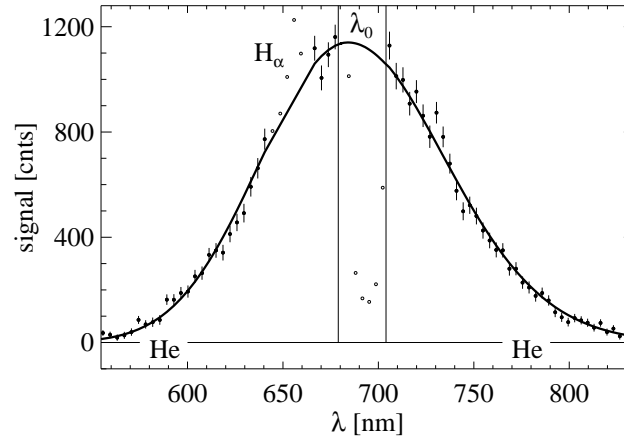


Figure 5.9: Typical Thomson scattering spectrum averaged over 12 discharges with a laser energy of 11.8 J, and the fit to this spectrum (line) giving $T_e = 1.33 \pm 0.02$ keV and $\Delta\lambda_d = 2.5 \pm 0.5$ nm. The vertical lines indicate the instrumental gap around the laser wavelength. The open dots without error bar are neglected in the analysis. This is the data around the H_α line and in the laser gap. At the positions of the He lines the spectrum is not disturbed. This is so because a separate, accurate plasma light measurement has been subtracted.

CCD background. This correction signal is the average of several zero signal images. This correction is superior to any fit to the background since it eliminates the global variation as well as the small details of the CCD background.

The spectra still have an offset with respect to zero. This is due to the long tails of the instrument profile, discussed in section 5.3.3. A coarse correction method for this is given in [21]: subtraction of a fraction $1 \cdot 10^{-6}$ of the total signal on the CCD of the spectra. This number has been determined empirically from the measurements and is confirmed by simulations.

Data of 16 adjacent spectral rows is added as well as data of a series of 7 up to 34 discharges. The data is corrected for the relative sensitivity and the perspective deviation. Since the pixel width is smaller than the spectral resolution, see Fig. 5.6b, four pixels in wavelength direction are binned. Now, the fit is done, in two iterations: The first iteration is used to determine the widths of the spectra approximately. The obtained values are used to limit the fit width in the second iteration to $2\Delta\lambda_e$. Both fit and moment method are limited within $2\Delta\lambda_e$ to avoid over-stressing the tails of the spectra.

$\Delta\lambda_d$ follows from subtraction of the results of the positive and negative current discharges. Once the shift is obtained, the $v_{d,e}$, j and q follow in a straightforward way, assuming $v_{d,i}$ is known.

In Fig. 5.9 a spectrum is given after correction for the CCD background and

Table 5.2: Summary of plasma parameters of the discharges discussed in this paper.

Description	I_p (kA)	$T_e(0)$ (keV)	$n_e(0)$ (10^{19}m^{-3})	$\#_{\text{pos}}$	$\#_{\text{neg}}$	ρ_{dep}	Section
Ohmic discharges	60	0.6	scan	15	34	-	5.5.1
ECH, profile A	80	1.2	4.8	12	16	0.1	5.5.4
ECH, profile B	80	0.6	5.0	20	14	0.23	5.5.4
ECH, profile C	80	0.5	5.3	7	12	0.34	5.5.4
ECH, profile D	80	0.4	5.3	20	11	0.38	5.5.4
Relaxation after off-axis ECH:							
• before crash	90	0.6	5.3	10	12	0.48	5.5.5
• after crash	"	"	5.3	10	10	"	5.5.5
$v_{d,e}$ fluctuations	60	~ 1.5	~ 1.5	-	-	0.0	5.5.6

the plasma light and after calibration for spectral sensitivity. In this example, the instrumental gap around λ_0 is clear. Further, the H_α line is cut from the spectrum softwarematically. The spectral positions of the He lines are indicated, although they are not visible on the data. The obtained fit to this spectrum is given as well.

5.5 Experimental results

In this section the results obtained with TTS are summarised. First, the measurement of the j profile in an Ohmic discharge will be discussed, section 5.5.1. In section 5.5.2, the results obtained with the fit method and the moment method will be compared. An estimate of the ion drift velocity from observations is given and its implications for the measurements will be discussed in section 5.5.3. In section 5.5.4 we study the j profiles in a set of Electron Cyclotron (EC) Heated discharges. The normalised deposition radius (ρ_{dep}) of the EC Heating (ECH) is varied along the radial axis. During the relaxation of the plasma after switch-off of ECH a fast MHD event happens, which interrupts the rapid increase of the density. A similar event is observed at the onset of the bifurcation of the Ohmic state reported earlier [25]. The current density j is measured just before and after this fast event, section 5.5.5. Finally, we will present a drift velocity fluctuation study using TTS in section 5.5.6. In Table 5.2 the relevant plasma parameters of the described experiments are given.

Before series of measurements are taken, it is desirable to evaluate the performance of the diagnostic on single discharges. This can be done most easily by comparing the results obtained from TTS and RTS, especially the T_e profiles obtained using both methods. Unfortunately, both measurements cannot be performed during one discharge. Therefore, results of similar discharges are compared.

For this comparison, the use of the high power ECH is appropriate, because by

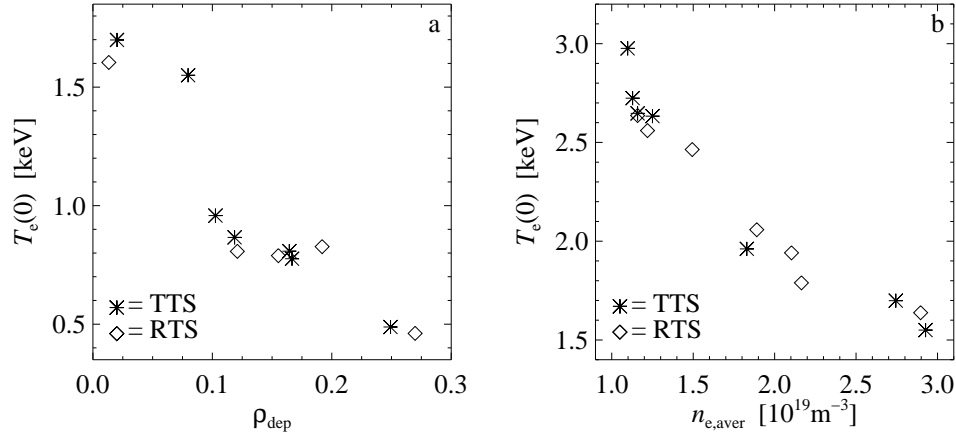


Figure 5.10: a) T_e obtained from TTS (stars) and RTS (diamonds) vs. B_φ .
 b) T_e obtained from TTS (stars) and RTS (diamonds) vs. the line averaged density.

variation of ρ_{dep} and n_e a wide range of T_e profiles is established.

In a rough scan of ρ_{dep} at constant n_e , agreement of the RTS and TTS temperatures was found, see Fig. 5.10a. We expect staircase-like behaviour of $T_e(0)$ as a function of ρ_{dep} , as reported in [26,27] and indeed three plateaus can be distinguished. Due to lack of data points the transitions between the plateaus are not clear.

In Fig. 5.10b the central T_e is plotted as a function of the line averaged density ($n_{e,\text{aver}}$) from central interferometric measurements for both TTS and RTS. ECH was deposited centrally. The results of both methods agree well above, except for the two shots with lowest $n_{e,\text{aver}}$. The TTS temperatures of these shots are significantly higher than the RTS ones at slightly higher $n_{e,\text{aver}}$.

This discrepancy between the RTS and TTS temperatures is probably not caused by any anisotropy in the EC heating, because the ECH is resonant to the perpendicular component of the velocity distribution ($f(v)$). Consequently, the most obvious anisotropy due to ECH would give a higher 'perpendicular temperature', giving an effect opposite to that observed.

On the instrumental side it must be noted that the transmission yield of the TTS branch is ~ 2.3 times lower than the RTS transmission yield. This becomes especially important at low n_e and corresponding low photon yield, and high T_e .

5.5.1 Results on Ohmic discharges

In Fig. 5.11a the resultant shift $\Delta\lambda_d$ for a series of 15 positive and 34 negative current Ohmic discharges is shown ($|I_p| = 60$ kA, $B_T = 2.04$ T). The central density was varied between $1 \cdot 10^{19}$ and $9 \cdot 10^{19} \text{ m}^{-3}$ in this series, but all data have been averaged to yield the above result. The shift in Fig. 5.11a was determined using the fit method. Application of the moment method yields a very similar result

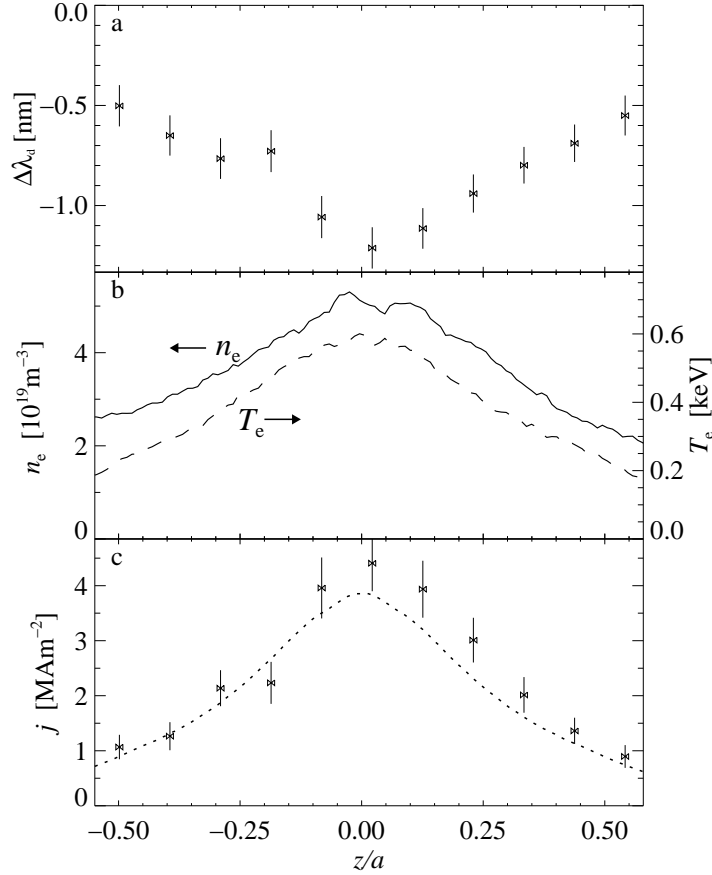


Figure 5.11: a) Doppler shift as obtained with TTS from a series of positive and negative plasma current Ohmic discharges ($I_p = 60$ kA, $B_T = 2.04$ T, $n_e(0) = 5 \cdot 10^{19} \text{ m}^{-3}$). b) Averaged n_e (full line) and T_e (dashed line) profiles from the series of Ohmic discharges used for a. c) j as calculated from the Doppler shift (symbols) and as obtained from NCR calculations (dotted line).

(section 5.5.2). The maximum $|\Delta\lambda_d|$ is ~ 1 nm, the corresponding $v_{d,e} = 4 \cdot 10^5$ m/s. In Fig. 5.11b the average n_e and T_e profiles of the series are shown. Assuming that $v_{d,i}$ is negligible, the j profile can now be calculated (Fig. 5.11c), according to $j = -en_e v_{d,e}$.

From the j profile, the q profile as a function of the normalized radius $\rho = r/a$ can be calculated (Fig. 5.12). For this, the average of the positive and negative- z parts of the $j(r)$ profile is taken. Since the plasma centre is Shafranov shifted with respect to the centre of the vessel by $\sim 10\%$ of a , no j values within $\rho \sim 0.1$ are obtained. To estimate the contribution of this area to q , n_e is extrapolated linearly

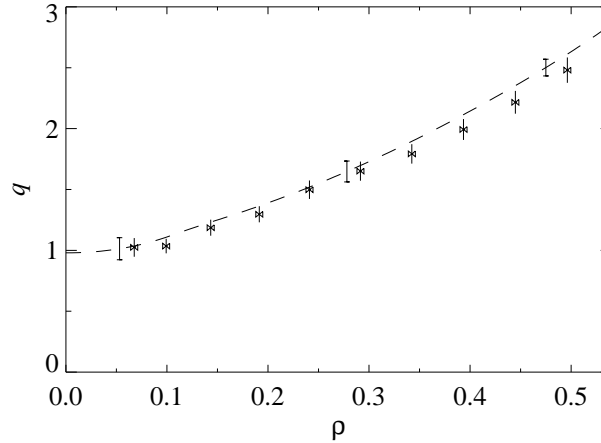


Figure 5.12: Safety factor q profile corresponding to the measurements (symbols) and the NCR calculations (dashed line) of Fig. 5.11c. To transform to $\rho = r/a$ the measured j profile has been symmetrized around $z = 0$ before integration.

to $\rho = 0$. This extrapolation is based on the assumption that the n_e profile is peaked in the centre. This is confirmed by interferometer measurements. The $\Delta\lambda_d$ profile is interpolated linearly between the inner points, because the scatter is too large to extrapolate well. The resulting central j is integrated numerically to obtain q .

For comparison, Figs. 5.11 and 5.12 also show the profiles as determined from the T_e and n_e profiles using neo-classical resistivity, assuming full current penetration (the TTS profiles were taken 10 current diffusion times after reaching thermal equilibrium), a flat Z_{eff} profile and taking the bootstrap current into account. The value of Z_{eff} is determined self-consistently in this calculation. The agreement with the data is good. These calculations will be referred to as NCR calculations.

5.5.2 Comparison fit method and moment method

The data is analyzed using the two methods discussed in section 5.4. In Fig. 5.13a the resulting spectral shifts of a series of Ohmic discharges are given, in Fig. 5.13b the results are given of a series of discharges with strong central ECH and $T_e > 1$ keV, cf. 'profile A' in Table 5.2 and Fig. 5.14. It is clear that the results of both methods are close to each other within each others error bar for both discharge types. For the Ohmic series, the results of the moment method are slightly higher than those of the fit method. This effect is not visible for the EC heated discharges and its cause is unknown. The asymmetry in Fig. 5.13b will be discussed later.

We have seen that the results of both data analysis methods agree well applied to simulated data as well as applied to measured data. There is no sign that the

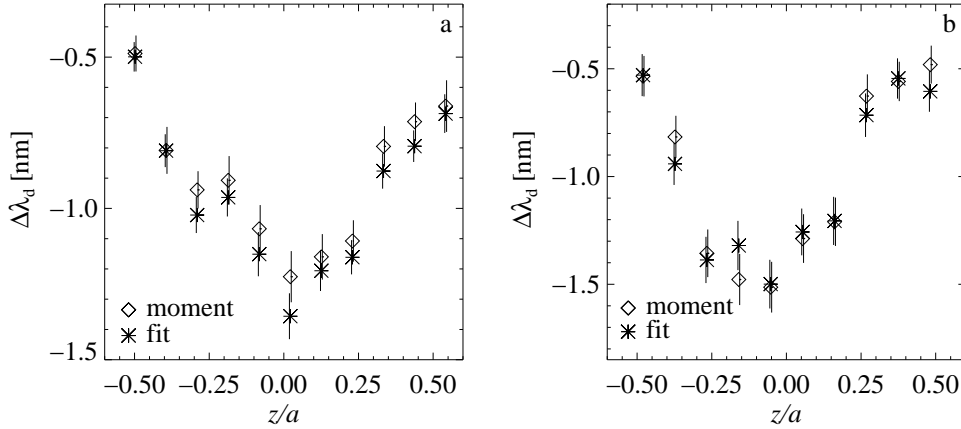


Figure 5.13: Comparison of the spectral shifts ($\Delta\lambda_d$) obtained with the two analysis methods for Ohmically heated discharges (a) and discharges with central ECH (b).

measured spectra deviate from the assumed Mattioli distribution. This result is important, since it holds for strongly EC heated as well as Ohmic plasmas. In the following only the fit method results will be presented.

5.5.3 Estimate of the ion drift velocity

The ion drift $v_{d,i}$, which was neglected in the result shown in Fig. 5.11c, was estimated from grazing incidence spectrometer measurements of excited carbon states. Typically, $v_{d,i} = 3 \pm 1 \cdot 10^3$ m/s is found, opposite to $v_{d,e}$. This measurement pertains to the edge of the plasma. No measurements of $v_{d,i}$ in the plasma core are available at RTP. The central $v_{d,i}$ can be estimated from the MHD frequency (f_{MHD}), which has to be corrected for the diamagnetic frequency (f_e^*) to obtain the plasma rotation frequency. Measurements give $f_{\text{MHD}} < 15$ kHz for the $m = 2, n = 1$ mode. The diamagnetic frequency is not measured directly, but can be obtained from the following equation:

$$f_e^* = \frac{m}{r} \frac{1}{2\pi en_e B} \frac{\partial p_e}{\partial r}. \quad (5.14)$$

Note, that f_e^* is proportional to the radial p_e gradient [28]. For the discharges with on- and off-axis ECH, which will be discussed in the next section, this equation gives $f_e^* = 10 - 15$ kHz. This value is of the order of f_{MHD} . The upper estimate of the rotation frequency is therefore 5 kHz, the corresponding $v_{d,i} \leq 20 \cdot 10^3$ m/s. For the Ohmic plasmas, neglecting such a $v_{d,i}$ profile leads to a 5% underestimate of j . For plasmas with lower $v_{d,e}$ values, the ion drift velocity might become more important.

5.5.4 Steady state on- and off-axis ECH experiments

In RTP experiments with ECH were performed with 350 kW power, exceeding the Ohmic input power by a factor three to seven and localisation within 10% of the minor radius [26,27]. The deposition radius (ρ_{dep}) was varied between 0 and ~ 0.5 on the low field side of the magnetic axis, by tuning the toroidal magnetic field.

It has been shown that a stair-step relationship between ρ_{dep} and $T_e(0)$ exists with sharp transitions separating plateaux (labelled A-D) in which $T_e(0)$ is insensitive to variation of ρ_{dep} [26,29]. The sharp transitions can be associated with the loss or gain of a simple rational q surface. These observations suggest that the electron thermal diffusivity χ_e is a direct function of q , with alternating layers of low and high χ_e . It has been shown [9] that such a model well describes the distinct profile shapes.

Here, the TTS measurements of the j and q profiles in the plateaux A-D are presented. These data were obtained from 4 series of discharges.

Fig. 5.14 shows a set of T_e profiles measured with TTS, for four values of ρ_{dep} , see also Table 5.2. The T_e profiles are peaked for central deposition and flat or even hollow inside ρ_{dep} for off-axis ECH. Outside ρ_{dep} the profiles are very similar.

In all cases, the measurements were taken > 150 ms (≈ 50 energy confinement times and 10 current diffusion times) after ECH was switched on. At this time all diagnostics indicate that the plasma has reached a thermal equilibrium.

The centrally heated plasmas provide an extra challenge to the TTS method since T_e is higher and $v_{d,e}$ will be an even smaller portion of $v_{th,e}$ than in Ohmic plasmas. For the off-axis heated discharges, the temperatures are similar to the Ohmic case.

For the levels A to D the $\Delta\lambda_d$, T_e and n_e profiles are shown in Fig. 5.15. The $\Delta\lambda_d$ profiles are obtained with the fit method according to the procedure described in section 5.4.2. The moment method gives equal results within error bars. The T_e and n_e profiles are averages of all used discharges. The j profiles are obtained using the $\Delta\lambda_d$ and n_e profiles mentioned above. The ion drift velocity $v_{d,i}$ has been neglected.

The data were taken with same I_p , almost same B_ϕ and almost the same line-integrated density. ρ_{dep} was varied between the different data sets, causing different T_e profiles. As a consequence, the q profiles of the data sets are different and there is some variation in the n_e profiles, as can be seen from the figures. It is clear that $|\Delta\lambda_d(0)|$ is highest for level A and lowest for level D. $\Delta\lambda_d$ is peaked for level A, flat for level B and hollow for levels C and D. This trend is also present in the j profiles though less clear.

We observe that the measured j profiles are not smooth. The variation between the profile points can be several error bars, for example in Fig. 5.15a at $z/a = -0.20$ or in Fig. 5.15d between $z/a = 0.46$ and 0.51 . The occurrence and amplitude of these variations are of random nature. Therefore, it is unlikely that a systematic instrumental effects causes this effect. In section 5.5.6 the presence of fluctuations in the raw data is discussed in more detail.

The averaging of the T_e and n_e profiles over up to 20 discharges brings the

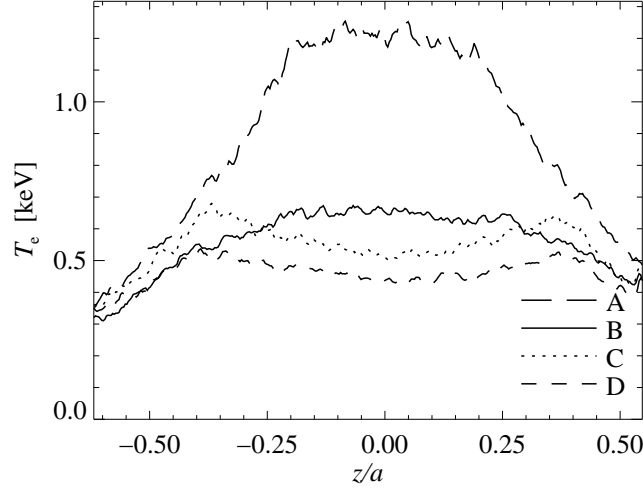


Figure 5.14: Four averaged T_e profiles from TTS obtained in a scan of the deposition radius, labelled A to D with deposition radii of 0.1, 0.23, 0.34 and 0.38, respectively.

error down below 1%. The error bars are indicated in Fig. 5.15, but can hardly be seen. The structures on the T_e and n_e profiles in Fig. 5.15 are probably due to the statistical error on the calibrations. The fluctuations on the profiles are discussed in section 5.5.6. The fluctuations on n_e are so small that they are unimportant for the determination of j .

In Fig. 5.16 the q profiles corresponding to the profiles of Fig. 5.14 are shown as a function of the normalised radius ρ . Additionally, the q profiles from NCR calculations were plotted. These calculations are justified because the on- and off-axis heated plasmas can be sustained for up to 200 ms (i.e. 20 current diffusion times). The data were taken at the end of this interval.

The error bars on the NCR calculations are obtained considering two sources of uncertainty in the q profiles: In the first place, the self-consistently determined value of the effective ion charge (Z_{eff}) might be non-constant throughout the profile. Second, the T_e profiles need to be extrapolated towards the edge and the centre. The precise shape of this extrapolation determines the amount of current in the edge region. The error bars are obtained by allowing Z_{eff} to vary by 20% over the plasma radius, in accordance with earlier soft X-ray measurements [30], and by 20% variation of the T_e extrapolation parameters.

The agreement of the q profiles deduced from the $v_{d,e}$ measurements with the calculations is good. The calculations and the measurements agree within error bars nearly everywhere. As expected from the j profiles, profiles C and D have negative central shear and profile B has zero shear within ρ_{dep} . Though its minimum value is not much below one, the centrally heated profile A has an considerable inversion radius. Both measurements and calculations have considerable error bars in the

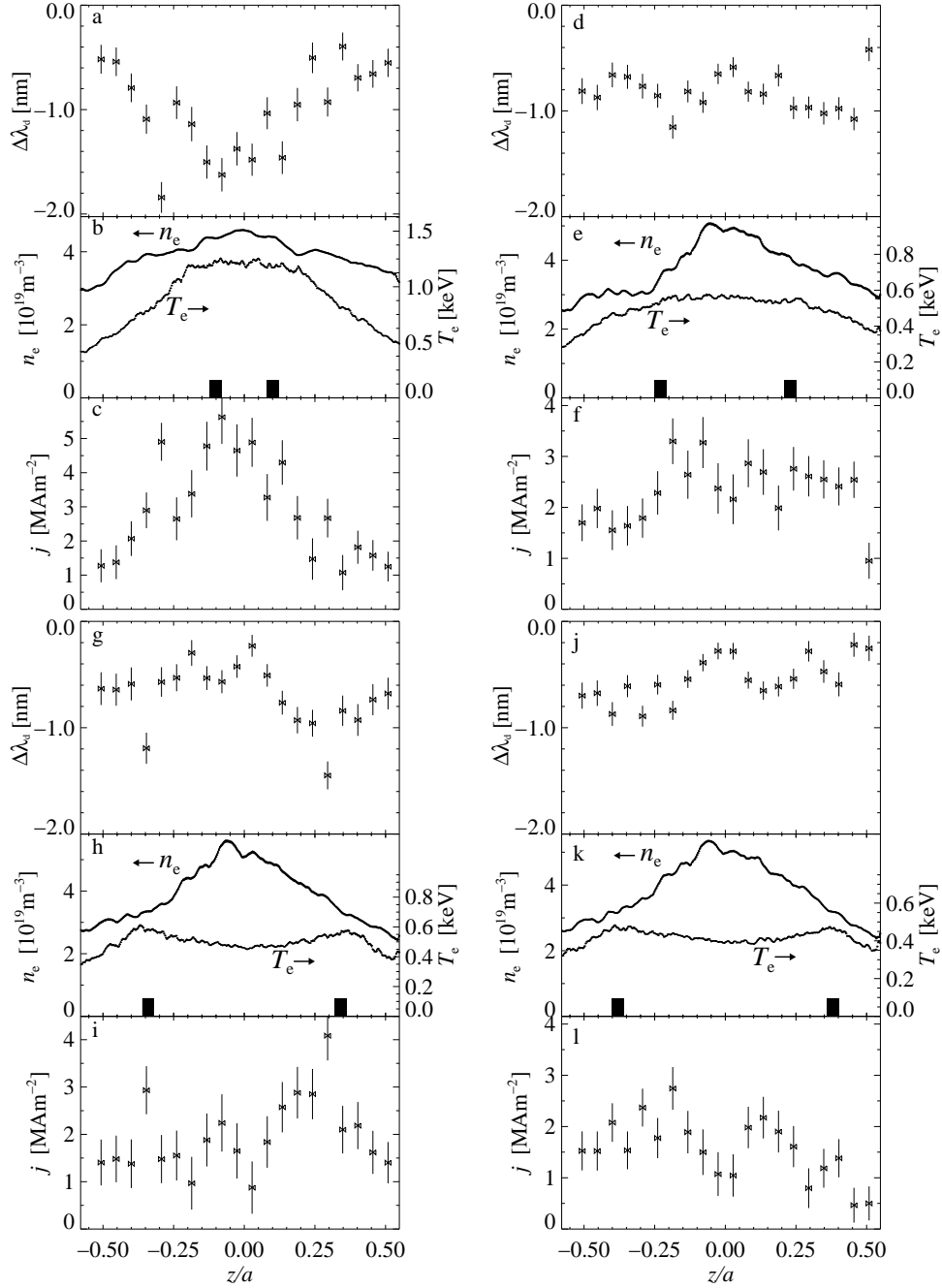


Figure 5.15: Measurements of $\Delta\lambda_d$, n_e , T_e and j for level A (a-c), level B (d-f), level C (g-i) and level D (j-l), cf. Fig. 5.14. The $\Delta\lambda_d$ data are averaged over the series of positive and negative I_p discharges and these averages are subtracted subsequently. The T_e and n_e data are both averaged over the positive and negative I_p discharges together. The j data is obtained from the $\Delta\lambda_d$ data. In Table 5.2 the numbers of averaged shots for the respective series are given.

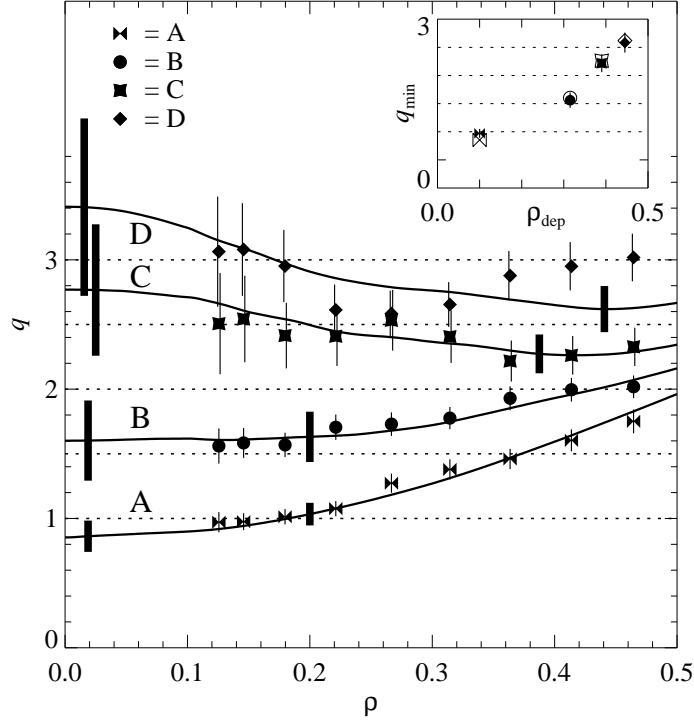


Figure 5.16: q profiles corresponding to the classes of T_e profiles of Fig. 5.14 as measured with TTS (symbols) and from NCR calculations (lines). In the box q_{\min} is plotted vs. ρ_{dep} for the measurements (closed symbols) and the calculations (open symbols).

negative shear area since j is very low there. Also, the minimum values of q (q_{\min}) of the measured and the calculated profiles are in good agreement to each other, as can be seen from the box in Fig. 5.16. Thus, it confirms the assumption that q_{\min} passes half-integer values between subsequent levels. This provides further backing for the RTP transport model, which assumes transport barriers at rational q surfaces [9,26,27,29].

5.5.5 Relaxation after off-axis ECH

In this subsection we focus on the relaxation of discharges with far off-axis ECH to the Ohmic mode after the switch-off of the ECH. In Fig. 5.17 the relaxation of the central T_e ($T_e(0)$) from ECE and the line-averaged density ($n_{e,\text{aver}} \equiv \int n_e dl / 2a$) after ECH switch-off are shown. The central temperature, which is low in off-axis heated discharges (cf. Fig. 5.14) rises to the Ohmic value it had before ECH was applied in about 60 ms. All ECE channels return to their pre-heating values similarly. The relaxation of $n_{e,\text{aver}}$ has multiple phases. The modest increase at

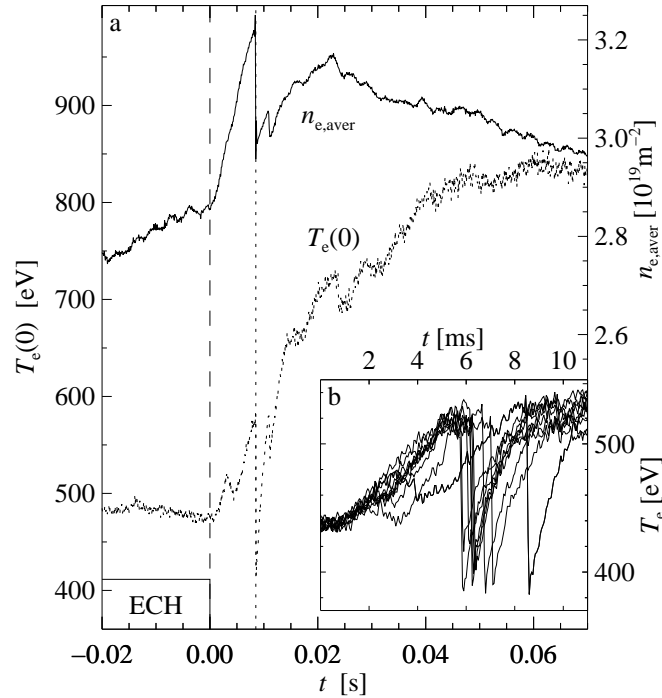


Figure 5.17: Central T_e ($T_e(0)$), as measured by ECH, dotted line) and line-averaged density ($n_{e,aver}$, as measured by interferometry, full line) around the switch-off of ECH at $t = 0$ (indicated by the vertical dashed line) ($\rho_{dep} = 0.53$). The vertical dotted line indicates an $m = 2$ MHD-event, which interrupts the n_e and T_e build-up (a). The insertion (b) shows T_e traces of eleven discharges, which all experience this event. $I_p = 90$ kA, $B_T = 2.26$ T, $\rho_{dep} = 0.48$.

the end of the ECH phase is due to gas puffing. After ECH switch-off, $n_{e,aver}$ has a sharp increase, ended by an MHD-event, which is also visible on ECE. The density reaches a maximum at $t = 23$ ms, which is a delayed response to the stop of the gas puff at $t = 2$ ms.

The relaxation after ECH switch-off of discharges with far off-axis ECH often experiences this MHD event. Actually, this crash occurs in most discharges at almost the same time, as can be seen from Fig. 5.17b. In this figure the ECE T_e traces of eleven similar discharges are shown, all having the crash between 5 and 9 ms from ECH switch-off. These eleven discharges are a subset of a series of 71 discharges ($\rho_{dep} \approx 0.53$) with such a crash. The magnetics are not clear, but do indicate a low poloidal mode number of 2 or 3.

Apparently, the event destroys an effective density build-up. The post-crash $n_{e,aver}$ rise is much slower than the pre-crash rise of $n_{e,aver}$. In contrast, the $T_e(0)$

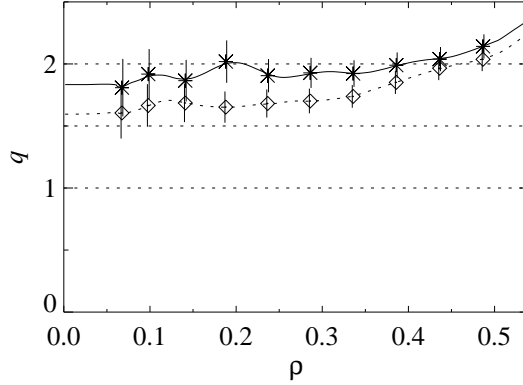


Figure 5.18: q profiles ~ 1 ms before (stars, full line) and after (diamonds, dotted line) the relaxational $m=2$ MHD crash as determined by TTS (See Fig. 5.17). The profiles are very flat inside $\rho = 0.4$.

trace picks up its previous pace quickly.

The inversion radius of the crash, as deduced from the ECE, $\rho \approx 0.5$, is comparable to ρ_{dep} during ECH. Though the T_e and p_e profiles are already peaked at the moment of the crash, the profile slopes are modest with respect to Ohmic discharges. Considering this and the fact, that at the start of the relaxation the magnetic shear is negative inside ρ_{dep} , it is interesting to know the q profile at the crash.

The crash characteristics match those of a similar event reported by De Baar *et al.* [25]. They found that this characteristic event is a necessary condition for the discharge to relax to the standard Ohmic state. In absence of the crash the discharge evolves to a regime with a high central n_e and low central T_e . They suggest also that the q profile plays a role determining the transport of heat and particles.

In series of similar discharges mentioned above, TTS measurements were taken around the crash to clarify the q profile. For the q profiles in Fig. 5.18 the data taken within 1 ms before and after the crash were used, obtained with TTS.

Both profiles are very flat within $\rho = 0.4$. The profile after the event is ~ 0.3 lower than that before the event. The corresponding j profiles suggest current penetration of ~ 3 kA from $\rho \sim 0.4$ to 0.2. This is in agreement with the q -profiles. The difference between the profiles is most pronounced in the region between $\rho = 0.2$ and 0.3. It has been reported earlier [27] that the absence of magnetic shear may lead to instabilities. This case represents an extreme situation, because the whole area between $\rho = 0.2$ and 0.4 has zero measured shear before the crash.

At the end of ECH a steady-state negative central shear discharge exist. Unfortunately, we have no direct q profile measurement, but based on section 5.5.4 it can be labelled as a 'level D' discharge with $q_{\text{min}} \approx 2.6$ and $\rho_{\text{dep}} \sim 0.45$. Since T_e is relatively low, the current diffusion is relatively fast, so that the measured flat

profile can be reached within 10 ms.

In the case of instabilities with low magnetic shear, the q value has usually a rational value with a low denominator. In this case the value of q just inside ρ_{dep} is ~ 2 before the crash. After the crash it is ~ 1.7 and the profile is monotonically increasing with ρ .

5.5.6 Electron drift velocity fluctuations

Up till here all presented data were averaged over several discharges. The single shot measurements can provide information on the level of fluctuations of the measured profile, in this case $\Delta\lambda_d$. From [31] we know that the spectra of the fluctuations on the T_e and n_e profiles from RTS are higher than expected from Poisson statistics for values of $1/k > 10$ mm, where k is the wave number. The T_e fluctuations are much stronger than the n_e fluctuations.

A fluctuation is defined as the signal after subtraction of the data filtered with a Gaussian filter with a Full Width Half Maximum (FWHM) of 20 mm (36 pixels). The fluctuations were determined in a series of 47 discharges with central ECH ($I_p = 60$ kA, $n_e(0) \approx 1.5 \cdot 10^{19} \text{m}^{-3}$, $B_\phi = 1.94$ T). In Fig. 5.19a to c a typical example taken from the series is shown, as well as the corresponding filtered data.

In Fig. 5.19d to f the power spectra of the fluctuations \tilde{T}_e/T_e , \tilde{n}_e/n_e and $\tilde{\Delta\lambda}_d$ are shown. To avoid spurious low frequency contributions the fluctuation analysis is restricted to the central part of the profile, i.e. z between -40 and 40 mm. The central parts of the 47 respective profiles are concatenated to form one long array before Fourier transformation. The shown noise spectra are known from the error analysis [21]. They have a high frequency cut-off due to the finite width of the instrument profile, which is 2.4 pixel FWHM. The instrument profile is indicated in Fig. 5.19d to f as well. For plotting reasons it is normalised to the simulated noise.

All three quantities have fluctuation levels higher than the noise levels for k values between 0.03 and 0.2 mm^{-1} . For k values close to and above the instrumental cut-off the curves of the simulated noise and the data come together. In case of the curves of \tilde{T}_e and \tilde{n}_e this is for $k \gtrsim 0.2$, in case of $\tilde{\Delta\lambda}_d$ for slightly lower values, $k \gtrsim 0.15$. This corresponds to minimum structure periods of 5 and 7 mm, respectively. The fluctuation level decreases towards low k because of the 2 cm FWHM Gaussian filter.

Though the spectra of the respective fluctuations have the same shape, their mutual linear regression correlation coefficients are small. From the shape of the power spectra it is clear that the high fluctuation level is not caused by erroneous error estimation.

In Fig. 5.20 the histogram of the 6862-element $\Delta\lambda_d$ fluctuation array is compared to the histogram of the simulated noise. The distribution resembles very well the normal distribution, as can be seen from the fit in the figure. The standard deviation of the distribution is 3.6 nm, which is 30% larger than the average statistical error of 2.8 nm. The χ^2_ν -distribution of the fits corresponding to the data in the histogram is shown in the box in Fig. 5.20. It is in good agreement with the theoretical distribution, backing the validity of the error estimation. For the T_e

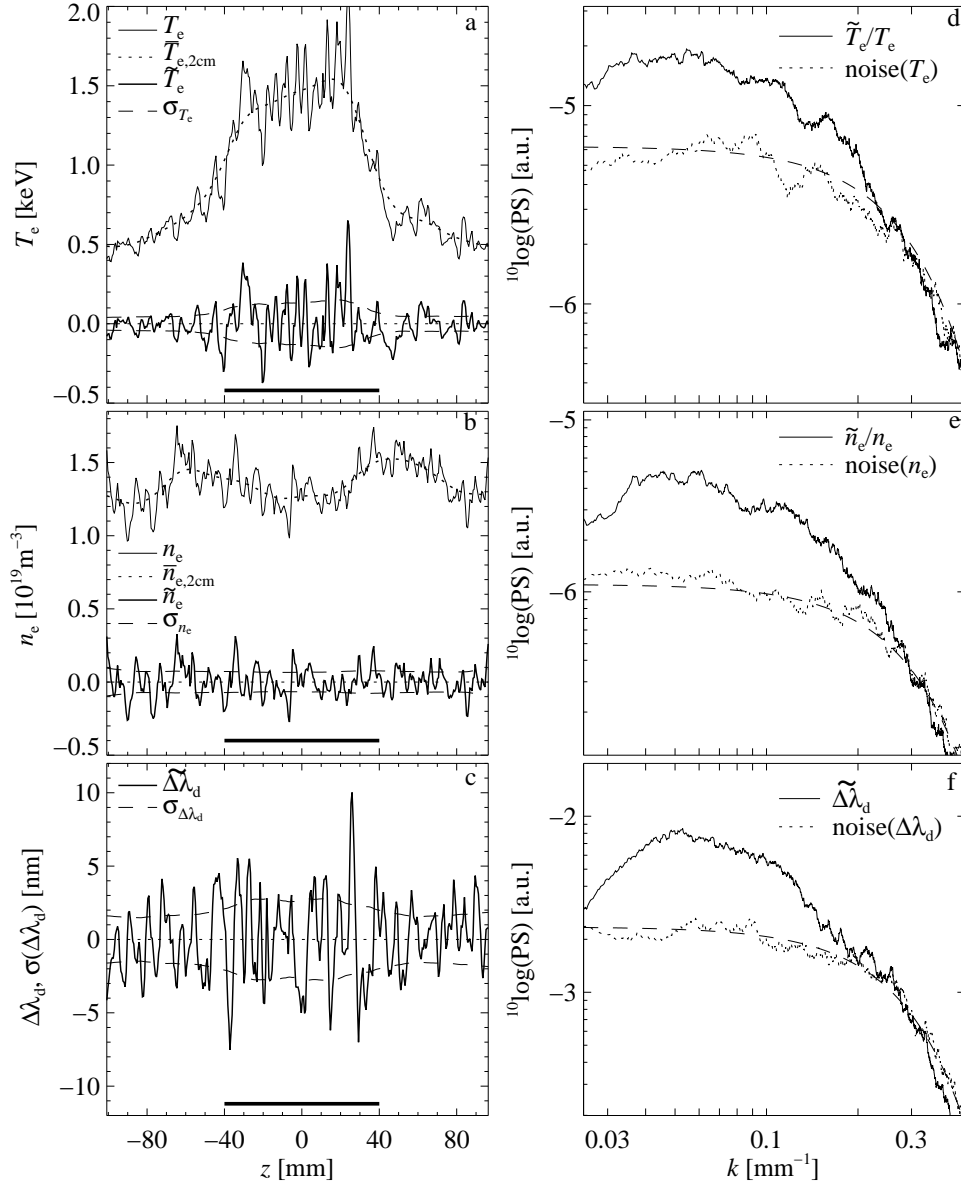


Figure 5.19: Typical profiles of T_e and \tilde{T}_e (a), n_e and \tilde{n}_e (b) and $\tilde{\Delta\lambda}_d$ (c) of a plasma with central ECH. The fluctuations are drawn with a thick line, the quantities themselves have thin lines. The fluctuation profiles are obtained by subtracting a low-pass filtered profile ($\bar{T}_{e,2\text{cm}}$, $\bar{n}_{e,2\text{cm}}$ and $\bar{\Delta\lambda}_{d,2\text{cm}}$, dotted lines. For clarity, the last one is hidden) from the measured profile (see also text). The horizontal bar drawn from $z = [-40, 40]$ mm, shows the area to which the power spectrum analysis is restricted. In figures d to f the full lines are the power spectra (for 47 discharges) of \tilde{T}_e/T_e (in d), \tilde{n}_e/n_e (in e) and $\tilde{\Delta\lambda}_d$ (in f). They are compared to the power spectra of simulated noise σ_{T_e} , σ_{n_e} and $\sigma_{\Delta\lambda_d}$, respectively (dotted). The dashed line is the instrument profile, normalised to the noise level for low frequency.

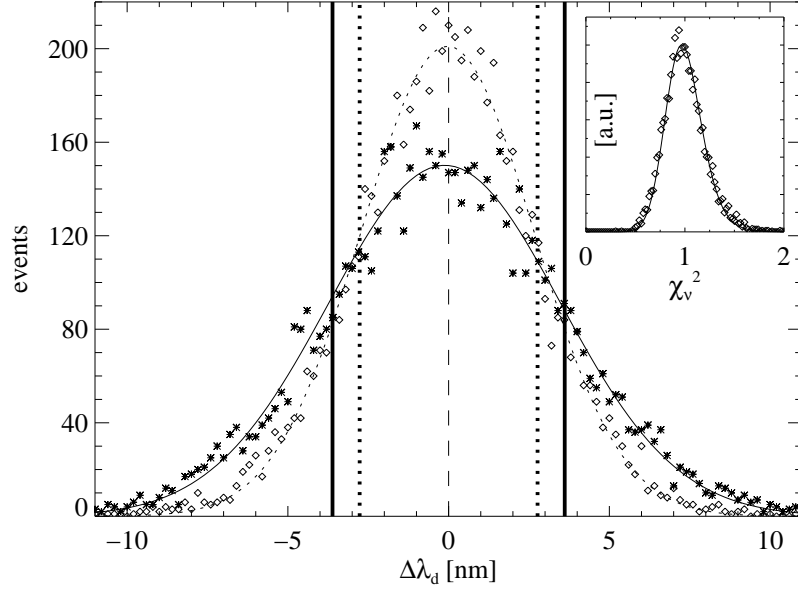


Figure 5.20: Histograms of the $\widetilde{\Delta\lambda}_d$ (stars) and the simulated error on $\Delta\lambda_d$ (diamonds), and the corresponding fitted normal distributions (full line and dotted line, respectively). The vertical bars indicate the standard deviation of the fluctuation distribution and is to be compared with the vertical dotted lines, which give the average error obtained from the data analysis. This error is the standard deviation of the simulated error distribution. The total number of data is 6862. In the box the χ_v^2 -distributions from the fits (points) and from theory (line) using the average number of degrees of freedom of the fit (60).

and n_e fluctuations, similar pictures can be made.

Since the statistical error on $\Delta\lambda_d$ is $\sim 100\%$, the relative fluctuation level on j is higher than on T_e or n_e . The average fluctuation has a shift of 3.6 nm and a period of ~ 10 mm ($k = 0.1\text{mm}^{-1}$). This amplitude corresponds to $j \sim 3\text{MAm}^{-2}$, which is significant with respect to the expected average $j \sim 4 - 5\text{MAm}^{-2}$. The ion drift velocity is unimportant, since its upper estimate corresponds to only 5% of j .

In similar analysis in [31], \widetilde{T}_e and \widetilde{n}_e were determined as well. The \widetilde{T}_e signals reported in [31] and here are in good agreement. The fluctuations on \widetilde{n}_e obtained here are higher than those reported in [31]. This difference is possibly caused by the difference in n_e and p_e between the two sessions. In [31], $n_e(0) = 2 \cdot 10^{19}\text{m}^{-3}$, in the session reported here, $n_e(0) < 1.5 \cdot 10^{19}\text{m}^{-3}$. The pressure differs a factor 2.2. This observation suggests an increase of the n_e fluctuation level with decreasing density.

5.6 Summary and discussion

The experiments in this paper have shown that current density (j) profile measurements are feasible in RTP with the tangential Thomson scattering set-up. 10-point profiles with errors of $\sim 10\%$ extending over 50 % of the plasma diameter were obtained in Ohmic plasmas and plasmas with dominant ECH deposited on- or off-axis. To obtain this statistical error, spectral information of 16 z pixel positions and 20 to 30 discharges was used. Very careful analysis was needed to suppress the systematic error. The full CCD resolution detector background was subtracted from both the TS and the plasma light measurements. Further, for each TS measurement the plasma light was determined within $100\mu\text{s}$ at full CCD resolution and subtracted from the measurement. The Doppler shift $\Delta\lambda_d$ of positive and negative current discharges were compared.

Two analysis methods have been presented and compared for simulated and measured data: The fit to a shifted Maxwellian corrected for relativistic effects according to Mattioli [23], and the calculation of the zeroth and first moment of the TS spectra. Both methods give results which are equal within error bars, both for simulated and measured data. Even for plasmas with dominant ECH no deviation from the Mattioli function was found.

From the TTS data the electron temperature (T_e) and the electron density (n_e) are determined simultaneously with the shift. In simulations it is shown that the introduction of $\Delta\lambda_d$ in the analysis does not influence the determination of T_e and n_e . Further, the results of radial TS (RTS) and TTS were compared and found to agree for T_e and n_e . In this case plasmas with dominant ECH were considered as well. A discrepancy is only found below $n_{e,\text{aver}} = 1.2 \cdot 10^{19}\text{m}^{-2}$. The T_e from TTS is higher, although the ECH heats the perpendicular velocity component. No plausible explanation for this effect has been found.

To obtain j both the electron and the ion drift velocity ($v_{d,e}$ and $v_{d,i}$, respectively) are needed. Since $v_{d,i}$ is not measured directly, it is estimated from edge measurements and the magnetic mode behaviour. Unfortunately, this estimate is not very precise. The upper limit on $v_{d,i}$ corresponds to an underestimate of j of 5 % in Ohmic discharges. For the plasmas with off-axis ECH this could be up to 15 % because j is lower. However, correction for this figure would not change the conclusions.

Current density profile measurements in Ohmically and ECH heated discharges were presented with $j(0)$ values varying between 1 and 4.5MAm^{-2} for far off-axis and on-axis ECH heated plasmas, respectively. The steady state measurements were in good agreement with neoclassical calculations of j from the T_e and n_e profiles, corrected for bootstrap current.

In discharges in which the deposition radius was varied between 0.1 and 0.4, the minimum values of the safety factor q are separated by half integer values. This observation is in agreement with the analysis of the MHD activity in these discharges and the neoclassical calculations mentioned above.

Fluctuation analysis of low density central EC heated discharges shows that the fluctuation level of T_e , n_e and $\Delta\lambda_d$ is significantly higher than the noise for the

scale length between 7 and 20 mm. If it is assumed these fluctuations represent current filaments, the current in such filaments can be estimated to be ~ 30 A. De Rover [32] uses similar current filaments in his numerical simulation of field line motion, giving magnetic field perturbations $\tilde{B}/B \sim 4 \cdot 10^{-4}$. This compares well with observations from cross-polarisation scattering at Tore Supra [33,34] and with estimates obtained from runaway confinement studies in TEXTOR-94 [35]. Thus, it cannot be excluded that the measured fluctuations correspond to physical j fluctuations in the plasma.

We have obtained j measurements with good accuracy from TTS by averaging several laser shots. If the number of detected photons per shot could be increased, less averaging is needed. This would mean a major improvement to the diagnostic. Recently, a multi-pass laser system was reported [36] which delivers a burst of 10 to 20 pulses of 80 to 150 J per pulse during the 1.5 ms flash-tube discharge, with a total energy of $\lesssim 1625$ J. Each pulse is passed multiple times through the plasma between two spherical mirrors after which it is returned to the laser. Laser pulses of this energy enable single shot TTS measurements with an accuracy comparable to or better than reported here.

Simultaneous TTS measurements along both directions of the tangent can be performed to suppress the systematic error. By this bi-directional detection the current reversal as applied here can be avoided.

Compared to the RTP plasma, large tokamak plasmas have one order higher electron temperatures, similar current densities and substantially higher electron densities. From our simulation we know that density variation does not influence the relative accuracy of the $\Delta\lambda_d$ determination. The simulation also shows that the error on $\Delta\lambda_d$ increases strongly with T_e for high T_e . This is due to two effects. The first is the limited spectral detection range used, which causes the spectrum to interfere with the edge. This edge effect can be suppressed by extension of the spectral width of the detector. Alternatively, the width of the observed spectrum can be varied between 0 and 100 % by an appropriate choice of the angle between laser injection and observation direction.

The second cause for the error increase is the reduction of the ratio between $\Delta\lambda_d$ and the width of the detected spectrum with increasing T_e . This ratio can be improved with up to 30 % with respect to the RTP set-up by increase of the angle between the laser and the plasma current.

By changing the scattering set-up, the edge effect, which is the major cause of the error increase, can be removed. The remaining error increase can be estimated from the simulation to be only a factor 2.5 at $T_e = 10$ keV with respect to 1 keV.

The duration of the discharges in large tokamaks enables multiple or repetitive laser operation during a discharge for higher photon yields. If the improvements mentioned above could be combined, the determination of j using tangential Thomson scattering on large tokamaks would become feasible.

Acknowledgements

This work was done under the association agreement of Euratom and the Stichting voor Fundamenteel Onderzoek der Materie (FOM) with financial support from the Nederlandse Organisatie voor Wetenschappelijk Onderzoek (NWO) and Euratom.

References

- [1] M. Mattioli and R. Papoular, *Plasma Phys.* **17**, 165 (1975).
- [2] I. H. Hutchinson, *Principles of Plasma Diagnostics* (Cambridge University Press, Cambridge, UK, 1987), ISBN 0-521-32622-2.
- [3] J. Sheffield, *Plasma scattering of electromagnetic radiation* (Academic Press, New York, US, 1975), ISBN 0-12-638750-8.
- [4] I. H. Hutchinson, *J. Phys. D: Appl. Phys.* **10**, L11 (1977).
- [5] F. Alladio and M. Martone, *Phys. Lett.* **60A**, 39 (1977), and *Phys. Lett.* **64A** 199.
- [6] C. J. Barth, *Rev. Sci. Instrum.* **60**, 2673 (1989).
- [7] C. D. Challis *et al.*, in *Proc. 26th Conf. Control. Fusion Plasma Phys., Maastricht 1999* (EPS, Vienna, Austria, 1999), p. 69.
- [8] G. Gormezano, *Plasma Phys. Control. Fusion* **41**, B367 (1999).
- [9] G. M. D. Hogewei, N. J. Lopes Cardozo, M. R. de Baar, and A. M. R. Schilham, *Nuc. Fus.* **38**, 1881 (1998).
- [10] H. Soltwisch, in *Proc. IAEA-CN-47/A-V-1* (IAEA, Vienna, 1986), p. 263.
- [11] D. Wróblewski, L. K. Huang, and H. W. Moos, *Rev. Sci. Instrum.* **59**, 2341 (1988).
- [12] H. Kuramoto *et al.*, *Fusion Eng. Design* **34-35**, 285 (1997).
- [13] W. P. West, *Rev. Sci. Instrum.* **57**, 1552 (1986).
- [14] F. M. Levinton, *Rev. Sci. Instrum.* **63**, 5157 (1992).
- [15] L. Kellerer, *Z. Physik* **239**, 147 (1970).
- [16] D. E. Evans and P. G. Carolan, *Phys. Rev. Lett.* **25**, 1605 (1970).
- [17] M. J. Forrest, P. G. Carolan, and N. J. Peacock, *Nature* **271**, 718 (1978).
- [18] A. C. A. P. van Lammeren *et al.*, *Nuc. Fus.* **32**, 655 (1992).
- [19] C. J. Barth *et al.*, *Rev. Sci. Instrum.* **68**, 3380 (1997).
- [20] C. J. Barth, B. J. J. Grobber, and G. C. H. M. Verhaag, *Appl. Opt.* **33**, 6062 (1994).
- [21] M. N. A. Beurskens, C. J. Barth, and N. J. Lopes Cardozo, *Rev. Sci. Instrum.* **70**, 1999 (1999).
- [22] C. C. Chu *et al.*, Calibration procedure and data processing for the multiposition Thomson scattering system at RTP, 2001, submitted to *Rev. Sci. Instrum.*
- [23] M. Mattioli, Incoherent light scattering from high temperature plasmas, EUR-CEA-FC-752, 1974, DPh-PFC-SPP Fontenay-aux-Roses, France.
- [24] M. N. A. Beurskens, C. J. Barth, N. J. Lopes Cardozo, and H. J. van der Meiden, *Plasma Phys. Control. Fusion* **41**, 1321 (1999).

-
- [25] M. R. de Baar, G. M. D. Hogeweij, and N. J. Lopes Cardozo, *Phys. Rev. Lett.* **82**, 89 (1999).
 - [26] N. J. Lopes Cardozo *et al.*, *Plasma Phys. Control. Fusion* **39**, B303 (1997).
 - [27] M. R. de Baar *et al.*, *Phys. Rev. Lett.* **78**, 4573 (1997).
 - [28] P. C. de Vries, Ph.D. thesis, Universiteit Utrecht, the Netherlands, 1997.
 - [29] M. R. de Baar *et al.*, *Phys. Plasmas* **6**, 4645 (1999).
 - [30] D. F. da Cruz, Ph.D. thesis, Universiteit Utrecht, the Netherlands, 1993.
 - [31] M. N. A. Beurskens, Ph.D. thesis, Technische Universiteit Eindhoven, the Netherlands, 1999.
 - [32] M. de Rover, Ph.D. thesis, Technische Universiteit Eindhoven, Eindhoven, the Netherlands, 1996.
 - [33] X. L. Zou, L. Colas, *et al.*, *Phys. Rev. Lett.* **75**, 1090 (1995).
 - [34] L. Colas *et al.*, *Nuc. Fus.* **38**, 903 (1998).
 - [35] I. Entrop, N. J. Lopes Cardozo, R. Jasper, and K. H. Finken, *Phys. Rev. Lett.* **84**, 3606 (2000).
 - [36] M. Y. Kantor and D. V. Kouprienko, *Rev. Sci. Instrum.* **70**, 780 (1999).

6

PARTICLE TRANSPORT IN THE RTP TOKAMAK

6.1 Introduction

The density profile in tokamaks is usually peaked, although the particle sources in the centre are small. Various observations of peaked density profiles have been reported (see the reviews [1–4]). It is generally assumed that an inward particle convection exists, that equilibrates the diffusion down the gradient. However, the nature of this flux is unknown.

Neoclassical theory predicts a particle pinch, called after the first reporter of this effect, Ware [5]. This theoretical pinch is in most reported cases too small to account for the observed density profile peaking. So, the neoclassical Ware pinch acts as a lower limit to the pinch, rather than a prediction.

The particle flux (Γ) is usually expressed in terms of a diffusive and a convective part:

$$\Gamma = -D\nabla n - \mathbf{V}n , \quad (6.1)$$

where D represents the diffusion coefficient, n is the particle density and \mathbf{V} has the dimension of velocity and is therefore called the pinch velocity. We dropped the subscript on n . For low Z_{eff} discharges like those in RTP, the ion and electron densities are to good approximation equal $n_e = n_i = n$.

In steady state, if the particle sources can be neglected, Γ is zero and the diffusive and convective parts balance each other. From the steady state density profile, the ratio of D and V can be determined. It is proportional to the density gradient length (L_n):

$$\frac{D}{V} = \frac{n}{|\nabla n|} \equiv L_n . \quad (6.2)$$

It has been reported for several tokamaks that the n profile shape is remarkably insensitive to variations of the plasma parameters, *i.e.* L_n is fixed [4].

The aim of the study in this chapter is to determine the relation between the particle transport and the plasma parameters T_e and j from the experiments in RTP. Since both D and V are anomalous, the study of the dependences of the particle transport coefficients is important for the understanding of the physical mechanisms causing the anomalous D and V . It is also important that the existing theoretical models and scaling expressions are tested against the experimental data. This is also part of the study in this chapter.

To determine the values of both D and V , it is necessary to perform time resolved measurements. Results reported by the different groups are contradicting. D and V are proportional to n^α with α between -1 and 0 . In TFTR [6,7] D and V are reported to be proportional to T_e^2 , but in other tokamaks [3,4] no dependence on the temperature has been found. The reported dependence on the edge safety factor q_a varies between power -1 and -2 . Summarising, the mechanisms determining the particle transport are not yet crystallised from the research.

The tokamak RTP is well equipped to study the particle transport, because the n_e profile can be measured with the 19-channel interferometer and multi-position Thomson scattering (TS) diagnostic independently (see Chapter 4 and 5, respectively). The interferometer gives the required time resolution. The profiles of the electron temperature (T_e) and safety factor (q) can be varied between very peaked and hollow shapes with the help of Electron Cyclotron Heating (ECH). The electron temperature T_e is determined with Electron Cyclotron Emission (ECE) and TS independently. Unfortunately, j can not be measured, but it can be calculated from the T_e and n profiles from neoclassical theory. The results of these calculations are confirmed by the measurements presented in Chapter 5.

The main tool for the study in this chapter is the transport code ASTRA [8]. With this code neoclassical theory as well as several expressions from the literature can be tested against experimental data.

The chosen approach is as follows: In section 6.2 a brief introduction into particle transport theory is given. The neoclassical expression for the particle fluxes is reviewed and several expressions for the particle transport are introduced. These expressions are tested against the data later.

The balance of particles is determined by the sources and sinks of charged particles and the particle fluxes. In section 6.3 the sources and sinks are discussed. In particular, the penetration of neutral particles into the plasma and the associated particle source are treated in detail.

The rest of the chapter focuses on the particle flux. In section 6.4 the RTP experiments relevant to the particle transport are presented. The presentation of this varied set of observations gives already clues about the mutual interaction of the plasma parameters. These provide the basis for the transport simulations with

ASTRA, presented in section 6.6. But before that, the previous particle transport results on RTP are reviewed and compared to simulations of the steady state in section 6.5.

Section 6.6 has the following cyclic structure: The observation of a transition in the plasma is presented. Subsequently, the various expressions introduced in section 6.2 are used to simulate this transition. The results of these simulations are discussed and compared. After this, the next cycle starts, with another transition.

Section 6.7 contains the summary of the results of this chapter, section 6.8 is the evaluation and discussion of the material presented in this chapter.

6.2 Theoretical background

In sections 6.2.1-6.2.5 the expressions are introduced, which are tested with ASTRA against the RTP data. First a brief description of particle transport is given and the neoclassical theory as introduced in section 2.2 is reviewed.

The transport of a particle species, *e.g.* electrons or ions, can be described by the conservation of particles:

$$\frac{\partial n}{\partial t} = -\nabla \cdot \Gamma + \Sigma S, \quad (6.3)$$

where ΣS represents the sum of all processes by which particles of the species under consideration come into existence and disappear, also referred to as the particle 'sources' and 'sinks', respectively.

The sources of particles come from ionization of neutrals. These neutrals can originate from sources like pellets or injected neutral beams. Here, only the neutrals entering the plasma from the edge are considered. In section 6.3 it is shown that the particle source is negligible with respect to $|\nabla \cdot \Gamma|$ in a large central part of the plasma.

The particle sinks are the various processes in which free electrons are captured in atoms and molecules. The most important of these is the recombination of hydrogen ions and electrons to neutral hydrogen. However, in the plasmas under consideration the cross-section for recombination is more than 6 orders below the ionization cross-section, and the particle sink can be neglected.

The reason for the absence of a subscript on Γ is that the plasma is 'quasi-neutral', *i.e.* there is no net charge in any volume and the electron and ion fluid motions are coupled to each other.

If we look at Eqs. 6.1 and 6.3, it is clear that if D and V are increased while V/D is kept constant, the diffusion and convection fluxes are higher. Hence, the time constant of the particle diffusion is shorter. Summarising, the ratio V/D can be obtained from the steady state profile, while the absolute values of D and V can only be obtained from the time development of $n_e(r)$.

In the formalism of Chapter 2 for the neoclassical transport the radial component of the particle flux can be expressed as follows (*c.f.* Eq. 2.19):

$$\Gamma_{\text{nc}} = -D_{\text{nc}}\nabla_r n - c_{12}n\nabla_r T_e - c_{13}n\nabla_r T_i - WE_{\parallel} , \quad (6.4)$$

where the coefficients are the neoclassical coefficients, E_{\parallel} is the amplitude of the parallel electric field, and ∇_r is the radial component of the ∇ -operator. The neoclassical coefficients are too small to explain the particle transport in RTP. If we assume that in case of anomalous transport the gradients in Eq. 6.4 determine the transport, the following equation is obtained:

$$\Gamma = -D\nabla_r n - (D_T \frac{\nabla_r T_e}{T_e} + V_W)n . \quad (6.5)$$

For convenience, the term proportional to $\nabla_r T_i$ has been dropped. At RTP no measurements of T_i are available and this term is not considered in the following. This is allowed since the ions are heated exclusively via the electrons, and the electron-ion exchange time is much larger the energy confinement time. Hence, T_i is much lower than T_e . Only if $c_{13} \gg c_{12}$, this assumption is not valid.

In this equation D and D_T are the anomalous diffusion and thermo-diffusion coefficient, respectively, and V_W is the anomalous pinch. The term with V_W is not explicitly dependent on E_{\parallel} as in Eq. 6.4. This is to allow for more general expressions for the pinch velocity.

If Eq. 6.5 is compared to Eq. 6.1, we find that the convective part of the flux in Eq. 6.1 is expressed in two parts in Eq. 6.5, a thermo-diffusion part and a part proportional to the parallel electric field. In the next subsections, these two terms of the particle flux will be discussed, as well as other proposed pinch effects.

6.2.1 Ware pinch

The Ware effect arises from the interaction of the parallel electric field (E) with the trapped particles in the banana orbits. The field E causes the banana orbits to be displaced by a small poloidal angle with respect to the horizontal plane. As a consequence, the effect of the curvature drift and the grad- B drift is no longer symmetric about the mid-plane and the trapped particle ends up a little step inward each time it completes a full banana orbit. The corresponding drift velocity V_W is:

$$V_W \sim \frac{E_{\parallel}}{B_{\theta}} . \quad (6.6)$$

It is directed radially, and because of the minus sign of this term in Eq. 6.5 it is directed inwards.

The Ware pinch follows directly from neoclassical theory with the following coefficient:

$$V_{W,\text{nc}} = 2.44 \frac{E}{B_{\theta}} . \quad (6.7)$$

Varma [9] argues that since the ions and the electrons have opposite charge, their banana orbits shift in opposite directions in θ . This leads to separation of charges and a vertical electric field. The corresponding $E \times B$ drift is directed towards the tokamak axis. Since the banana orbits are mainly at the LFS the net effect is an increased inward drift of the trapped particles:

$$V_{\text{Varma}} = \frac{8}{9} \epsilon^{-1/2} (1 - \sqrt{\epsilon})^{-1} \frac{E}{B_\theta} \equiv f_V \frac{E}{B_\theta} . \quad (6.8)$$

Note that the incremental factor with respect to Eq. 6.6 (f_V) is a geometrical factor, because it depends on the inverse aspect ratio (ϵ) only. For RTP, $\epsilon \leq 0.227$ and $V_{\text{Varma}} \geq 3.56E/B_\theta$. At half radius, $f_V = 4.00$.

As mentioned before, the predicted value of the neoclassical Ware pinch $V_{W,nc}$ is usually smaller than the measured pinch effect. Varma claims that with his correction the pinch is strong enough to take account for the measurements. This claim is tested in section 6.5.2.

The pinches described in this section involve only the trapped particles. To obtain the effect on the plasma as a whole they have to be corrected for the relative concentration of the trapped particles. This consists of two factors. The first factor gives the trapped particle fraction (f_t) in a collisionless plasma. In a tokamak plasma with circular cross-section this is [10]:

$$f_t = 1.46\sqrt{\epsilon} . \quad (6.9)$$

The other factor (f_ν) corrects for the collisionality of the plasma:

$$f_\nu = \frac{1}{1 + \nu^*} . \quad (6.10)$$

This factor accounts for the fact that electrons that make a collision before completing a full banana orbit are effectively not trapped.

The final expression for the Ware pinch is:

$$W = f_V f_t f_\nu \frac{E}{B_\theta} . \quad (6.11)$$

If the text is referring to the Ware pinch, this expression is meant with the Varma factor $f_V = 2.44$. In case the Varma pinch is mentioned, the expression for f_V is used (*c.f.* Eq. 6.8)

6.2.2 Thermo-diffusion

Neoclassical theory predicts a non-zero electrical thermo-diffusion coefficient like D_T we defined before. This coefficient is negative, *i.e.* in a plasma with zero density

gradient, a T_e gradient causes a particle flux towards the hot region. In the case of tokamaks, where T_e is usually peaked at the centre of the plasma this represents an inward particle flux, in the same direction as the Ware pinch. The predicted D_T is of the order of the neoclassical D and as a consequence the neoclassical thermo-diffusion flux is negligible with respect to the anomalous convective flux. In [11] an anomalous thermo-diffusion coefficient has been proposed.

The anomalous thermo-diffusion has been shown to be appreciable in case of low-frequency electrostatic turbulence. It is possibly driven by a temperature gradient [12,13]. The physical mechanism responsible for the convection in this case is the decrease of the diffusion coefficient with velocity within the velocity distribution, *i.e.* the high velocity part of the distribution diffuses slower than the low velocity part. This effect introduces an electron temperature gradient dependence.

Terry [12] argues that only in the collisionless case, above a threshold temperature the effect occurs, but Miskane [13] finds it occurs in the general case. He finds the following relation between D and D_T :

$$D_T = D_{T,0} - \frac{1}{2}D, \quad (6.12)$$

where both D and $D_{T,0}$ can be expressed as integrals over the velocity distribution. He obtains values between $D_T = -0.02D$ and $-0.46D$, for various strengths of the electrostatic turbulence. The strength of the effect decreases with increasing magnetic shear.

6.2.3 Electrostatic Turbulence

It is noted [14–16] that the typical potential fluctuation amplitude of generic low-frequency electrostatic turbulence is tens of Volts. This number is large compared to the macroscopic parallel electric field of typically 1 V/m or lower. Hence, the pinch associated with such fluctuations might be large. However, the turbulence has zero average, so it does not give an average convection, but only diffusion. In the absence of convection, any diffusion makes the steady state n profile flat.

In Ref. 14–16 it is shown that the steady state density profile from this diffusion is not uniform. We will not go into the details of the argumentation, but give the results and the important restrictions instead.

It is argued that the average trapped particle distribution as obtained from the turbulence induced diffusion, is constant in ψ , the poloidal magnetic flux coordinate. From this density uniform in ψ , the density profile in the radial coordinate r can be calculated. This calculation can be done independently of the exact shape and strength of the turbulence and the resulting profile is a so-called 'consistent' profile. It is inversely proportional to qH , where q is the safety factor and H is a geometrical factor. For plasmas with circular cross-section and large aspect ratio H is equal to 1.0. Note that this profile is peaked in case of monotonically increasing q .

The consistency of the profile means that in non-steady state the plasma will try to relax to the steady state, giving the following convection velocity [16]:

$$V = -D\nabla_r \ln q \quad (6.13)$$

Note that with this pinch the ratio V/D is proportional to s/r , where s is the magnetic shear. In the following, (*i.e.* section 6.6) this convection expression is referred to as the ' q^{-1} -pinch'.

Though the result is obtained strictly for trapped particles, it is shown in [16] that the inclusion of the passing particles will not give a significant modification to the obtained profile shape. For the perturbative transport study performed in section 6.6, we can assume these are not important.

6.2.4 Scaling with neutral density

Becker [17,18] presented an experimental scaling of V/D with the neutral density (n_n) profile:

$$\frac{V}{D}(\rho) \sim n_n(\rho)\rho . \quad (6.14)$$

The argument for this scaling is the notion that if the sources are neglected, the steady state n profile has an L_n^{-1} increasing strongly towards the edge, just like the n_n profile. Since n_n is rather insensitive to the plasma parameters, this scaling also explains the observed stiffness of the n profile shape.

Towards the edge Becker finds an exponential increase of V . However, this increase might be an artifact caused by incorrect neglect of the electron source close to the edge. Despite our doubts about this neglect, also this expression is tested against the experimental data.

6.2.5 Other pinch mechanisms

There are other suggested mechanisms for the anomalous particle pinch. It has been attributed to anomalous viscosity in the presence of sheared toroidal rotation [19,20] and inductive electric fields caused by the edge plasma source [21,22]. It has also been suggested that it is a consequence of the conservation of angular momentum of the ions in a slightly non-neutral plasma [23]. These models will not be discussed here, since they involve transport via the ion channel, which we are unable to study.

6.3 Particle source and Neutral density

In the particle diffusion equation Eq. 6.3 the right hand side contains the sum of all sources and sinks in the plasma. The sources are due to the ionization of neutral atoms and molecules in the plasma, the sinks are caused by recombination of charges into neutral particles. In this section we consider a pure hydrogen plasma and make an estimation of the sources and sinks in this plasma. This estimate is

important to determine what the origin of the particles in the centre is: Do they come from a central source or are they transported towards the centre, *e.g.* by a pinch term in the flux?

The transitions from neutrals to ions and electrons and vice versa happen during collisions. Quantitative analysis makes use of the collision 'cross-sections'. Each kind of collision has its specific cross-section σ . From the cross-section the collision rate $\langle\sigma v\rangle$ can be determined, where v is the velocity of the fastest incident particle, determining the velocity of impact. The average is taken over the velocity distribution of this particle. In a tokamak plasma, the particle determining the velocity of impact is the hot charge from the plasma.

The collision rate for recombination in a tokamak plasma is much lower than that for ionization by electrons. Hence, the neutral concentration in the plasma is determined by the balance between neutrals which enter the plasma from the wall and the ionization. The charged particles which are lost from the plasma cool down at the vessel wall and recombine to neutral particles. These neutrals re-enter the plasma.

The processes concerning the production of the neutrals, which take place between the last closed flux surface and the vessel wall and at the limiter are not discussed here. We will assume that the neutrals, which enter the plasma can be characterised by one temperature. This assumption might be violated regarding the reported differences between the circumstances at the wall and at the limiter [24]. Further, both atomic and molecular hydrogen enter the plasma. We assume that the molecules dissociate in a short distance from the wall and can be neglected. We will come back to this assumption in section 6.3.2.

In this simplified problem two collision types are dominant: The electron-impact ionization in which an incident electron (e^-) scatters the bound electron from the neutral hydrogen (H):



and ion-impact charge-exchange, in which the incident ion (i) takes over the electron and becomes atomic hydrogen:



These two processes have comparable cross-sections. Further, for the incoming particles in the temperature range $10\text{-}10^4$ eV, both cross-sections vary less than one order of magnitude. Therefore they are treated as constants: $\langle\sigma_{\text{ion}}v_e\rangle = 1.5 \cdot 10^{-14} \text{ m}^3\text{s}^{-1}$ and $\langle\sigma_{\text{cx}}v_i\rangle = 2.0 \cdot 10^{-14} \text{ m}^3\text{s}^{-1}$.

The input particles of the charge-exchange reaction in Eq. 6.16 are the same as the products, but the energetic incident ion has become a hot neutral, and the incident cold neutral has become a cold ion. This means that the charge-exchange reaction creates a second neutral population with a much higher temperature than the original one, which has the temperature of the edge. The original population will

be referred to as 'cold' neutrals, the charge-exchanged population will be referred to as 'hot' neutrals. In equations the indices 'c' and 'h' are put on the neutral density if only one of the populations is referred to: $n_{n,c}$ for the cold neutral density and $n_{n,h}$ for the hot neutral density.

In section 6.3.1 an analytic solution for the neutral transport problem is presented assuming a plasma density which increases linearly with the distance from the wall. After that, the RTP neutral density will be discussed in section 6.3.2.

6.3.1 Analytic solution of the Neutral Diffusion Equation

The distribution of neutrals can be considered as a diffusive process if random scattering of the neutrals occurs. Suppose the charge exchange process is this process: The number of neutrals is constant in this reaction and the resulting velocity has little correlation with the incident velocity. The step size of the random walk of the neutrals is the mean free path for charge exchange (λ_{cx}):

$$\lambda_{cx} \sim \frac{v_n}{n \langle \sigma_{cx} v_i \rangle} \quad (6.17)$$

The neutral velocity v_n is replaced by the ion thermal velocity $v_{t,i}$, assuming thermal equilibrium between the charged exchanged neutrals and the ions.

If we assume that the plasma density n increases linearly with the distance from the edge, $n = \beta(a - r) + n_a$, where β is a constant and n_a is the offset edge density, then the stationary diffusion equation in one dimension can be solved analytically. This is shown in the appendix of this chapter. The resulting expression for n_n is as follows:

$$n_n = \frac{n_{n,0}}{2\gamma} \exp \left(-\frac{1}{2} \gamma [(a - r)^2 - (n_a/\beta)^2] \right), \quad (6.18)$$

$$\gamma^2 = \frac{\beta^2}{v_{t,i}^2} \langle \sigma_{cx} v_i \rangle \langle \sigma_{ion} v_e \rangle,$$

which is a Gaussian. In the appendix an estimate for $n_{n,0}$ is made as well.

For RTP, λ_{cx} yields values between 0.3 and 1 m for the typical RTP parameter values, if we assume that the neutrals are thermalised with the plasma. Hence, a charge-exchanged neutral has a small chance to participate in a charge exchange or ionization reaction again while inside the plasma ($a = 0.164$ m). The physical length between reactions is clearly too long for the assumption of random walk diffusion to hold.

Therefore, we must conclude that the obtained expression for n_n is not applicable to RTP. Nevertheless, for a larger tokamak with higher edge temperature and density, the result can be valuable. In section 6.3.2 we will discuss an alternative approach to the problem of the neutrals in RTP. In this section the following finding is used: In good approximation, the neutral experiences only one or two reactions in the plasma before being ionised or being lost to the wall, and not more than

that. With this as a starting point, the stationary n_n profile can be calculated numerically. The model is bench-marked against the EIRENE code [25] and is used to calculate the RTP n_n profile.

6.3.2 A Numerical Model of Neutral Penetration and the Benchmarking Against the EIRENE Code

Above we found that the penetration of neutrals can not be considered as a diffusive process. Alternatively, the n_n profile can be determined numerically. A well-known code for the calculation of the behaviour of neutral particles is the EIRENE-code [25]. This is a two-dimensional Monte Carlo code to simulate the neutral concentration of multiple species in the tokamak plasma and its scrape-off layer.

Unfortunately, we have not been able to do many runs with EIRENE, due to circumstances. Nevertheless, two runs could be performed with the RTP geometry implemented in the code. With these runs, we could benchmark the numerical model we developed for RTP. First, this model is introduced. Then, the results of the model are compared to the EIRENE runs. Since the results of both methods agree well, the model is used to calculate n_n in RTP.

description of the model

We found in section 6.3.1 that the penetration depth of charge-exchanged neutrals exceeds the minor radius of RTP. Hence, the concentration $n_{n,h}$ is likely to be constant over the system. However, the penetration depth of the cold neutrals from the edge is much smaller than the minor radius, so their concentration $n_{n,c}$ will fall rapidly with the distance from the edge.

Most incoming neutrals have only one or two interactions in the plasma. Ionization acts as a sink for the neutrals, so only the charge-exchanged neutrals remain neutral. these are however hot and consequently have a high chance to be lost to the wall.

The task is to determine the ratio between $n_{n,c}$ and $n_{n,h}$. The n_n profile has its maximum at the edge, caused by the $n_{n,c}$ profile, but in the centre $n_{n,h}$ determines n_n . For deduction of the central n_n from the edge value, the ratio of $n_{n,c}$ and $n_{n,h}$ has to be known.

For this a simple iterative scheme is set-up to calculate the steady-state n_n . As a consequence of the fact that the hot neutrals experience few reactions, we must keep track of the direction of their motion. This is the main difference with the treatment of section 6.3.1, where the random walk of the neutrals is one of the basic assumptions. The $n_{n,h}$ and $n_{n,c}$ profiles are calculated iteratively using the fluxes, sources and sinks of the previous $n_{n,h}$ and $n_{n,c}$ profiles.

We take a one-dimensional slab of plasma with a fixed background plasma density n . For this, the measured density can be taken, but in this case a linear approximation to the measured density is used. The fluxes and sources of the two constituents are calculated and from those new concentrations are calculated. At one side a constant influx of cold neutrals of constant velocity is assumed. This

wall is a perfect absorber for incident neutrals. At the other side, a reflecting wall is imposed: Incident particles come back with identical but reversed velocity. This resembles the case where a particle crosses the tokamak centre. The ionization and charge exchange rates are assumed constant over the slab, as well as the temperature of the hot neutrals. This last assumption holds because the major part of the hot neutrals is formed in a single charge exchange reaction close to the edge.

The effect of the reactions are treated as three-dimensional in the slab. The motion of the entering neutrals has no preferential direction and the reactions act as direction-randomising events. In our one-dimensional calculation the average projection of the velocity on the dimension x is taken. For the motion along the positive or negative x axis, this is the average of a half sphere onto its symmetry axis, which is $1/2$ times the radius.

For the cold neutrals there is one flux, the influx from the edge, and one sink, the combined effect of charge exchange and ionization. For the hot neutrals, there are in- and out-fluxes. The source is the charge-exchange of cold neutrals, the sink is ionization of hot neutrals.

First, the results of the slab calculation are compared to calculations with the EIRENE code. In Fig. 6.1 the results of the EIRENE simulation and the slab calculation are shown for a low density ($n(0) = 2 \cdot 10^{19} \text{m}^{-3}$) and a high density ($n(0) = 7 \cdot 10^{19} \text{m}^{-3}$) RTP plasma. Both EIRENE and the slab calculation were run with parabolic T_e and n_e profiles.

The results are in quantitative agreement with each other. For low x , the n_n curves fall off strongly with x . For higher x , the curves become more or less independent of x , at a low value. The EIRENE results do not decrease immediately at $x = 0$, probably due to the effect of the scrape-off layer.

The EIRENE results also indicate that the neglect of other hydrogen species is allowed: Their densities are more than one order below the atomic hydrogen density.

Summarising, since the results of the slab calculation and the EIRENE simulation agree well, the slab calculation is appropriate for calculations of n_n in RTP.

In Fig. 6.2 the result of a calculation with central n of $3 \cdot 10^{19} \text{m}^{-3}$ is shown. The neutral density decreases strongly with the distance to the edge up to $x/a \sim 0.3$, above which it converges to a more or less constant level of less than 5% of the edge neutral density. The decreasing part is the 'cold' neutral density ($n_{n,c}$), the constant level is due to the 'hot' neutrals ($n_{n,h}$). For $x/a \gtrsim 0.35$, $n_{n,h}$ is larger than $n_{n,c}$.

If we assume perfect recycling at $x = 0$ and neglect the convection of the ions and the hot neutral out-flux:

$$D \frac{\partial n}{\partial x}(0) + v_{n,x} n_n(0) = 0, \quad (6.19)$$

where $v_{n,x}$ is the velocity of the cold neutrals in x -direction. With the parameters of Fig. 6.2 and $D = 1 \text{ rmm}^2/\text{s}$, the estimate $n_n(x = 0) = 5 \cdot 10^{15} \text{m}^{-3}$ is obtained. Note that a higher n gives a higher $n_n(0)$. This is in agreement with the experimental situation, where stronger gas puffing leads to higher densities.

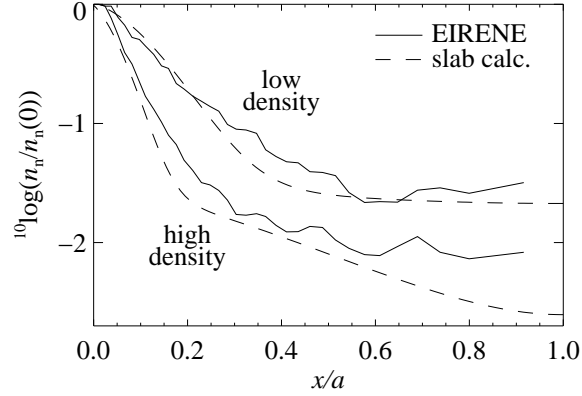


Figure 6.1: Neutral densities obtained with EIRENE (full lines) and the slab calculation (dashed lines for low density ($n(0) = 2 \cdot 10^{19} \text{m}^{-3}$) and high density ($n(0) = 7 \cdot 10^{19} \text{m}^{-3}$) plasmas with parabolic T_e and n_e profiles. Note that x/a is along the tokamak minor radius in the EIRENE calculation, while it is the distance to the wall in the slab calculation.

In Fig. 6.3 n_n is shown for three different n profiles. Only the $n(0)$ value is varied, the profile shape is kept constant. The 'cold' neutrals penetrate much further for lower density plasmas. The lower n , the higher the central $n_{n,h}$ value, but for the lowest density, it still goes below 5% of $n_n(0)$. In Fig. 6.4 the sources $n_i n_n \langle \sigma_{\text{tot}} v \rangle$ corresponding to the n and n_n profiles of Fig. 6.3 are shown for fixed $n_n(a) = 5 \cdot 10^{15} \text{m}^{-3}$. Note the three curves are rather close for $x/a > 0.6$. Assuming instead of a fixed n_n , a n_n rising with n , like mentioned above, then the relative source is independent of the density.

In all cases a constant velocity of the charge exchanged neutrals has been assumed. This velocity depends on the average of the thermal velocity of the ions involved and is unknown. However, the calculation is rather insensitive to the exact value of this temperature: Variation between 50 and 200 eV gives a variation of less than 15% on the resulting n_n profile.

The ratio $n(x=0)/n(x=a)$ was set to 10% in the calculations. This is a typical value for RTP, though it is not a constant. The width of the n_n profile increases with decreasing ratio. The central n_n value is almost independent of this ratio.

Both EIRENE and the slab calculation give relative profiles. These can be calibrated by a single local determination of n_n . In the appendix an estimate is given using the assumption of perfect recycling in the edge. Another estimate was obtained by Christian Ingesson [26] by analysing the tomogram of the H_α emission.

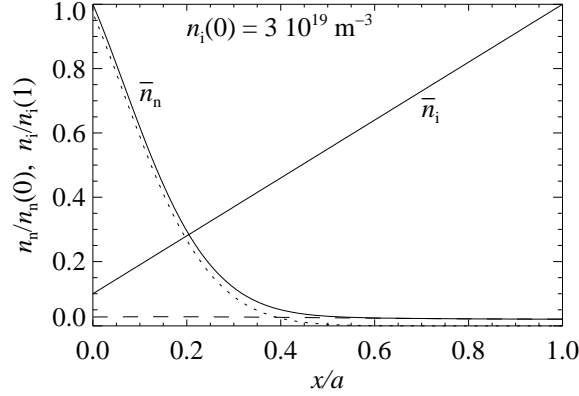


Figure 6.2: Neutral density versus normalised distance (full line) from the edge obtained from self-consistent calculation on a 1d slab. The assumed n profile is shown as well. The dotted line indicates $n_{n,c}$, the dashed line is $n_{n,h}$.

He finds a distribution with a strong local peak of $n_n \approx 4 \cdot 10^{16} \text{ m}^{-3}$ at the edge (line averaged density $2.4 \cdot 10^{19} \text{ m}^{-3}$). The decrease of this peak towards the centre suffers from large error bars, but is in agreement with the presented calculations.

This value is higher than our estimate in the appendix, which assumes perfect wall recycling. It should be kept in mind, though, that the latter is rather crude. Since we are mainly interested in an upper estimate of the neutral source in the central plasma, we adopt the value of [26].

To find out whether the electron and ion source associated with the obtained n_n is important in the centre, we compare this source with the typical electron/ion fluxes in the plasma. Consider the flux surface with minor radius $r_1 = 0.05 \text{ m}$. The source of neutrals in this torus is $2\pi R_0 \cdot \pi r_1^2 \cdot 0.02 n_n(r=a) n(0) \langle \sigma_{\text{ion}} v \rangle = 0.4 n(0) [\text{s}^{-1}]$, where the $n_n(r_1) = 0.02 n_n(r=a)$ is estimated from Figs. 6.1-6.3. If we assume that n decreases linearly with r and take an typical value for the anomalous diffusion coefficient $D = 1 \text{ m}^2 \text{ s}^{-1}$, then the particle flux through the surface is $2\pi R_0 \cdot 2\pi r_1 \cdot D n(0) / a = 8 n(0) [\text{s}^{-1}]$. The anomalous particle diffusion flux exceeds the electron source by the neutrals by more than one order of magnitude. The obtained electron source cannot explain the observed steepness of the n profile. An inward convection flux must exist balancing the diffusion flux and thus exceeding the electron source by more than one order of magnitude. This allows the neglect of the central electron source in the next sections.

The ionization of the neutrals represents a central heat sink. The neutral density in the centre consists mainly of single charge exchanged neutrals of which the temperature is between 50 and 200 eV. For an Ohmic plasma with $T_e(0) = 700 \text{ eV}$, $n_e(0) = 5 \cdot 10^{19} \text{ m}^{-3}$, the heat lost to the heating of the ionised neutrals in the

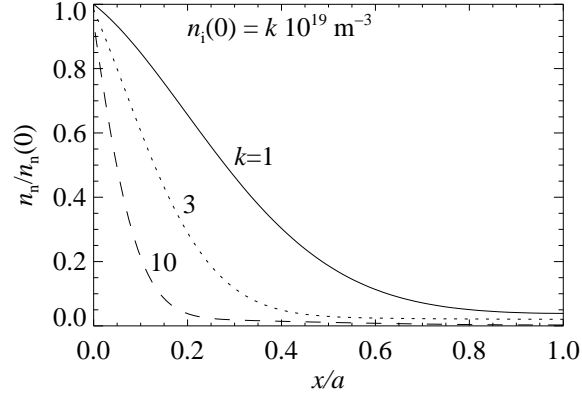


Figure 6.3: Neutral density versus normalised distance from the edge obtained from self-consistent calculation on a one-dimensional slab for $n(0) = 1$ (full line), 3 (dotted line) and $10 \cdot 10^{19} \text{m}^{-3}$ (dashed line).

central cylinder of 5 cm is between 1.7 and 2.2 kW. This is negligible with respect to the Ohmic input power: For a central current density ($j(0)$) of 5MAm^{-2} and a loop voltage of 1.5 V, the Ohmic power dissipated in our test cylinder is $\sim 60 \text{kW}$. Even in the case of off-axis Electron Cyclotron heated plasmas, in which $j(0)$ is a factor 3 to 4 lower and the loop voltage is $\sim 1 \text{V}$, the neutral heat sink is only a minor fraction of the Ohmic heat source.

For future use a simple analytical expression for the n_n profile would be convenient. The n_n profile has more or less the shape of a power dependence

$$n_n = n_n(r = a) \left(\frac{r}{a} \right)^{\iota_1 n(0) + \iota_2}, \quad (6.20)$$

especially if we neglect the central n_n . It turns out this expression is in good agreement with the results of the slab calculation if we take $\iota_1 = 1$, $\iota_2 = 2$ and $n(0)$ in 10^{19}m^{-3} . As expected, this rule of thumb gives a narrower peak at the edge if $n(0)$ is increased.

Summary of the Modelling of Neutral Penetration in RTP

Summarising, it has been found in section 6.3.1 that the penetration of neutrals in RTP is not a diffusive process, but a flow-like process. In section 6.3.2 a numerical model for the neutral penetration in RTP has been presented and bench-marked against the EIRENE code. Starting from an experimental value of the neutral density at the edge, the neutral density profile has been calculated. It has been found

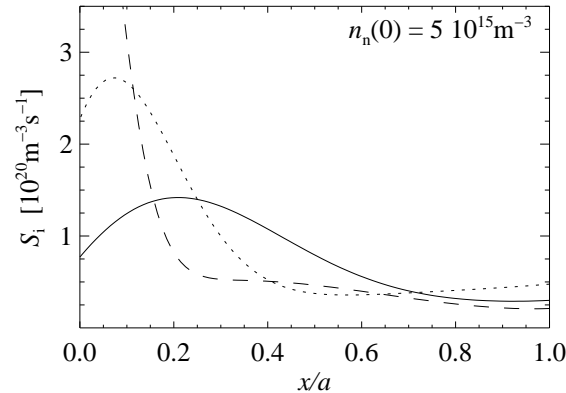


Figure 6.4: Electron sources associated with n_n versus normalised distance from the edge obtained from self-consistent calculation on a 1d slab for the profiles and corresponding n profiles of Fig. 6.3. $n_i = 1$ (full line), 3 (dotted line) and $10 \cdot 10^{19} \text{m}^{-3}$ (dashed line).

that the particle source and heat sink corresponding to the hot neutral concentration can be neglected in transport analysis. The remaining cold neutral density falls off strongly with the distance from the edge and it is negligible in the core.

In section 6.5-6.6 the obtained results on n_n are used in the analysis and simulation of the particle transport in RTP.

6.4 RTP observations

The aim of this section is to give an overview of the observations on particle transport in RTP. Several different plasma experiments are shown, which have in common that the density reacts to a change of the plasma state. First, the steady state n profiles during on- and off-axis ECH (section 6.4.1) and during Electron Cyclotron Current Drive (ECCD) (section 6.4.2) are presented: After that, the following time-dependent situations are shown: The density change after switch-on of central ECH (section 6.4.3), spontaneous transitions between plasma states during ECH (section 6.4.4) and the bifurcation of the Ohmic state after the off-axis ECH is switched off (section 6.4.5).

This section also serves as an introduction to the data that is simulated in section 6.6, using the expressions introduced in section 6.2.

6.4.1 Steady state Ohmic and ECH discharges

In this section the steady state n profiles in Ohmic state and during ECH, deposited both on- and off-axis, are discussed. The ECH system used is a 110 GHz gyrotron,

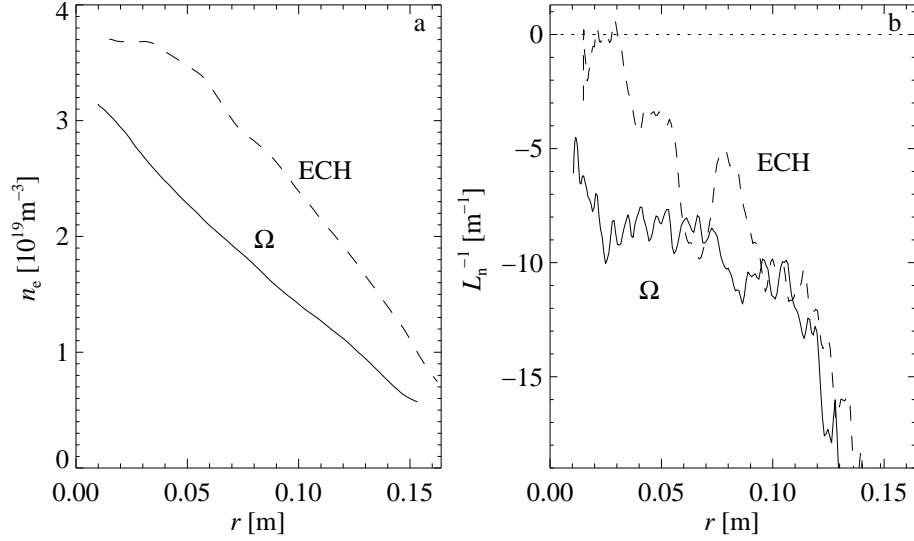


Figure 6.5: a) Steady state n profiles averaged over 22 Ohmic discharges (full line) and 11 discharges with central ECH (dashed line) as obtained from Thomson scattering; b) the reciprocal gradient lengths corresponding to the profiles in a). The roughness of these curves is due to the involved numerical differentiation.

delivering up to 350 kW for up to 200 ms. The Ohmic input power is 100 – 150 kW in the Ohmic state, but it decreases to 50 – 80 kW during ECH, depending on the plasma parameters and the deposition radius (ρ_{dep}).

If the launch angle of the microwave radiation is tilted in the toroidal plane, a localised current can be driven non-inductively. Results with this current drive are presented in the next section.

In Fig. 6.5a the average n profiles in the steady state of a series of Ohmic discharges and a series with central ECH are shown. The profile from the ECH discharges has a flat central area. In Fig. 6.5b the corresponding reciprocal n gradient lengths $1/L_n = \nabla_r n/n$ are shown. The small n gradient in the centre for the ECH case is even more pronounced in this figure. As will be shown later, the reaction of the n profile to the switch-on of ECH is localised in the centre. In the calculation of $1/L_n$, the edge source was neglected, so the values are underestimated there.

If the deposition radius of the ECH (ρ_{dep}) is scanned, a discrete set of steady state T_e profiles can be distinguished [28]. This scan can be done statically, by varying ρ_{dep} between discharges, and dynamically, by varying ρ_{dep} during the discharge. In Fig. 6.6 this discrete set of T_e profiles is shown, in Fig. 6.7 the corresponding central T_e ($T_e(0)$) as a function of ρ_{dep} . For central deposition the T_e profile is high in the centre, for off-axis ECH it is flat or slightly hollow with a maximum close to ρ_{dep} . Outside ρ_{dep} the profiles are equal.

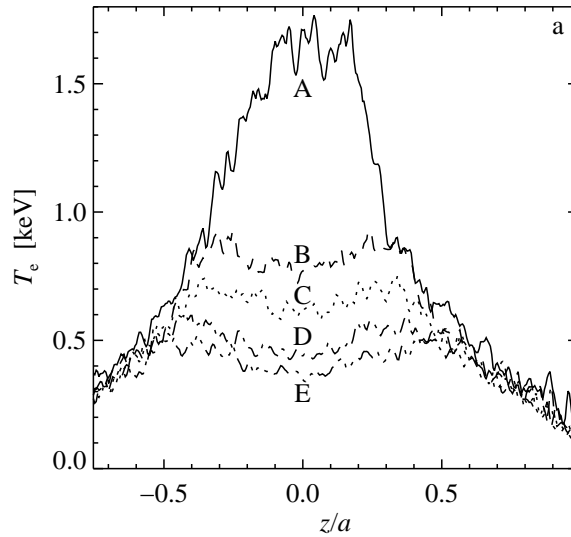


Figure 6.6: Five typical T_e profiles obtained with TS, taken in the indicated plateaux of Fig. 6.7.

In Fig. 6.8 the corresponding n profiles are shown as well as the line peaking factor $l_n \equiv an(0)/\int ndr$ as a function of ρ_{dep} for the series of discharges of intermediate density ($n(0) \sim 4 - 5 \cdot 10^{19} \text{ m}^{-3}$) of Fig. 6.6. The profiles are averages of several discharges in the same levels.

The trend of the n profile is opposite to that of the T_e profile: The larger ρ_{dep} , the higher $n(0)$. For central ECH, n is flat in the core region. l_n is constant within level A up to $\rho_{\text{dep}} = 0.15$ where it starts a gradual increase through level B and C to its end value of level D and E. This gradual increase differs from the behaviour of $T_e(0)$ in that $T_e(0)$ has no intermediate values in between the levels. The l_n value of level D and E remains just below that of Ohmic discharges, which is typically $l_n = 2.0$.

The behaviour of T_e as a function of ρ_{dep} can be described with an electron thermal convection ($U_{\text{th,e}}$), which is an explicit function of q [29]. $U_{\text{th,e}}$ is zero except for thin layers where it is high and inward directed. These layers are located at the q values which are simple rational numbers. The sharp transitions are associated with the loss and gain of these convective layers. In the states B to E the magnetic shear is negative. For the levels A to D the q profiles have been determined with tangential TS (see Fig. 5.16).

6.4.2 Density profiles during ECCD

An extreme example of the opposite behaviour of the T_e and n profiles has been found in case of counter current drive with ECH (ECCD, [30, p. 109]) in low density discharges. Analysis of the current drive indicates that the central current

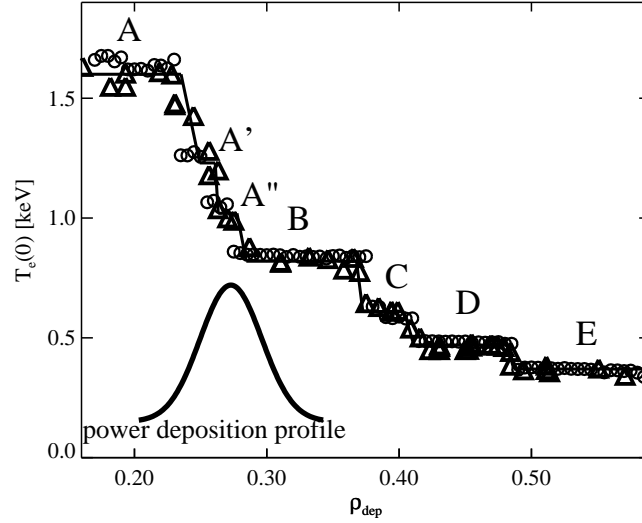


Figure 6.7: Measured central T_e (triangles) versus deposition radius ρ_{dep} . These data are obtained with TS in a series of similar 80 kA discharges of intermediate density in which ρ_{dep} was scanned along the horizontal axis. The circles are obtained from simulations using the RTP thermal transport barrier model [27].

might be reversed in this particular case. The resulting steady state T_e profile has an extremely high gradient at the hot centre, see Fig. 6.9. The high T_e gradient corresponds to a reversed gradient of the n profile.

The central decrease of $\nabla_r n$ can in principle be caused by increased diffusion or decreased convection. This experiment shows that the convection is decreased, because increased diffusion cannot produce a positive $\nabla_r n$. Apparently, the central n profile is dominated by convection.

6.4.3 Changes of the density profile upon switch-on of ECH

In sections 6.4.1 and 6.4.2 steady state n profiles were discussed and presented data was mainly obtained with TS. Now, we turn to the time-dependence of the n profile. For this, mainly data obtained from Abel inversion of the multi-channel interferometer is used (see Chapter 4).

We focus on the time dependence in a discharge ($I_p = 80$ kA, $B_T = 2.14$ T, $q_a = 5.0$) in which central ECH is switched-on in the steady state Ohmic phase. Due to the ECH the temperature rises strongly to the profile labelled by 'A' in Fig. 6.6. In Fig. 6.10 the n traces of the experimental data are given. The observations show a sharp decrease at the centre. This density decrease does not involve the full profile, but only the central 4 traces shown. The central part of the n profile becomes flat according to the profile shown in Fig. 6.5. The profiles obtained from

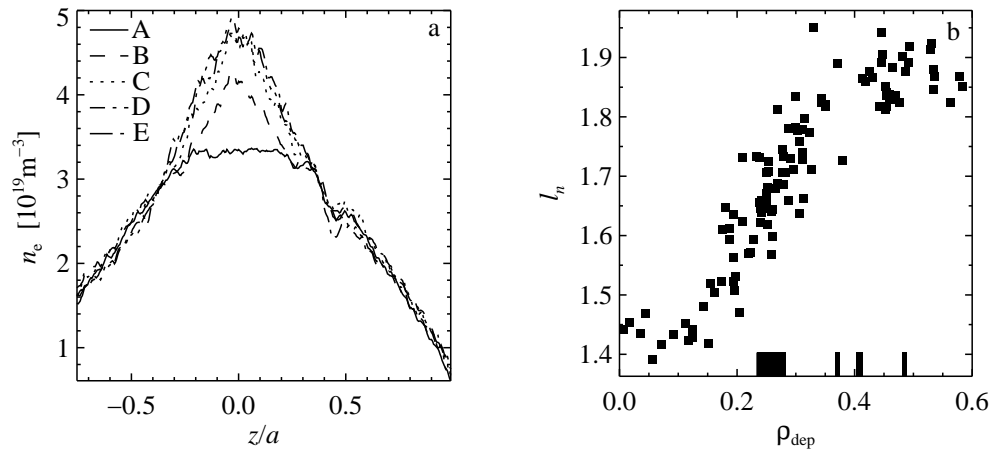


Figure 6.8: a) n profiles from TS averaged over the levels indicated in Fig. 6.6. For clarity the n profiles are scaled to each other in the edge with a constant factor. This is allowed because the original edge gradients are almost equal to each other. The structure around $z/a = 0.5$ is due to an error in the TS calibration. b) Corresponding density line peaking factor l_n vs. ECH deposition radius ρ_{dep} . The blocks on the ρ_{dep} -axis indicate the positions of the transitions in Fig. 6.6

the interferometer are usually not flat like that, and they lack the sharp change of gradient observed around $|z/a| = 0.4$ in Fig. 6.5. This is due to the Abel inversion.

There is a density pulse from the edge to the centre as well. It looks as if there was a gas-puff, but there was no puff from the valves around the ECH switch-on. Apparently, the EC waves release gas from the wall, which acts like an externally induced gas-puff.

The decreased peaking of the n profile in discharges with central ECH is observed in several tokamaks and is generally referred to as 'pump-out' [31–33]. The presented material shows that this pump-out is the most pronounced effect of the applied ECH on the n profile. The transitions from the Ohmic regime to the centrally heated regime and back, and the transitions between regime A and B will therefore obtain the highest attention.

6.4.4 Spontaneous transitions during ECH

The temporal behaviour of the T_e profile and the n profile in the intermediate density discharges of Figs. 6.6 and 6.8 is illustrated in Fig. 6.11. This discharge jumps spontaneously from profile A' to A'' during ECH. The central density and $T_e(0)$ crash at the transition on a MHD time scale. $T_e(0)$ reaches its new value on a short time scale. The whole n profile decreases with a time scale of 20–30 ms. This is comparable with the current diffusion time scale (τ_η) during ECH.

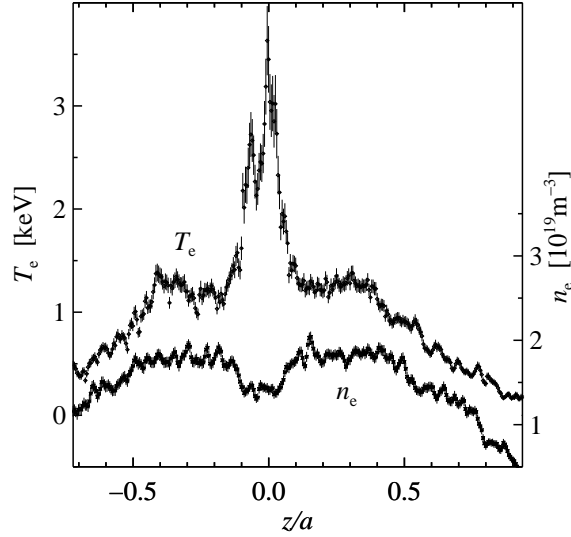


Figure 6.9: T_e and n profiles from TS obtained with Electron Cyclotron Current Drive in counter current direction. $I_p = 120$ kA, $B_T = 1.93$ T

Nevertheless, the final value of $l_n = 1.7$ is in agreement with Fig. 6.8.

In Fig. 6.12 similar behaviour is observed for a discharge which goes to sub-level A” at switch-on of ECH and falls to level B in about 13 ms. The central n trace reacts as rapid as the T_e traces on the transitions, but long time scale changes are visible on the n traces as well. At $t = 233$ ms an off-axis sawtooth-like instability sets in [34]. This instability is associated with negative central shear and a minimum value of q just below 2.

6.4.5 Bifurcation after switch-off off-axis ECH

After the ECH is switched off in discharges which are heated around half radius, the Ohmic state bifurcates into two distinct branches. One branch is the usual Ohmic state (state ‘I’), the second state features a much broader temperature profile while n has a very pronounced gradient near half-radius (state ‘II’). These profiles are shown in Fig. 6.13a and b. This figure was taken from a paper by the De Baar *et al* [35], in which the bifurcated Ohmic states were first published.

In Ref. 30 it was argued that the decisive incident, determining the final state of the discharge is the occurrence of an $m = 2$ MHD event, shortly after ECH switch-off. If this instability occurs, the steep $\nabla_r n$ which already formed is destroyed and the discharge evolves to the usual Ohmic state. If the instability is absent the state II discharge develops.

Neoclassical calculations have shown that the minimum q value for the state II discharges remains around 2, while the state I reaches $q \lesssim 1$, which is the usual value for Ohmic discharges. Tangential Thomson scattering measurements of q

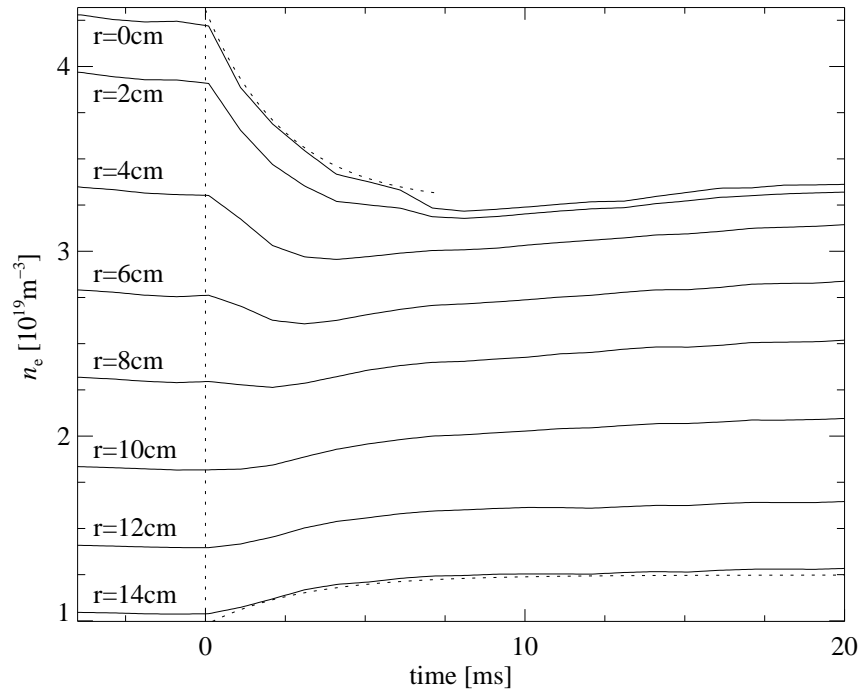


Figure 6.10: Time traces of n (solid lines) around the switch-on of ECH at $t = 0$. The dotted lines are negative exponents $\exp(-t/\tau)$, with $\tau = 2.5$ and 3 ms for the curves at $r = 0$ and 14 cm, respectively. The central T_e and n relaxation have similar time constants.

around a similar instability (see section 5.5.5) indicate that q profile is very flat up to the deposition radius and crosses $m=2$ during the instability.

The opposite shapes of the T_e and n profiles in the two states result in electron pressure (p_e) profiles, which are very similar to each other (see Fig. 6.13c).

6.4.6 Summary of the RTP Observations

In section 6.4 plasma states with several combinations of n , T_e and q profiles have been presented. The most striking feature is the opposite behaviour of the T_e and n profiles: When T_e peaks, n becomes flat, and vice versa. This is not only the case for ECH heated plasmas; The bifurcated Ohmic states show the same behaviour.

It was found that the central area is convection dominated. The negative $\nabla_r n$ in the ECCD discharges indicates that the inward convection that is decimated during on-axis ECH, can even change sign, as in the case of counter-current drive.

In the scan of ρ_{dep} not only the T_e profile but also the j profile is changed significantly. The T_e profile usually relaxes on a short, energy confinement time scale only, whereas the j profile relaxation can take up to 30 ms. The time dependent

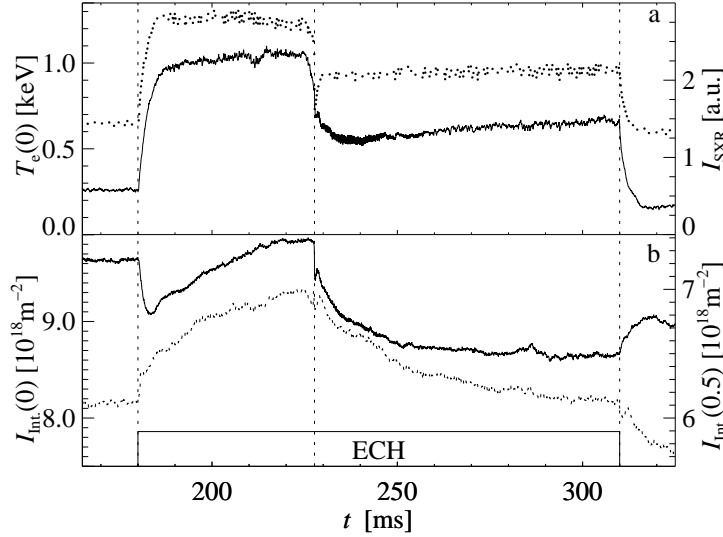


Figure 6.11: Time traces of central ECE (dots) and soft X-ray (a) and of interferometer channels at zero (upper curve) and half radius (b) of a discharge with ECH from 180 to 310 ms at $\rho_{\text{dep}} \sim 0.28$. At $t = 228$ ms a spontaneous transition from level A' to A'' occurs. There is no gas-puff in the indicated interval.

signals showed that the changes in n can occur on two time-scales: A short time scale comparable to the energy confinement time, and a long time scale of the order of the current diffusion time.

In section 6.5 the determination of the transport coefficients from the data like presented in section 6.4 will be treated. The focus is put on the transport simulation code ASTRA, that can analyse the time development during the transitions between the different states and link the plasma parameter profiles. In section 6.6 the data presented in this section are simulated with the ASTRA transport code.

6.4.7 Profile consistency

It is often observed that the p_e and j profiles have similar shapes. This is confirmed by several theories [36–39] and is called profile consistency. The profile consistency as formulated by [40] states that the normalised gradients of the p_e and j profiles are equal:

$$\frac{\partial}{\partial r} \left(\frac{p_e(r)}{p_e(0)} \right) = \frac{\partial}{\partial r} \left(\frac{j(r)}{j(0)} \right). \quad (6.21)$$

This means that the normalised p_e and j profiles are equal apart from a constant offset.

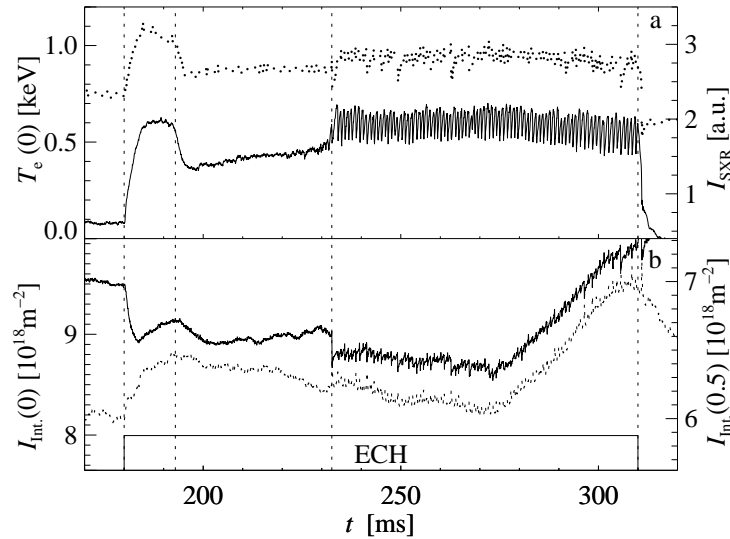


Figure 6.12: Time traces of central ECE (dots) and soft X-ray (a) and of interferometer channels at zero (upper curve) and half radius (b) of a discharge with ECH from 180 to 310 ms at $\rho_{\text{dep}} \sim 0.32$. At $t = 193$ ms a spontaneous transition from level A' to B occurs. At $t = 233$ ms an off-axis sawtooth instability starts. The increase of n between 280 and 310 ms is due to gas-puff.

The resistivity is a strong function of T_e , so the j profile is coupled to the T_e profile. Consequently, the n profile is assumed to behave in such a way that the profile consistency holds.

Profile consistency is no conventional transport theory, because it assumes the fluxes in the plasma are driven in such a way that abovementioned relation remains satisfied. The description of this transport with transport coefficients is not particularly useful. Therefore, we will not treat profile consistency with simulations like the other transport models treated in section 6.2. Instead, we simply test whether Eq. 6.21 holds for the data presented until now.

In Fig. 6.14 the p_e and j profiles of several steady state plasmas discussed in this chapter are compared:

- a. Ohmic state
- b. slightly off-axis ECH ($\rho_{\text{dep}} = 0.28$, see Fig. 6.11)
- c. far off-axis ECH, *c.f.* state 'E' in Figs. 6.6, 6.7 and 6.8a.
- d. bifurcated Ohmic state II (see Fig. 6.13)

The j profiles are obtained from neoclassical calculations, the p_e profiles are obtained from the T_e profiles from ECE and the n profiles from Abel inversion of

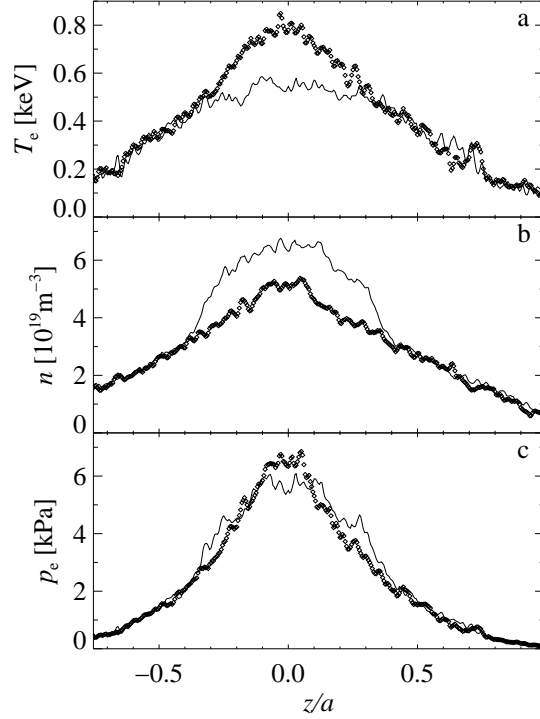


Figure 6.13: Profiles of T_e , n and p_e measured with Thomson scattering at 75 ms into the post-ECH phase for the bifurcated Ohmic states (symbols=state I, line=state II, see text). In state II the n profile develops a localised gradient near $\rho = 0.38$. The differences are very pronounced in the T_e and n profiles but largely cancel in the p_e profile, which nonetheless is more peaked in state I than in state II. For the presented discharges, the electron energy confinement times are $\tau_{Ee}^I = 4.4$ ms and $\tau_{Ee}^{II} = 4.2$ ms.

the interferometer data. The n profiles of the shown steady states are all peaked, so the Abel inversion is reliable. The hollow p_e profiles are entirely due to the corresponding hollow T_e profiles.

The correspondence of the p_e and j profiles is excellent in the Ohmic state. However, with off-axis ECH the profiles deviate from each other in the core. This deviation is more extended for the far off-axis heated state. In the bifurcated Ohmic state II the p_e profile is similar to the p_e profile in the Ohmic state I, but the j profile is much lower and even slightly hollow.

In the off-axis EC heated discharges it seems that profiles deviate inside the deposition radius: The difference is larger in the far off-axis heated case. Due to the strong dependence of j on the T_e profile, the j profiles are quite hollow for these plasma states. The p_e profile is only slightly hollow or even peaked, due to the peakedness of the n profile we already discussed in section 6.4.1. The discrepancy

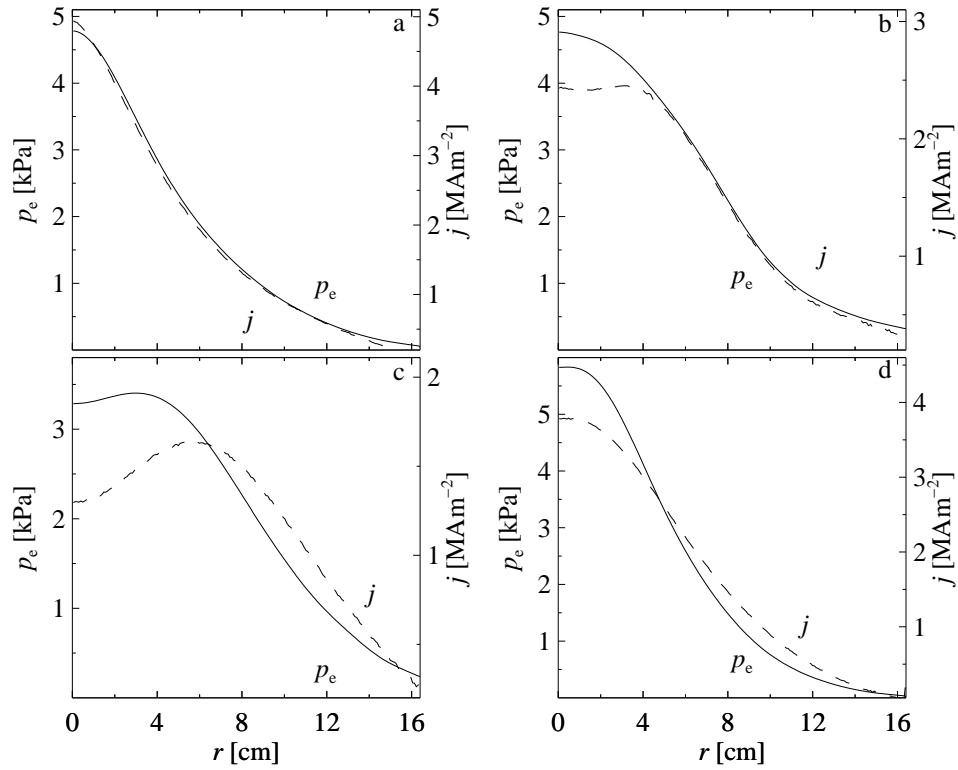


Figure 6.14: p_e (full line) and j (dashed line) profiles during four steady states: a) Ohmic state; b) slightly off-axis ECH; c) far off-axis ECH; d) bifurcated Ohmic state II. The offset and scale of the j profiles has been adapted to match the p_e profiles. All four plasma states have peaked n profiles (not shown).

may be smaller than shown, since the uncertainty on j in the hollow part of the profiles is significant. Nevertheless, the hollow T_e profile is unlikely not to cause a hollow j profile.

In the bifurcated Ohmic state II the peaking of the p_e profile is mainly due to the strong peaking of the n profile. The T_e profile is more or less flat (see Fig. 6.13), and so is the corresponding j profile.

Concluding, although the agreement is remarkably good in the Ohmic case, it is not satisfactory in the other test cases. Apparently, strong off-axis heating causes breaking of profile consistency.

6.5 Determination of Particle Transport Coefficients; the ASTRA transport code

In section 6.4 several combinations of n , T_e and q profiles have been presented, and transitions between them. In section 6.6 the transitions are simulated with ASTRA [8]. This section serves as introduction to ASTRA. It contains also the basic simulations that validate the approach.

First, the previous particle transport analyses performed at RTP are reviewed (section 6.5.1). In section 6.5.2 the main tool for our transport study is introduced, the transport code ASTRA. In section 6.5.3 ASTRA is used to determine the transport in steady state conditions. The results are compared with the previous results in section 6.5.1.

In general, the diffusion and convection coefficients determined in experiments with perturbations of the stationary plasma are the incremental transport coefficients D^{inc} and V^{inc} , respectively [3,41]:

$$D^{\text{inc}} \equiv \frac{\partial \Gamma}{\partial (\nabla_r n)}, \quad (6.22)$$

$$V^{\text{inc}} \equiv \frac{\partial \Gamma}{\partial n}. \quad (6.23)$$

6.5.1 Previous RTP particle transport analysis

In previous studies two analyses of the density modulation in the sawtooth instability have been performed. This has the obvious advantage that the central transport coefficients are obtained. Further, several similar sawteeth can be averaged to decrease the measurement error.

In the sawtooth collapse the density profile becomes flat within the mixing radius. J. A. Konings realised that the diffusion driven flux is zero in this flat part and the relaxation directly after the collapse is dominated by the particle pinch alone [42, p. 63]. He calculated a pinch velocity $V^{\text{stat}} = 1.2 \pm 0.2$ m/s within $r/a = 0.2$ with $n = 2.5 \cdot 10^{19} \text{ m}^{-3}$. The superscript 'stat' is used because this coefficient is not determined from a perturbed, but from a stationary situation. Once the pinch velocity is known, the diffusion coefficient can be obtained from the steady state profile, in this case $D^{\text{stat}} = 0.25 \text{ m}^2/\text{s}$.

The sawtooth collapse also causes a density pulse outwards. The propagation of this pulse was studied by A. C. A. P. van Lammeren [43, p. 101] by use of the ACCEPT-code [44]. This code simulates a set of coupled diffusion equations for the particle and heat transport. From the low-field side measurements a diffusion coefficient $D^{\text{inc}} = 1.0 \pm 0.3 \text{ m}^2/\text{s}$ was found in a high density plasma ($n(0) = 9 \cdot 10^{19} \text{ m}^{-3}$). This D^{inc} holds for just outside the mixing radius, which is ~ 4 cm. Unfortunately, no information on the pinch velocity or the thermo-diffusion coefficients was provided by [43].

An alternative approach is the numerical solution of the equation for conservation of particles, Eq. 6.3. This is done in one dimension by J. de Kloe [45, Ch. 5]. He estimates the D^{inc} profile and deduces the V^{inc} profile from it using the steady state n profile. He neglects the particle sources. With the obtained coefficients the time evolution of the n profile was simulated and compared to the measurements. The optimum value for the transport coefficients is obtained for the best fit of both the phase and amplitude of the n variation to the data. For the boundary condition at $r = 0$ the condition of zero flux was taken. For large r the outermost measured density was taken as boundary condition. In this way, any uncertainties in the area between this channel and the edge were avoided.

For a quiet Ohmic discharge with gas-puff pulses J. de Kloe found a value for the average of $D^{\text{inc}} = 2.0 \pm 1.0 \text{ m}^2/\text{s}$. In the case of pellet ablation a parabolic D^{inc} profile was obtained with $D^{\text{inc}}(r = 0) = 1 \text{ m}^2/\text{s}$ and $D^{\text{inc}}(r = a) = 5 \text{ m}^2/\text{s}$, which is in agreement with the average $D^{\text{inc}} = 2 \text{ m}^2/\text{s}$ result.

The results of Van Lammeren and De Kloe are in agreement with each other, the values obtained by Konings are substantially lower. It should be noted that Konings analysed n during the sawtooth instability. It is possible that his assumption that the n build-up in between the crashes is determined by transport is not valid.

In section 6.5.2 the transport simulation code ASTRA is introduced. With ASTRA simulations, the transport coefficients can be estimated as well.

6.5.2 Introduction to ASTRA

ASTRA (Automatic System of TRansport Analysis) is a flexible and effective tool for the study of transport mechanisms in tokamaks [8]. Flexibility is provided within the ASTRA system by a wide choice of standard relations, functions and subroutines representing various transport coefficients, heating methods and other physical processes, as well as the possibility to set the variables in the transport equations beforehand and to set variables for data output in a simple form.

ASTRA uses the system of one-dimensional transport equations obtained by averaging over the toroidal magnetic surfaces. The set of equations describes the transport of particles, heat and current through the conservation of mass, charge and energy. In this study the equation for the density is most important:

$$\frac{\partial}{\partial t}(\mathcal{V}'n) + \frac{\partial}{\partial \rho} \left[\mathcal{V}' \left(\langle (\nabla \rho)^2 \rangle \Gamma - \frac{1}{2} \frac{\dot{B}_{\phi 0}}{B_{\phi 0}} \rho n \right) \right] = \mathcal{V}' \Sigma S . \quad (6.24)$$

In this equation all quantities depend on two arguments: time t and the radial variable ρ . $\dot{B}_{\phi 0}$ is the time derivative of the vacuum toroidal magnetic field on axis $B_{\phi 0}$, \mathcal{V}' is the radial derivative of the volume, $\partial \mathcal{V} / \partial \rho$, ΣS is the sum of all particle sources and sinks, as introduced in Eq. 6.3. With the essential input parameters, the set of equations and the Grad-Shafranov equation for the magnetic equilibrium are solved.

The strength of ASTRA is its flexibility. It can handle arbitrary input: Not only can various experimental data be introduced, but the transport model describing

the various coefficients can be chosen from an extensive library or can be given by user-supplied codes. Furthermore, ASTRA allows the reduction of the number of parameters in the transport problem. The user can choose to assign values to one or more of the parameters n , T_e , T_i and j . The assigned values can be in the form of an explicit, analytical expression or can be taken from experimental data.

We used ASTRA to simulate the j and n profile. The T_e data are assigned from the experimental ECE and TS data. The ion temperature is calculated from the thermal coupling with the electrons. The transport coefficients for the parallel j transport are taken from neoclassical theory according to [46].

The boundary condition for n is taken from the Abel inverted interferometer measurements. In this data the effect of the gas-puff is incorporated in a natural way: From the experimental n profiles we know that the gradient length in the edge does not change much during a gas-puff nor after ECH switch-on. This indicates that a change of the edge density leads to an inward density pulse. The simulations show that this boundary condition is well suitable.

It should be noted that the edge n is not measured directly, but is deduced from the outermost interferometer channel, at 14 cm or $\rho = 0.85$. Before Abel inversion a point outside this channel is added to the measured phase profile where the measured phase is supposed to be zero. The phase is linearly interpolated between the outermost measurement and this zero point. The position of the zero point is optimised by comparing the inverted n profile to the n profile obtained with Thomson scattering. This profile extends to $r = a$. The zero point lies typically 1-2 cm outside the plasma.

It is preferable to apply the outermost measurement as a boundary condition. Unfortunately, this is not possible in ASTRA without neglect of the area outside this measurement chord. The limitation of the plasma in this way is however not attractive, because it will compromise the simulation of j . Therefore, the value of n at the edge is used, following from the interpolation. Concerning the time behaviour this is acceptable, realising that the transport coefficients are commonly observed to increase strongly towards the edge. This makes it acceptable to take $n(a)$ as a boundary condition.

The simulated n is compared to the n from the Abel inverted measurements. The alternative is to calculate the line integrated density from the simulated n and compare this to the measurements directly. The fact that a code to perform the Abel inversion with refraction correction is routinely available at RTP favours the first possibility. Moreover, the n boundary condition is obtained after inversion only. For a discussion of the inversion routine, see section 4.4.2.

ASTRA has the minor flux surface radius r as the working coordinate. To calculate the measurement positions as a function of this coordinate, the Shafranov shift (δ) must be known. Symmetry considerations applied to the experimental ECE and interferometer profiles are used to estimate δ . The obtained values of the shift are in agreement with the values calculated by ASTRA in the simulation ($\delta = 1 - 2$ cm)

In section 6.5.3 ASTRA is used to estimate the transport coefficients D^{inc} and V^{inc} from the simulation of gas-puff in Ohmic and EC Heated discharges. The

obtained coefficients are compared to the previous results, reviewed in section 6.5.1. They serve as a starting point for the simulations in section 6.6.

6.5.3 Simulation of steady state Ohmic and EC Heated discharges

The D^{inc} and V^{inc} profiles must be set in the simulation of the particle diffusion. If one of these profiles is estimated, the other follows from the steady state n profile. Alternatively, both profiles can be parametrised. As will be shown, this approach gives good results.

We use the expression for n_n obtained in section 6.3 for a source function. This function dominates the transport in the edge. This study is focused on the particle transport in the central area, so the used function does not need to be very accurate.

An important boundary condition is the condition of zero particle flux at $r = 0$. This is satisfied with $V^{\text{inc}}(0) = 0$: Zero convection at $r = 0$ makes the n gradient disappear and as a consequence there is no flux. Note that some of the theory based expressions for V^{inc} in section 6.2 do not fulfill this requirement. We will come back to this when these expressions are simulated.

The expressions for V^{inc} , D^{inc} and the source S as used in ASTRA are:

$$\begin{aligned} D^{\text{inc}} &= D_0 + (D_a - D_0)\rho^k \\ V^{\text{inc}} &= V_0 \cdot \rho \\ S &= S_0 \cdot \rho^l \cdot n \\ k &\geq 1, \quad l = 2 + n(0)[10^{19} \text{ m}^{-3}], \end{aligned} \tag{6.25}$$

with k and l integers. The expression for l is taken from Eq. 6.20. D_0 is the central value of D^{inc} , D_a the edge value. We take $k = 2$, unless stated otherwise. V^{inc} and S both increase towards the edge.

Since from steady state only the ratio $V^{\text{inc}}/D^{\text{inc}}$ can be determined, a time-varying n is used to determine the values of the coefficients in Eq. 6.25. Here, three discharges with gas-puff are simulated: a) An Ohmic discharge with a single block/step function-like gas-puff; b) An Ohmic discharge with several block function like gas-puffs; c) A discharge with central ECH with a block function like gas-puff during steady state ECH, 30 ms after the switch-on of ECH. For the plasma parameters, see Table 6.1. All three discharges were selected for the absence of the sawtooth instability. To limit the degrees of freedom, $D_a = 10D_0$ is taken. In Fig. 6.15 the time evolution and corresponding profiles for the second case are shown. The coefficients are $D_0 = 1 \text{ m}^2/\text{s}^2$, $D_a = 10 \text{ m}^2/\text{s}^2$, $V_0 = 6 \cdot 10^1 \text{ m/s}$ and $S_0 = 1 \cdot 10^4 \text{ s}^{-1}$. With these coefficients, the time evolution of the other two cases can be simulated as well, provided V_0 is decreased to $V_0 = 5 \cdot 10^1 \text{ m/s}$ in the ECH case.

It is remarkable that the ECH and Ohmic discharges have the same diffusion coefficient. It should however be realised that the error bar on the determined coefficients is 30-40 % in the centre. This is due to the nature of the gas-puff: It is an edge perturbation, which is smeared out on its way to the centre.

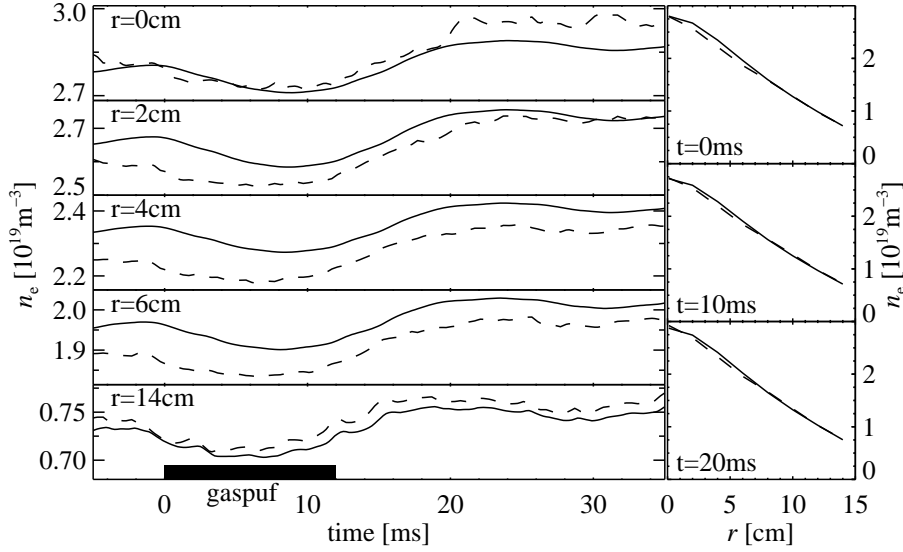


Figure 6.15: Time traces of n at $r = 0, 2, 4, 6$ and 14 cm and n profiles at $t = 0, 10$ and 20 ms for a discharge with gas-puff between 0 and 12 ms. The full lines are from the ASTRA simulation, the dashed lines are the experimental data. Time is taken with respect to the start of the gas-puff.

Table 6.1: Plasma parameters of the discharges with gas-puff used to simulate the density-pulse propagation.

	Discharge	Plasma Parameters			P_{ECH} (kW)	Simulation Parameters			
		I_p (kA)	q_a	$n(0)$ (10^{19}m^{-3})		D_0 (m^2/s)	D_a (m^2/s)	V_0 (m/s)	S_0 (s^{-1})
a	r19980511.013	62	6.6	2.8	-	1	10	$6 \cdot 10^1$	$8 \cdot 10^3$
b	r19980320.049	79	4.5	4.3	-	1	10	$6 \cdot 10^1$	10^4
c	r19971126.044	92	4.6	4.0	300	1	10	$5 \cdot 10^1$	10^4

The obtained value for D_0 is in agreement with the previous results on RTP obtained by Van Lammeren en De Kloe (see section 6.4), and is much higher than the values obtained by Konings.

Summarising, we have introduced the tool ASTRA and made an estimation of the coefficients determining the particle transport, summarised in Table 6.1 This estimation is appropriate to simulate gas-puff discharges with and without central ECH. The results are in agreement with previous results on RTP. In section 6.6 we use the results obtained in section 6.5 to test several particle transport against the experimental data.

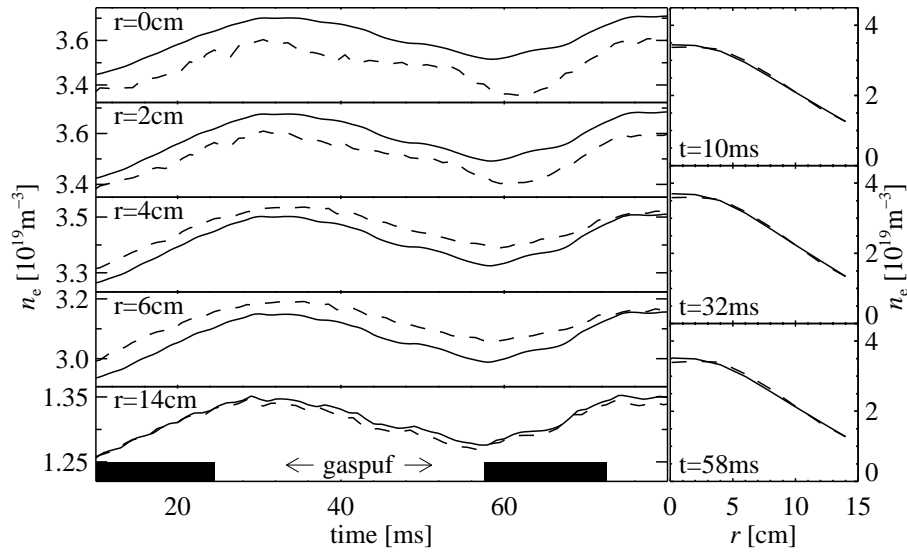


Figure 6.16: Time traces of n at $r = 0, 2, 4, 6$ and 14 cm and n profiles at $t = 10, 32$ and 58 ms for a discharge with central ECH from $t = 0$ on and with gas-puffs between 2 and 22 ms and between 57 and 72 ms. The full lines are from the ASTRA simulation, the dashed lines are the experimental data.

6.6 Test of Transport Models

In the following the various expressions of section 6.2 concerning the anomalous pinch are used to simulate n and the results are compared to the observed n behaviour. Apart from these physics-based expressions, two additional simulations are performed for reference. In one simulation, fixed coefficients for D^{inc} and V^{inc} are taken. The coefficients are as obtained in section 6.5 for the Ohmic case. In the other simulation, the value of V_0 is changed at the transition. So in the Ohmic phase, the coefficients for Ohmic discharges are taken and in the ECH phase the coefficients for EC heated discharges are taken as obtained in section 6.5 and listed in Table 6.1, *i.e.* V_0 changes at switch-on from 50 to 60 m/s.

The results of the simulations are compared with the data using three criteria, in the following order: First, the time scales of the simulated and observed changes are compared with each other. Secondly, the signs of the relaxations given by simulation and data are compared. The third criterion is how the change of the profile shape compares to the observed profile shape change. To keep these tests as clear as possible the main focus is put on the time scale and sign criteria. For optimal comparison of the simulations the coefficients of the expressions are kept fixed for all transitions, unless stated otherwise.

As we are only interested in the trends predicted by the transport expressions,

we will allow a multiplication factor in the model expressions for V^{inc} . These multiplication factors are chosen such that the initial Ohmic n profile is reproduced as good as possible. The multiplication factors are kept fixed for all simulations which start from the Ohmic state (section 6.6.1-6.6.3).

In case the model expression for convection is not zero at the axis, we will apply an extra modification. In this case, the expression is multiplied with the function

$$f_{\text{cut}} = (1 - \exp(-r/r_{\text{cut}})) \quad (6.26)$$

to fulfill this condition, with $r_{\text{cut}} \sim 1$ cm.

Note that the modifications are independent of the plasma parameters. They are kept constant at the transitions, *e.g.* between the Ohmic and ECH phases. At a transition the model expressions change only according to their functional dependences.

The following transitions are studied:

1. transition between the Ohmic state and the state with central ECH \rightarrow Section 6.6.1;
2. transition between the Ohmic state and a slightly off-axis ECH state ($\rho_{\text{dep}} = 0.3$), as shown in Fig. 6.11 \rightarrow Section 6.6.2;
3. transition from the Ohmic to the far off-axis EC Heated state ($\rho_{\text{dep}} = 0.5$) \rightarrow Section 6.6.3;
4. relaxation after switch-off of off-axis ECH towards the bifurcated Ohmic state II (see Fig. 6.13) \rightarrow Section 6.6.4.

6.6.1 Transition from Ohmic to Centrally EC Heated State

In this section one particular discharge with central ECH is analysed. This discharge was selected for its lack of the sawtooth instability, to keep the input signals as smooth as possible. The sawteeth are suppressed by depositing the ECH at the edge of the high T_e region, in this case $\rho_{\text{dep}} = 0.16$ [30]. In general, discharges with central ECH are not sawteeth-free. The results for discharges with sawteeth are similar to the results presented.

The experimental density development has been treated in section 6.4.3 and Fig. 6.10. In Fig. 6.17 the time traces of the experimental data are shown, as well as various simulated traces. The presented radii are 2, 6, 10 and 14 cm, respectively. Fig. 6.18 contains the profiles just before and 30 ms after ECH switch-on for the nine simulations. In the following, the various simulations are discussed. For each simulation, the implementation of the expression as well as the results of the simulation are presented in a subsection.

1. No change of D^{inc} and V^{inc}

In the first simulation the D^{inc} and V^{inc} profiles as found for Ohmic discharges are kept fixed during ECH. This case is indicated with 'No change' in Fig. 6.17. The profile shapes of initial and final state are equal because of this condition and the simulation gives us the density development as a consequence of the ECH induced gas-puff only. Indeed the observed behaviour resembles the gas-puff analysis data in the Ohmic plasma of Fig. 6.15 rather well. The central density increases modestly with a time constant and delay like we observed before.

This simulation serves as a reference simulation to determine the influence of the edge density on the n profile. It is not expected to reproduce the observed behaviour. Indeed, the time constant is wrong and the sign of the change is opposite to the experimental data. The profile shape remains like in the Ohmic state.

2. Instantaneous change of V_0

The second simulation has the determined Ohmic V_0 in the Ohmic phase ($6 \cdot 10^1$ m/s) and the ECH V_0 during ECH ($5 \cdot 10^1$ m/s), as given in Table 6.1 in row a and c, respectively. The transition between the two values is instantaneous, *i.e.* with the time step of the simulation, which was $100 \mu\text{s}$ in this case. D^{inc} is unchanged with respect to section 6.5. This simulation is labelled ' V_0 change'. This simulation gives the response of the system to a step function, so it has the shortest possible time scale.

Indeed we see that this simulation has a faster decrease of the central n than the data. After this fast n decrease, the whole profile rises, again as a consequence of the increased edge density. Since the applied change gives a decrease only, the effect of the ' V_0 change' is almost over as soon as the gas-puff pulse takes over. At $r = 2$ cm, that is already after about 3 ms.

This simulation serves as a lower estimate of the time scale of the change with the parameters obtained from the gas-puff simulations (section 6.5).

Transport matrix formalism

In the transport matrix formalism the convection is the sum of thermo-diffusion caused by the T_e and T_i gradients, and a term proportional to the parallel electric field. Here, Eq. 6.5 is taken to take account of the anomalous transport. As noted before, the T_i gradient driven term will not be considered here. The simplest case is considered here, in which the off-diagonal elements of the transport matrix are constants. For D^{inc} , Eq. 6.25 is used.

3. Thermo-diffusion

First, we consider the effect of the thermo-diffusion only, setting $V_W = 0$ in Eq. 6.5. In Fig. 6.17 this effect is indicated with 'Thermo-diffusion'. This simulation shows a strong increase at ECH switch-on. The central trace resembles the behaviour of the central T_e . This causes the peak at $t \sim 7$ ms as well.

Since the T_e profile during ECH is flat in the core, the pinch is to decrease in the core. However, just outside ρ_{dep} , $\nabla_r T_e$ is enhanced with respect to the Ohmic state. Apparently, since n increases in the core, this effect dominates the result.

The sign of the change of $n(0)$ is wrong and the final n profile does not resemble the observations.

4. E-driven pinch

The simulation with a single constant term proportional to E_{\parallel} , *i.e.* $D_T = 0$ in Eq. 6.5, is labelled with ' E_{\parallel} -driven pinch' in Fig. 6.17. During ECH, it gives a strong overall decrease of the inward convection and corresponding decrease of n . The time scale of the relaxation of the E_{\parallel} profile is comparable to the T_e relaxation. The T_e change is relatively large, and so is the change of E_{\parallel} . The effect on the n profile is stronger than observed.

The simulated j profiles in the Ohmic and ECH states are similar. This is the reason that the E_{\parallel} profile relaxation is as fast the T_e relaxation. The final profile shape is much flatter than the observed profile. This is due to the fact that the E_{\parallel} profile is very low in steady state. The final pinch profile is constant like the steady state E_{\parallel} profile, so the E_{\parallel} -driven pinch gives no local structures.

5. Full transport matrix

In the more general case, the E_{\parallel} and $\nabla_r T_e$ -driven pinches are taken non-zero, *c.f.* Eq. 6.5. Since they have opposite effects on n at the ECH switch-on, their ratio can be used as an additional free parameter. Both off-diagonal terms change on the same fast time scale. The result is shown in the trace labelled with 'Constant matrix'. The result has more or less the right quantitative effect on the profile. However, the profile shape is not reproduced very well, because the effect of ECH switch-on on the E_{\parallel} profile is a global decrease, whereas the effect on the thermo-diffusion term is a local increase around $r = 0.03$ m. There is no trace of such a local increase of n in the measurements.

6. Varma pinch

The Varma pinch consists of four factors, as discussed in section 6.2, Eq. 6.11. The local dependence on ϵ at the axis of the respective factors is as follows: $f_V \sim \epsilon^{-1/2}$, $f_t \sim \epsilon^{1/2}$, $f_\nu \sim \epsilon^0$ and $E_{\parallel}/B_\theta \sim \epsilon^{-1}$. Hence, the pinch goes as ϵ^{-1} approaching the axis. To compensate this divergence and let the pinch be zero at $\epsilon = 0$, it is multiplied with f_{cut} in Eq. 6.26.

The field E_{\parallel} decreases strongly during the transition, while f_ν increases due to the decreasing collisionality. The factor f_V is a geometrical factor and B_θ changes only slightly with central ECH.

From the figures it appears that the changes balance each other and the net effect on the pinch velocity is very small. The sign of the effect is wrong. Moreover, the profile shapes with the Varma pinch strongly deviate from the observed profile shapes. This is due to the increase of the pinch towards the axis, which causes the profiles to become strongly peaked. The peakedness is strongest in the ECH phase.

7. Electrostatic turbulence

From electrostatic turbulence theory the q^{-1} pinch is obtained. This pinch diverges neither at $r = 0$ nor at $r = a$ so Eq. 6.13 can be applied directly, $V^{\text{inc}}/D^{\text{inc}} \propto$

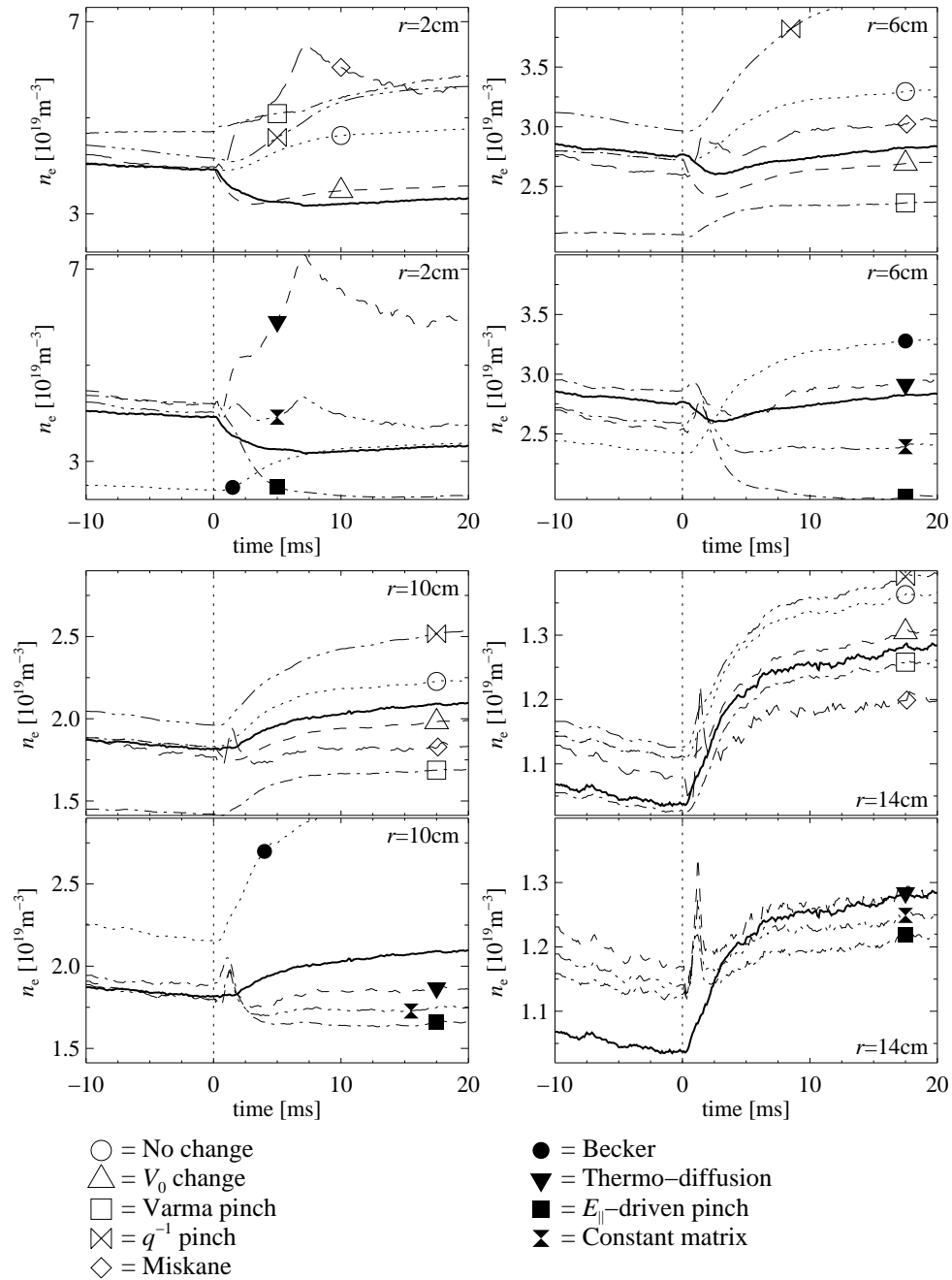


Figure 6.17: Time traces of n at $r = 2$ cm (upper left), $r = 6$ cm (upper right), $r = 10$ cm (lower left) and $r = 14$ cm (lower right) of the experimental data (thick, solid curve) and of simulations with various transport coefficient expressions (see index). For each radius, the plot is split into two parts for clarity.

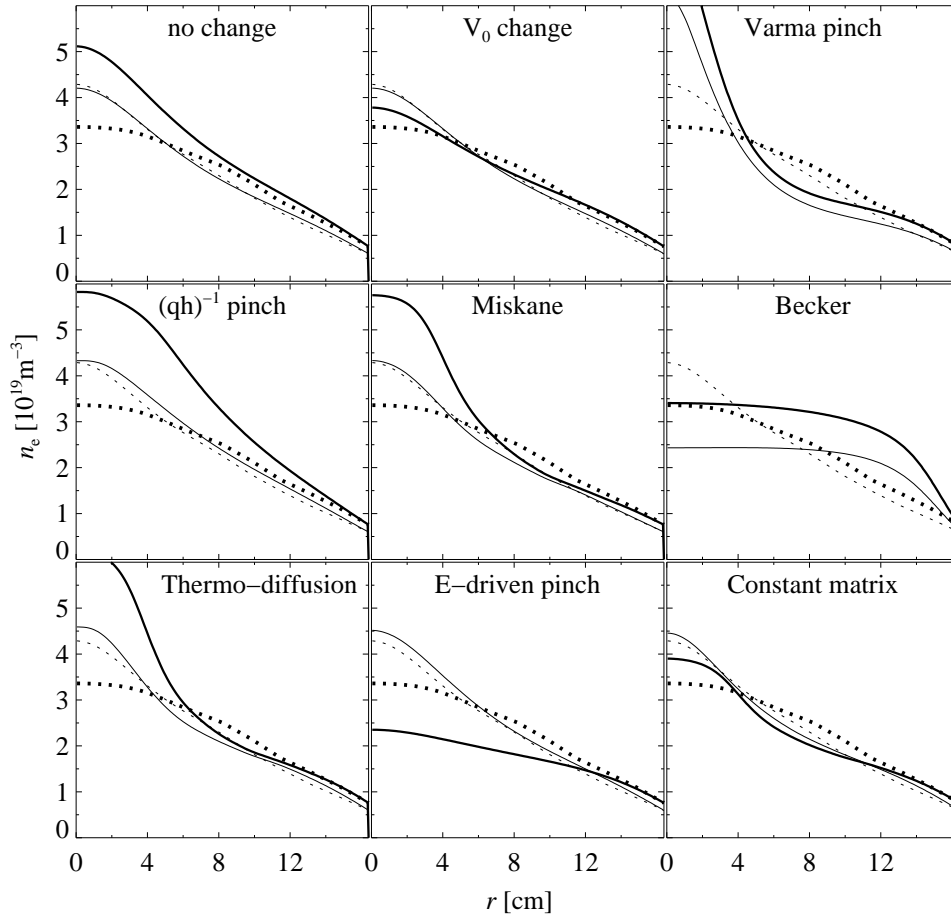


Figure 6.18: n_e profiles of all simulations of Fig. 6.17 and discussed in section 6.6.1. The thin curves are the profiles just before central ECH is switched on, the thick curves are the profiles 30 ms after ECH switch-on. The dotted curves represent the experimental data at the same time points. They are identical for all nine plots.

$-\nabla_r(\ln q)$. The resultant central trace rises quite strongly, in contrast with the observed decrease of $n(0)$.

The simulation of the q profile development indicates that the magnetic shear s decreases close to the axis, and s increases further away from the centre. This causes the n profile to increase stronger than the 'No change' simulation. The time scale is much longer than the observed time scale and longer than in the case of the E_{\parallel} -driven pinch.

8. Miskane thermo-diffusion

Miskane predicts a rigorous coupling between the outward diffusion and the inward electron thermo-diffusion (see Eq. 6.12). The flux driven by thermo-diffusion is zero at the axis because $\nabla_r T_e$ is zero, thus satisfying the boundary condition. It turns out that the coupled thermo-diffusion term alone is too small to establish the observed Ohmic n profile, and therefore a constant thermo-diffusion coefficient is added, like in Eq. 6.12, $D_{T,0} < 0$. This is a generalisation of the equations in [13] where $D_{T,0} > 0$.

If we compare the steady state T_e profile in the ECH phase with that of the Ohmic phase, the central gradient in the ECH phase is zero and the gradient just outside this region is strong. The first effect leads to a reduction of the central V^{inc} , the second effect leads to an increase of V^{inc} around $r = 0.03$ m. From Fig. 6.17 it becomes clear that the increase of the gradient at $r \approx 0.03$ m dominates the zero gradient effect, because $n(0)$ increases.

The time scale of the increase is similar to the time scale of the T_e change. This can also be seen from the structure in the time trace, especially the peak at $t \approx 7$ ms, which correlates with the T_e relaxation.

The Miskane thermo-diffusion performs better than the off-diagonal thermo-diffusion in the transport matrix formalism. The differences between the two expressions are the that Miskane uses the shape of the (parabolic) D^{inc} profile and adds a constant, whereas in the transport matrix formalism a single constant coefficient is used.

Although the time scales of the n development from the observations and from the simulation of the Miskane scheme are comparable, the n change simulated with this expression is of the wrong sign. Further, if the expression is interpreted strictly, *i.e.* $D_{T,0} > 0$, the steady state n profiles cannot be reproduced. This makes the expression less suitable to explain the observed n profile development.

9. Becker scaling

We recall that according to Becker the $V^{\text{inc}}/D^{\text{inc}}$ profile scales with the neutral density profile, neglecting the sources up to the very edge (see section 6.2.4). As a consequence, S_0 in Eq. 6.25 is taken zero in the simulation. The parabolic D^{inc} profile from the Ohmic phase is maintained and $V^{\text{inc}} = D^{\text{inc}} n_n$ is taken. We have no measurements of the development of n_n , so we deduce it from other observations.

The ECH increases T_e , which in turn affects the n_n profile in two ways. The effect of the higher T_e on the cross-section is incorporated in the ASTRA simulation. Another consequence of the higher T_e is that the velocity of the charge-exchanged neutrals is higher. This makes a difference if the neutral penetration is a diffusive process. However, the slab calculation in section 6.3 indicated that the hot neutral concentration is rather insensitive to T_e .

The second effect of ECH is that the n_n in the edge is increased. This increase is estimated to be proportional to the observed increase in $n(a)$. Note that according to Eq. 6.14 the an increase of n_n in the edge leads to increase of the $V^{\text{inc}}/D^{\text{inc}}$. This is not supported by the measurements, because $V^{\text{inc}}/D^{\text{inc}}$ is equal in the Ohmic and ECH phases, *c.f.* Fig. 6.5.

Table 6.2: Performance of the applied expressions in the simulation of the development of the n profile around switch-on of ECH, as presented in section 6.6.1. The order corresponds to the order in Fig. 6.17. The qualifications are as follows: +=good, □=neither good, nor bad, -=bad, --=very bad.

expression	time constant	sign of change	profile shape
1. no change	–	–	□
2. V_0 change	□	+	□
3. Thermo-diffusion	+	–	–
4. E_{\parallel} driven pinch	+	+	–
5. Constant matrix	+	□	□
6. Varma pinch	–	–	--
7. q^{-1} pinch	–	--	–
8. Miskane expression	+	–	–
9. Becker expression	–	–	--

The traces labeled 'Becker' mark the simulation of this expression. The effect of the expression has the wrong sign and is smaller than observed, and it is delayed with respect to the observed n reaction. It closely resembles the curve in which no change was applied to the transport parameters: The density pulse originating in the edge is much larger than any effect of T_e on n_n .

Note that this expression does not reproduce the observed profile shape. The reason for this is that the n_n profile decreases strongly with the distance to the edge. To obtain a pinch in the core similar to observed, a hot neutral density similar to the cold neutral density must be assumed. The shown result is obtained with $n_{n,h}/n_{n,c} = 10\%$, which is much larger than the ratio obtained in section 6.3 ($n_{n,h}/n_{n,c} \sim 2\%$).

Summarising, this expression fails on all our criteria to resemble the data.

Summary

In Table 6.2 the performances of all expressions applied to simulate n around the switch-on of ECH are summarised. The performance is judged using the three criteria introduced at the beginning of section 6.6: time constant, sign of change and profile shape. The applied qualification is explained in the caption. The time constant is qualified '–' if the time scale is comparable to the density pulse stemming from the edge. The qualification '□' indicates that the sign of the change cannot be determined for sure. The profile shape is '+' when the flat n area is obtained and the gradient outside the flat part is not enhanced. It is '□' in case local subtleties, like the strong $\nabla_r T_e$, modify the simulated profile in a way not observed on the measured profile. The profile shape is '–' when there is a peak instead of a flat area in the core. The qualification '--' is reserved for the simulated profiles that do not look like either the Ohmic or the ECH profiles at all.

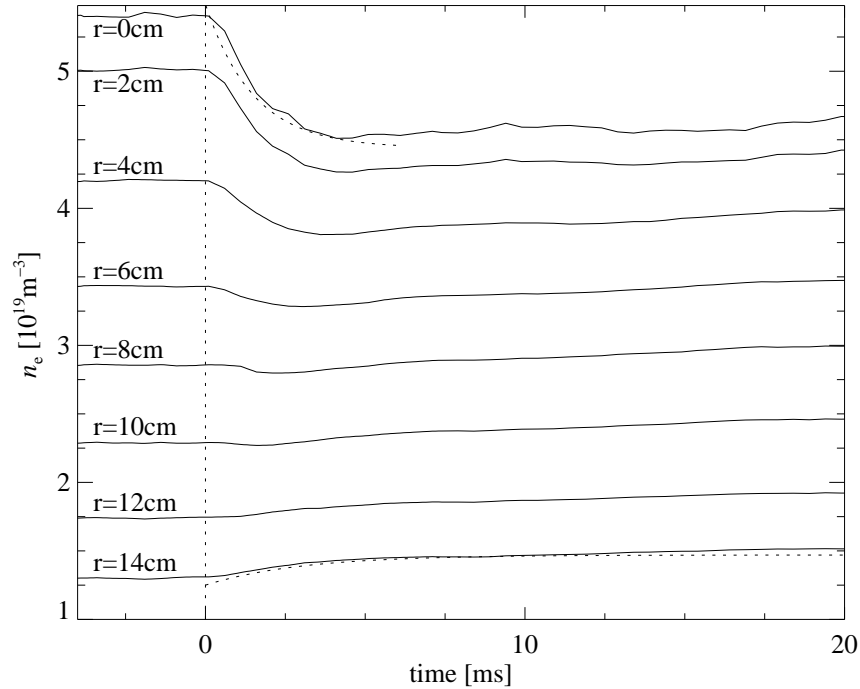


Figure 6.19: Time traces of n around the switch-on of ECH at $t = 0$ and during the relaxation to the new steady state for a discharge with off-axis ECH ($\rho_{\text{dep}} = 0.32$, $r_{\text{dep}} = 4.5$ cm). The dotted lines serve as guide to the eyes. They are negative exponents $\exp(-t/\tau)$, with $\tau = 2.5$ and 3 ms for the curves at $r = 0$ and 14 cm, respectively.

6.6.2 Transition from Ohmic to Off-axis EC Heated state - case I

In this section we study the discharge in Fig. 6.11, in which off-axis ECH is applied with $\rho_{\text{dep}} = 0.28$, $r_{\text{dep}} = 4.5$ cm. At switch-on of ECH, the discharge first develops to a state A' (*c.f.* Fig. 6.6). After 48 ms it experiences a spontaneous transition to state A". In this section the density around ECH switch-on, as illustrated in Fig. 6.19, is simulated. The spontaneous transition is accompanied by an MHD event and is therefore less suitable for simulation.

In Fig. 6.20 the n traces of the experimental data and the simulations are shown at the radii 2, 6, 10 and 14 cm. Fig. 6.21 contains the profiles just before and 45 ms after ECH switch-on for the nine simulations. At ECH switch-on, the n profile experiences a relaxation similar to reported in section 6.6.1: First there is a fast central density decrease, which is taken over by a density pulse from the edge on a longer time scale. Apparently, there is a pump-out effect with off-axis ECH as well.

In the following the results of the simulations are discussed. The parameters of all expressions are kept constant with respect to section 6.6.1. In this way, the tests

are kept as pure as possible and the simulations resemble the Ohmic start profile in an optimal way.

1. No change of D and V

As argued in section 6.6.1 this simulation gives us the n profile development due to the change of the edge conditions only. Indeed we recognise in these traces, labelled with 'No change', the behaviour of the edge density. This simulation confirms that the change of the n profile at the transition is not related to the changes in the edge.

2. Instantaneous change of V_0

Like in section 6.6.1 the value of V_0 is changed instantaneously at ECH switch-on between the values for the Ohmic and ECH phase in Table 6.1.

For the transition at ECH switch-on the imposed change is too large. The resulting profile is significantly lower than the experimental profile. The time scales of observation and simulation are similar, whereas we found that the instantaneous change was faster than the observations in the case with central ECH.

Transport matrix formalism

In the following three related simulations are discussed: The first two, labelled 'Thermo-diffusion' and ' E_{\parallel} -driven pinch' are combined in the 'Constant matrix' simulation. The coefficients of all three simulations are kept constant with respect to section 6.6.1. The simulations are discussed in the mentioned order.

3. Thermo-diffusion

Because of the off-axis deposition, the T_e profile becomes flatter within ρ_{dep} after ECH switch-on. The same trend is seen on the simulated n profile. The final n profile at $t = 45$ ms is slightly hollow in the centre. The time scale of the reaction is similar to the observed time constant.

The hollow n profile indicates that the convective flux due to the thermo-diffusion has changed sign in the centre and is directed outwards. This is in contradiction with the measured profile, which remains peaked. It should be noted that the hollow n profile obtained with counter ECCD (see section 6.4.2) is obtained with central ECH.

The time scales of simulation and observation do agree for this model. However, the profile from the thermo-diffusion simulation does not resemble the observed profile.

4. E-driven pinch

The E -driven pinch decreases strongly at ECH switch-on over almost the full profile. The final value of E_{\parallel} is nearly as low as with central ECH. The decrease takes longer than the observed relaxation.

The longer duration of the change is due to the current diffusion. In contrast to the switch-on of central ECH in section 6.6.1, the j profile changes significantly in this case.

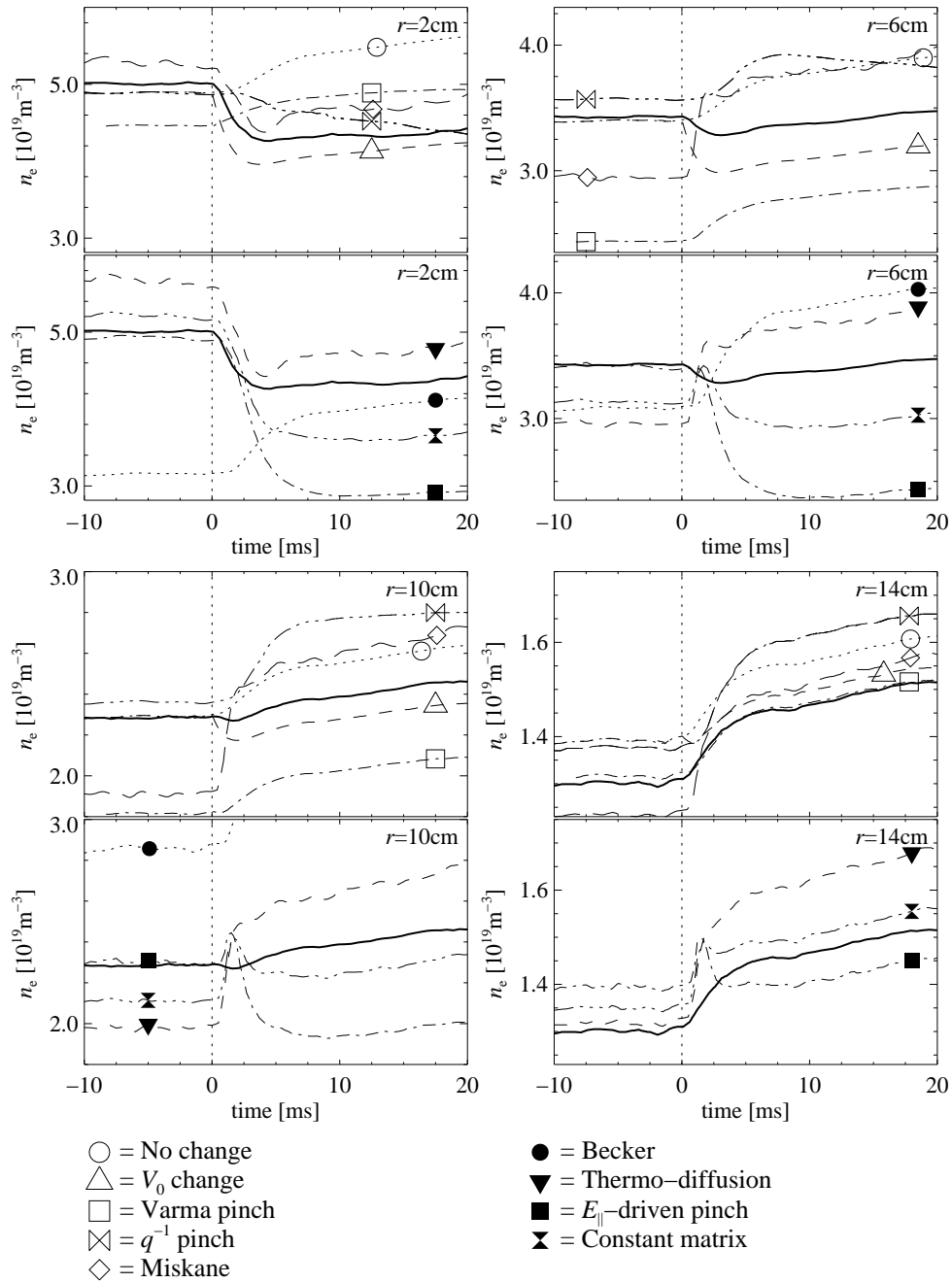


Figure 6.20: Time traces of n of the discharge discussed in section 6.6.2 with $\rho_{\text{dep}} = 0.28$, $r_{\text{dep}} = 4.5$ cm, around the switch-on of ECH at $r = 2$ cm (upper left), $r = 6$ cm (upper right), $r = 10$ cm (lower left) and $r = 14$ cm (lower right) of the experimental data (thick, solid curve) and of simulations with various transport coefficient expressions (see index). For each radius, the plot is split into two parts for clarity.

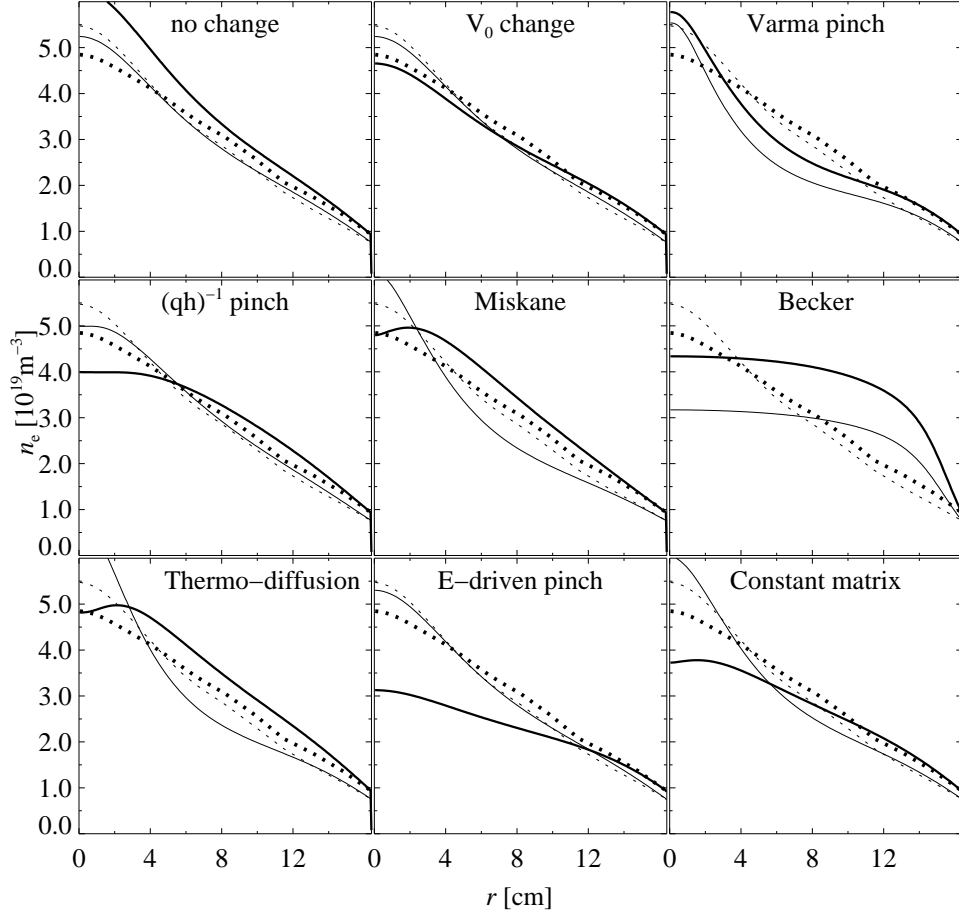


Figure 6.21: n_e profiles of all simulations of Fig. 6.20 and discussed in section 6.6.2. The thin curves are the profiles just before central ECH is switched on, the thick curves are the profiles 125 ms after ECH switch-on. The dotted curves represent the experimental data. They are identical for all nine plots.

As with central ECH (section 6.6.1) the reduction of the E-driven pinch is too strong due to the strong decrease of E_{\parallel} . As the observed change of the n profile is smaller in the off-axis heated case, the mismatch between observation and simulation is even larger.

5. Full transport matrix

In the constant matrix simulation both terms are combined with a fixed ratio, the ratio of section 6.6.1. At ECH switch-on the whole n profile decreases stronger than observed. The time scale of the decrease is between the time scales of the constituent terms, and is longer than observed.

In the previous case we could use the ratio between the two effects to optimise the final result. Unfortunately, the thus obtained transport matrix does not perform satisfactory in the test case presented here. This calls into question the validity of the obtained transport matrix coefficients.

6. Varma pinch

The simulated time behaviour nor the initial profile resemble the data well, so this expression seems not to contain the right physical mechanism.

7. Electrostatic turbulence

Shortly after ECH switch-on the profile from the simulation with the ' q^{-1} pinch' becomes flatter in the centre. The increase has a time constant comparable to the edge gas-puff effect. The final simulated profile is flat in a substantial central area and lower than the observed profile.

In section 6.6.1 we found that the n profile peaks up after switch-on of ECH as a consequence of the ' q^{-1} pinch'. Here, we find the opposite effect in the simulation, while the observed effect is similar to before. The q profile increases inside ρ_{dep} and hence the pinch is decreased.

8. Miskane thermo-diffusion

The simulation of the Miskane thermo-diffusion expression can best be compared to the thermo-diffusion simulation in the constant matrix subsection. Both involve T_e gradient thermo-diffusion, only the coefficients are different.

The initial n profile with the Miskane expression is better than with thermo-diffusion. However, the time behaviour of both simulations is similar. As a consequence, the conclusion for this simulation is similar to that for thermo-diffusion: The simulation changes with the right time scale, but the development towards a hollow profile in the centre is incorrect.

9. Becker scaling

The initial nor the final n profiles resemble the observed profiles. The simulation with the Becker expression gives an enhanced edge effect throughout the whole profile, since the edge is dominant for the profile in this expression. Note that the edge traces of the Becker expression do not fit into the figure ($r = 10$ and 14 cm), due to the particular shape of the profiles simulated with this expression.

Summary

In Table 6.3 the performance of the applied expressions at the switch-on of off-axis ECH with $\rho_{\text{dep}} = 0.28$ is summarised. The performance is judged using the three criteria time constant, sign of change and profile shape. The criteria were already discussed in section 6.6.1. The results are summarised further in section 6.7.

Table 6.3: Performance of the applied expressions in the simulation of the n profile around switch-on of off-axis ECH presented in section 6.6.2. The qualifications are as follows: +=good, □=reasonable, -=bad, --=very bad.

expression	time constant	sign of change	profile shape
1. no change	–	–	+
2. V_0 change	+	+	+
3. Thermo-diffusion	+	+	□
4. E_{\parallel} driven pinch	–	+	□
5. Constant matrix	□	+	□
6. Varma pinch	–	–	–
7. q^{-1} pinch	–	□	–
8. Miskane expression	+	+	□
9. Becker expression	–	–	--

6.6.3 Transition from Ohmic to Off-axis EC Heated state - case II

In this section a discharge with far off-axis ECH is discussed ($\rho_{\text{dep}} = 0.48$, $r_{\text{dep}} = 8$ cm). The plasma reaches a new steady state characterised by the T_e profile 'E' in Fig. 6.6 in ~ 75 ms. The reason why the relaxation takes so long is probably because of the interaction of the T_e and j profiles. In this section not only the n profile around switch-on of ECH is studied, but also during this long relaxation to steady state.

In Fig. 6.22 the time development of the density is shown for the first 75 ms after switch-on of ECH. Like in the other EC Heated cases there is a pump-out effect, decreasing n in the centre, and a gas-puff like density pulse induced by ECH. These effects are illustrated with negative exponent curves, like in Fig. 6.10. Apart from these switch-on effects, the n profile flattens on a long time scale. The profile does not become flat like in the case with central ECH, but the peaking is significantly reduced with respect to the Ohmic phase at the time the n traces reach a minimum at $t \sim 30$ ms. After that n increases again in the centre on a similar time scale as the decrease. The n traces usually reach a maximum shortly before the T_e profile reaches steady state. The simulations indicate that the j profile reaches steady state at the same moment. The development of n after this moment is not further discussed here.

There are a couple of local effects on the core of the n profile visible, *e.g.* at $t \sim 33, 52$ and 62 ms. Though these effects are characteristic for the n relaxation with off-axis ECH, they are not considered any further.

In Fig. 6.23 the experimental data and the simulations are shown for this discharge. In Fig. 6.24 the n profiles obtained from the simulations just before as well as 85 ms after switch-on can be found. In the same figure the experimental profiles are given for reference.

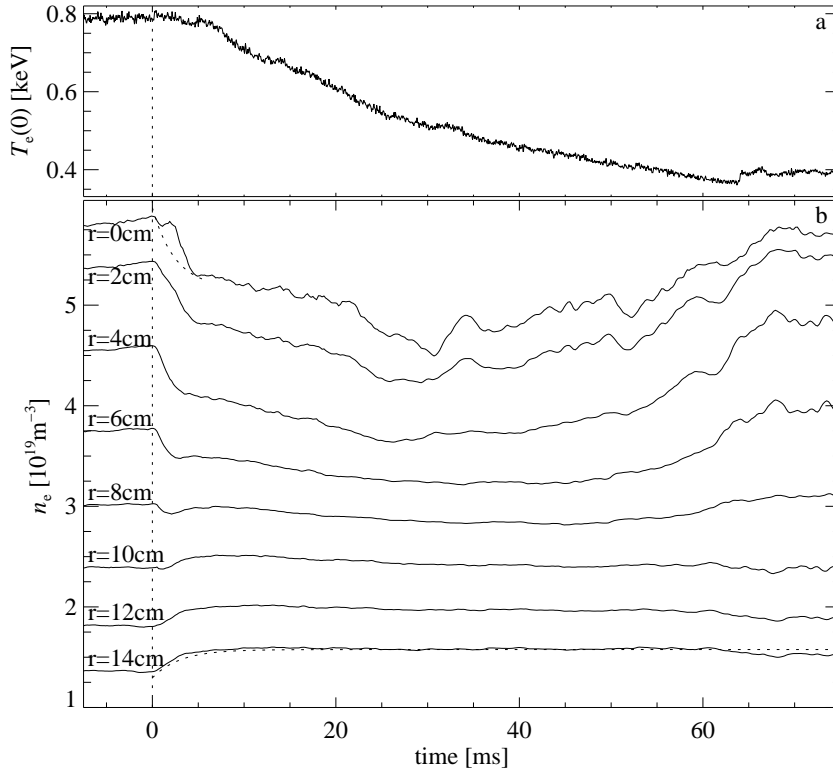
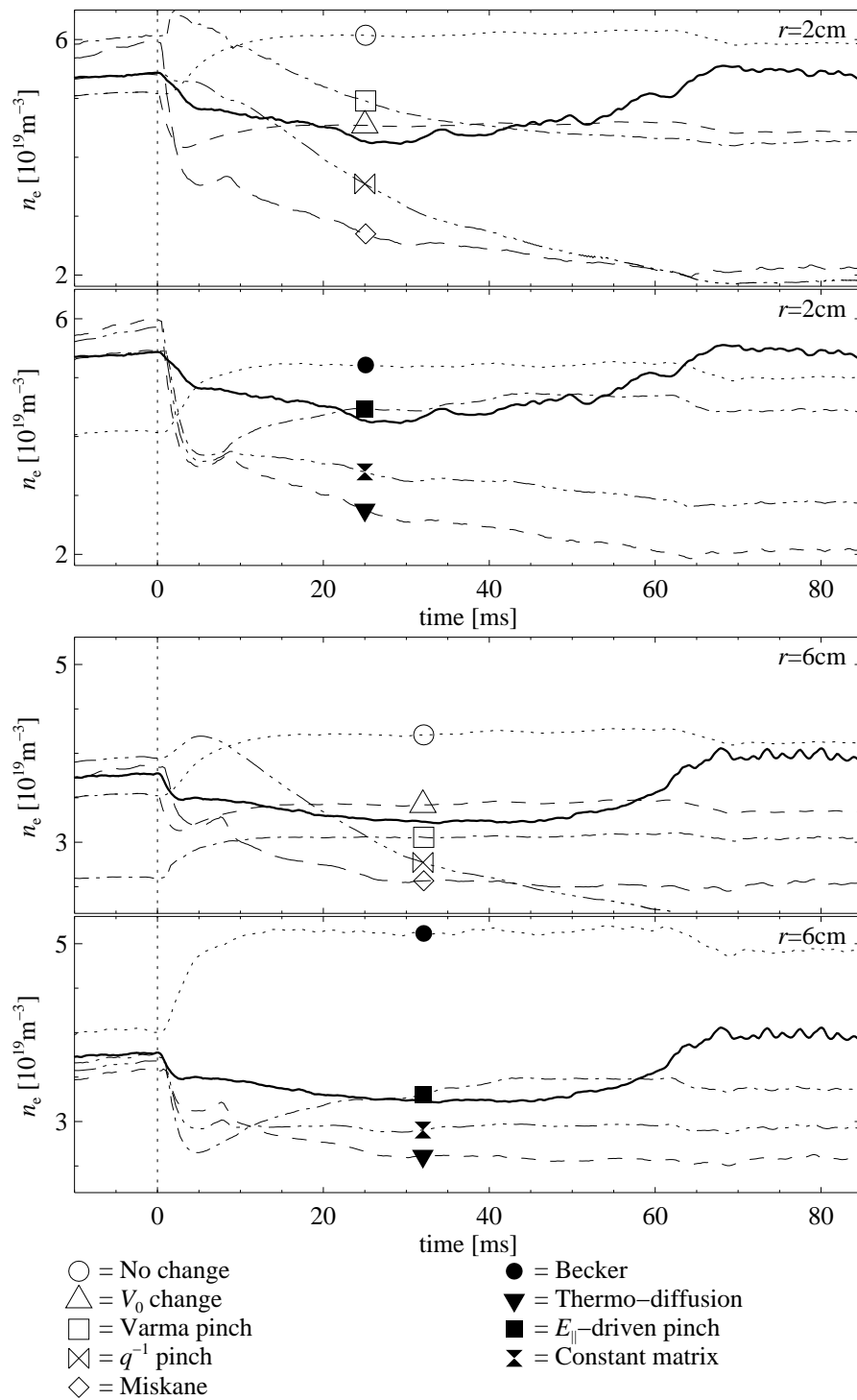


Figure 6.22: Time traces of $T_e(0)$ (a) and n at several radii (b), around the switch-on of ECH at $t = 0$ and during the relaxation to the new steady state for a discharge with far off-axis ECH ($\rho_{\text{dep}} = 0.48$, $r_{\text{dep}} = 8 \text{ cm}$). Note the time scale on which T_e reaches a new steady state is much longer than the energy confinement time (1-3 ms) and the current diffusion time (10-15 ms). The dotted lines in b serve as guide to the eyes. They are negative exponents $\exp(-t/\tau)$, with $\tau = 2.5$ and 3 ms for the curves at $r = 0$ and 14 cm, respectively. Note the time axis is extended with respect to Fig. 6.10.

This special discharge can be used as yet another test of the expressions for particle transport. In the following the results of the various simulations on this test case are discussed. The simulations as well as their coefficients are kept constant with respect to section 6.6.1.

In the previous sections, 6.6.1 and 6.6.2, the behaviour of the simulations of n at switch-on of ECH has been discussed extensively. Therefore, we will only consider the switch-on effects sideways and focus mainly on the long term behaviour, despite the significant change of the input ρ_{dep} .



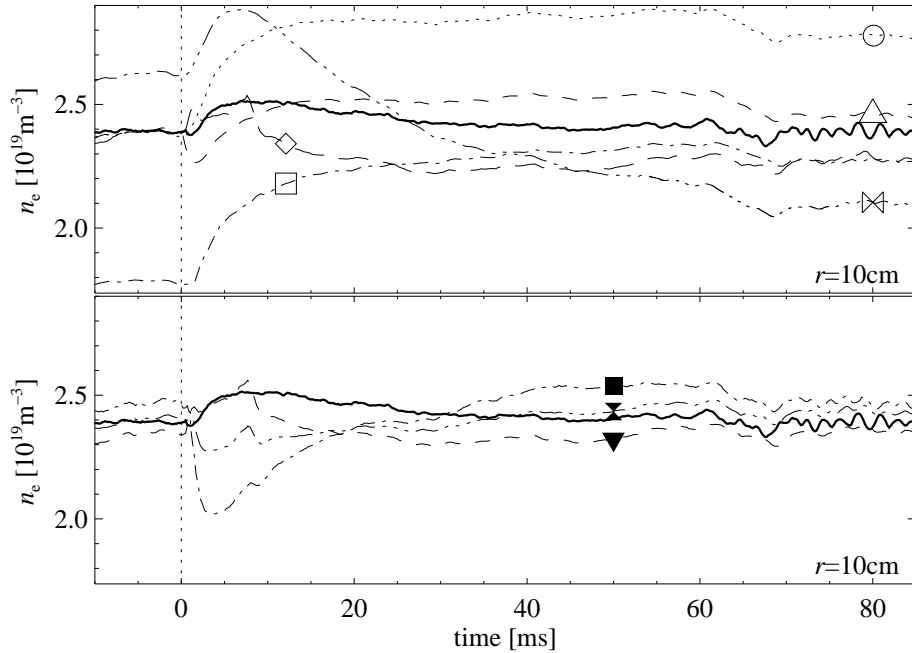


Figure 6.23: Time traces of n at $r = 2, 6$ and 10 cm of the experimental data (thick, solid curve) and of simulations with various transport coefficient expressions (see index). For each radius, the plot is split into two parts for clarity. Note that the time axis is extended with respect to Fig. 6.23.

1. No change of D^{inc} and V^{inc}

As discussed before, this simulation gives the result of the edge effects only. Apparently, the edge is only influenced at switch-on of ECH and after ~ 65 ms. Note that this last decrease of the edge density coincides with the peaking of n in the centre just before steady state is reached.

Although the edge density is decreased at the end of the simulation, it is not as low as in the Ohmic state. The observed particle confinement remains lower than that in the Ohmic confinement case.

2. Instantaneous change of V_0

In this simulation the pump-out is approximated by an instantaneous change of the parameter V_0 . We used the same change as with central ECH, *i.e.* -14 m/s. The effect of this change is significantly larger than the observed pump-out effect. After ~ 20 ms the two traces do cross each other in the centre. The time constant of the instantaneous change simulation is shorter than of the measured data.

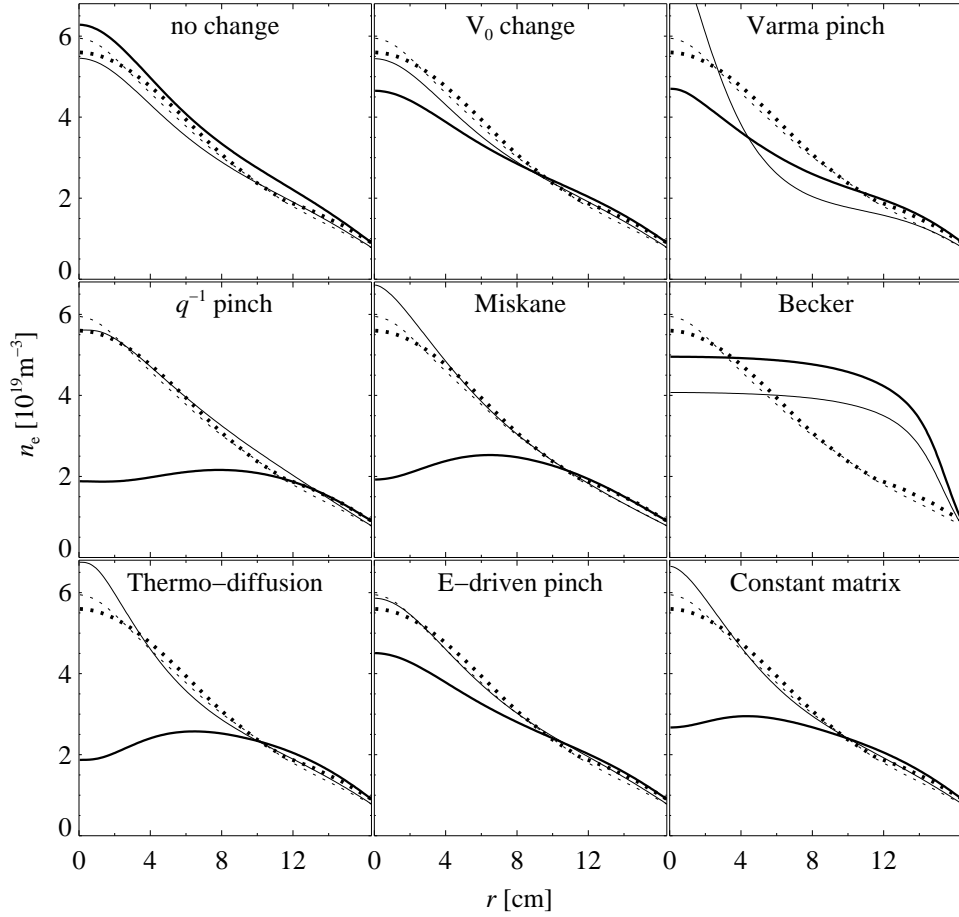


Figure 6.24: n_e profiles of all simulations of Fig. 6.23 and discussed in section 6.6.2. The thin curves are the profiles just before far off-axis ECH is switched on, the thick curves are the profiles 75 ms after ECH switch-on. The dotted curves represent the experimental data. They are identical for all nine plots.

Transport matrix formalism

3. Thermo-diffusion

After the initial decrease due to the decrease of T_e and its gradient in the centre like we observed in section 6.6.2, the simulated n at $r = 2$ cm decreases on a time scale comparable to the observed time scale. The $r = 6$ cm trace does not change anymore after $t = 30$ ms, when the observed n reaches its minimum. However, the $r = 2$ cm trace decreases further until $t \sim 65$ ms. The simulation decreases more strongly than the observation.

4. E-driven pinch

This simulation with a constant coefficient for the pinch proportional to $E_{||}$, decreases strongly immediately after switch-on of ECH, like in the test cases described in sections 6.6.1 and 6.6.2. The time scale of this decrease is similar to but longer than the observed time scale. After this decrease the simulated n starts to increase on a long time scale. It reaches a stationary value at $t \sim 40$ ms and follows the edge effects from then on. The profile shape seems to be fixed as well.

Like the previous simulation this effect does not explain the peaking of the n profile after the initial flattening. There is no indication that it reverses sign.

5. Full transport matrix

This simulation, lying in between the two previous ones, is not in agreement with the observations. With a change of the ratio of the two terms, which is kept fixed with respect to section 6.6.1, the behaviour would probably not resemble the observations better, because the E-driven pinch simulation saturates for $t > 40$ ms. It can be argued though, that the final profile shape could be improved.

6. Varma pinch

Centrally, the Varma pinch causes a very fast increase of n . Further out, n increases as well, but on a somewhat longer time scale. These traces become constant after this initial increase, the central trace starts to decrease with a very long time scale until the end of the simulation. The final profile is more or less comparable to the observed profile, due to a substantial reduction of the central convection with respect to the initial profile. However, the initial profile does not resemble the initial observed profile.

The balance between the factors constituting this pinch, is subject to fast changes at the ECH switch-on. This causes the early peak in the centre. With the gradual decrease of the central j , B_{θ} decreases in the core and the Varma pinch is reduced here. Contrary to the E-driven pinch simulation, the B_{θ} -profile remains sensitive to small changes in the central j . That is why the relaxation of the central n takes much longer in this case.

7. Electrostatic turbulence

The central trace of this simulation is unchanged for a couple of ms after which it starts to decrease. The other two channels first increase to reach a maximum at $t \sim 7$ ms, after which they also decrease. This decrease takes as long as the decrease seen on the Varma pinch, except for the channel at $r = 10$ cm, which is outside ρ_{dep} . This channel follows saturates after $t \sim 50$ ms. The final profile is slightly hollow within ρ_{dep} , which indicates that the change is strongest in the centre.

8. Miskane thermo-diffusion

Although the Miskane expression prescribes a more comprehensive expression for the thermo-diffusion than the constant, which is taken in the thermo-diffusion simulation, the results of the Miskane simulation can hardly be distinguished from this previous simulation. The initial and final profiles are slightly better, though the

Table 6.4: Performance of the applied expressions in the simulation of the n profile after switch-on of far off-axis ECH presented in section 6.6.3. The qualifications are as follows: +=good, □=reasonable, -=bad, --=very bad.

expression	relaxation	sign of change	profile shape
1. no change	–	–	+
2. V_0 change	–	□	□
3. Thermo-diffusion	□	+	--
4. E_{\parallel} driven pinch	□	–	□
5. Constant matrix	□	+	--
6. Varma pinch	□	+	–
7. q^{-1} pinch	–	+	--
8. Miskane expression	□	+	--
9. Becker expression	–	–	--

reaction to the application of ECH is very similar. A similar decrease of n in the centre is observed, leading to the final hollow n profile.

This simulation has no added value with respect to the simpler thermo-diffusion simulation.

9. Becker scaling

As stated before the reaction of the simulation with Becker scaling reacts predominantly on the edge effects. None of the observed more central effects can be recognised in this simulation. The trace at $r = 10$ cm is beyond the plotting region, due to the peculiar shape of the predicted n profile (see Fig. 6.24). The shapes of the profiles do not resemble the observed profile.

This simulation is not useful to see central changes, nor does it outperform the other simulations in the edge.

Summary

The performance of the simulations of this section is summarised in Table 6.4. The performance of the simulation on the observed long term change of the n profile is evaluated with neglect of the initial changes. Since the time constant is difficult to define for this n development, the ability of the simulation to follow the observed pattern is evaluated. The sign of change is taken between 10 and 30 ms.

In this section the long term behaviour of n was considered, neglecting local characteristic events. None of the simulations predicts the observed n behaviour with any detail. The significant changes to the j , q and T_e profile modify the expressions significantly, whereas the observed n profile is hardly changed. On the other hand, n shows very pronounced behaviour in intervals where the other plasma parameters are subject to little change.

The results are summarised further in section 6.7.

6.6.4 Relaxation to Bifurcated Ohmic State

The data on bifurcated Ohmic states presented in Fig. 6.13 show the two states that originate from the same far off-axis EC Heated state. As soon as ECH is switched off, the n profile starts to develop towards a state with more peaked n profile and flatter T_e profile. If and only if a particular, characteristic MHD crash occurs, the development towards this state II is interrupted and the discharge relaxes to the pre-ECH Ohmic state, state I [35].

The occurrence of the MHD crash makes the relaxation to state I unsuitable for transport simulation. However, the relaxation to the interesting state II can be simulated.

In Fig. 6.25 the development of $T_e(0)$ and n at several radial positions is shown. The density increases strongly in the centre and is more or less constant between $r = 6$ and 12 cm. Note that the edge density decreases, because the ECH induced gas release from the wall is stopped. This decrease, however, is much slower than the increase at ECH switch-on. The density reaches a maximum at $t \sim 52$ ms after which it decreases to its new steady state. The profiles plotted in Fig. 6.13 are taken in the new steady state at $t = 75$ ms.

It should be noted that the change of n in this case is much slower than after switch-on of ECH which indicates that a different physical mechanism is dominant in the observed density growth than we observed at switch-on of ECH.

The increase of the central n is not monotonic. At $t \sim 12$ ms the peaking is temporarily interrupted. At $t \sim 31$ ms a minor MHD crash with a post-cursor occurs, which is smoothed in the data analysis. This crash is much smaller than the crash with which the two Ohmic states bifurcate. Therefore, the evolution of simulation and experiment is only compared up to this crash.

In Fig. 6.26 the observations and the various simulations of n are shown at the radii $r = 2, 6, 10$ and 14 cm. Fig. 6.27 shows the profiles of the simulations just before and 50 ms after switch-off of ECH, as well as the experimental profiles at these points in time. In the following the results of the simulations are discussed in detail.

The start situation for the simulations is different from the previously described test transitions, because the simulation starts during the far off-axis ECH. Therefore, the model expressions for V^{inc} can be re-optimised for this particular plasma state, *i.e.* instead of the Ohmic n profile the initial profiles can now be optimised for the steady state far off-axis EC Heated discharges. The coefficients of the convection in the Varma pinch and Becker scaling expressions are increased by 25 %, in the E-driven pinch it is increased by 28 %. The start parameters of the no-change and instantaneous change models are taken according to the ECH case in Table 6.1, *i.e.* V_0 is 50 instead of 60 m/s. For the expressions which depend on a parameter with a hollow start profile (*i.e.* the thermo-diffusion, full transport matrix, Miskane and q^{-1} pinch expressions), adaptation does not improve the agreement with the measured profile.

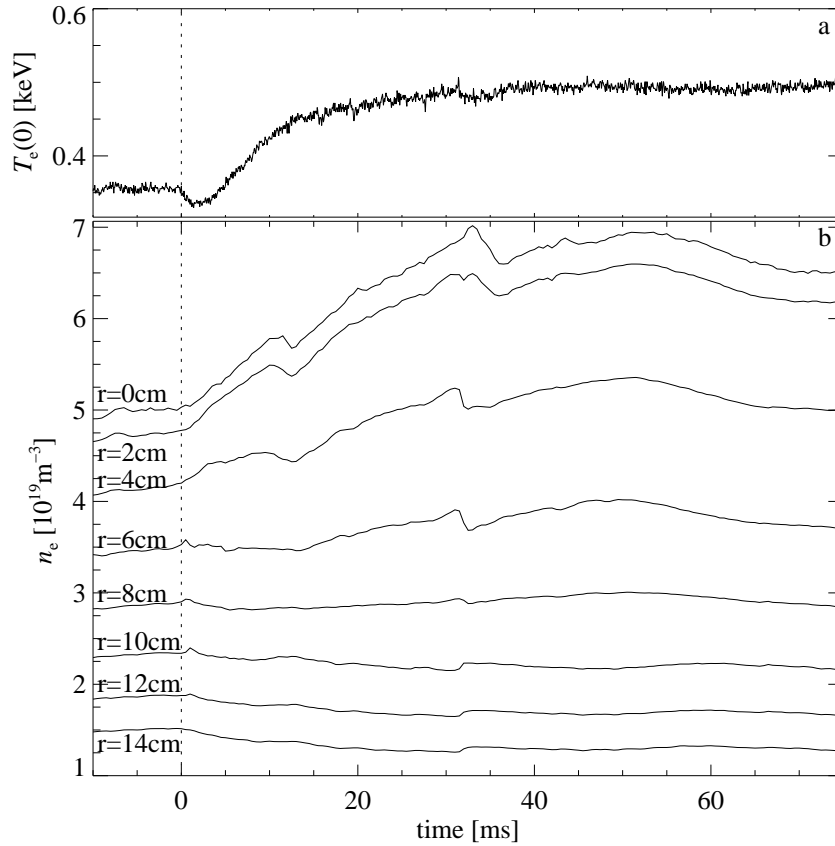


Figure 6.25: Time traces of $T_e(0)$ (a) and n at several radii (b) around the switch-off of far off-axis ECH at $t = 0$ for a discharge developing to the state II in Fig. 6.13 ($\rho_{\text{dep}} = 0.48$, $r_{\text{dep}} = 8$ cm). Note the y-axis of (a) is reduced with respect to Fig. 6.22.

1. No change of D^{inc} and V^{inc}

The no change simulation profile is slowly decreasing like the edge density does. The small interrupt of the edge density decrease around $t = 12$ ms is hardly visible on the central simulation trace.

2. Instantaneous change of V_0

For the Ohmic phase here $V_0 = 70$ m/s is taken, higher than the normal Ohmic value (60 m/s, *c.f.* Table 6.1) to reflect that the measured profile is more peaked.

The instantaneous change leads to a much faster increase of n than observed. Also, n increases on all channels shown, whereas only on the two inner channels an increase of n is measured. After this initial, fast decrease, this simulation follows the edge effect. The final profile shape resembles the observed final profile shape

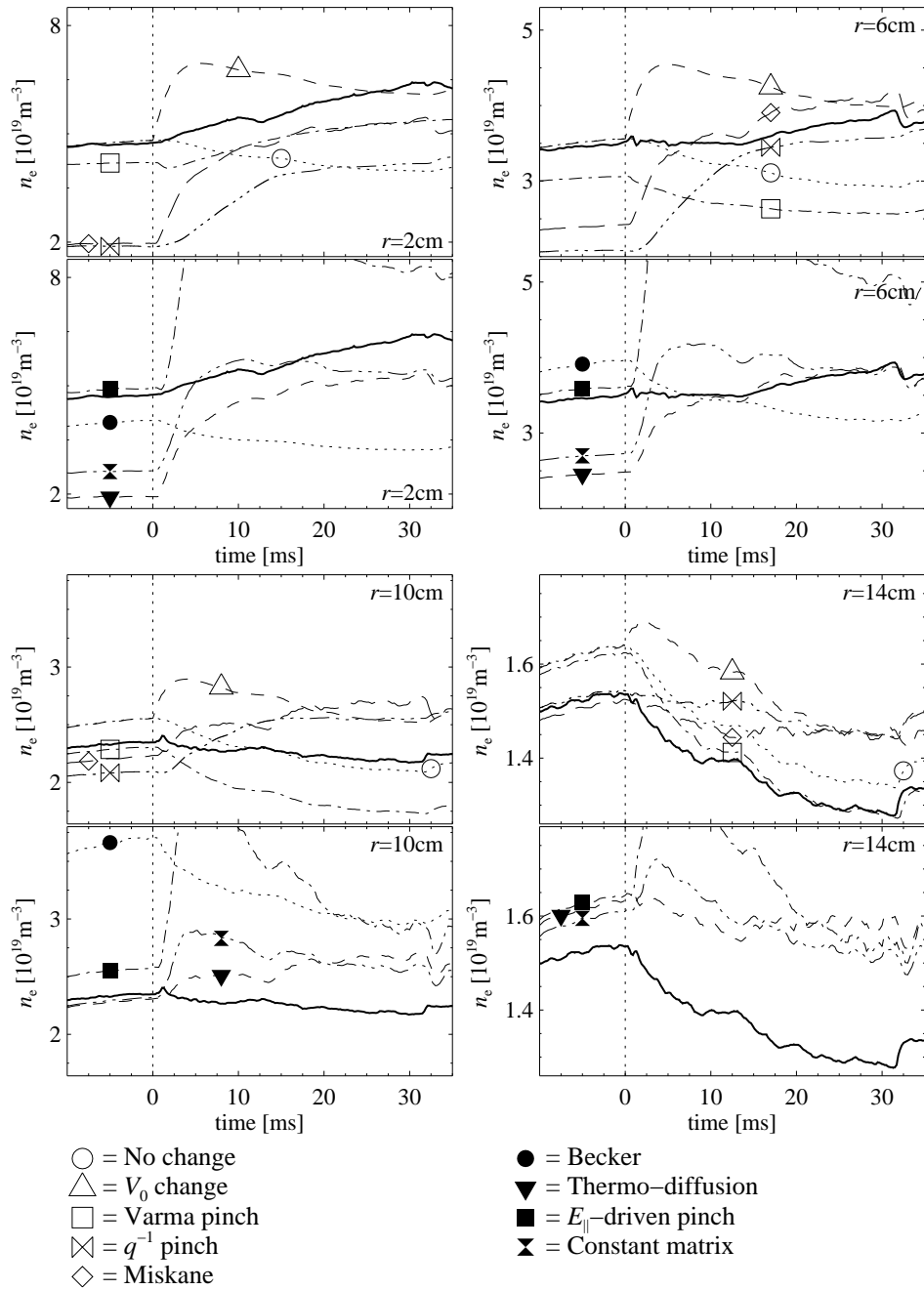


Figure 6.26: Time traces of n of the discharge discussed in section 6.6.2 with $\rho_{\text{dep}} = 0.48$, $r_{\text{dep}} = 8$ cm, around the switch-on of ECH at $r = 2$ cm (upper left), $r = 6$ cm (upper right), $r = 10$ cm (lower left) and $r = 14$ cm (lower right) of the experimental data (thick, solid curve) and of simulations with various transport coefficient expressions (see index). For each radius, the plot is split into two parts for clarity. Note that the axis is extended with respect to Fig. 6.17.

well.

Transport matrix formalism

3. Thermo-diffusion

At switch-off of ECH this simulation increases on a faster time scale than the data. After the initial rise, a longer time scale increase follows, which is nicely parallel to the observed data on the inner channels. The final profile is less peaked than the measured profile, in contrast with the simulations up to now, in which the thermo-diffusion profiles were more peaked than the data.

The fast increase at switch-off is due to the fast increase of T_e in the centre. Its time constant is comparable though larger than the ' V_0 change' simulation. The long time scale is due to the interaction of T_e and j in the relaxation, which was also observed in section 6.6.3. The final profile shape of the simulation is less peaked than in the Ohmic state I, because the T_e profile is flatter. This does not agree with the observed profile, which is more peaked in Ohmic state II.

4. E-driven pinch

The change of this pinch at switch-off is much too fast and much too large. On all traces shown, the simulation exceeds the plotting scale, which has been taken rather large. Only at the end of the plotted interval the simulated curves at $r = 2$ and 6 cm re-enter the plot. The final profile shape is in reasonable agreement with the observed profile, though elevated relatively too much close to the edge.

5. Full transport matrix

This simulation performs worse than the thermo-diffusion solely. The final profile is reasonable, but not as peaked as the observed profile.

6. Varma pinch

The time scale of this simulation is similar to the one observed. However, the final profile is not very good.

7. Electrostatic turbulence

At switch-off of ECH, n increases in two phases: The first phase is a strong increase, larger than on the data, up to $t \sim 15$ ms, in the second phase the rise is slower than the data. The final profile is too low and too flat. The simulation indicates that the final minimum value of q is just below 1.5 and lies on-axis.

Since T_e is low with respect to the usual Ohmic state I, q remains relatively high, as the simulation indicates. This explains why the final n profile is relatively low and flat.

8. Miskane thermo-diffusion

Though a small difference is visible on the time traces, the conclusions drawn for the thermo-diffusion simulation hold for the Miskane simulation as well.

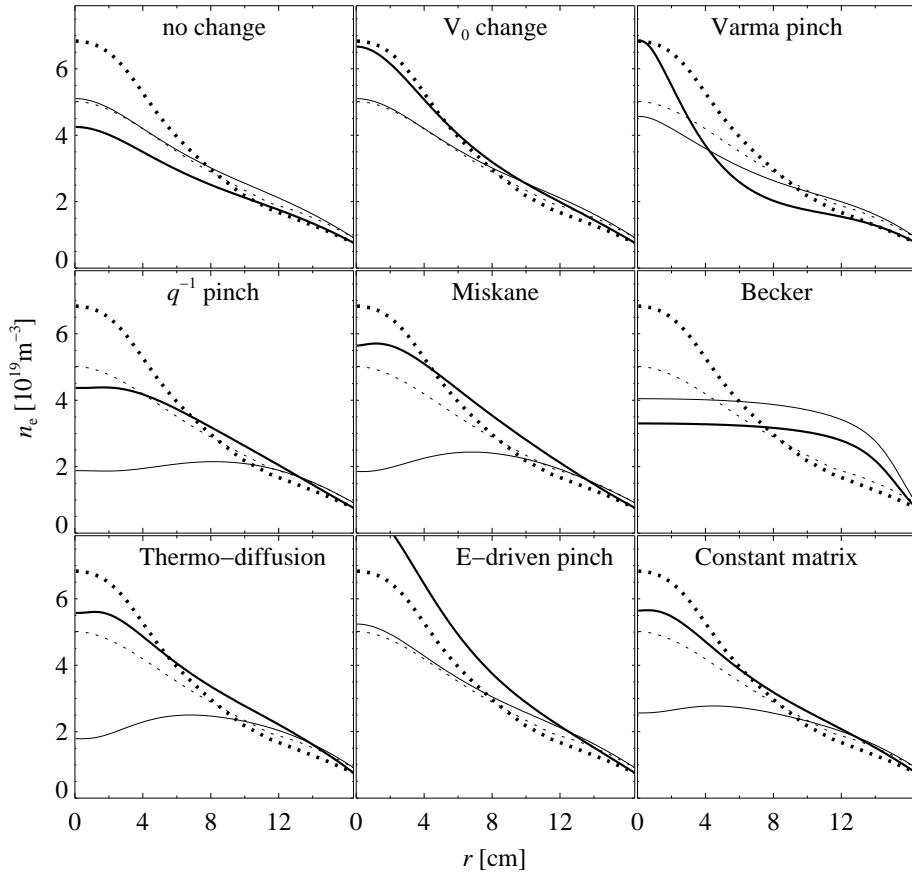


Figure 6.27: n_e profiles of all simulations of Fig. 6.26 and discussed in section 6.6.4. The thin curves are the profiles just before the far off-axis ECH is switched off, the thick curves are the profiles 50 ms after ECH switch-off. The dotted curves represent the experimental data. They are identical for all nine plots.

9. Becker scaling

This simulation again indicates that the edge effects are dominant for this expression. There is no indication that this simulation resembles the measured n behaviour.

Summary

The performance of the simulated expressions on the switch-off of far off-axis ECH and the subsequent relaxation towards the peaked- n , flat- T_e Ohmic state II is evaluated in Table 6.5 with symbols. This table has the same principle as Tables 6.2-6.4, but the time constant and sign of change columns are divided into two parts. The

Table 6.5: Performance of the applied expressions in the simulation of the n profile after switch-off of ECH deposited far off-axis, presented in section 6.6.4. The time constant and sign of change columns are divided into parts for $t = 0 - 10$ ms and $t = 13 - 30$ ms (A and B, respectively). The qualifications are as follows: +=good, □=reasonable, -=bad, --=very bad.

expression	time constant		sign of change		profile shape
	A	B	A	B	
1. no change	+	+	-	-	-
2. V_0 change	-	+	+	-	+
3. Thermo-diffusion	-	+	+	+	□
4. E_{\parallel} driven pinch	-	+	□	-	□
5. Constant matrix	-	+	+	□	□
6. Varma pinch	+	+	□	□	-
7. q^{-1} pinch	+	+	□	+	-
8. Miskane expression	-	+	+	+	□
9. Becker expression	+	+	-	-	--

first part is for the phase between switch-off and the interruption of the density build-up at $t \sim 12$ ms, *i.e.* 0 – 10 ms, and is labelled 'A'. The second part is for the phase between this interruption and the MHD event, discussed at the beginning of this section, *i.e.* 13 – 30 ms, labelled 'B'. This division is made, because several simulations show a double time scale relaxation, separated by the interruption at $t \sim 12$ ms. The interruption at $t \sim 12$ ms can be seen on shots on both bifurcation branches and is therefore characteristic for the density increase after switch-off of far off-axis ECH.

The time scale in phase 'B' is correct for all simulations. It should be noted that the change of n happens gradually, so the exact time constant is hard to determine exactly. Further, the 'No change' and Becker simulations follow the edge effect only. Nevertheless, the other simulations relax on a time scale comparable to the length of phase 'B'.

The relaxation of the n profile discussed has basically three characteristics: 1) Strong density increase on a very long time scale; 2) Enhanced peaking of the final n profile in the centre; 3) Interruption of the density build-up. The simulations do reasonably well on the first point.

Concerning the second point it should be noted that none of the simulated profiles is as peaked as the corresponding profiles in the conventional Ohmic state. Further, no simulation shows localisation of the relaxation in the centre. The localised character of the observed change suggests that the diffusion or convection is strongly varying with radius.

The interruption of the density build-up in the observed data around $t = 12$ ms is not reproduced at all in the simulations. It suggests that the transport coefficients

are temporarily varying. It is not caused by MHD, since both the n and T_e data lack any crash (see Fig. 6.25).

6.7 Summary

In this chapter the particle transport on RTP has been studied. The particle balance consists of sources and sinks of charged particles and particle fluxes. Both parts have been studied.

To know the particle sources in the plasma, the neutral density (n_n) must be estimated. The neutral transport in RTP is not diffusive, and the n_n profile has been obtained from an equilibrium calculation of the neutral convection in slab geometry. This has been bench-marked against Monte Carlo simulations with the EIRENE code. The calculations showed that the central charged particle source associated with the calculated n_n profiles is negligible.

The calculated n_n profile falls off fast with the distance from the edge. A simple expression is fitted to the obtained n_n profile: $n_n = n_n(r = a) \cdot (r/a)^l$, with $l = 2 + 1 \cdot n(0)/n_0$ ($n_0 = 10^{19} \text{ m}^{-3}$).

In the part of the plasma where the particle source is negligible, the transport has been described with diffusion (D) and convection (V) profiles. All observed profiles have zero or negative density gradient in the core, except for those with central counter ECCD, which show a marked 'hole' in the centre.

The T_e and n profile behave oppositely with ECH. In centrally EC heated discharges, the T_e profile becomes very peaked, while the n profile becomes flat. In a scan of the deposition radius (ρ_{dep}) of ECH, the T_e profile becomes less peaked with increasing ρ_{dep} , while the n profile peaking increases with ρ_{dep} . Without ECH, the same antagonism of T_e and n is observed in the bifurcated Ohmic states.

This behaviour cannot be explained by profile consistency, as proposed in *e.g.* [36–38,47], which states that the profile shapes of the current density (j) gradient and the electron pressure (p_e) gradient are identical. In the discharges with off-axis ECH, the j profile becomes more hollow than the p_e profile. Comparison of the p_e and j profiles obtained in the simulations shows, that the time scale of the j profile change is at least that of the p_e profile change, but usually longer.

From previous work on the electron thermal transport we know that this is dominated by thermal barriers [48]. The particle transport does not seem to be governed by similar transport barriers. The only clear indication for the existence of barriers in the particle transport is obtained in the 'state II' of the bifurcated Ohmic states. The n profile has a pronounced gradient in this case and the T_e gradient is very low inside the radius of the strong n gradient.

The analysis of the particle transport observations in RTP was performed with the ASTRA code. In the presented simulations experimental data of T_e was input to a model calculating the n and j profiles. The j profile was calculated from neoclassical theory, the n profile was calculated from model expressions for the transport coefficients. To obtain an estimate of the transport coefficients the temporal reaction of n to gas-puffs was studied. The central value of D is $1.0 \pm 0.4 \text{ m}^2/\text{s}$

and $V = 6 \cdot 10^1 \cdot \rho$ m/s, where ρ is the normalised minor radius. These values are in agreement with previous observations of D and V on RTP. Remarkably, simulation of gas-puffs in discharges with central ECH results in the same value of D , while V is somewhat smaller at $V = 5 \cdot 10^1 \cdot \rho$ m/s.

Four transitions between plasma states have been simulated with the ASTRA code:

1. Transition from Ohmic to centrally heated plasma states (section 6.6.1);
2. Transition from Ohmic to mildly off-axis heated states (section 6.6.2);
3. Transition from Ohmic to far off-axis heated states (section 6.6.3);
4. Transition from the far off-axis heated state to the bifurcated Ohmic state II (section 6.6.4).

The time evolution of these discharges has been simulated in detail during and after the switch of ECH, using expressions for the particle transport coefficients obtained from nine models. These are: 1) model with fixed transport coefficients; 2) model with fixed transport coefficients except for fixed, instantaneous change of parameter V_0 (see Eq. 6.25); 3) thermo-diffusion with fixed coefficient; 4) pinch driven by E_{\parallel} ; 5) transport matrix with fixed coefficients; 6) anomalous Ware pinch, enhanced according to Varma [9]; 7) convection proportional to $\nabla_r(\ln q)$; 8) Miskane thermo-diffusion; and 9) scaling of V/D with n_n as proposed by Becker [17].

In the first period after switch-on of ECH, the central density always decreases. This 'pump-out' effect is more or less independent of the deposition radius of ECH, though it seems to decrease slightly with increasing ρ_{dep} . The pump-out occurs on a time scale of ~ 2.5 ms. This is equal to the characteristic time associated with thermal transport. For centrally heated plasmas the pump-out is the only effect on n , in the other cases other relaxation processes occur as well. After switch-off of ECH in centrally heated discharges the pump-out effect disappears on the same time scale as it comes into existence. In off-axis heated discharges this 'reversed pump-out' is not observed, so the pump-out seems to be reduced already during ECH in these discharges.

None of the applied model expressions performs well on all four transitions. The positive results are highlighted here.

The fast time-scale of the pump-out effect observed in all three transitions at ECH switch-on is reproduced well by the plain thermo-diffusion coefficient simulation as well as by Miskane's thermo-diffusion expression, and reproduced reasonably well by the simulation with a transport matrix with fixed coefficients. The longer time scales observed with off-axis ECH and in the relaxation to the bifurcated Ohmic state are slightly better predicted by the simulation with the enhanced neo-classical Varma pinch and the pinch proportional to $\nabla_r(\ln q)$.

The simulation with the transport matrix with fixed coefficients gives the best prediction of the sign of the n changes at the transitions, followed by the two thermo-diffusion expressions, after which come the simulation with the pinch driven by the parallel electric field (E_{\parallel}) and the $\nabla_r(\ln q)$ pinch simulation.

Although we applied several expressions with various physical parameters in the particle transport coefficients, the two empirical models resemble the final profile of the simulations best: the simulation in which the transport coefficients are fixed and the simulation in which the pre-factor of the convection coefficient was changed instantaneously by a factor, taken equal for all ECH switch-on transitions, and taken similar in the bifurcated Ohmic state. The changes to the plasma parameters used in the physics-based expressions are generally so strong that the predicted n change exceeds the observations.

The performances of the thermo-diffusion proportional to D as proposed by Miskane and the plain thermo-diffusion cannot be distinguished in the presented simulations, since their mutual difference during the various simulations is smaller than the difference of both of them with the observations.

With the scaling of V/D with the neutral density as proposed by Becker neither the Ohmic n profile nor the final n profiles are obtained with any similarity to the observed profiles. The transient profiles from the simulation with this model only reflect the behaviour of the edge density and are useless for the understanding of the behaviour of the central n .

6.8 Discussion and Conclusion

The observations of the n profile show that n is remarkably indifferent to the substantial changes of the profiles of T_e and j . The expressions derived from theoretical transport models predict a much stronger sensitivity. Apparently, the dominant parametrical dependence is not contained in the applied expressions.

The insensitivity of n to the variations applied in this study is in contradiction with results on TFTR [6] where $D \propto T_e^2$ was found. It should be noted that in the literature no other T_e -dependences of D have been reported [4].

The 'stiffness' of the n profile suggests it is dominated by some kind of profile consistency. This cannot be the profile consistency as proposed in [36–40], in which the p_e profile shape follows the j profile shape, because this holds only in normal Ohmic discharges and fails in off-axis ECH and bifurcated Ohmic state discharges.

In this study, the ion temperature (T_i) has been neglected, because no measurements on the T_i were available. It could be argued that the poor performance of the electron channel models indicates that the particle transport is dominated by T_i . We do expect (on the basis of neoclassical calculations) that the T_i profile variation is much less than that of T_e . This can be understood from the fact that the electron-ion exchange decreases with increasing T_e . Therefore, we expect that T_i does not play an important role in the described experiments. Since the RTP plasmas are characterised by relatively strong n gradients and mild T_i gradients, we expect that they are stable to so-called 'ion temperature gradient' modes.

From the fact that the pump-out effect at switch-on of ECH is independent of the deposition radius it must be concluded that this effect cannot be described by the expressions used in this chapter, since the corresponding effects do vary significantly and even change sign in the scan of ρ_{dep} . Another hypothesis is that somehow the

ECH changes the transport coefficients directly [49]. The time scale corresponding to the pump-out is clearly the energy confinement time, so the pump-out effect seems indirectly temperature-related.

Note that the lack of dependence of the pump-out on ρ_{dep} is a direct violation of profile consistency as proposed in [36–40], for the j profile is constant on a short time scale after switch-on, the central n is decreased by the pump-out in all cases while the sign of the reaction of T_e in the core does depend on ρ_{dep} .

The pump-out effect with on-axis ECH has been observed in other tokamaks [31,32]. For off-axis ECH it can be verified, since on most nowadays tokamaks ECH systems are routinely available. In many tokamaks the j profile can be varied independently of the T_e profile by non-inductive current drive, offering the possibility to perform similar tests of the particle transport theories.

Apart from the pump-out effect, other, longer time scale n changes have been observed. The disagreement of the predicted n profile shape on the long term with the observations is the most serious failure of the expressions considered in this paper. We cannot exclude that the theoretical models contain the relevant physics, but the expressions derived from these theories do not work.

While the common observation is that the measured n profile does not change when the expressions predict a large change, also the reverse happens. Characteristic minor variations have been observed on the temporal behaviour of n , *e.g.* the interruption of the density increase observed after ECH switch-off in section 6.6.4. In section 6.6.3 we found that the change of n reverses sign during the relaxation of the j and T_e profile. These observations suggest that the particle transport coefficients have local variations, and they might be inhomogeneous in space or in one of the plasma parameters. The expressions do not predict these local inhomogeneities.

The observations presented in this chapter clearly pose a challenge for the modeller. Perhaps, we should conclude that the simplification to treat particle transport as a one-dimensional phenomenon, which is generally made in tokamak physics, is not justified. We appear to miss essential physics. If the transport is enhanced by local phenomena, *e.g.* convective cells, these may not necessarily be described correctly by transport coefficients. In a truly two-dimensional system, *e.g.* intermittency could play an important role, leading to essentially non-diffusive transport

Appendix

In this appendix we give an analytical solution of the stationary, one-dimensional diffusion equation for the neutrals in the special case that the plasma density n increases linearly with the distance from the edge. Though the result is not applicable to RTP, as argued in section 6.3.1, it can be valid for other, larger tokamaks.

If we limit our consideration to the plasma close to the edge, we can consider the plasma as a one-dimensional slab for $x > 0$. The plasma is in contact with a wall at $x=0$ at which charged particles recombine into neutrals, which are then re-injected back into the plasma. All dependences perpendicular to x are neglected, and a one-dimensional diffusion equation for the neutral density n_n can be written:

$$\frac{\partial n_n}{\partial t} = \frac{\partial}{\partial x} \left(D_n \frac{\partial n_n}{\partial x} \right) - n n_n \langle \sigma_{\text{ion}} v_e \rangle. \quad (6.27)$$

In this equation D_n is the neutral particle diffusion coefficient and x is the distance from the wall. The second term on the right represents the loss of neutrals caused by ionization. If we assume that n_n decreases strongly with x compared to the minor radius a , x can be taken unlimited.

Consider the stationary situation ($\partial n_n / \partial t = 0$) and assume that n is a linearly increasing function of x with a constant coefficient β :

$$n = \beta x, \quad \beta(x) = \beta \quad (6.28)$$

The distribution of neutrals is only a diffusive process if a random scattering of the neutrals occurs. Suppose the charge exchange process is this process: The number of neutrals is constant in this reaction and the resulting velocity has little correlation with the incident velocity. The neutral diffusion coefficient D_n can be estimated from a random walk argument with the mean free path for charge exchange λ_{cx} as the step size, and $n \langle \sigma_{\text{cx}} v_i \rangle$ as the frequency:

$$\lambda_{\text{cx}} \sim \frac{v_n}{n \langle \sigma_{\text{cx}} v_i \rangle} \quad (6.29)$$

$$D_n \approx n \langle \sigma_{\text{cx}} v_i \rangle \lambda_{\text{cx}}^2 \approx \frac{v_{i,i}^2}{n \langle \sigma_{\text{cx}} v_i \rangle}, \quad (6.30)$$

where the neutral velocity v_n is replaced by the ion thermal velocity $v_{i,i}$, assuming thermal equilibrium between the charged exchanged neutrals and the ions. From Eq. 6.30 we only take into account the n dependence of D_n , $D_n = \alpha/n$ and neglect spatial dependences other than that of n , $\alpha(x) = \alpha$. In particular, this means that T_i and $\langle \sigma_{\text{cx}} v_i \rangle$ are treated as essentially constant in the edge region. This gives for Eq. 6.27:

$$\frac{\partial}{\partial x} \left(\frac{\alpha}{\beta x} \frac{\partial n_n}{\partial x} \right) - \beta x n_n \langle \sigma_{\text{ion}} v_e \rangle = 0 \quad (6.31)$$

$$\frac{\alpha}{\beta x} \frac{\partial^2 n_n}{\partial x^2} - \frac{\alpha}{\beta x^2} \frac{\partial n_n}{\partial x} - \beta x n_n \langle \sigma_{\text{ion}} v_e \rangle = 0 \quad (6.32)$$

$$\frac{\partial^2 n_n}{\partial x^2} - \frac{1}{x} \frac{\partial n_n}{\partial x} - \frac{\beta^2 x^2}{\alpha} n_n \langle \sigma_{\text{ion}} v_e \rangle = 0 \quad (6.33)$$

This equation is of the form $F(x, y, y', y'') = 0$ and has the special property $F(x, ty, ty', ty'') = tF(x, y, y', y'')$, *i.e.* it is homogeneous in y and its derivatives. Its solution can be written in the form:

$$n_n = \exp\left(\int u(x)dx\right) \Rightarrow \frac{n'_n}{n_n} = u(x), \frac{n''_n}{n_n} = u' + u^2 \quad (6.34)$$

The diffusion equation (6.33) reduces to:

$$u' = \gamma^2 x^2 + \frac{1}{x}u - u^2, \quad (6.35)$$

where $\gamma^2 \equiv \frac{\beta^2}{\alpha} \langle \sigma_{\text{ion}} v_e \rangle$ is defined for convenience. This is a so-called Ricatti equation which can be solved with the help of the special solution $u_1(x) = \gamma x$. The general solution has the form $u = u_1 + 1/z(x)$. Using this in Eq. 6.35 gives:

$$z'(x) + U(x)z - 1 = 0 \quad (6.36)$$

$$U(x) = -2\gamma x + \frac{1}{x} \quad (6.37)$$

This can be solved to yield a solution for u :

$$(u - \gamma x) \left[C_1 + \int X(x)dx \right] = X(x) \quad (6.38)$$

where

$$X(x) = \exp \int U(x)dx = \exp[-\gamma x^2 + \ln x] = x e^{-\gamma x^2} \quad (6.39)$$

$$\Rightarrow \int X(x)dx = -\frac{1}{2\gamma} e^{-\gamma x^2} \quad (6.40)$$

giving for Eq. 6.38:

$$(u - \gamma x) \left[\frac{C_1}{x} e^{\gamma x^2} + \frac{1}{2\gamma x} \right] = 1 \quad (6.41)$$

$$\Rightarrow u = \gamma x \left(1 + \frac{2}{2\gamma C_1 e^{\gamma x^2} - 1} \right) \quad (6.42)$$

Now n_n follows from this with a little algebra:

$$\int \frac{2\gamma x}{2\gamma C_1 e^{\gamma x^2} - 1} dx = \int \frac{2x dx}{2C_1 e^{\gamma x^2} - 1/\gamma} \quad (6.43)$$

$$\stackrel{q \equiv x^2}{\underset{dq = 2x dx}}{\int} \frac{dq}{2C_1 e^{\gamma q} - 1/\gamma} = -\gamma q + \ln \left(-\frac{1}{\gamma} + 2C_1 e^{\gamma q} \right)$$

$$\begin{aligned}
n_n &= \exp \int u(x) dx \\
&= \exp \left[\frac{1}{2} \gamma x^2 - \gamma x^2 + \ln \left(-\frac{1}{\gamma} + 2C_1 e^{\gamma x^2} \right) + C_2 \right] \\
&= e^{-\frac{1}{2} \gamma x^2 + C_2} \left(-\frac{1}{\gamma} + 2C_1 e^{\gamma x^2} \right),
\end{aligned} \tag{6.44}$$

where C_2 is an integration constant. The first boundary condition is that the neutral density goes to zero for $x \rightarrow \infty$. As a consequence, $C_1 = 0$. For the other boundary condition, so-called 'perfect recycling' can be imposed, meaning that the outward ion diffusion at the edge is compensated for by inward flux of neutrals:

$$D \frac{\partial n}{\partial x} + D_n \frac{\partial n_n}{\partial x} = 0 \tag{6.45}$$

where D is the particle diffusion coefficient. This gives for the neutral density at the edge, $n_{n,0}$:

$$n_{n,0} \equiv -\frac{e^{C_2}}{2\gamma} = D \sqrt{\frac{\beta^2}{\alpha}} / \langle \sigma_{\text{ion}} v_e \rangle \tag{6.46}$$

The assumed value of n is zero for $x = 0$ and as a consequence D_n diverges at $x = 0$. It is better to introduce a non-zero edge density n_0 : $n(x) = \beta x + n_{i0}$. This can be treated as a linear coordinate transformation of the initial coordinate $x \rightarrow x + n_0/\beta$. Hence, the solution of the differential equation is like presented above. Only the boundary condition at $x = 0$ is changed. This gives an additional factor $\exp \frac{1}{2} \gamma (n_0/\beta)^2$ in Eq. 6.44 for n_n . For $n_0 = 1 \cdot 10^{19} \text{ m}^{-3}$ this factor is 1.04, for a typical RTP value of $n_0 = 2 \cdot 10^{18} \text{ m}^{-3}$ it is only 1.002.

For a typical RTP discharge with $n = 5 \cdot 10^{19} \text{ m}^{-3}$ in the centre ($x = a$), $a = 0.164 \text{ m}$,

$$\beta = 3 \cdot 10^{20} \text{ m}^{-3} \tag{6.47}$$

$$\langle \sigma_{\text{ion}} v_e \rangle = 1.5 \cdot 10^{-14} \text{ m}^3/\text{s} \tag{6.48}$$

$$\langle \sigma_{\text{cx}} v_i \rangle = 2.0 \cdot 10^{-14} \text{ m}^3/\text{s} \tag{6.49}$$

$$\alpha = v_{i,i}^2 / \langle \sigma_{\text{cx}} v_i \rangle = 2eT_i / m_i \langle \sigma_{\text{cx}} v_i \rangle = 10^{22} T_i \text{ (in eV)} \tag{6.50}$$

$$\gamma^2 = \frac{\beta^2}{\alpha} \langle \sigma_{\text{ion}} v_e \rangle = 1.35 \cdot 10^5 / T_i \tag{6.51}$$

$$n_{n,0} = 2.5 \cdot 10^{16} \frac{D}{\sqrt{T_i}} \text{ m}^{-3} \tag{6.52}$$

Since α is assumed to be constant, an average value for T_i should be used. For a realistic edge ion temperature $T_i(x=0) \sim 10 \text{ eV}$ and a typical anomalous $D \sim 1 \text{ m}^2/\text{s}$, the neutral density is about 0.1% of the central n . The 1/e-width of n_n is 0.13 m for this case.

References

- [1] K. H. Burrell, K. W. Gentle, N. C. Luhmann Jr, *et al.*, Phys. Fl. **2**, 2904 (1990).
- [2] F. Wagner and U. Stroth, Plasma Phys. Control. Fusion **35**, 1321 (1993).
- [3] N. J. Lopes Cardozo, Plasma Phys. Control. Fusion **37**, 799 (1995).
- [4] ITER Physics Expert Groups on Confinement and Transport and Confinement Modelling and Database, ITER Physics Basis Editors, and ITER EDA, Nuc. Fus. **39**, 2175 (1999).
- [5] A. A. Ware, Phys. Rev. Lett. **25**, 15 (1970).
- [6] P. C. Efthimion *et al.*, Phys. Rev. Lett. **66**, 421 (1991).
- [7] P. C. Efthimion *et al.*, Phys. Fl. B **3**, 2315 (1991).
- [8] G. V. Pereverzev *et al.*, ASTRA: an Automatic system for transport analysis in a tokamak, Max-Planck- IPP, 1991, IPP 5/42, Garching, Germany.
- [9] R. K. Varma, PPCF **40**, 1999 (1998).
- [10] S. P. Hirshman, Phys. Fl. **31**, 3150 (1988).
- [11] G. Becker, Nuc. Fus. **27**, 11 (1987).
- [12] P. W. Terry, Phys. Fl. B **1**, 1932 (1989).
- [13] F. Miskane *et al.*, Phys. Plasmas **7**, 4197 (2000).
- [14] M. B. Isichenko, A. V. Gruzinov, and P. H. Diamond, Phys. Rev. Lett. **74**, 4436 (1995).
- [15] J. Nycander and V. V. Yankov, Phys. Plasmas **2**, 2874 (1995).
- [16] D. R. Baker, Phys. Plasmas **4**, 2229 (1997).
- [17] G. Becker, Nuc. Fus. **39**, 95 (1999).
- [18] G. Becker, Effect of perpendicular momentum dissipation on anomalous inward drift, IPP, 1999, 5/89, Garching, Germany.
- [19] S.-I. Itoh, J. Phys. Soc. Japan **59**, 3431 (1990).
- [20] K. Ida, S.-I. Itoh, K. Itoh, *et al.*, Phys. Rev. Lett. **68**, 182 (1992).
- [21] T. K. Chu, Phys. Plasmas **4**, 3306 (1997).
- [22] T. K. Chu, Phys. Plasmas **7**, 3537 (2000).
- [23] S. Puri, Plasma Phys. Control. Fusion **41**, L35 (1999).
- [24] A. Pospieszczyk and G. G. Ross, RSI **59**, 1491 (1988).
- [25] D. Reiter, The EIRENE code, Users manual, Jül 2599, 1992, KFA Jülich, Germany.
- [26] L. C. Ingesson, Ph.D. thesis, Technische Universiteit Eindhoven, The Netherlands, 1995.
- [27] G. M. D. Hogeweyj, N. J. Lopes Cardozo, M. R. de Baar, and A. M. R. Schilham, Nuc. Fus. **38**, 1881 (1998).
- [28] N. J. Lopes Cardozo *et al.*, Plasma Phys. Control. Fusion **39**, B303 (1997).
- [29] P. Mantica, G. Gorini, G. M. H. Hogeweyj, N. J. Lopes Cardozo, A. M. R. Schilham, and RTP Team, Phys. Rev. Lett. **85**, 4534 (2000).
- [30] M. R. de Baar, Ph.D. thesis, Technische Universiteit Eindhoven, the Netherlands, 1999.

-
- [31] V. Erckmann and U. Gasparino, *Plasma Phys. Control. Fusion* **36**, 1869 (1994), and references therein.
 - [32] B. Lloyd, *Plasma Phys. Control. Fusion* **40**, A119 (1998), and references therein.
 - [33] H. Weisen, I. Furno, T. Goodman, and the TCV team, Particle transport with high power central ECH and ECCD in TCV, private communication.
 - [34] R. F. G. Meulenbroeks *et al.*, *Phys. Plasmas* **6**, 3898 (1999).
 - [35] M. R. de Baar, G. M. D. Hogeweyj, and N. J. Lopes Cardozo, *Phys. Rev. Lett.* **82**, 89 (1999).
 - [36] D. Montgomery, L. Turner, and G. Vahala, *J. Plasma Phys.* **21**, 239 (1979).
 - [37] D. Biskamp, *Comm. Plasma Phys. Control. Fusion* **10**, 165 (1986).
 - [38] B. B. Kadomtsev, *Phil. Trans. R. Soc. Lond.* **A322**, 125 (1987).
 - [39] J. B. Taylor, *Phys. Fluids B* **5**, 4378 (1993).
 - [40] E. Minardi, *Phys. Lett.* **240A**, 70 (1998).
 - [41] K. W. Gentle, *Phys. Fl.* **31**, 1105 (1988).
 - [42] J. A. Konings, Ph.D. thesis, Universiteit Utrecht, The Netherlands, 1994.
 - [43] A. C. A. P. van Lammeren, Ph.D. thesis, Universiteit Utrecht, The Netherlands, 1991.
 - [44] G. M. D. Hogeweyj, J. O'Rourke, and A. C. C. Sips, *Plasma Phys. Control. Fusion* **33**, 189 (1991).
 - [45] J. de Kloe, Ph.D. thesis, Technische Universiteit Eindhoven, The Netherlands, 2000.
 - [46] F. L. Hinton and R. D. Hazeltine, *Rev. Mod. Phys.* **48**, 239 (1976).
 - [47] J. B. Taylor, *Natural Current Profiles in a Tokamak*, Institute for Fusion Studies, 1990, IFSR 447, Austin, Texas, US.
 - [48] M. R. de Baar *et al.*, *Phys. Plasmas* **6**, 4645 (1999).
 - [49] U. Stroth, *Plasma Phys. Control. Fusion* **40**, 9 (1998).

7

EVALUATION AND DISCUSSION

In this thesis the particle transport in the RTP tokamak has been studied. This has been done by exploring the relation between the density profile and the different thermodynamic forces. For such a study good diagnosis of the electron temperature (T_e), the electron density (n_e) and the current density (j) is essential. No routine measurement of j was available and a substantial effort has been put in the tests and error analyses of two experimental techniques to determine j . Chapter 4 contains the description and analysis of the polarimeter/interferometer and the j measurements performed with this diagnostic. Chapter 5 contains the description of the tangential Thomson scattering set-up and all data measured with it. In Chapter 6 the study of the particle transport in RTP using the transport simulation code ASTRA is reported. In this study, four transitions from Ohmic to EC heated plasmas, or vice versa, were considered. In these transitions, the profiles of T_e and j are decoupled, and q profiles are produced that differ strongly from that in an Ohmic or centrally heated discharge.

In this evaluation chapter, first the performances of the diagnostics are reviewed (section 7.1). In section 7.2 the findings of the particle transport study are summarised and the research goal as formulated in Chapter 1 is discussed. The last section, section 7.3, of this chapter is devoted to prospects for future research.

7.1 Current Density Diagnosis

7.1.1 Review of polarimetry

A triple-laser 19-channel double heterodyne polarimeter/interferometer had just become available at RTP at the start of this thesis research project. The aim of this diagnostic was to measure j over almost the full plasma diameter with sufficient spatial and temporal resolution to resolve local modifications to the j profile.

The main aspects of the performance of this set-up are the following:

- Up to 19-point profiles of line-integrated measurements of the product of the poloidal magnetic field (B_θ) and the electron density n_e are performed, while simultaneously the line-integrated n_e is measured.
- The spatial resolution of the system is comparable to the detector width of 14mm. The detectors can be shifted along the major radius over almost the full diameter of the plasma.
- The time resolution is limited by the signal-to-noise ratio. If the statistical noise is averaged to an acceptable level of 0.1° , a temporal resolution of 0.5 ms is obtained.
- The digital recording of the electric field component of the mixing frequencies gives the flexibility of numerical data analysis.
- A data interpretation routine insensitive to local structures on the measured profiles was developed. In this routine known physical constraints on the j profile are imposed on the measurements.

With this diagnostic j measurements have been obtained in discharges with current ramps, pellet injection and on- and off-axis Electron Cyclotron Heating (ECH). The results corroborate the current diffusion predicted by neoclassical theory.

However, after extensive testing it was found that the measurement suffers from a systematic error of approximately 0.3° , which could not be eliminated completely. Two possible causes were identified, which probably add up in the measurement: 1) Interference loops caused by the interaction of reflected power with the probing beam phase; 2) Diffractive distortion of the phase front by inhomogeneities in the vessel windows. Due to the systematic errors a lot of data is lost and the spatial resolution of the remaining data must be strongly reduced in the data analysis. The observed variation of the systematic error with the plasma parameters further compromises the reliability.

Despite the effort put in the development and test of the diagnostic, it is not suitable for the local time and space resolved measurements required in this thesis. To improve the system such that it satisfies these requirements would have required investments of time and money which were incompatible with the budgets of either. Therefore, it was decided to stop the efforts at this point.

As an alternative for time-resolved j measurements, the time development of j can be calculated from neoclassical theory. To test this theory, a tangential Thomson scattering set-up was developed that can measure a snapshot of the j profile. With the TTS measurements the validity of neoclassical resistivity could be confirmed in several EC heated plasma states.

7.1.2 Review of Tangential Thomson Scattering

A high resolution double recording multi-position tangential Thomson scattering (TTS) set-up was available at RTP. The extensive calibration and detailed data correction processes necessary to obtain valuable measurements have been described. The main aspects of the performance of this diagnostic are the following:

- 10-point j profiles with errors of $\sim 10\%$ extending over 50% of the plasma diameter were obtained in Ohmic plasmas and plasmas with dominant ECH. For the reduction of the statistical error to this number, 8 to 30 discharges and 16 vertical positions were averaged to yield a single data point.
- Simultaneously, vertical profiles of T_e and n_e are measured with spatial resolution of 1.5% of the RTP minor radius and relative statistical errors for a single measurement of 5-7% and 4-5%, respectively.
- Careful correction for systematic errors was possible and proved to be crucial to the obtained results on j . The correction involves:
 1. CCD offset correction at full spatial and spectral resolution
 2. Plasma light correction at full spatial and spectral resolution
 3. CCD offset correction of the plasma light measurements at full spatial and spectral resolution
 4. Comparison of measurements in negative and positive current discharges
- Analysis of the fluctuations on the measured profiles indicates that the level is enhanced for structures with a size between 7 and 20 mm.

With the TTS system j profiles have been measured in Ohmic discharges, in discharges with on- and off-axis ECH and during the relaxation after ECH switch-off. The measured steady state profiles are in agreement with neo-classical predictions.

Summary of Current Density Diagnosis

Summarising, it has not been possible to measure the j profile resolved in time. However, all the (steady state and time-resolved) experimental evidence on j obtained from the polarimeter and from TTS indicates that the j profile evolution is well described by neoclassical theory. The time scales of the relaxations are in agreement with this theory. Hence, the calculation of j from neoclassical theory is demonstrated to be a reliable alternative to the measurement of j .

7.2 Particle Transport in RTP

The aim of this thesis is to understand the behaviour of the n_e profile under different transitions of the plasma, and to use this experimental information to test expressions for the particle convection derived from theoretical models. Emphasis

was placed on the question if the particle transport can be described with a transport matrix in which off-diagonal elements play a significant role. Observations and simulations yielded the following results:

- Both particle conduction and convection have anomalous coefficients.
- The n_e profile peaks when the T_e profile flattens and vice versa.
- In discharges with central ECH, the fast, central n_e decrease is due to the change of the inward convection in the core which decreases and with counter EC current drive even changes direction.
- The density pump-out in the core at switch-on of ECH is not dependent on the ECH deposition radius. On a longer time scale the effect disappears, except for discharges with central ECH, in which effect is visible in the steady state n profile as well.
- In discharges with off-axis ECH, apart from the fast pump-out, a profile adaptation occurs on a much larger time scale (which is similar to the current diffusion time).

Results from the simulations of the transitions are summarised in Tables 6.2-6.5. The strategy was to keep the coefficients of the model expressions unchanged at the transition. The conclusions from the simulations are:

- The density pump-out in the core at switch-on of ECH is not described by any of the applied expressions.
- The density profile is relatively insensitive to the changes of the plasma parameters in the investigated transitions. It varies less than predicted by the expressions derived from theoretical models.
- During transition periods, we have observed 'events' in the density profile that are very well defined in space and time. These events are very reproducible and are not associated with MHD activity. They are not predicted by any of the expressions considered.

The density profile is remarkably stiff. The variation of the n profile is modest, even when the expressions for the convection derived from theoretical models predict strong changes. The density profile also varies less than is necessary for profile consistency to hold. The final density profile shape is best described by the simulation with an empirical, fixed change of the convection coefficient at the transitions. But, even simulations in which all transport coefficients are kept fixed at their 'Ohmic' values, do relatively well.

The relatively good performance of these models suggests that the description of the particle transport with a transport matrix is a proper description. The empirical models for the convection are remarkably simple. Though part of their success is due to the stiffness of the n profile, this observation proves that the transport matrix can be successful.

The bad news was that the expressions for particle transport derived from theoretical models, generally performed poorly. The best results were obtained with thermo-diffusion models, *i.e.* models in which the T_e gradient drives a convective particle flux. We should remark here that we have tested expressions which are derived from more complex physical mechanisms. It is well possible that they are a too much simplified representation of the physics. Therefore, although we have found that the expressions perform badly, we cannot reject the physical bases of these expressions. But, certainly, the predictive power of the expressions as they are published, is very limited.

It can be argued that the combined observation of the n profile stiffness and the reproducible, local variations of the n profile calls into question the validity of the transport matrix formalism. It is possible that a transport matrix with strongly varying coefficients gives the convection observed in this thesis. On the other hand it might be more favourable to formulate such an inhomogeneity differently. We must consider the possibility that transport is dominated by essentially two-dimensional structures such as convective cells and filaments. Such a system could show intermittency, and a description of transport as one-dimensional diffusion and convection may be inadequate.

7.3 Future Research

A varied set of observations on the particle transport has been presented and not all the observations have been studied in detail. The results have not been unified in a grand model for the particle transport. It is important that the RTP results are included in the global picture of particle transport because of the unique experimental conditions under which they were performed: Weak electron-ion thermal coupling, dominant ECH and high resolution T_e and n_e diagnostics. The experiments described in Chapter 6 of this thesis are unique in their extreme variation of the T_e and q profiles.

From Chapter 6 it is apparent that the particle transport is subject to several effects, with several time constants. Therefore future transport experiments should aim at the decoupling of the plasma parameters like T_e , n_e , j and p_e , to clarify the mutual dependencies. The occurrence of density pump-out with off-axis ECH should be verified on other tokamaks.

There is a clear need for theoretical considerations leading to realistic predictions of the complex multiple relations of the particle transport and the plasma parameters as well as the opposite behaviour of density and temperature profiles. It may be necessary that the physical processes are treated fully numerically, since the simplified, one-dimensional transport expressions tested in this thesis appeared to be inadequate.

DANKWOORD

Onvermijdelijk in het proefschrift is een dankwoord, want welke promovendus is geen dank verschuldigd aan vele helpende handen. Onvermijdelijk is het dankwoord daarom ook een meer of minder lange opsomming. Onvermijdelijk is het dankwoord helaas ook onvolledig. Daarom wil ik hen die ik in het komende onbedoeld ben vergeten, bij deze hartelijk bedanken voor hun bijdrage aan de totstandkoming van dit proefschrift.

Ik wil mijn promotor Niek bedanken, die vaak met een vroege versie van een deel van dit werk in een vliegtuig of trein moet zijn gesignaleerd. Door zijn scherpe observaties wist hij mij steeds op het juiste spoor te rangeren. Met zijn vliegensvlugge formuleringen markeerde hij de juiste koers.

Mijn copromotor en begeleider Dick had altijd een tomeloze inzet. Ondanks zijn vele werk, bleef zijn deur toch open staan, zodat ik altijd kon binnenlopen om een antwoord op mijn vragen te krijgen. Als hij het antwoord niet wist, wat niet vaak gebeurde, zei hij dat ook eerlijk. Samen discussiërend kwamen we dan toch een heel eind.

Gedurende de eerste jaren zat ik met Jeroen, Theo en Jaco in het Interpol-team. Dat team heeft veel tijd gestoken in de speurtocht naar het onzichtbare. En vele keren zijn wij de trap afgestormd om de frequenties van de laser precies af te stellen. Ik hoor nog het gongachtige gerinkel van het laserwaarschuwingsbordje tegen de deur, als je die in volle sprint openrukte.

Daarna zat ik in het T-team: Het Thomson team. Met Marc, Hennie, Oktay en Eric heb ik vele uurtjes in het donker doorgebracht, omringd door optica ingepakt in zwart karton en turend naar zoenvormige data op een zwartwit-monitor. Ook heb ik kunnen proeven en genieten van de fabelachtige kennis van Thomson verstrooiing van Roly. Ik herinner mij de keren dat we in het laserhok stonden: 'Nu allemaal even je ogen dicht, jongens'.

Ik wil ook graag de leden van het voormalige RTP team roemen voor hun on-

voorwaardelijke inzet, vaak tot in de late uurtjes. Cor, Paul, Jeroen, Ogé, Marlies, Raymond, Remco, Simon, Bart, Noud, Tony, Ruud, Martin, Peter, Wim, Christina, Christian, Ralph, Hans, Frans, Erik, Ben: Bedankt voor jullie betrokken medewerking om de meetsessies tot goed resultaat te brengen en zo soepel mogelijk te laten verlopen. Dat is de grote kracht van Rijnhuizen: De verregaande bereidwilligheid van een ieder om in goede sfeer het onderzoek en al haar deelonderzoekjes en projectjes te ondersteunen en verder te helpen. Ik hoop dat tot in de verre toekomst het unieke karakter van Rijnhuizen als gezellig topinstituut mag blijven bestaan.

Ook wil ik André en Erik bedanken. Zij vormden een helpdesk zoals je je die wenst: je krijgt niet alleen antwoord, er wordt zelfs aan je problemen gewerkt.

I would like to thank prof. dr. Detlev Reiter for our pleasant collaboration. Unfortunately, our effort to understand the behaviour of the neutrals in RTP with the help of his code EIRENE, as described in Chapter 6, was ended preliminary by a snow storm. I am also grateful to dr. Pereverzev for making available the ASTRA transport code which is used in Chapter 6.

De middagpauzes waren altijd goed gevuld met een stevige pot voetbal. De emoties liepen soms hoog op, maar onder de douche was alles al weer vergeven. Voetballers, bedankt dat ik af en toe ook een bal in het doel mocht schoppen.

Hajnal wil ik bedanken voor de diepgaande wandelingen rond het fort en door het park. Je hebt de gave mensen die niet praten te laten praten.

Marco, Marc, Gert Jan, Jos, Francisco, mijn kamergenoot Arnold (die veel warmer is dan hij zelf wel denkt) en ik: Samen vormden wij niet alleen een generatie, maar ook een soort vriendenclub van OIO's op het lab. Ik zal die club missen.

Zonder mijn ouders was dit alles niet mogelijk geweest. Max en Anke, en mijn broers Rutger, Anne en Chris, en Opa en Oma: zij bleven altijd in mij geloven, ook in de (soms) diepe dalen tussen de toppen. Bij Dinda, mijn meisje, vond ik onvoorwaardelijke en broodnodige, emotionele steun. Zij kon aan de stand van mijn neus altijd al zien, hoe ik me voelde, en speelde daarop in.

Tot slot wil ik RTP zelve bedanken, ondanks het feit dat zij haar geheimen nukkig en met grote vasthoudendheid binnen haar ijzeren jukken voor mij verborgen probeerde te houden.

CURRICULUM VITAE

Ik ben geboren op 5 januari 1971 aan de Frankenslag in Den Haag, als zoon van Max en Anke Karelse. Na twee jaar in Maassluis te hebben gewoond, verhuisden wij naar Dordrecht. Daar doorliep ik de basisschool 'De Keerkring' en de middelbare school 'Titus Brandsma College', de laatste afgesloten met een diploma atheneum.

In die tijd ben ik ook actief geworden in de Nederlandse Jeugdbond voor Natuurstudie (NJN). Ik werd opgenomen in de bestuurlijke structuur van de jeugdnatuurclub, uiteindelijk resulterend in het penningmeesterschap in het hoofdbestuur. Op leeftijd gekomen ben ik lid-af gemaakt en sta ik als 'ouwe sok' in de boeken.

Ik heb Technische Natuurkunde gestudeerd aan de Universiteit Twente in Enschede, in maart 1995 afgerond met een diploma en een afstudeerscriptie getiteld 'On the Kosterlitz-Thouless phase transition'. Ik was toen al vanaf 1 februari aan de slag als Onderzoeker In Opleiding (OIO) op Rijnhuizen. Het onderzoek vanaf die datum tot nu is neergeslagen in dit proefschrift.